The Convective instability of non-Newtonian of boundary-layer flow over rough rotating-disk

Department of Engineering, University of Leicester

PhD Thesis

This report is submitted in fulfilment of requirements for the degree of Doctor of Philosophy in Mechanical Engineering and Applied Mathematics.

Department of Engineering, University of Leicester 2021

The Convective instability of non-Newtonian of boundary-layer flow over rough rotating-disk

Aishah Alqarni

Abstract

This thesis considers the local linear convective stability behaviour of non-Newtonian boundary-layer flows over rotating disks and the effects of surface roughness. A non-Newtonian fluid is modelled via the Carreau model, which represents a type of generalised Newtonian fluid. Using the Carreau model for a range of shear-thinning and shear-thickening fluids, we determine, for the first time, steady-flow profiles under the partial-slip model for surface roughness. The partial-slip approach of Miklavčič & Wang [1] is modified in such a way that the viscosity is no longer constant and depends on the shear rate. The non-linear ordinary differential equations are reduced via the introduction of a suitable similarity solution. The stability equations are solved to obtain the disturbance eigenfunctions and to plot curves showing neutral stability using the Chebyshev collocation method. The stability of a non-Newtonian boundary-layer flows is investigated with different boundary conditions: the no-slip boundary conditions and the partial-slip. Thereby the neutral curves for the convective instabilities associated with the boundary-layer flow due to a rotating disk can be determined over a broad range of parameter values. The subsequent linear stability analyses of these flows indicate that isotropic and azimuthally anisotropic surface roughness leads to the stabilisation of both shear-thinning and -thickening fluids. This is evident in the behaviour of the critical Reynolds number and growth rates of both Type I (inviscid cross flow) and Type II (viscous streamline curvature) modes of instability. The underlying physical mechanisms are clarified using an integral energy equation.

Acknowledgments

Upon to the completion of this research, I am grateful to a number of people, as without their help I could not have completed this work. Due to that, I would like to thank the following people as they have a great contribution to this research.

Foremost, I would like to express my deepest appreciation to my supervisor Prof. Stephen Garrett for the continuous support of my PhD study and research, for his patience, motivation, enthusiasm, and immense knowledge. His guidance helped me throughout the research and writing of this thesis. I could not have imagined having a better advisor and mentor for my PhD study.

Besides my supervisor, I would like to thank Dr. Paul Griffiths and Dr. Burhan Alveroğlu for their encouragement, insightful comments, and hard questions. My sincere thanks also goes to Dr. Antonio Segalini, for offering me the internship opportunities in his group at KTH, Sweden and leading me to working on diverse and exciting projects.

Financial support from the Saudi Embassy is also gratefully acknowledged. Many thanks to the School of Engineering in the University of Leicester for providing me with the resources and workspace necessary to complete this thesis.

Last but not the least, I also take this opportunity to express a wealth of gratitude to my parents, my brothers and sisters for their moral, personal support, constant encouragement and motivation. My heartfelt thanks to my husband, Abdulaziz Alqarni, for his love, support, encouragement and his spiritually in every step of my life. I also would like to thank my cute little daughter Joanna Alqarni, for giving me unlimited happiness and pleasure in my life. Special thanks to the many friends I have made during my stay in Leicester for bringing me so many joyful moments.

Contents

List of Figures

Chapter 1

Introduction

Problems of hydrodynamic stability have been used to investigate the transition mechanisms of three-dimensional boundary layers. The problems are an important subject in fluid mechanics, because they help in the understanding prediction, and control of the associated phenomena required in the fields of mechanical engineering. The underlying principle of stability analysis imposes small perturbations on a mean flow. If the disturbances decay, the flow at that point is stable. However, if they grow as time progresses, the flow is unstable. Such an unstable disturbance can affect flow in two ways referred to as convective and absolute instabilities (see Figure 1.1). Indeed, there are many experimental and theoretical reports of flow phenomena in the literature. They provide an excellent basis for understanding linear stability, including the neutral curve for the upper and lower branches, stationary and travelling modes (for more details, see Schmid & Henningson [5], Drazin [6] and Huerre [7], [8]).

The pioneering study of the steady incompressible flow was induced by the rotation of a smooth, infinite plane with a fixed angular velocity was performed by Kármán [9]. He revealed that the accurate solution for the Navier-Stokes equations was a constant incompressible flow brought by rotating infinite plane at a uniform angular speed. Later, Cochran [10] produced the first accurate numerical result for von Kármán's equations that solved the mean flow in the laminar region. Therefore, by introducing an appropriate similarity solution, the governing partial differential equations (PDEs) for the aforementioned boundary layer flows can be transformed to a set of coupled ordinary differential equations (ODEs).

The lack of a radial pressure gradient near the disk is a characteristic of the boundary-layer flow. It helps the centrifugal forces to balance; therefore, the fluid comes out in the radial direction. As for the disk which behaves as a centrifugal fan, it moves the outgoing fluid replaced by an axial flow at an

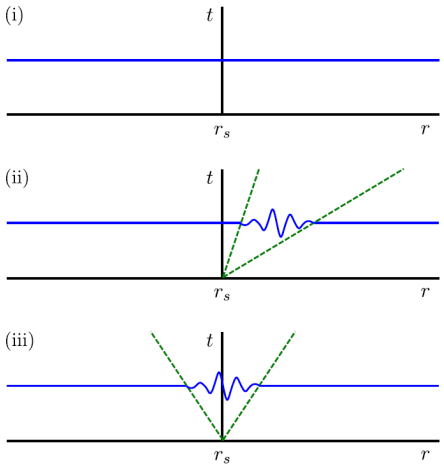

Figure 1.1: A sketch of various disturbances (i) stable, (ii) convectively unstable, and (iii) absolutely unstable. Reproduced from Griffiths' thesis [2].

angle to the surface. According to Batchelor [11], this sort of flow is indeed a restricting case of various flows that have similarity solution. During these flows, each fluid along with the infinite plane rotates infinitely with different angular speeds. However, as Bödewadt [12] later identified the restricting case for times when the infinite plane was motionless although the fluid rotated infinitely at a steady angular speed.

Gregory, Stuart & Walker [3] aimed to understand the flow of the boundary layer on the swept wing and examined the steadiness of the Kármán boundary layer for the first time. Since flows are subject to reciprocal flow instabilities, show flexural speed profiles. On the other hand, the rotating disk drawback is easy to examine because it provides an explicit answer to the Navier-Stokes equations, adding that it is complicated to model by experimentation. Also, the researchers investigated the spiral states of instability and observed them as rotational vortices. By using clay-porcelain techniques, Gregory and Walker made an experiment to observe the laminar-turbulent transition. This helped them to measure the normal-radius vector angle and the tangent-vortices that were around 13.

Theoretically speaking, Stuart proposed a linear stability analysis of a high Reynolds number that flowed and tended to be turbulent. He predicted the wave angle of the disturbances which was in agreement with the outcomes of Gregory and Walker's experiments. Based on studies by Gregory *et al.* [3], Figure 1.2 shows what happens when the radius of the disk increases; i.e spiral vortices, laminar flow, and advanced turbulent flow occur. It is obvious that such experiments, which are performed solely through visualization, only show

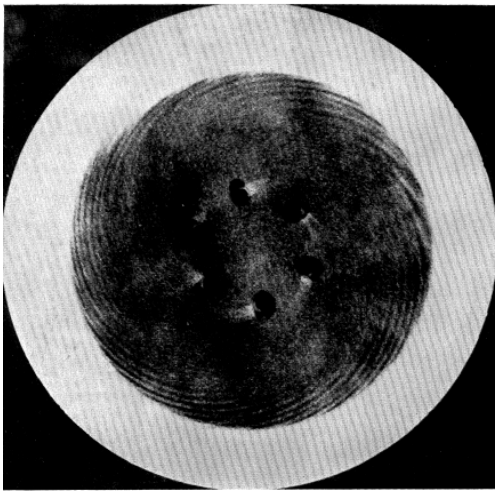

Figure 1.2: Visualization of the flow rotating disk using china-clay record, reproduced from Gregory *et al.* [3], to observe the transition from laminar to turbulent flow.

standing waves and disturbances that are immobilized in line with the disk's movement. Nevertheless, because the rotating disk boundary-layer is at risk of moving wave disturbances, experiments have been performed to analyse the instabilities of this matter (see Lingwood [13]). Similar to the von Karman's boundary-layer studies by Gregory *et al.* [3], it is argued that at low Reynolds number ($Re = \Omega Re^2 \nu$), the fluid tends to be smooth, and the flow occurs in circular wave shapes at low Reynolds number. Therefore, when the Reynolds number increases, its velocity governs, thereby allowing more spiral vortices to emerge and exist along with circular wave shapes. In other words, the higher the Reynolds number, the fewer these circular waves become until they vanish. As a result, spiral vortices turn into the flows dominant behaviour. This condition is a somehow chaotic and turbulent, and, as a result, it becomes difficult to distinguish spiral structures.

Moreover, the study of stationary disturbances with the rotating disk boundary layer was numerically conducted by Malik for the first time [14]. He calculated the neutral stability curves by a sixth-order system of linear disturbance equations. He also employed a parallel-flow approximation, to focus attention on the flow's local stability behavior. Similar to the previous research studies, there are two types of distinct neutral branches, namely an upper-branch referred to as type I and a lower-branch, referred to as type II. These numerical results were confirmed by the linear asymptotic analysis of Hall [15]. He retrieved Type I resolution proposed by Gregory [3] and modified later by Gajjar [16]). As Hall argues, there is an extra short-wavelength mode whose structure is proved by the balance between the Coriolis and the viscous forces. This

mode directly relates to Type II branch.

To expand the theory of the rotating disk, a rotating BEK boundary-layer flows system was considered by Lingwood & Garrett [17]. This class includes a family of rotating flows such as Bödewadt, Ekman and von Kármán's boundary layer. Their result indicates that a high Rossby number (a number that has no dimension to determine variations in differential rotation) leads to a high instability of flows (flows in both the absolute and convective senses). Moreover, the beginning of absolute and convective non-stability modes occur around the same time with a small Reynolds number in Bödewadt's boundary-layer. Figure 1.1 displays schematic sketches of various types of behaviours for disturbances(i) stable, (ii) convectively unstable and (iii) absolutely unstable. For case (i), the disturbances dissipate so that the fluid is damped and stable at certain point, whilst for (ii) the disturbances are convected away form the source. For the absolute instability, i.e. case (iii) the localised disturbances propagate, both down and up streams. The convective and absolute instabilities are related to a disturbances growth in time and space respectively.

Further research interests have addressed transition and the stability of the boundary-layer on cones and rotating spheres. Indeed, the inherent association with spinning projectile applications has been an incentive to advance this investigation and learn more about the delay of laminar-turbulent transition within such systems. Regarding the boundary layer of the rotating sphere, Garrett & Peake [18] state that the cross-flow mode prevails for latitudes below $\theta = 66°$. As for higher latitudes, the streamline curvature mode is marked as dangerous.

For broad cones, the instability mechanism appears as co-rotating vortices, and for slender cones, counter-rotating vortices are detected, Garrett, Hussain & Stephen [19] conducted a study to examine the stability of the boundary layer on a rotating cone. This cross-flow study resonates with experimental data for cones with a half-angle of more than forty. Yet, for the cones that are half-angle less than forty, another formula with an emphasis on centrifugal effects is needed, Hussain, Garrett & Stephen [20]. Therefore, there is a favourable agreement with experimental data again, this time for cones with a half-angle less than forty.

1.1 *Non-Newtonian boundary-layer flows*

The non-Newtonian flow is essentially an importation in the nature and it has many applications in engineering. The behaviour of the fluid can be affected by many different characteristics. Is important to mention that the viscosity determine the behaviour of the fluid. Therefore, the fluid can be divided into two sections: Newtonian and non-Newtonian fluids. For the Newtonian flow the viscosity independent from the shear rate i.e (the viscosity is constant). Moreover, in the Newtonian fluid the relation between the strain and the shear stress is linear. A non-Newtonian fluid has different properties from Newtonian fluids. Most commonly the viscosity of non-Newtonian fluid may change with shear rate and it is not independent of the share rate itself. Roughly non-Newtonian fluids can be classified into three types according to the relationship between the shear stress and shear rate : time-independent which including (purely viscous, inelastic or generalised Newtonian fluids),viscoelastic and time-dependent fluids. Depending on how the apparent viscosity changes with shear rate the flow behaviour of non-Newtonian flow is characterized as follows: shear-thickening, shear shear-thinning and a Generalised Newtonian fluids. Shear-thinning characterised by apparent viscosity which gradually decreases with increasing shear rate. Conversely, shear-thickening the apparent viscosity of this fluid increases with increasing shear rate.

There are many research studies on generalised Newtonian flow due to rotating disks. As for the von Kármán's similarity to include the power law governing viscosity relation, Mitschka [21] amended the von Kármán rotating disk-flow. In this case, a boundary-layer estimation is required to provide definite generalised Navier-Stokes equations along with the base flow. The main flow resolutions for shear-thickening and shear-thinning power-law fluids are presented by Ulbrecht & Mitschka [22] and Andersson *et al.* [23]. Although the authors did not match the boundary layer solutions with the external flow, Denier & Hewitt [24] proposed modified solutions for each of these cases. In addition to solving this problem, they showed that the structure of solutions shear-thickening and shear-thinning fluids were fundamentally different.

Recently, the base flows for various generalised Newtonian models have been derived by Griffiths [25]. This work is extended by the same author to generate the neutral curve of convective instability utilising asymptotic and numerical methods. He also improved power law studies to include different models such as the Bingham [26] and Carreau [27] models of non-Newtonian fluids. As Griffith argues, the von Kármán similarity solution can be applied when the Carreau model is used instead of power-law and Bingham models. In

addition, Griffiths *et al.*[28] carried out an asymptotic stability analysis of the shear-thinning boundary-layer flow over a rotating disk for various generalised Newtonian models. Interestingly, they identified an agreement between the results of asymptotic analysis and numerical solutions.

1.2 *Rough rotating disk*

The impact of roughness on the boundary-layer flow, however, has been found to represent a greater importance. This is because roughness is beneficial to the stability of the flow and helps to control and reduce drag Carpenter [29]. Besides, many studies have found that carefully applied drag reduction on rough surfaces can delay the transition to turbulence for most technological applications. Therefore, studies in this area could be clearly beneficial (Carrillo *et al.* [30]; Fransson *et al.* [31]).

However, less attention is given to non-Newtonian flow and its interaction with roughness. For this reason, this project aims to study the effect of a distributed roughness on the incompressible rotating disk boundary-layer. It intends to examine how a distributed roughness can impact the points of initial instability, the transition location, and the behaviour of the stationary vortices. The study uses the Chebyshev method to carry out a linear stability analysis. The numerical method is an extension of the stability work done by Alveroğlu [32]; however, it incorporates the method developed by Miklavčič & Wang [33] to add roughness to the disk surface.

Two theoretical models exist in the literature to describe steady boundary layer flow over rough rotating disks. The models are introduced by Miklavčič & Wang [33] and Yoon *et al.* [34] and are herein referred to as the MW and YHP models, respectively. Both models demonstrate how surface roughness can lead to modifications in the classic von Kármán solution over a smooth disk. Nevertheless, the two models are fundamentally different in their formulations. For example, the YHP model imposes a surface roughness function on the disk surface along the radial direction and assumes rotational symmetry. Consequently, it leads to a particular case of anisotropic roughness composed of concentric grooves. The roughness is thus felt as one traverses the disk in the radial direction. In contrast, the MW approach models the surface roughness by replacing the usual no-slip conditions at the disk surface with partial-slip conditions. By modifying the boundary conditions in the radial and azimuthal directions, the MW approach can independently model roughness in these two directions. This leads to isotropic roughness when the roughness parameters

are identical in both directions and to anisotropic roughness when they differ. Due to its greater flexibility, the MW approach has received considerable attention with regard to Newtonian fluids; accordingly, it will be used throughout the course of the current investigation.

Under the MW formulation, Cooper *et al.* [35] examined the possibility of delaying the onset of instability within the rotating disk system via the introduction of distributed surface roughness. The convective stability analysis examined both isotropic and anisotropic surface roughnesses and led to the clear conclusion that surface roughness stabilised Type I mode. In contrast, Type II mode is significantly destabilised by anisotropic roughness in the form of the concentric grooves. Following this, Garrett *et al.* [36] considered the effects on the stability predictions of using the two roughness models. Similar results were found under the MW and YHP models for Type I modes; however, differences in the response of Type II mode were observed. That is, Reynolds-stress energy production increases with increasing roughness, where the increase is slightly less pronounced for the YHP model than for the MW one.

Complementary research continues using the MW model. For example, Stephen [37] has recently confirmed the neutral curve described by Cooper *et al.* using a rigorous asymptotic approach. Furthermore, Alveroglu *et al.* [32, 38] have extended Cooper *et al.*'s work to the entire BEK family of boundary layer flows (i.e., Bödewadt, Ekman and von Kármán). Again, surface roughness was found universally stabilising for the dominant Type I mode. However, increased concentric grooves destabilise Type II mode as it moves upstream and eventually becomes the critical mode at the lowest Reynolds number. In general, it is possible to have a delay in laminar-turbulent transition; however, it seems necessary to use the appropriate type of surface roughness. There is a space for a lot of room for future research on this issue, and the authors tend to conduct an experimental research studies to confirm these theoretical outcomes.

1.3 *Motivation and aim of the current study*

The author of this study was motivated by the problem posed by Schlumberger [*] regarding the erosion of calcite disks when they are rotated and submersed in acidic solutions. The problem was addressed by researchers at King Abdullah

[*]The world's largest oil field services company.

University of Science and Technology (KAUST) in association with the Oxford Centre for Collaborative Applied Mathematics (OCCAM) in 2011 (Figure 1.3). In this work, the fluids are assumed to be Newtonian and report on it as as "mass transfer modeling in a rotating disk reaction vessel" which is accessible online.

Since the report was used to model the reaction between the acidic fluids and the calcite rotating disks, the problem had to be investigated chemically and mathematically. Arguably, fluids are considered Newtonian during the building of the mathematical model. However, in practice, gelling agents are often added to acidic fluids to reduce the reaction rate of fluids with calcite discs. Introducing these gelling agents changes the vicious structure of the fluids completely; therefore, the gelled acids act as non-Newtonian shear-thinning fluids in these experiments.

To add more accuracy and details to the experimental setup and procedure, Schlumberger representatives provided the study group with supplementary materials together with the previous experimental data (see Al-Mohammad, Nasr-El-Din, Al-Fuwaires & Al-Aamri [4]). For example, Nasr-El-Din *et al.* [4] used the power-law constitutive relationship to model gelled acidic fluids. According to Figure 1.3, the etching pattern of swirling flow is observed on the calcite disk. So, it becomes more pronounced as the Reynolds number of the flow increases. On the other hand, there are significant similarities between the experimental imageries and the images taken by Gregory *et al.* These observations helped to formulate the research questions in the present study which became the basic content for this thesis.

Figure 1.3: Calcite disks used during experiment. Reproduced from Nasr-El-Din *et al.* [4].

In light of the above studies, it is important to consider a non-Newtonian flow due to a rough surface using the Carreau [27] model. The present study will determine the stability of the three-dimensional boundary layer of a generalised Newtonian fluid when the no-slip boundary condition is replaced by a partial-slip condition. To date, there has been relatively little work on the analysis of Carreau-type fluids taking into account the effects of surface rough-

ness. From here, we aim to fill the associated gap in the existing literature. In this work we will combine the work by Griffiths on the non-Newtonian flow for the Carreau model [25] with the MW approach [1]. Following the method suggested by Sahoo [39], the boundary condition is derived with some modifications to the viscosity because the viscosity is no longer constant and depends on the shear rate.

Our main goal is to investigate how successively increasing levels of distributed surface roughness and different roughness types affect the transition and the overall flow of the generic fully 3D rotating-disk boundary layer. The approach is split into two distinct, but closely interconnected, sections of experimental and theoretical research. A further goal of this preliminary investigation is to clarify the modifications to the well-known stability characteristics of smooth disks with increasing levels of roughness; following this, the possibility of a potential bypass transition will be studied. There is a growing interest in the literature about the effects of non-Newtonian boundary layer flows. Fundamental to the modelling of non-Newtonian flows is the underlying viscosity model, where a good overview of the most widely used models can be found in [40]. Mitschka [41] was the first to generalise the von Kármán solution to non-Newtonian flows using a power law fluid. More recently, the base flows for various generalised Newtonian models have been derived by Griffiths [42]. He then proceeded to explore convective instability characteristics of the models[43, 44], utilising both asymptotic and numerical methods. In particular, the power law studies are extended to include more sophisticated models due to Bingham [45] and Carreau [46]. Griffiths demonstrates that, unlike the power law and Bingham models, the Carreau model preserves the von Kármán similarity solution, which has certain mathematical advantages within the formulation. Furthermore, the Carreau model is highlighted in this study due to the limitations of the power law, especially for very low and very high shear rates. In general, the linear stability analyses of the rotating disk boundary layer have revealed that different results are reached when power law shear-thinning results are compared to those from the Carreau fluid mode [2]. Thereby, the growing interest in Carreau fluids has been the motivation for the current investigation. Motivated by the above work, the effects of surface roughness on the convective instability will be considered using two different boundary conditions.

In light of the above points, this thesis aims to analyse the convective stability of non-Newtonian fluids with the effect of roughness surface disturbances for the rotating disk. As for the thesis structure, it is organised as follows. Chapter 2 briefly introduces the class of non-Newtonian fluids known as generalised Newtonian fluids. It then goes on to derive the governing steady mean flow equations using the MW model. The perturbation equations and

the energy analysis are formulated in the same chapter. The flow solver and the spectral Chebyshev method are included, too. Chapters 3, 4 and 5 examine the effects of surface roughness generated by azimuthally anisotropic roughness (radial grooves), radially anisotropic roughness (concentric grooves) and isotropic roughness, respectively. Chapter 6 analyses the effects of shear-thinning and shear-thickening on roughness surface to identify a range of roughness parameters. In each of these chapters, the steady mean flow solutions are provided and convective neutral stability curves and the growth rate are illustrated. These results are confirmed by conducting an energy balance analysis at the location of the maximum amplification of each instability mode. This is because the energy balance approach provides deeper insights into the physics of the stabilisation process. Finally, Chapter 7 summarises the central argument of each chapter and brings together the different findings from the chapters. Finally, a future work section is presented to highlight how the scope of this thesis could potentially be extended.

A significant portion of the work presented in Chapter 6 has been presented in the following publication:

1. **Alqarni, A. A., et al. "The instability of non-Newtonian boundary-layer flows over rough rotating disks." Journal of Non-Newtonian Fluid Mechanics 273 (2019): 104174**.

The published work focuses on the mean flow, neutral stability, energy analysis and growth rate for Carreau model rotating disk with the effect of roughness parameters. An additional publication entitled "Application of new partial-slip boundary conditions to non-Newtonian flow over a rough rotating disk" is currently in preparation for submission to the Journal of Fluid Mechanics (JFM). Parts of this paper are presented in Chapters 3, 4 and 5.

Chapter 2

The governing equations of the non-Newtonian flow

This chapter examines the governing equations of a non-Newtonian fluid over a rough rotating-disk. The generalised Newtonian fluid and governing equations are first established in 2.1. The governing equations are then dimensioned and scaled to the boundary layer region close to the disk surface where, the problem is reduced to a set of ordinary differential equations using similarity solutions, as is seen in 2.2 and 2.3. Then, the system is solved using boundary value problem solver, bvp4c, for both shear-thinning and -thickening fluids under the Carreau model in 2.3.1. The formulation of the linear convective instability associated with the generalised Newtonian boundary-layer flow on a rotating disk is outlined in 2.4. After that, the eigenvalue problem represented by the linear perturbation equations is solved with the Chebyshev collocation method in 2.4.1. Finally, the energy analysis is given in 2.5.

2.1 *Generalised Newtonian fluids*

The viscosity of a non-Newtonian fluid changes with the shear rate, as is observed in many industrial processes and flow problems such as lubrication and polymer processing. This change in the viscosity, often by two or three orders of magnitude, cannot be ignored. The modification of Newton's law of the viscosity to allow for the viscosity change with shear rate was empirically derived by Bird, Armstrong & Hassager [40]. The model is commonly known to lead to a *generalised Newtonian fluid*.

The constitutive relation for a Newtonian fluid in a simple flow has a constant viscosity at all shear rates. From this definition, the following governing relationship for an incompressible Newtonian fluids occurs

$$\boldsymbol{\tau} = \mu\dot{\boldsymbol{\gamma}}, \tag{2.1}$$

where τ is defined as the shear stress tensor, the parameter μ is the fluid viscosity that is assumed to be constant in Newtonian fluid. The quantity $\dot{\boldsymbol{\gamma}} = \boldsymbol{\nabla u} + (\boldsymbol{\nabla u})^T$ is the rate of deformation tensor for an arbitrary flow field $\boldsymbol{u} = \boldsymbol{u}(x, y, z, t)$ in an arbitrary coordinate system. Therefore, shear stress is a linear function of the shear rate in the Newtonian fluid.

$$\mu(\dot{\boldsymbol{\gamma}}) = \frac{\dot{\boldsymbol{\gamma}}}{\boldsymbol{\tau}}, \tag{2.2}$$

For generalised Newtonian fluids, the constitutive relation is given by

where μ is a scalar and is a function of the invariants of the tensor (i.e., viscosity function depending on the invariants of the tensor $\dot{\gamma}$). Also, it can be defined as $\mu = \mu\dot{\gamma}$ where $\dot{\gamma}$ values are independent of the choice of coordinate system. The three invariants are defined (see Bird *et al.* [40]) by selecting the following tensor component combinations:

$$\begin{aligned} I &= tr\dot{\boldsymbol{\gamma}} = \sum \dot{\gamma}_{ii}, \\ II &= tr\dot{\boldsymbol{\gamma}}^{\mathbf{2}} = \sum_i \sum_j \dot{\gamma}_{ij}\dot{\gamma}_{ji} = \sum \dot{\gamma}_{ij}^2, \\ III &= tr\dot{\boldsymbol{\gamma}}^{\mathbf{3}} = \sum_i \sum_j \sum_k \dot{\gamma}_{ij}\dot{\gamma}_{jk}\dot{\gamma}_{ki}. \end{aligned}$$

For the incompressible fluids given $\dot{\boldsymbol{\gamma}} = \boldsymbol{\nabla u} + (\boldsymbol{\nabla u})^T$, the first invariant is clearly zero (i.e. $I = 2(\boldsymbol{\nabla . u}) = 0$). Also, the third invariant III vanishes to zero for flows dominated by shearing, such as axial annular flow, tube flow and the flow between rotating disks (Bird *et al.* [40]). Thus, more attention should be given to the second invariant II because μ depends only on the second invariant of the rate-of-strain tensor for the type of flow considered within this thesis. The quantity μ is assumed to be a function of II only. The second can be expressed in terms of $\dot{\gamma}$, the magnitude of $\dot{\boldsymbol{\gamma}}$ is given by

$| \dot{\boldsymbol{\gamma}} | = \dot{\gamma} = \sqrt{(\dot{\boldsymbol{\gamma}} : \dot{\boldsymbol{\gamma}})/2}$. The double dot operation is defined by ([2]) as

$$\begin{aligned}
(\dot{\boldsymbol{\gamma}} : \dot{\boldsymbol{\gamma}}) &= \Big[\Big(\sum_i \sum_j \boldsymbol{\delta_i}\boldsymbol{\delta_j}\dot{\gamma}_{ij}\Big) : \Big(\sum_k \sum_l \boldsymbol{\delta_k}\boldsymbol{\delta_l}\dot{\gamma}_{kl}\Big)\Big] \\
&= \sum_i \sum_j \sum_k \sum_l (\boldsymbol{\delta_i}\boldsymbol{\delta_j} : \boldsymbol{\delta_k}\boldsymbol{\delta_l})\dot{\gamma}_{ij}\dot{\gamma}_{kl} \\
&= \sum_i \sum_j \sum_k \sum_l ((\boldsymbol{\delta_j}\dot{\boldsymbol{\delta}}_{\boldsymbol{k}})(\boldsymbol{\delta_k}\dot{\boldsymbol{\delta}}_{\boldsymbol{l}})\dot{\gamma}_{ij}\dot{\gamma}_{kl} \\
&= \sum_i \sum_j \sum_k \sum_l \delta_{il}\delta_{jk}\dot{\gamma}_{ij}\dot{\gamma}_{kl} \\
&= \sum_i \sum_j \dot{\gamma}_{ij}\dot{\gamma}_{ji} = \sum_i \sum_j \dot{\gamma}_{ij}^2 = II
\end{aligned}$$

Regarding the literature, the generalised Newtonian viscosity is a function of the shear rate. This means that the viscosity of non-Newtonian fluid is commonly written as $\boldsymbol{\tau} = \boldsymbol{\mu}(\dot{\gamma})\dot{\boldsymbol{\gamma}}$.

A number of empirical relationships for generalised Newtonian fluids have been investigated in the literature. The most commonly used types of generalised Newtonian fluids models are Power law, Carreau, and Bingham models. These models are studied to determine the relation between shear stress and shear rate. The most popular model is Power law model (Ostwald).

The Power law, Bingham [26] and Carreau-Yasuda models are expressed respectively as:

$$\mu = m(\dot{\gamma})^{(n-1)},$$

$$\mu = \begin{cases} 0, & \tau \leqslant \tau_0 \\ \mu_p + (\frac{\tau_0}{\dot{\gamma}}), & \tau \geqslant \tau_0, \end{cases}$$

$$\mu = \mu_\infty + (\mu_0 - \mu_\infty)\big[1 + (\lambda\dot{\gamma})^a\big]^{(n-1/a)}.$$

Here, m is the consistency coefficient and n is the flow behaviour index. When $n < 1$ the fluid is shear-thinning, and for $n > 1$ the fluid is shear-thickening. For $n = 1$, $\tau_0^* = 0$ and $\mu_0^* = \mu_\infty^*$ and the fluid is returned to a Newtonian flow. The quantities μ_p, μ_0^* and μ_∞^* are the plastic-shear-rate viscosity, the zero-shear-rate viscosity and the infinite-shear-rate viscosity, respectively. The quantity λ^* refers to the time constant, often defined as the 'relaxation time'. It is noted that when $a = 2$, the Carreau-Yasuda model reduced to the better known Carreau model. From the above models we will choose the Carreau model to model the viscosity. According to Nouar & Frigaard [47] and Nouar, Bottaro & Brancher[48], the Carreau model is more realistic in its descriptions of the rheological behaviour of shear-thinning fluids. Moreover, it is capable

of modelling the steady shear, complex viscosity, stress growth and stress relaxation functions. Therefore, this model is flexible because it can fit a wide range of experimental data. Based on this, the Carreau model is adopted for the current study.

The Carreau model was first developed by Pierre Carreau [27]. It is called shear-thinning (pseudoplastic) for $n < 1$ so that the fluid's viscosity decreases when the shear rate increases. For shear-thickening (dilatant) flows, the fluid's viscosity increases with an increase in the shear rate $n > 1$. This shows that this model is able to provide a physical description of fluid behaviour in regions of both very high and very low shear as is seen in Figure (2.1):

$$\text{for } n < 1 : \lim_{\dot{\gamma}\to 0} \mu(\dot{\gamma}) \to \mu_0, \quad \lim_{\dot{\gamma}\to \infty} \mu(\dot{\gamma}) \to \mu_\infty,$$
$$\text{for } n > 1 : \lim_{\dot{\gamma}\to 0} \mu(\dot{\gamma}) \to \mu_0, \quad \lim_{\dot{\gamma}\to \infty} \mu(\dot{\gamma}) \to \infty.$$

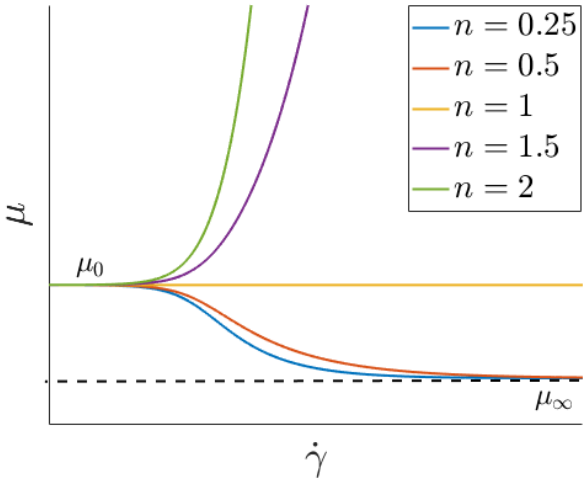

Figure 2.1: Viscosity as a function of shear rate for shear-thickening and shear-thinning Carreau fluids and Newtonian fluids.

2.2 *The governing boundary-layer equations*

The approach developed by Griffiths [42] is adopted to obtain the mean-flow profiles under the Carreau [46] viscosity model. However, some modifications are required to incorporate the partial-slip approach to surface roughness. The disk is assumed to be of an infinite radius and rotating at a constant angular

velocity, Ω^*, within an incompressible Carreau fluid. Cylindrical polar coordinates exist within the rotating reference frame and the governing equations are given by

$$\boldsymbol{\nabla \cdot u^*} = 0, \tag{2.3a}$$

$$\frac{\partial \boldsymbol{u^*}}{\partial t^*} + \boldsymbol{u^* \cdot \nabla u^*} + \boldsymbol{\Omega^* \times (\Omega^* \times r^*)} + 2\boldsymbol{\Omega^* \times u^*} = -\frac{1}{\rho^*}\nabla p^* + \frac{1}{\rho^*}\boldsymbol{\nabla \cdot \tau^*}. \tag{2.3b}$$

Here $\boldsymbol{u^*} = (u^*, v^*, w^*)$ is the total velocity vector; t^* is time; p^* is the fluid pressure; $\boldsymbol{r^*} = (r^*, 0, z^*)$ is the position vector in space; $\boldsymbol{\Omega^*} = (0, 0, \Omega^*)$ is the constant angular velocity; and ρ^* is the fluid density. An asterisk, where used, refers to a dimensional variable.

The stress tensor for generalised Newtonian models is given by $\boldsymbol{\tau^*} = \mu^*\dot{\boldsymbol{\gamma}}^*$, where $\mu^* = \mu^*(\dot{\gamma}^*)$ is the non-Newtonian viscosity. The magnitude of the rate of strain tensor is given by $\dot{\gamma}^* = \sqrt{\dot{\boldsymbol{\gamma}}^* : \dot{\boldsymbol{\gamma}}^*/2}$ and, for a Carreau fluid, we have

$$\mu^*(\dot{\gamma^*}) = \mu^*_\infty + (\mu^*_0 - \mu^*_\infty)\left[1 + (\lambda^*\dot{\gamma}^*)^2\right]^{(n-1)/2}. \tag{2.4}$$

The power index n characterises the fluid behaviour, such as being shear-thinning when $n < 1$, Newtonian when $n = 1$ and shear-thickening when $n > 1$. The quantities μ^*_0 and μ^*_∞ denote the zero-shear-rate and infinite-shear-rate viscosities, respectively. λ^* is referred to as the time constant or 'relaxation time'.

Equations (2.3) can be expressed without the vector notation as

$$\frac{1}{r^*}\frac{\partial(r^*u^*)}{\partial r^*} + \frac{1}{r^*}\frac{\partial v^*}{\partial \theta} + \frac{\partial w^*}{\partial z^*} = 0, \tag{2.5a}$$

$$\frac{\partial u^*}{\partial t^*} + u^*\frac{\partial u^*}{\partial r^*} + \frac{v^*}{r^*}\frac{\partial u^*}{\partial \theta} + w^*\frac{\partial u^*}{\partial z^*} - \frac{(v^* + r^*\Omega^*)^2}{r^*} = -\frac{1}{\rho^*}\frac{p^*}{r^*} \\ \frac{1}{\rho^*}\left[\frac{1}{r^*}\frac{\partial(r^*\tau^*_{r^*r^*})}{\partial r^*} + \frac{1}{r^*}\frac{\partial \tau^*_{r^*\theta}}{\partial \theta} + \frac{\partial \tau^*_{r^*z^*})}{\partial z^*} - \frac{\tau^*_{\theta\theta}}{r^*}\right], \tag{2.5b}$$

$$\frac{\partial v^*}{\partial t^*} + u^*\frac{\partial v^*}{\partial r^*} + \frac{v^*}{r^*}\frac{\partial v^*}{\partial \theta} + w^*\frac{\partial v^*}{\partial z^*} + \frac{u^*v^*}{r^*} + 2\Omega^*U^* = -\frac{1}{r^*\rho^*}\frac{\partial p^*}{\partial \theta} \\ + \frac{1}{\rho^*}\left[\frac{1}{r^{*2}}\frac{\partial(r^{*2}\tau^*_{\theta r^*})}{\partial r^*} + \frac{1}{r^*}\frac{\partial \tau^*_{\theta\theta}}{\partial \theta} + \frac{\partial \tau^*_{\theta z^*})}{\partial z^*}\right], \tag{2.5c}$$

$$\frac{\partial w^*}{\partial t^*} + u^*\frac{\partial w^*}{\partial r^*} + \frac{v^*}{r^*}\frac{\partial w^*}{\partial \theta} + w^*\frac{\partial w^*}{\partial z^*} = -\frac{1}{\rho^*}\frac{\partial p^*_1}{\partial z^*} \\ \frac{1}{\rho^*}\left[\frac{1}{r^*}\frac{\partial(r^*\tau^*_{z^*r^*})}{\partial r^*} + \frac{1}{r^*}\frac{\partial \tau^*_{z^*\theta}}{\partial \theta} + \frac{\partial \tau^*_{z^*z^*})}{\partial z^*}\right]. \tag{2.5d}$$

Here the stress tensor components in Equations (2.5) are found as

$$\tau^*_{r^*r^*} = 2\mu^*\Big(\frac{\partial u^*}{\partial r^*}\Big), \tag{2.6a}$$

$$\tau^*_{\theta\theta} = 2\mu^*\Big(\frac{1}{r^*}\frac{\partial v^*}{\partial \theta} + \frac{u^*}{r^*}\Big), \tag{2.6b}$$

$$\tau^*_{z^*z^*} = 2\mu^*\Big(\frac{\partial w^*}{\partial z^*}\Big), \tag{2.6c}$$

$$\tau^*_{r^*\theta} = \mu^*\Big[r^*\frac{\partial}{\partial r^*}\Big(\frac{v^*}{\partial r^*}\Big) + \frac{1}{r^*}\frac{\partial u^*}{\partial \theta}\Big) = \tau^*_{\theta r^*}, \tag{2.6d}$$

$$\tau^*_{r^*z^*} = \mu^*\Big(\frac{\partial u^*}{\partial z^*} + \frac{\partial w^*}{\partial r^*}\Big) = \tau^*_{z^*r^*}, \tag{2.6e}$$

$$\tau^*_{\theta z^*} = \mu^*\Big(\frac{\partial u^*}{\partial z^*} + \frac{1}{r^*}\frac{\partial w^*}{\partial \theta}\Big) = \tau^*_{z^*\theta}, \tag{2.6f}$$

where $\dot{\gamma}^*$ is the rate-of-strain tensor and takes the form

$$\dot{\gamma}^* = \Bigg\{2\Bigg[\Big(\frac{\partial u^*}{\partial r^*}\Big)^2 + \Big(\frac{1}{r^*}\frac{\partial v^*}{\partial \theta} + \frac{u^*}{r^*}\Big)^2 + \Big(\frac{\partial w^*}{\partial z^*}\Big)^2\Bigg] + \Bigg[r^*\frac{\partial}{\partial r^*}\Big(\frac{v^*}{r^*}\Big) + \frac{1}{r^*}\frac{\partial u^*}{\partial \theta}\Bigg]^2 + \Big(\frac{\partial u^*}{\partial z^*} + \frac{\partial w^*}{r^*}\Big)^2 + \Big(\frac{\partial v^*}{\partial z^*} + \frac{1}{r^*}\frac{\partial w^*}{\partial \theta}\Big)^2\Bigg\}^{\frac{1}{2}} = \sqrt{\frac{II}{2}} \tag{2.7}$$

with $II = \sum_i \sum_j \dot{\gamma}^2_{ij} = \dot{\gamma}^2_{r^*r^*} + \dot{\gamma}^2_{\theta\theta} + \dot{\gamma}^2_{z^*z^*} + 2(\dot{\gamma}^2_{r^*\theta j} + \dot{\gamma}^2_{r^*z^*} + \dot{\gamma}^2_{\theta z^*})$.

The system will be reduced to a non-dimensional form with the following dimensionless variables

$$U(r,\theta,z) = \frac{u^*}{\Omega^* l^*}, \qquad V(r,\theta,z) = \frac{v^*}{\Omega^* l^*}, \qquad W(r,\theta,z) = \frac{w^*}{\Omega^* l^* \delta}, \tag{2.8}$$

$$r = \frac{r^*}{l^*}, \qquad z = \frac{z^*}{\delta l^*}. \qquad t^* = (\Omega^* t^*), \qquad P(r,\theta,z) = \frac{p^*}{\rho^*(\Omega^* l^*)^2}. \tag{2.9}$$

here $\Omega^* l^*$ is natural velocity, l^* is length scales and non-dimensional boundary-layer thickness δ will be determined later. by substituting Equations (2.8) and Equations (2.9) into Equations (2.5) to give the dimensionless continuity and momentum equations

$$\frac{1}{r}\frac{\partial (rU)}{\partial r} + \frac{1}{r}\frac{\partial V}{\partial \theta} + \frac{\partial W}{\partial z} = 0, \tag{2.10a}$$

$$\frac{\partial U}{\partial t} + U\frac{\partial U}{\partial r} + \frac{V}{r}\frac{\partial U}{\partial \theta} + W\frac{\partial U}{\partial z} - \frac{(V+r)^2}{r} = -\frac{\partial P}{\partial r} + \frac{1}{\rho^*(l^*\Omega^*)^2}\Big[\frac{1}{r}\frac{\partial (r\tau_{rr})}{\partial r} + \frac{1}{r}\frac{\partial \tau_{r\theta}}{\partial \theta} + \frac{\partial \tau_{rz}}{\partial z} - \frac{\tau_{\theta\theta}}{r}\Big], \tag{2.10b}$$

$$\frac{\partial V}{\partial t}+U\frac{\partial V}{\partial r}+\frac{V}{r}\frac{\partial V}{\partial \theta}+W\frac{\partial V}{\partial z}+\frac{UV}{r}+2U=-\frac{1}{r}\frac{\partial P}{\partial \theta}+\frac{1}{\rho^*(l^*\Omega^*)^2}\Big[\frac{1}{r^2}\frac{\partial(r^2\tau_{\theta r})}{\partial r}+\frac{1}{r}\frac{\partial \tau_{\theta\theta}}{\partial \theta}+\frac{\partial \tau_{\theta z})}{\partial z}\Big], \quad (2.10c)$$

$$\frac{\partial W}{\partial t}+U^*\frac{\partial W}{\partial r}+\frac{V}{r}\frac{\partial W}{\partial \theta}+W\frac{\partial W}{\partial z}=-\frac{1}{\delta^2}\frac{\partial P}{\partial z}+\frac{1}{\rho^*(l^*\Omega^*)^2}\Big[\frac{1}{r}\frac{\partial(r\tau_{zr})}{\partial r}+\frac{1}{r}\frac{\partial \tau_{z\theta}}{\partial \theta}+\frac{\partial \tau_{zz})}{\partial z}\Big]. \quad (2.10d)$$

The non-dimensionalisation of $\dot{\gamma}$ can be obtained from $\dot{\gamma}=\dot{\gamma}^*(\frac{\delta}{\Omega^*})$, leading to

$$\dot{\gamma}^2=\left(\frac{\partial U}{\partial z}\right)^2+\left(\frac{\partial V}{\partial z}\right)^2+\delta^4\left[\frac{1}{r^2}\left(\frac{\partial W}{\partial \theta}\right)^2+\left(\frac{\partial W}{\partial r}\right)^2\right]+\delta^2\Bigg\{2\left[\left(\frac{\partial U}{\partial r}\right)^2+2\left(\frac{1}{r}\frac{\partial V}{\partial \theta}+\frac{U}{r}\right)^2+2\left(\frac{\partial W}{\partial z}\right)^2+\left[r\frac{\partial}{\partial r}\left(\frac{V}{r}\right)+\frac{1}{r}\frac{\partial U}{\partial \theta}\right]^2+\frac{2}{r}\frac{\partial V}{\partial z}\frac{\partial W}{\partial \theta}+2\frac{\partial U}{z}\frac{\partial W}{r}\Bigg\}. \quad (2.11)$$

Now, it is possible to determine the dimensionless form of the viscous terms τ_{ij} that appear in Equations (2.10) as

$$\frac{1}{r}\frac{\partial(r\tau_{rr})}{\partial r}=\mu_0^*\Omega^*\frac{2}{r}\frac{\partial}{\partial r}\Big(\tilde{\mu}r\frac{\partial U}{\partial r}\Big) \quad (2.12a)$$

$$\frac{1}{r}\frac{\partial \tau_{r\theta})}{\partial \theta}=\mu_0^*\Omega^*\frac{1}{r}\frac{\partial}{\partial \theta}\Big\{\tilde{\mu}\Big[r\frac{\partial}{\partial r}\Big(\frac{V}{r}\Big)+\frac{1}{r}\frac{\partial U}{\partial \theta}\Big]\Big\} \quad (2.12b)$$

$$\frac{\tau_{\theta\theta}}{r}=\mu_0^*\Omega^*\frac{2\tilde{\mu}}{r^2}\Big(\frac{\partial V}{\partial \theta}+U\Big), \quad (2.12c)$$

$$\frac{\partial \tau_{rz}}{\partial z}=\mu_0^*\Omega^*\frac{1}{\delta^2}\frac{\partial}{\partial z}\Big[\tilde{\mu}\Big(\frac{\partial U}{\partial z}+\delta^2\frac{\partial W}{\partial r}\Big)\Big], \quad (2.12d)$$

$$\frac{1}{r^2}\frac{r^2\partial(r\tau_{\theta r})}{\partial r}=\mu_0^*\Omega^*\frac{1}{r^2}\frac{\partial}{\partial r}\Big\{\tilde{\mu}\Big[r^3\frac{\partial}{\partial r}\Big(\frac{V}{r}\Big)+r\frac{\partial U}{\partial \theta}\Big]\Big\}, \quad (2.12e)$$

$$\frac{1}{r}\frac{\partial(r\tau_{\theta\theta})}{\partial r}=\mu_0^*\Omega^*\frac{2}{r}\frac{\partial}{\partial \theta}\Big[\tilde{\mu}\Big(\frac{1}{r}\frac{\partial V}{\partial \theta}+\frac{U}{r}\Big)\Big], \quad (2.12f)$$

$$\frac{\partial \tau_{\theta z}}{\partial z}=\mu_0^*\Omega^*\frac{1}{\delta^2}\frac{\partial}{\partial z}\Big[\tilde{\mu}\Big(\frac{\partial V}{\partial z}+\frac{\delta^2}{r}\frac{\partial W}{\partial \theta}\Big)\Big], \quad (2.12g)$$

$$\frac{1}{r}\frac{\partial(r\tau_{zr})}{\partial r}=\mu_0^*\Omega^*\frac{1}{\delta}\Big\{\frac{1}{r}\frac{\partial}{\partial r}\Big[\tilde{\mu}r\Big(\frac{\partial U}{\partial z}+\delta^2\frac{\partial W}{\partial r}\Big)\Big]\Big\}, \quad (2.12h)$$

$$\frac{1}{r}\frac{\partial \tau_{z\theta}}{\partial \theta}=\mu_0^*\Omega^*\frac{1}{\delta}\Big\{\frac{1}{r}\frac{\partial}{\partial \theta}\Big[\tilde{\mu}\Big(\frac{\partial V}{\partial z}+\frac{\delta^2}{r}\frac{\partial W}{\partial \theta}\Big)\Big]\Big\}, \quad (2.12i)$$

$$\frac{\partial \tau_{zz}}{\partial z}=\mu_0^*\Omega^*\frac{1}{\delta}\Big[2\frac{\partial}{\partial z}\Big(\tilde{\mu}\frac{\partial W}{\partial z}\Big)\Big]. \quad (2.12j)$$

Here $\tilde{\mu} = \left[1 + (r^{-1}k\dot{\gamma})^2\right]^{\frac{(n-1)}{2}}$ is the non-dimensional Carreau model with respect to μ_0^*. This is normalised with respect to μ_0^* to facilitate direct quantitative comparisons with the corresponding Newtonian mean-flow profiles. In practical applications, the zero-shear-rate viscosity is typically larger three to four orders than the infinite-shear-rate viscosity. Accordingly, μ_∞^*/μ_0^* is assumed negligible and neglected in the current analysis. Here $k = \frac{r^*\lambda^*\Omega^*}{l^*\delta}$ is the dimensionless of the constant λ^*. Again, δ remains, as of yet, undetermined. By substituting Equations (2.12) in Equations (2.10), the system can be written as

$$\frac{1}{r}\frac{\partial(rU)}{\partial r} + \frac{1}{r}\frac{\partial V}{\partial \theta} + \frac{\partial W}{\partial z} = 0, \tag{2.13a}$$

$$\begin{aligned}\frac{\partial U}{\partial t} + U\frac{\partial U}{\partial r} + \frac{V}{r}\frac{\partial U}{\partial \theta} + W\frac{\partial U}{\partial z} - \frac{(V+r)^2}{r} = -\frac{\partial P}{\partial r} + \frac{{\mu_0}^*}{\rho^*\Omega^*(l^*\delta^*)^2}\\ \Big(\frac{2}{r}\frac{\partial}{\partial r}\Big[\tilde{\mu}r\frac{\partial U}{\partial r}\Big)\Big] + \frac{1}{r}\frac{\partial}{\partial \theta}\Big\{\tilde{\mu}\Big[r\frac{\partial}{\partial r}\Big(\frac{V}{r}\Big) + \frac{1}{r}\frac{\partial U}{\partial \theta}\Big]\Big\}\\ + \frac{\partial}{\partial z}\Big[\tilde{\mu}\Big(\frac{\partial U}{\partial z} + \frac{\partial W}{\partial r}\Big)\Big] - \frac{2\tilde{\mu}}{r^2}\Big[\frac{\partial V}{\partial \theta} + U\Big]\Big),\end{aligned} \tag{2.13b}$$

$$\begin{aligned}\frac{\partial V}{\partial t} + U\frac{\partial V}{\partial r} + \frac{V}{r}\frac{\partial V}{\partial \theta} + W\frac{\partial V}{\partial z} + \frac{UV}{r} + 2U = -\frac{1}{r}\frac{\partial P}{\partial \theta} + \frac{{\mu_0}^*}{\rho^*\Omega^*(l^*\delta^*)^2}\\ \Big(\frac{1}{r^2}\frac{\partial}{\partial r}\Big\{\tilde{\mu}r^2\Big[r\frac{\partial}{\partial r}\Big(\frac{V}{r}\Big) + \frac{1}{r}\frac{\partial U}{\partial \theta}\Big]\Big\} + \frac{1}{r}\frac{\partial}{\partial \theta}\Big[2\tilde{\mu}\Big(\frac{1}{r}\frac{\partial V}{\partial \theta} + \frac{U}{r}\Big)\Big] +\\ + \frac{\partial}{\partial z}\Big[\tilde{\mu}\Big(\frac{\partial V}{\partial z} + \frac{1}{r}\frac{\partial W}{\partial \theta}\Big)\Big]\Big),\end{aligned} \tag{2.13c}$$

$$\begin{aligned}\frac{\partial W}{\partial t} + U^*\frac{\partial W}{\partial r} + \frac{V}{r}\frac{\partial W}{\partial \theta} + W\frac{\partial W}{\partial z} = -\frac{1}{\delta^2}\frac{\partial P}{\partial z} + \frac{{\mu_0}^*}{\rho^*\Omega^*(l^*\delta^*)^2}\\ \Big\{\frac{1}{r}\frac{\partial}{\partial r}\Big[\tilde{\mu}r\Big(\frac{\partial U}{\partial z} + \frac{\partial W}{\partial r}\Big)\Big] +\\ + \frac{1}{r}\frac{\partial}{\partial \theta}\Big[\tilde{\mu}\Big(\frac{\partial V}{\partial z} + \frac{1}{r}\frac{\partial W}{\partial \theta}\Big)\Big] + \frac{\partial}{\partial r}\Big[2\tilde{\mu}\Big(\frac{\partial W}{\partial z}\Big)\Big]\Big\},\end{aligned} \tag{2.13d}$$

with

$$\frac{{\mu_0}^*}{\rho^*\Omega^*(l^*\delta^*)^2} = \mathcal{O}(1).$$

Here the Reynolds number is scaled by the infinite-shear-rate velocity

$$Re = \frac{\rho^*\Omega^*{l^*}^2}{{\mu_0}^*}. \tag{2.14}$$

The boundary layer thickness of the Carreau model fluid driven by a rotating disk is defined as

$$\delta = \mathcal{O}(Re^{-\frac{1}{2}}).$$

Thus, Equations (2.13) are scaled and given by

$$\frac{1}{r}\frac{\partial(rU)}{\partial r} + \frac{1}{r}\frac{\partial V}{\partial \theta} + \frac{\partial W}{\partial z} = 0, \tag{2.15a}$$

$$\frac{\partial U}{\partial t} + U\frac{\partial U}{\partial r} + \frac{V}{r}\frac{\partial U}{\partial \theta} + W\frac{\partial U}{\partial z} - \frac{(V+r)^2}{r} = -\frac{\partial P}{\partial r} + \frac{\partial}{\partial z}\Big(\tilde{\mu}\frac{\partial U}{\partial z}\Big) + \mathcal{O}(Re^{-1}) \tag{2.15b}$$

$$\frac{\partial V}{\partial t} + U\frac{\partial V}{\partial r} + \frac{V}{r}\frac{\partial V}{\partial \theta} + W\frac{\partial V}{\partial z} + \frac{UV}{r} + 2U = -\frac{1}{r}\frac{\partial P}{\partial \theta} + \frac{\partial}{\partial z}\Big(\tilde{\mu}\frac{\partial V}{\partial z}\Big) + \mathcal{O}(Re^{-1}) \tag{2.15c}$$

$$\frac{\partial W}{\partial t} + U^*\frac{\partial W}{\partial r} + \frac{V}{r}\frac{\partial W}{\partial \theta} + W\frac{\partial W}{\partial z} = -Re\frac{\partial P}{\partial z} + \frac{1}{r}\frac{\partial}{\partial r}\Big(\tilde{\mu}r\frac{\partial U}{\partial z}\Big) + \frac{1}{r}\frac{\partial}{\partial \theta}\Big(\tilde{\mu}r\frac{\partial V}{\partial z}\Big) + 2\frac{\partial}{\partial z}\Big(\tilde{\mu}r\frac{\partial W}{\partial z}\Big) + \mathcal{O}(Re^{-1}) \tag{2.15d}$$

where

$$\tilde{\mu} = \Big\{1 + \Big(\frac{k}{r}\Big)^2\Big[(U'^2) + (V'^2) + \mathcal{O}(Re^{-1}) + \mathcal{O}(Re^{-2})\Big]\Big\}^{(n-1)/2}. \tag{2.16}$$

Here the prime denotes differentiation with respect to z and $\Big[(U'^2) + (V'^2)\Big] = \dot{\gamma}^2$ after scaling. The details of the $\dot{\gamma}$ calculation and scaling are given in Equation (2.11).

A boundary layer approximation is applied to the system of equations to eliminate the terms that involve inverse powers of the Reynolds number by assuming that $Re \gg 1$. A solution is proposed inside the boundary layer, where the velocity components, pressure and viscosity have the following asymptotic expansions

$$\begin{aligned}
U(r,\theta,\bar{z}) &= U_0(r,\theta,z) + Re^{-1}U_1(r,\theta,z) + ..., \\
V(r,\theta,\bar{z}) &= V_0(r,\theta,z) + Re^{-1}V_1(r,\theta,z) + ..., \\
W(r,\theta,\bar{z}) &= W_0(r,\theta,z) + Re^{-1}W_1(r,\theta,z) + ..., \\
P(r,\theta,\bar{z}) &= P_0(r,\theta,z) + Re^{-1}P_1(r,\theta,z) + ..., \\
\tilde{\mu}(r,\theta,\bar{z}) &= \tilde{\mu_0}(r,\theta,z) + Re^{-1}\tilde{\mu_1}(r,\theta,z) + ...,
\end{aligned}$$

where $\bar{z} = \frac{z^*}{l^*} = Re^{-\frac{1}{2}} z$ is the coordinate corresponding to the region outside of the boundary layer.

The zero order equation is thus reached and will be solved later to find solutions for the steady mean flow

$$\frac{1}{r}\frac{\partial(rU_0)}{\partial r} + \frac{\partial W_0}{\partial z} = 0, \tag{2.17a}$$

$$U_0\frac{\partial U_0}{\partial r} + W_0\frac{\partial U_0}{\partial z} - \frac{(V_0+r)^2}{r} = \frac{\partial}{\partial z}\Big(\tilde{\mu_0}\frac{\partial U_0}{\partial z}\Big), \tag{2.17b}$$

$$U_0\frac{\partial V_0}{\partial r} + W_0\frac{\partial V_0}{\partial z} + \frac{U_0 V_0}{r} + 2U_0 = \frac{\partial}{\partial z}\Big(\tilde{\mu_0}\frac{\partial V_0}{\partial z}\Big), \tag{2.17c}$$

$$U_0\frac{\partial W_0}{\partial r} + W_0\frac{\partial W_0}{\partial z} = -\frac{\partial P_1}{\partial z} + \frac{1}{r}\frac{\partial}{\partial r}\Big(\tilde{\mu_0} r\frac{\partial U_0}{\partial z}\Big) + 2\frac{\partial}{\partial z}\Big(\tilde{\mu_0} r\frac{\partial W_0}{\partial z}\Big), \tag{2.17d}$$

where

$$\tilde{\mu_0} = \Big\{1 + \Big(\frac{k}{rRe^{1/2}}\Big)^2\Big[(U_0'^2) + (V_0'^2)\Big]\Big\}^{(n-1)/2}, \tag{2.18}$$

is the zero-order viscosity function.

2.3 *Steady mean flow solutions*

The dimensionless of the system 2.17 are scaled as

$$U(z) = \frac{U_0^*}{r^*\Omega^*}, \quad V(z) = \frac{V_0^*}{r^*\Omega^*}, \quad W(z) = \frac{W_0^*}{l^*\Omega^*}, \quad P(z) = \frac{P_1^*}{\rho^* l^{*2}\Omega^{*2}},$$

where $l^* = \big[\frac{\nu^*}{\Omega^*}\big]^{(1/2)}$ is a characteristic length scale. Assuming the mean flow is steady and axisymmetric, i.e., the mean flow velocities (U_0, V_0, W_0) and pressure P_1 term are independent of time t and azimuthal direction θ, these lead to the following non-dimensional equations for the mean flow

$$2U + W' = 0, \tag{2.19a}$$

$$U^2 - (V+1)^2 + WU' - (\mu U')' = 0, \tag{2.19b}$$

$$2U(V+1) + WV' - (\mu V')' = 0, \tag{2.19c}$$

$$WW' + P' - qU' + 2\mu' U - (\mu W')' = 0. \tag{2.19d}$$

where a prime denotes a derivative with respect to z and

$$q = \frac{k^2(n-1)(U'^2+V'^2)}{1+k^2(U'^2+V'^2)}, \quad \mu = 1+k^2[(U')^2+(V')^2]^{(n-1)/2}.$$

$$k = r^*\lambda^*\Omega^*(\nu/\Omega)^{-1/2}.$$

Rearranging Equation (2.19b) and Equation (2.19c) result in

$$U'' = \frac{[U^2-(V+1)^2+U'W](\bar{\varsigma_1}+\bar{\varsigma_2}V'^2)-U'V'\bar{\varsigma_2}[2U(V+1)+V'W]}{\tilde{\mu_0}[\bar{\varsigma_1}+\bar{\varsigma_2}(U'^2+V'^2)]} \tag{2.20}$$

$$V'' = \frac{[2U(V+1)+V'W](\bar{\varsigma_1}+\bar{\varsigma_2}U'^2)-U'V'\bar{\varsigma_2}[U^2-(V+1)^2+U'W]}{\tilde{\mu_0}[\bar{\varsigma_1}+\bar{\varsigma_2}(U'^2+V'^2)]} \tag{2.21}$$

where $\bar{\varsigma_1} = 1+k^2(U'^2+V'^2)$ and $\bar{\varsigma_2} = k^2(1-n)$.

This formulation will lead to the first order ordinary differential equations in five unknowns U,U', V, V', W.

What follows is a discussion of the use the MW model [33] for surface roughness to determine the boundary conditions at the disk surface. This approach suggests that roughness can be modelled using partial-slip conditions instead of the usual no-slip conditions at the disk surface. Here, the boundary condition at the upper edge of the boundary layer is identical to the smooth-disk formulation. To derive the boundary conditions, the method proposed by Navier [49], where the partial-slip condition in the radial and azimuthal directions are respectively given by

$$U\mid_{z=0} = \lambda\tau_r^z\mid_{z=0}, \quad V\mid_{z=0} = \eta\tau_\theta^z\mid_{z=0}.$$

Here λ and η are the respective the slip coefficients defined as,

$$\lambda = \lambda_1\mu\sqrt{\frac{\Omega l^2}{v}} \quad \text{and} \quad \eta = \eta_1\mu\sqrt{\frac{\Omega l^2}{v}}. \tag{2.22}$$

Using the above transformations, Equation (2.22) enables the boundary conditions to be determined as

$$\begin{aligned} U(0) &= \lambda\, U'[1+k^2(U'^2+V'^2)^{(n-1)/2}], \\ V(0) &= \eta\, V'[1+k^2(U'^2+V'^2)^{(n-1)/2}], \end{aligned} \tag{2.23}$$

$$W(0) = 0. \tag{2.24}$$

To derive the above Equations (2.23) we start from the generalised Navier [49] partial slip in the radial direction,

$$U\mid_{z=0}= \lambda\tau_r^z\mid_{z=0}, \tag{2.25}$$

and the azimuthal direction

$$V\mid_{z=0}= \eta\tau_\theta^z\mid_{z=0}\,. \tag{2.26}$$

The quantities λ and η are slip coefficients. The shear stress components in the above equations can be defined from Equations (2.6e) and (2.6f) and the viscosity can be defined from Equation (2.16). Therefore, Equation (2.25) after non-dimensionlising will take the from

$$U\mid_{z=0}= \lambda_1\tilde{\mu_0}Re^{\frac{1}{2}}\Big\{1+k^2\Big[\Big(\frac{\partial U}{\partial z}\Big)^2+\Big(\frac{\partial V}{\partial z}\Big)^2\Big]\Big\}^{(n-1)/2}\ \frac{\partial U(z)}{\partial z} \tag{2.27}$$

Where $(Re^{\frac{1}{2}})=\Big(\frac{\Omega l}{\mu_0}\Big)^{\frac{1}{2}}$ so

$$U\mid_{z=0}= \lambda_1\tilde{\mu_0}\Big(\frac{\Omega l}{v_0}\Big)^{\frac{1}{2}}\Big\{1+k^2\Big[\Big(\frac{\partial U}{\partial z}\Big)^2+\Big(\frac{\partial V}{\partial z}\Big)^2\Big]\Big\}^{(n-1)/2}\ \frac{\partial U(z)}{\partial z} \tag{2.28}$$

with $\lambda=\lambda_1\tilde{\mu_0}\Big(\frac{\Omega l}{v_0}\Big)^{\frac{1}{2}}$ such that

$$U\mid_{z=0}= \lambda\Big\{1+(k)^2\Big[\Big(\frac{\partial U}{\partial z}\Big)^2+\Big(\frac{\partial V}{\partial z}\Big)^2\Big]\Big\}^{(n-1)/2}\ \frac{\partial U(z)}{\partial z} \tag{2.29}$$

Therefore, the partial slip conditions reduce to

$$U\mid_{z=0}= \lambda U'\Big\{1+k^2[U'^2+V'^2]\Big\}^{(n-1)/2}. \tag{2.30}$$

Similarly to that the partial slip in Equations (2.26) the azimuthal direction

$$V\mid_{z=0}= \eta V'\Big\{1+k^2[U'^2+V'^2]\Big\}^{(n-1)/2}. \tag{2.31}$$

with $\eta=\eta_1\mu(\frac{\Omega l}{v_0})^{\frac{1}{2}}$ and the prime denotes differentiation with respect to z. Furthermore,

$$U=0,\ V=-1\quad \text{as } z\to\infty. \tag{2.32}$$

The coefficients λ and η give a measure of the roughness in the radial and azimuthal directions, respectively. When $\lambda=\eta=0$, the boundary conditions reduce to the no-slip boundary conditions for a smooth disk. The scenario of anisotropic roughness is exemplified by concentric grooves ($\eta>0,\lambda=0$) and radial grooves ($\eta=0,\lambda>0$); whereas isotropic roughness corresponds to the case $\lambda=\eta>0$. In the particular case that $n=1$ and $\lambda=\eta=0$, the system defined by Equations (2.19), (2.23) and (E.6) reduces to the standard von Kármán system. Similarly, when $n=1$ and $\lambda\neq 0$, $\eta\neq 0$ we recover the governing equations for the standard MW model [33] for Newtonian fluids.

2.3.1 *Matlab solver for the steady mean flow*

The MATLAB solver function bvp4c is used to obtain the mean-flow solutions. This method is a finite difference code that implements the three-stage Lobatto IIIa formula, that can be viewed as an implicit Runge-Kutta formula with a continuous interpolate. This is a collocation formula, and the collocation polynomial provides a C_1-continuous solution that is fourth-order accurate uniformly in the interval [a,b] and is divided into subintervals by using mesh selection points. Mesh selection and error control are based on the residual of the continuous solution. The points of the initial mesh and an initial approximation of the solution at the mesh points are used to solve the equations.

Our goal is to obtain the mean flow velocity profiles U, V, W. The governing equations are transformed into the first order ordinary differential equations in order to apply the bvp4c routine. The transformed variables are written as follows

$$\phi_1(z) = U, \qquad \phi_2(z) = U', \qquad \phi_3(z) = V, \qquad \phi_4(z) = V', \qquad \phi_5(z) = W, \tag{2.33}$$

The system of the ordinary differential Equations (2.20) and (2.21) become

$$\begin{aligned}
\phi_1' &= \phi_2, \\
\phi_2' &= \frac{\Big\{1 + k^2\Big((\phi_2)^2 + n(\phi_4)^2\Big)\Big\}F - (1-n)k^2\phi_2\phi_4 G}{\mu\Big\{1 + nk^2\Big((\phi_2)^2 + n(\phi_4)^2\Big)\Big\}}, \\
\phi_3' &= \phi_4, \\
\phi_4' &= \frac{\Big\{1 + k^2\Big(n(\phi_2)^2 + (\phi_4)^2\Big)\Big\}G - (1-n)k^2\phi_2\phi_4 F}{\mu\Big\{1 + nk^2\Big((\phi_2)^2 + n(\phi_4)^2\Big)\Big\}}, \\
\phi_5' &= -2\phi_1.
\end{aligned} \tag{2.34}$$

Here

$$\begin{aligned}
F &= \phi_1^2 - (\phi_3 + 1)^2 + \phi_2\phi_5, \\
G &= 2\phi_1(\phi_3 + 1) + \phi_4\phi_5, \\
\mu &= \Big\{1 + k^2\Big((\phi_2)^2 + (\phi_5)^2\Big)\Big\}^{(n-1)/2}.
\end{aligned}$$

Also, the partial-slip conditions are transformed as

$$\begin{aligned}\phi_1 &= \lambda\phi_2\Big\{1+k^2\Big((\phi_2)^2+(\phi_5)^2\Big)\Big\}^{(n-1)/2},\\ \phi_3 &= \eta\phi_4\Big\{1+k^2\Big((\phi_2)^2+(\phi_5)^2\Big)\Big\}^{(n-1)/2},\\ \phi_5 &= 0,\end{aligned} \tag{2.35}$$

and

$$\phi_1 \to 0,\ \phi_3 \to -1 \text{ as } z \to \infty. \tag{2.36}$$

Equations (2.34) and (2.35) define a two-point boundary value problem. The size of the domain is determined to be $z \in (0, 20)$.

2.4 *Derivation of the perturbation equations*

A linear stability analysis will be conducted by introducing the dimensional governing boundary-layer equations from Equations (2.17). These equations are non-dimensionalised with respect to the local radial position r_a and a local similarity variables are defined by

$$U(z) = \frac{U^*}{\Omega^* r_a^*}, \qquad V(z) = \frac{V^*}{\Omega^* r_a^*}, \qquad W(z) = \frac{W^*}{\Omega^* r_a^*}, \qquad P(z) = \frac{P^*}{\rho^* \Omega^{*2} r_a^{*2}}. \tag{2.37}$$

$$r = \frac{r_a^*}{l^*}, \qquad z = \frac{z^*}{l^*}, \qquad l^* = \sqrt{\Omega^* \nu^*}, \qquad t = \frac{t^*}{l^*/(\Omega^{*2} r_a^{*2})}. \tag{2.38}$$

Perturbations are applied at a specific radius by imposing sufficiently small disturbances on the steady-mean flow at some fixed local Reynolds number. The local Reynolds number for Carreau fluids is defined as

$$Re = \frac{\Omega^* r_a^* l^*}{\nu^*} = r_a. \tag{2.39}$$

The velocity, pressure and time are cast in dimensionless form using the scalings $r_a^*\Omega^*$, $\rho^*(r_a^*\Omega^*)$ and $l^*/(r_a^*\Omega^*)$, respectively. The instantaneous non-dimensional velocities and pressure component, including the mean values and small per-

turbations, are therefore given by

$$U_0(r,\theta,z,t) = \frac{r}{Re}U(z) + u(r,\theta,z,t), \tag{2.40a}$$

$$V_0(r,\theta,z,t) = \frac{r}{Re}V(z) + v(r,\theta,z,t), \tag{2.40b}$$

$$W_0(r,\theta,z,t) = \frac{1}{Re}W(z) + w(r,\theta,z,t), \tag{2.40c}$$

$$P_{0,1}(r,\theta,z,t) = \frac{1}{Re^2}P(z) + p(r,\theta,z,t), \tag{2.40d}$$

where u,v, w and p are small perturbation quantities. At this stage, it is necessary to apply the so called *parallel-flow approximation* to ensure the linearised equations are separable in r, θ and t. This involves replacing the variable r with the local Reynolds number and neglecting all terms $\mathcal{O}(Re^{-2})$, and leads to

$$\frac{\partial u}{\partial r} + \frac{u}{Re} + \frac{1}{Re}\frac{\partial v}{\partial \theta} + \frac{\partial w}{\partial z} = 0, \tag{2.41a}$$

$$\frac{\partial u}{\partial t} + U\frac{\partial u}{\partial r} + \frac{V}{Re}\frac{\partial u}{\partial \theta} + \frac{W}{Re}\frac{\partial u}{\partial z} + U'w + \frac{Uu - 2(V+1)v}{Re} = -\frac{\partial p}{\partial r}$$
$$+ \frac{1}{Re}\Big[\mu\Big(\frac{\partial^2 u}{\partial r^2} + \frac{1}{Re^2}\frac{\partial^2 u}{\partial \theta^2} + \frac{\partial^2 u}{\partial z^2}\Big) + \mu'\Big(\frac{\partial u}{\partial z} + \frac{\partial w}{\partial r}\Big) + \frac{\partial\Big(\hat{\mu}U'\psi\Big)}{\partial z}\Big], \tag{2.41b}$$

$$\frac{\partial v}{\partial t} + U\frac{\partial v}{\partial r} + \frac{V}{Re}\frac{\partial v}{\partial \theta} + \frac{W}{Re}\frac{\partial v}{\partial z} + V'w + \frac{Uv - 2(V+1)u}{Re} = -\frac{1}{Re}\frac{\partial p}{\partial \theta}$$
$$+ \frac{1}{Re}\Big[\mu\Big(\frac{\partial^2 v}{\partial r^2} + \frac{1}{Re^2}\frac{\partial^2 v}{\partial \theta^2} + \frac{\partial^2 v}{\partial z^2}\Big) + \mu'\Big(\frac{\partial v}{\partial z} + \frac{1}{Re}\frac{\partial w}{\partial \theta}\Big) + \frac{\partial\Big(\hat{\mu}V'\psi\Big)}{\partial z}\Big], \tag{2.41c}$$

$$\frac{\partial w}{\partial t} + U\frac{\partial w}{\partial r} + \frac{V}{Re}\frac{\partial w}{\partial \theta} + \frac{W}{Re}\frac{\partial w}{\partial z} + \frac{W'w}{Re} = -\frac{\partial p}{\partial z}$$
$$+ \frac{1}{Re}\Big[\mu\Big(\frac{\partial^2 w}{\partial r^2} + \frac{1}{Re^2}\frac{\partial^2 w}{\partial \theta^2} + \frac{\partial^2 w}{\partial z^2}\Big) + 2\mu'\frac{\partial w}{\partial z} + \hat{\mu}\Big(U'\frac{\partial}{\partial r} + \frac{V'}{Re}\frac{\partial}{\partial \theta}\Big)\psi\Big], \tag{2.41d}$$

where

$$\hat{\mu} = \frac{k^2(n-1)\mu}{1 + k^2\big[(U')^2 + (V')^2\big]},$$

$$\psi = \Big(U'\frac{\partial u}{\partial z} + V'\frac{\partial v}{\partial z}\Big).$$

by assuming the normal-mode form for the perturbing quantities as

$$(u, v, w, p) = (\hat{u}, \hat{v}, \hat{w}, \hat{p})(z; \alpha, \beta, \omega; Re, k)e^{\mathrm{i}(\alpha r + \beta\theta - \omega t)}.$$

Here $\alpha = \alpha_\mathrm{r} + \mathrm{i}\alpha_\mathrm{i}$ is the radial wave number, β is the azimuthal wave number (which is real) and ω is the frequency of the disturbances expressed in the rotating frame. We therefore rewrite Equation (2.41) as

$$\Big(i\alpha + \frac{1}{Re}\Big)\hat{u} + i\bar{\beta}\hat{v} + \frac{\partial \hat{w}}{\partial \hat{z}} = 0, \tag{2.42a}$$

$$\Big[\Big(i\alpha U + i\bar{\beta}V - i\omega\Big) + \frac{U}{Re}\Big]\hat{u} - \frac{2(v+1)\hat{v}}{Re} + \frac{W}{Re}\frac{\partial \hat{w}}{\partial z} + U'\hat{w} = -i\alpha\hat{p} + \frac{1}{Re}\frac{\partial}{\partial z}\Big(\mu\frac{\partial \hat{w}}{\partial z} + \hat{\mu}U'\Big), \tag{2.42b}$$

$$\Big[\Big(i\alpha U + i\bar{\beta}V - i\omega\Big) + \frac{U}{Re}\Big]\hat{v} + \frac{2(v+1)\hat{v}}{Re} + \frac{W}{Re}\frac{\partial \hat{w}}{\partial z} + V'\hat{w} = -i\bar{\beta}\hat{p} + \frac{1}{Re}\frac{\partial}{\partial z}\Big(\mu\frac{\partial \hat{w}}{\partial z} + \hat{\mu}V'\Big), \tag{2.42c}$$

$$\Big[\Big(i\alpha U + i\bar{\beta}V - i\omega\Big) + \frac{W'}{Re}\Big]\hat{w} = -\frac{\partial \hat{p}}{\partial z} + \frac{1}{Re}\frac{\partial}{\partial z}\Big(\mu\frac{\partial \hat{w}}{\partial z}\Big), \tag{2.42d}$$

with $\bar{\beta} = \beta/Re$. The orientation angle of the stationary vortices with respect to a circle centred on the axis of rotation as well as the mode number (i.e., number of spiral vortices on the disk surface) are given, respectively, as

$$\phi = \tan^{-1}\left(\frac{\bar{\beta}}{\bar{\alpha}}\right) \Leftrightarrow \tan\left(\frac{\pi}{2} - \phi\right) = \frac{\alpha r}{\beta}, \tag{2.43}$$

$$\bar{n} = \bar{\beta}Re. \tag{2.44}$$

2.4.1 *Numerical method for the perturbation equations*

A spectral method based on Chebyshev polynomials is implemented to solve the perturbation Equations (2.42). This helps to generate the neutral curves for range of different values of roughness and power-law index. This method has been recently used for the rotating disk for Newtonian fluids [32, 36, 50]

and the method has also been adapted for the generalised Newtonian fluids [51]. Previously a shooting method was been used in the literature to solve linear governing perturbation equations. However this approach transformed the perturbation system to a set of first order ODE system and solved one eigenvalue per iteration, whilst the spectral method solved all eigenvalues in one iteration. The Chebyshev polynomials of the first kind are defined as

$$T_m(y) = \cos(m \cos^{-1}(y)).$$

and it satisfied the recurrence relation in the interval $y \in [-1, 1]$

$$\begin{aligned} T_0(y) &= 1 \\ T_1(y) &= y \\ T_{m+1}(y) &= T_{m+1}(y) = 2yT_m(y) - T_{m-1}(y) \end{aligned}$$

Accordingly, the stability equations are linearised with respect to the perturbation quantities and solved via a Galerkin projection method, using Chebyshev polynomial decomposition. The method used here is presented by Appelquist and Imayama [52] to eliminate the need for algebraic transformation and provides higher accuracy solutions to prior shooting methods. The governing perturbation equations are solved using a Chebyshev polynomial discretisation method in the wall-normal direction to obtain solutions of the dispersion relation $D(\alpha, \beta; Re, [a, b]) = 0$ with the aim of studying the occurrence of convective instabilities for various values of the roughness and fluid parameters. The use of the polynomials ensures a higher accuracy compared to standard finite differences methods with a similar discretisation. An exponential map is adopted to map the Gauss-Lobatto grid points used for the Chebyshev polynomials into the physical space: 100 points are therefore distributed between the disk surface $z = 0$ and the top of the domain $z_{max} = 20$ which is chosen to match the outer bound of the mean-flow solution.

$$y_i = \cos\left(\frac{i\pi}{m}\right).$$

The stability equations are written and solved in primitive variables at all the collocation points except the ones at the boundaries

$$\begin{aligned} z &= -4 \log(\frac{y - A}{B}) \\ A &= -1 - B \\ B &= 2/e^{-\frac{z_{max}}{4}} - 1. \end{aligned}$$

The Chebyshev polynomials and their derivatives in the physical space of the rotating disk flows are constructed using the chain rule as follows in the truncated series at collocation points $S_i(z) = T_i(y)$. Then, the truncated series

of the perturbation quantities $(\hat{u};\hat{v};\hat{w};\hat{p})$ and their derivatives at collocation points are later formed as the sum of the contributions of all the transformed Chebyshev polynomials

$$\hat{u}(z_j) = \sum_{i=0}^{N} C_i^{\hat{u}} S_i(z_j) \qquad \hat{v}(z_j) = \sum_{i=0}^{N} C_i^{\hat{v}} S_i(z_j)$$
$$\hat{w}(z_j) = \sum_{i=0}^{N} C_i^{\hat{w}} S_i(z_j) \qquad \hat{p}(z_j) = \sum_{i=0}^{N} C_i^{\hat{p}} S_i(z_j)$$

$$\hat{u}'(z_j) = \sum_{i=0}^{N} C_i^{\hat{u}} S_i'(z_j) \qquad \hat{v}'(z_j) = \sum_{i=0}^{N} C_i^{\hat{v}} S_i'(z_j)$$
$$\hat{w}'(z_j) = \sum_{i=0}^{N} C_i^{\hat{w}} S_i'(z_j) \qquad \hat{p}'(z_j) = \sum_{i=0}^{N} C_i^{\hat{p}} S_i'(z_j)$$

$$\hat{u}''(z_j) = \sum_{i=0}^{N} C_i^{\hat{u}} S_i''(z_j) \qquad \hat{v}''(z_j) = \sum_{i=0}^{N} C_i^{\hat{v}} S_i''(z_j)$$
$$\hat{w}''(z_j) = \sum_{i=0}^{N} C_i^{\hat{w}} S_i''(z_j) \qquad \hat{p}''(z_j) = \sum_{i=0}^{N} C_i^{\hat{u}} S_i''(z_j)$$

The perturbation quantities will be solved so that the perturbed flows (e.g. $U + \hat{u}$) satisfy the partial-slip condition and are subject to zero boundary conditions at the disk surface and in the far-field. This ensures that the perturbations to the steady flow are contained within the boundary layer, and that the effects of surface roughness are not double-counted within the analysis [35, 50]. All perturbation quantities are normally set to be zero at the far end of the physical domain. Moreover, the Chebyshev expansions of the perturbation quantities along with the boundary conditions will be inserted into the linearised governing equations. Furthermore, a new method of partial-slip will be implemented through the thesis, and perturbation quantities will be solved with the effect of the MW model. Therefore, the Chebyshev expansions of the perturbation quantities will be substituted into the linearised perturbation Equations (2.42) that lead to the matrix system

$$(A_2\alpha^2 + A_1\alpha + A_0)\nu = 0. \tag{2.45}$$

where A_2, A_1 and A_0 are square matrices and coefficients of α^2, α and α^0 respectively, while $\nu = (\hat{u}, \hat{v}, \hat{w}, \hat{p})^T$ is the matrix of eigenfunctions. The form of the matrices are stated below as

$$A_2 = \begin{pmatrix} S_0(z_0) & 0 & 0 & 0 & \cdots \\ 0 & S_N(z_0) & 0 & 0 & \cdots \\ 0 & 0 & S_N(z_0) & 0 & \cdots \\ 0 & 0 & 0 & S_N(z_0) & \cdots \\ (1/Re)S_0(z_1) & 0 & 0 & 0 & \cdots \\ 0 & (1/Re)S_0(z_1) & 0 & 0 & \cdots \\ 0 & 0 & (1/Re)S_0(z_1) & 0 & \cdots \\ 0 & 0 & 0 & (1/Re)S_0(z_1) & \cdots \\ \vdots & \vdots & \vdots & \vdots & \cdots \\ S_N(z_N) & 0 & 0 & 0 & \cdots \\ 0 & S_N(z_N) & 0 & 0 & \cdots \\ 0 & 0 & S_N(z_N) & 0 & \cdots \\ 0 & 0 & S'_N(z_N) & 0 & \cdots \end{pmatrix},$$

$$A_1 = \begin{pmatrix} \varepsilon S_N(z_0) & 0 & 0 & 0 & \cdots \\ 0 & \varepsilon S_N(z_0) & 0 & 0 & \cdots \\ 0 & 0 & \varepsilon S_N(z_0) & 0 & \cdots \\ 0 & 0 & 0 & \varepsilon S_N(z_0) & \cdots \\ iUS_0(z_1) & 0 & 0 & 0 & \cdots \\ 0 & iUS_0(z_1) & 0 & 0 & \cdots \\ 0 & 0 & iUS_0(z_1) & 0 & \cdots \\ iUS_0(z_1) & 0 & 0 & 0 & \cdots \\ \vdots & \vdots & \vdots & \vdots & \cdots \\ \varepsilon S_N(z_N) & 0 & 0 & 0 & \cdots \\ 0 & \varepsilon S_N(z_N) & 0 & 0 & \cdots \\ 0 & 0 & \varepsilon S_N(z_N) & 0 & \cdots \\ 0 & 0 & \varepsilon S'_N(z_N) & 0 & \cdots \end{pmatrix},$$

$$A_0 = \begin{pmatrix} \varepsilon S_N(z_0) & 0 & 0 & 0 & \cdots \\ 0 & \varepsilon S_N(z_0) & 0 & 0 & \cdots \\ 0 & 0 & \varepsilon S_N(z_0) & 0 & \cdots \\ 0 & 0 & 0 & \varepsilon S_N(z_0) & \cdots \\ A_{51} & A_{52} & A_{53} & 0 & \cdots \\ A_{61} & A_{62} & A_{63} & A_{64} & \cdots \\ 0 & 0 & A_{73} & A_{74} & \cdots \\ A_{81} & A_{82} & A_{83} & 0 & \cdots \\ \vdots & \vdots & \vdots & \vdots & \cdots \\ \varepsilon S_N(z_N) & 0 & 0 & 0 & \cdots \\ 0 & \varepsilon S_N(z_N) & 0 & 0 & \cdots \\ 0 & 0 & \varepsilon S_N(z_N) & 0 & \cdots \\ 0 & 0 & \varepsilon S'_N(z_N) & 0 & \cdots \end{pmatrix}.$$

The complex parameter ε in the matrices A_2 and A_1 is set to $\varepsilon = -20i$, where $i = \sqrt{-1}$, this ensures that the boundary conditions are properly imposed and

$$\begin{aligned}
A_{51} &= \Big(i\bar{\beta}V + \frac{U}{Re}\Big)S_0(z_1) + \frac{1}{Re}\Big[W - \mu' - \hat{\mu}'(U')^2 - 2\hat{\mu}U'U''\Big]S'_0(z_1) \\
&\quad - \frac{1}{Re}\Big[\mu + \hat{\mu}(U')^2\Big]S''_0(z_1), \\
A_{52} &= -\frac{2(V+1)}{Re}S_0(z_1) - \frac{1}{Re}\Big[\hat{\mu}U'V' + \hat{\mu}(U'V'' + V'U'')\Big]S'_0(z_1) \\
&\quad + \frac{1}{Re}(\hat{\mu}U'V')S''_0(z_1), \\
A_{53} &= U'S_0(z_1), \\
A_{61} &= -\frac{2(V+1)}{Re}S_0(z_1) - \frac{1}{Re}\Big[\hat{\mu}U'V' + \hat{\mu}(U'V'' + V'U'')\Big]S'_0(z_1) \\
&\quad + \frac{1}{Re}(\hat{\mu}U'V')S''_0(z_1), \\
A_{62} &= \Big(i\bar{\beta}V + \frac{U}{Re}\Big)S_0(z_1) + \frac{1}{Re}\Big[W - \mu' - \hat{\mu}'(U')^2 - 2\hat{\mu}U'U''\Big]S'_0(z_1) \\
&\quad - \frac{1}{Re}\Big[\mu + \hat{\mu}(U')^2\Big]S''_0(z_1), \\
A_{63} &= V'S_0(z_1), \quad A_{64} = i\bar{\beta}S_0(z_1), \\
A_{73} &= \Big(i\bar{\beta}V + \frac{W'}{Re}\Big)S_0(z_1) + \frac{1}{Re}\Big(W - \mu'\Big)S'_0(z_1) - \frac{1}{Re}\mu S''_0(z_1), \\
A_{74} &= S'_0(z_1), \\
A_{81} &= \frac{1}{Re}S_0(z_1), \quad A_{82} = i\bar{\beta}S_0(z_1), \quad A_{83} = S'_0(z_1).
\end{aligned}$$

The system of a quadratic eigenvalue problem in Equation (2.45) can be

solved in MATLAB with the function polyeig that computes possible eigenvalues and eigenvectors of the system for fixed values of Re and various values of β iteratively. The branch point is selected with the smallest imaginary part of eigenvalue $\mathrm{Im}(\alpha_i)$ for each β such as the imaginary part of α for the next iteration of β is zero; that is, a neutral point. This process is often used for a wide range of Reynolds numbers to plot the entire neutral curve of convective instability for Carreau fluids with no-slip and partial-slip boundary conditions for different values of power-index.

2.5 *Derivation of the energy balance equations*

Following various studies in the literature [35, 36, 53], an integral energy equation for disturbances within the Carreau model is derived to analyse the underlying physical mechanisms behind the effects of surface roughness. In order to derive the energy equation, one needs to compute the sum of the resulting expressions leading to the kinetic-energy equation for the disturbances

$$
\begin{aligned}
E = {} & \Delta_1 K + (uU' + vV')w + \frac{U(u^2+v^2) + W'w^2}{R} - \frac{u}{R} \\
& \left[\mu\Delta_2 u + \mu'\left(\frac{\partial u}{\partial z} + \frac{\partial w}{\partial r}\right) + \frac{\partial(\tilde{\mu}U'\psi)}{\partial z}\right] + \frac{\partial(up)}{\partial r} + \frac{1}{R}\frac{\partial(vp)}{\partial\theta} + \frac{\partial(wp)}{\partial z} + \frac{up}{R} \\
& - \frac{v}{R}\left[\mu\Delta_2 v + \mu'\left(\frac{\partial v}{\partial z} + \frac{1}{R}\frac{\partial w}{\partial\theta}\right) + \frac{\partial(\tilde{\mu}V'\psi)}{\partial z}\right] \\
& - \frac{w}{R}\left[\mu\Delta_2 w + 2\mu'\frac{\partial w}{\partial z} + \tilde{\mu}\left(U'\frac{\partial}{\partial r} + \frac{V'}{R}\frac{\partial}{\partial\theta}\right)\psi\right] \\
E = {} & \Delta_1 K + (uU' + vV')w + \frac{U(u^2+v^2) + W'w^2}{R} \\
& - \frac{u}{R}\left[\mu'\left(\frac{\partial u}{\partial z} + \frac{\partial w}{\partial r}\right) + \frac{\partial(\tilde{\mu}U'\psi)}{\partial z}\right] \\
& + \frac{\partial(up)}{\partial r} + \frac{1}{R}\frac{\partial(vp)}{\partial\theta} + \frac{\partial(wp)}{\partial z} + \frac{up}{R} - \frac{v}{R}\left[\mu'\left(\frac{\partial v}{\partial z} + \frac{1}{R}\frac{\partial w}{\partial\theta}\right) + \frac{\partial(\tilde{\mu}V'\psi)}{\partial z}\right] \\
& - \frac{\mu}{R}\left[\frac{\partial}{\partial x_i}(u_j\sigma_{ij}) - \sigma_{ij}\frac{\partial u_j}{\partial x_i}\right] - \frac{w}{R}\left[2\mu'\frac{\partial w}{\partial z} + \tilde{\mu}\left(U'\frac{\partial}{\partial r} + \frac{V'}{R}\frac{\partial}{\partial\theta}\right)\psi\right],
\end{aligned}
\tag{2.46}
$$

where

$$\Delta_1 = \frac{\partial}{\partial t} + U\frac{\partial}{\partial r} + \frac{V}{R}\frac{\partial}{\partial \theta} + \frac{W}{R}\frac{\partial}{\partial z},$$
$$\Delta_2 = \frac{\partial^2}{\partial r^2} + \frac{1}{R^2}\frac{\partial^2}{\partial \theta^2} + \frac{\partial^2}{\partial z^2}.$$

$K = (u^2 + v^2 + w^2)/2. u_1 = u,\ u_2 = v,\ u_3 = w,$

$$\frac{\partial}{\partial x_1} = \frac{\partial}{\partial r}, \quad \frac{\partial}{\partial x_2} = \frac{1}{R}\frac{\partial}{\partial \theta}, \quad \frac{\partial}{\partial x_3} = \frac{\partial}{\partial z},$$

and

$$\sigma_{11} = 2\frac{\partial u}{\partial r}, \quad \sigma_{12} = \frac{\partial v}{\partial r} + \frac{1}{R}\frac{\partial u}{\partial \theta}, \quad \sigma_{13} = \frac{\partial w}{\partial r} + \frac{\partial u}{\partial z}, \tag{2.47}$$
$$\sigma_{21} = \frac{1}{R}\frac{\partial u}{\partial \theta} + \frac{\partial v}{\partial r}, \quad \sigma_{22} = \frac{2}{R}\frac{\partial v}{\partial \theta}, \quad \sigma_{23} = \frac{1}{R}\frac{\partial w}{\partial \theta} + \frac{\partial v}{\partial z}, \tag{2.48}$$
$$\sigma_{31} = \frac{\partial u}{\partial z} + \frac{\partial w}{\partial r}, \quad \sigma_{32} = \frac{1}{R}\frac{\partial w}{\partial \theta} + \frac{\partial v}{\partial z}, \quad \sigma_{33} = 2\frac{\partial w}{\partial z}. \tag{2.49}$$

Substituting Equations (2.47), (2.48) and (2.49) into (2.5) gives the following equation

$$\begin{aligned}
E &= \Delta_1 K + (uU' + vV')w + \frac{U(u^2+v^2) + W'w^2}{R} \\
&- \frac{u}{R}\left[\mu'\left(\frac{\partial u}{\partial z} + \frac{\partial w}{\partial r}\right) + \frac{\partial(\tilde{\mu}U'\psi)}{\partial z}\right] \\
&+ \frac{\partial(up)}{\partial r} + \frac{1}{R}\frac{\partial(vp)}{\partial \theta} + \frac{\partial(wp)}{\partial z} + \frac{up}{R} - \frac{v}{R}\left[\mu'\left(\frac{\partial v}{\partial z} + \frac{1}{R}\frac{\partial w}{\partial \theta}\right) + \frac{\partial(\tilde{\mu}V'\psi)}{\partial z}\right] \\
&- \frac{\mu}{R}\left[\frac{\partial}{\partial x_i}(u_j\sigma_{ij}) - \sigma_{ij}\frac{\partial u_j}{\partial x_i}\right] - \frac{w}{R}\left[2\mu'\frac{\partial w}{\partial z} + \tilde{\mu}\left(U'\frac{\partial}{\partial r} + \frac{V'}{R}\frac{\partial}{\partial \theta}\right)\psi\right] \\
&= \Delta_1 K + (uU' + vV')w + \frac{U(u^2+v^2) + W'w^2}{R} - \frac{u}{R}\left[\mu'\frac{\partial w}{\partial r} + \frac{\partial(\tilde{\mu}U'\psi)}{\partial z}\right] \\
&+ \frac{\partial(up)}{\partial r} + \frac{1}{R}\frac{\partial(vp)}{\partial \theta} + \frac{\partial(wp)}{\partial z} + \frac{up}{R} - \frac{v}{R}\left[\mu'\frac{1}{R}\frac{\partial w}{\partial \theta} + \frac{\partial(\tilde{\mu}V'\psi)}{\partial z}\right] \\
&- \frac{\mu}{R}\left[\frac{\partial}{\partial x_i}(u_j\sigma_{ij}) - \sigma_{ij}\frac{\partial u_j}{\partial x_i}\right] - \frac{\mu'}{R}\frac{\partial K}{\partial z} - \frac{w}{R}\left[\mu'\frac{\partial w}{\partial z} + \tilde{\mu}\left(U'\frac{\partial}{\partial r} + \frac{V'}{R}\frac{\partial}{\partial \theta}\right)\psi\right].
\end{aligned} \tag{2.50}$$

Therefore

$$
\begin{aligned}
E = {} & \Delta_1 K + (uU' + vV')w + \frac{U(u^2+v^2)+W'w^2}{R} \\
& + \frac{\partial(up)}{\partial r} + \frac{1}{R}\frac{\partial(vp)}{\partial\theta} + \frac{\partial(wp)}{\partial z} + \frac{up}{R} - \frac{\mu}{R}\left[\frac{\partial}{\partial x_i}(u_j\sigma_{ij}) - \sigma_{ij}\frac{\partial u_j}{\partial x_i}\right] \\
& - \frac{\mu'}{R}\frac{\partial K}{\partial z} - \frac{\mu'}{R}\left[\frac{\partial(uw)}{\partial r} + \frac{1}{R}\frac{\partial(vw)}{\partial\theta} + \frac{\partial(ww)}{\partial z} + \frac{uw}{R}\right] \\
& - \frac{u}{R}\left[\frac{\partial(\tilde{\mu}U'\psi)}{\partial z}\right] - \frac{v}{R}\left[\frac{\partial(\tilde{\mu}V'\psi)}{\partial z}\right] - \frac{w}{R}\left[\tilde{\mu}\left(U'\frac{\partial}{\partial r} + \frac{V'}{R}\frac{\partial}{\partial\theta}\right)\psi\right],
\end{aligned}
$$

where

$$
\psi = \left(U'\frac{\partial u}{\partial z} + V'\frac{\partial v}{\partial z}\right).
$$

Hence

$$
\begin{aligned}
\tilde{\mu}U'\psi &= \tilde{\mu}(U'U')\frac{\partial u}{\partial z} + \tilde{\mu}(U'V')\frac{\partial v}{\partial z}, \\
\tilde{\mu}V'\psi &= \tilde{\mu}(U'V')\frac{\partial u}{\partial z} + \tilde{\mu}(V'V')\frac{\partial v}{\partial z}.
\end{aligned}
$$

We get

$$
\begin{aligned}
& - \frac{u}{R}\left[\frac{\partial(\tilde{\mu}U'\psi)}{\partial z}\right] - \frac{v}{R}\left[\frac{\partial(\tilde{\mu}V'\psi)}{\partial z}\right] = -\frac{u}{R}\frac{\partial}{\partial z}\left(\tilde{\mu}(U'U')\frac{\partial u}{\partial z}\right) \\
& - \frac{u}{R}\frac{\partial}{\partial z}\left(\tilde{\mu}(U'V')\frac{\partial v}{\partial z}\right) - \frac{v}{R}\frac{\partial}{\partial z}\left(\tilde{\mu}(U'V')\frac{\partial u}{\partial z}\right) - \frac{v}{R}\frac{\partial}{\partial z}\left(\tilde{\mu}(V'V')\frac{\partial v}{\partial z}\right) \\
& = -\frac{(\tilde{\mu}U'V')'}{R}\frac{\partial(uv)}{\partial z} - \frac{(\tilde{\mu}U'V')}{R}\left(u\frac{\partial^2 v}{\partial z^2} + v\frac{\partial^2 u}{\partial z^2}\right) - \frac{(\tilde{\mu}U'U')'}{2R}\frac{\partial u^2}{\partial z} \\
& - \frac{(\tilde{\mu}V'V')'}{2R}\frac{\partial v^2}{\partial z} - \frac{(\tilde{\mu}U'U')}{R}u\frac{\partial^2 u}{\partial z^2} - \frac{(\tilde{\mu}V'V')}{R}v\frac{\partial^2 v}{\partial z^2} \\
& = -\frac{(\tilde{\mu}U'U')'}{2R}\frac{\partial u^2}{\partial z} - \frac{(\tilde{\mu}V'V')'}{2R}\frac{\partial v^2}{\partial z} - \frac{(\tilde{\mu}U'V')'}{R}\frac{\partial(uv)}{\partial z} \\
& - \frac{(\tilde{\mu}U'U')}{R}\left[\frac{\partial}{\partial z}\left(u\frac{\partial u}{\partial z}\right) - \left(\frac{\partial u}{\partial z}\right)^2\right] - \frac{(\tilde{\mu}V'V')}{R}\left[\frac{\partial}{\partial z}\left(v\frac{\partial v}{\partial z}\right) - \left(\frac{\partial v}{\partial z}\right)^2\right] \\
& - \frac{(\tilde{\mu}U'V')}{R}\left[\frac{\partial}{\partial z}\left(v\frac{\partial u}{\partial z}\right) + \frac{\partial}{\partial z}\left(u\frac{\partial v}{\partial z}\right) - 2\frac{\partial u}{\partial z}\frac{\partial v}{\partial z}\right]
\end{aligned}
$$

Therefore

$$
\begin{aligned}
E = {} & \Delta_1 K + (uU' + vV')w + \frac{U(u^2+v^2) + W'w^2}{R} \\
& + \frac{\partial(up)}{\partial r} + \frac{1}{R}\frac{\partial(vp)}{\partial\theta} + \frac{\partial(wp)}{\partial z} + \frac{up}{R} - \frac{\mu}{R}\left[\frac{\partial}{\partial x_i}(u_j\sigma_{ij}) - \sigma_{ij}\frac{\partial u_j}{\partial x_i}\right] \\
& - \frac{\mu'}{R}\frac{\partial K}{\partial z} - \frac{\mu'}{R}\left[\frac{\partial(uw)}{\partial r} + \frac{1}{R}\frac{\partial(vw)}{\partial\theta} + \frac{\partial(ww)}{\partial z} + \frac{uw}{R}\right] \\
& - \frac{(\tilde{\mu}U'U')'}{2R}\frac{\partial u^2}{\partial z} - \frac{(\tilde{\mu}V'V')'}{2R}\frac{\partial v^2}{\partial z} - \frac{(\tilde{\mu}U'V')'}{R}\frac{\partial(uv)}{\partial z} \\
& - \frac{(\tilde{\mu}U'U')}{R}\left[\frac{\partial}{\partial z}\left(u\frac{\partial u}{\partial z}\right) - \left(\frac{\partial u}{\partial z}\right)^2\right] - \frac{(\tilde{\mu}V'V')}{R}\left[\frac{\partial}{\partial z}\left(v\frac{\partial v}{\partial z}\right) - \left(\frac{\partial v}{\partial z}\right)^2\right] \\
& - \frac{(\tilde{\mu}U'V')}{R}\left[\frac{\partial}{\partial z}\left(v\frac{\partial u}{\partial z}\right) + \frac{\partial}{\partial z}\left(u\frac{\partial v}{\partial z}\right) - 2\frac{\partial u}{\partial z}\frac{\partial v}{\partial z}\right] \\
& - \frac{w}{R}\left[\tilde{\mu}\left(U'\frac{\partial}{\partial r} + \frac{V'}{R}\frac{\partial}{\partial\theta}\right)\psi\right].
\end{aligned}
$$

Then

$$
\begin{aligned}
E = {} & \Delta_1 K + (uU' + vV')w + \frac{U(u^2+v^2) + W'w^2}{R} \\
& + \frac{\partial(up)}{\partial r} + \frac{1}{R}\frac{\partial(vp)}{\partial\theta} + \frac{\partial(wp)}{\partial z} + \frac{up}{R} - \frac{\mu}{R}\left[\frac{\partial}{\partial x_i}(u_j\sigma_{ij}) - \sigma_{ij}\frac{\partial u_j}{\partial x_i}\right] \\
& - \frac{\mu'}{R}\frac{\partial K}{\partial z} - \frac{\mu'}{R}\left[\frac{\partial(uw)}{\partial r} + \frac{1}{R}\frac{\partial(vw)}{\partial\theta} + \frac{\partial(ww)}{\partial z} + \frac{uw}{R}\right] \\
& - \frac{(\tilde{\mu}U'U')'}{2R}\frac{\partial u^2}{\partial z} - \frac{(\tilde{\mu}V'V')'}{2R}\frac{\partial v^2}{\partial z} - \frac{(\tilde{\mu}U'V')'}{R}\frac{\partial(uv)}{\partial z} \\
& - \frac{(\tilde{\mu}U'U')}{R}\left[\frac{\partial}{\partial z}\left(u\frac{\partial u}{\partial z}\right) - \left(\frac{\partial u}{\partial z}\right)^2\right] - \frac{(\tilde{\mu}V'V')}{R}\left[\frac{\partial}{\partial z}\left(v\frac{\partial v}{\partial z}\right) - \left(\frac{\partial v}{\partial z}\right)^2\right] \\
& - \frac{(\tilde{\mu}U'V')}{R}\left[\frac{\partial}{\partial z}\left(v\frac{\partial u}{\partial z}\right) + \frac{\partial}{\partial z}\left(u\frac{\partial v}{\partial z}\right) - 2\frac{\partial u}{\partial z}\frac{\partial v}{\partial z}\right] \\
& - \frac{\tilde{\mu}U'U'}{R}\left[\frac{\partial}{\partial z}\left(w\frac{\partial u}{\partial r}\right) - \frac{\partial w}{\partial z}\frac{\partial u}{\partial r}\right] - \frac{\tilde{\mu}U'V'}{R}\left[\frac{\partial}{\partial z}\left(w\frac{\partial v}{\partial r}\right) - \frac{\partial w}{\partial z}\frac{\partial v}{\partial r}\right] \\
& - \frac{\tilde{\mu}U'V'}{R}\left[\frac{\partial}{\partial z}\left(w\frac{1}{R}\frac{\partial u}{\partial\theta}\right) - \frac{\partial w}{\partial z}\frac{1}{R}\frac{\partial u}{\partial\theta}\right] - \frac{\tilde{\mu}V'V'}{R}\left[\frac{\partial}{\partial z}\left(w\frac{1}{R}\frac{\partial v}{\partial\theta}\right) - \frac{\partial w}{\partial z}\frac{1}{R}\frac{\partial v}{\partial\theta}\right].
\end{aligned}
$$

Removing the t and θ derivatives to ensure the steady and rotationally sym-

metric flow leads to

$$
\begin{aligned}
E = {} & \Delta K + (uU' + vV')w + \frac{U(u^2+v^2) + W'w^2}{R} \\
& + \frac{\partial(up)}{\partial r} + \frac{\partial(wp)}{\partial z} + \frac{up}{R} - \frac{\mu}{R}\left[\frac{\partial}{\partial x_i}(u_j\sigma_{ij}) - \sigma_{ij}\frac{\partial u_j}{\partial x_i}\right] \\
& - \frac{\mu'}{R}\frac{\partial K}{\partial z} - \frac{\mu'}{R}\left[\frac{\partial(uw)}{\partial r} + \frac{\partial(ww)}{\partial z} + \frac{uw}{R}\right] \\
& - \frac{(\tilde{\mu}U'U')'}{2R}\frac{\partial u^2}{\partial z} - \frac{(\tilde{\mu}V'V')'}{2R}\frac{\partial v^2}{\partial z} - \frac{(\tilde{\mu}U'V')'}{R}\frac{\partial(uv)}{\partial z} \\
& - \frac{(\tilde{\mu}U'U')}{R}\left[\frac{\partial}{\partial z}\left(u\frac{\partial u}{\partial z}\right) - \left(\frac{\partial u}{\partial z}\right)^2\right] - \frac{(\tilde{\mu}V'V')}{R}\left[\frac{\partial}{\partial z}\left(v\frac{\partial v}{\partial z}\right) - \left(\frac{\partial v}{\partial z}\right)^2\right] \\
& - \frac{(\tilde{\mu}U'V')}{R}\left[\frac{\partial}{\partial z}\left(v\frac{\partial u}{\partial z}\right) + \frac{\partial}{\partial z}\left(u\frac{\partial v}{\partial z}\right) - 2\frac{\partial u}{\partial z}\frac{\partial v}{\partial z}\right] \\
& - \frac{\tilde{\mu}U'U'}{R}\left[\frac{\partial}{\partial z}\left(w\frac{\partial u}{\partial r}\right) - \frac{\partial w}{\partial z}\frac{\partial u}{\partial r}\right] - \frac{\tilde{\mu}U'V'}{R}\left[\frac{\partial}{\partial z}\left(w\frac{\partial v}{\partial r}\right) - \frac{\partial w}{\partial z}\frac{\partial v}{\partial r}\right],
\end{aligned}
$$

where

$$\Delta = U\frac{\partial}{\partial r} + \frac{W}{R}\frac{\partial}{\partial z},$$

$u_1 = u$, $u_2 = v$, $u_3 = w$,

$$\frac{\partial}{\partial x_1} = \frac{\partial}{\partial r}, \quad \frac{\partial}{\partial x_2} = 0, \quad \frac{\partial}{\partial x_3} = \frac{\partial}{\partial z},$$

and

$$
\begin{aligned}
&\sigma_{11} = 2\frac{\partial u}{\partial r}, && \sigma_{12} = \frac{\partial v}{\partial r}, && \sigma_{13} = \frac{\partial w}{\partial r} + \frac{\partial u}{\partial z}, \\
&\sigma_{21} = \frac{\partial v}{\partial r}, && \sigma_{22} = 0, && \sigma_{23} = \frac{\partial v}{\partial z}, \\
&\sigma_{31} = \frac{\partial u}{\partial z} + \frac{\partial w}{\partial r}, && \sigma_{32} = \frac{\partial v}{\partial z}, && \sigma_{33} = 2\frac{\partial w}{\partial z}.
\end{aligned}
$$

Integrate across the boundary layer

$$
\begin{aligned}
E = {} & \int_0^\infty \left[\Delta K + (uU' + vV')w + \frac{U(u^2+v^2) + W'w^2}{R}\right] \mathrm{d}z \\
& + \int_0^\infty \frac{\partial(up)}{\partial r}\,\mathrm{d}z - (wp)_\mathrm{w} + \int_0^\infty \frac{up}{R}\,\mathrm{d}z - \int_0^\infty \frac{\mu}{R}\frac{\partial(u\sigma_{11} + v\sigma_{12} + w\sigma_{13})}{\partial r}\,\mathrm{d}z \\
& - \int_0^\infty \frac{\mu}{R}\left[\frac{\partial}{\partial z}(u\sigma_{31} + v\sigma_{32} + w\sigma_{33})\right] \mathrm{d}z + \int_0^\infty \frac{\mu\sigma_{ij}}{R}\frac{\partial u_j}{\partial x_i}\,\mathrm{d}z \\
& - \int_0^\infty \frac{\mu'}{R}\frac{\partial K}{\partial z}\,\mathrm{d}z - \int_0^\infty \frac{\mu'}{R}\left[\frac{\partial(uw)}{\partial r} + \frac{\partial(ww)}{\partial z} + \frac{uw}{R}\right] \mathrm{d}z + \int_0^\infty \chi\,\mathrm{d}z,
\end{aligned}
$$

where

$$\begin{aligned}\chi = &- \frac{(\tilde{\mu}U'U')'}{2R}\frac{\partial u^2}{\partial z} - \frac{(\tilde{\mu}V'V')'}{2R}\frac{\partial v^2}{\partial z} - \frac{(\tilde{\mu}U'V')'}{R}\frac{\partial (uv)}{\partial z} \\ &- \frac{(\tilde{\mu}U'U')}{R}\left[\frac{\partial}{\partial z}\left(u\frac{\partial u}{\partial z}\right) - \left(\frac{\partial u}{\partial z}\right)^2\right] - \frac{(\tilde{\mu}V'V')}{R}\left[\frac{\partial}{\partial z}\left(v\frac{\partial v}{\partial z}\right) - \left(\frac{\partial v}{\partial z}\right)^2\right] \\ &- \frac{(\tilde{\mu}U'V')}{R}\left[\frac{\partial}{\partial z}\left(v\frac{\partial u}{\partial z}\right) + \frac{\partial}{\partial z}\left(u\frac{\partial v}{\partial z}\right) - 2\frac{\partial u}{\partial z}\frac{\partial v}{\partial z}\right] \\ &- \frac{\tilde{\mu}U'U'}{R}\left[\frac{\partial}{\partial z}\left(w\frac{\partial u}{\partial r}\right) - \frac{\partial w}{\partial z}\frac{\partial u}{\partial r}\right] - \frac{\tilde{\mu}U'V'}{R}\left[\frac{\partial}{\partial z}\left(w\frac{\partial v}{\partial r}\right) - \frac{\partial w}{\partial z}\frac{\partial v}{\partial r}\right].\end{aligned}$$

Using integration by parts, the perturbations are averaged over a single time period and azimuthal mode. Later, they are integrated across the entire boundary layer. This leads to

$$\begin{aligned}E = &\int_0^\infty \left[\Delta K + (uU' + vV')w + \frac{U(u^2+v^2) + W'w^2}{R}\right] \mathrm{d}z \\ &- (wp)_\mathrm{w} + \int_0^\infty \frac{up}{R}\,\mathrm{d}z + \int_0^\infty \frac{\partial (up)}{\partial r}\,\mathrm{d}z - \int_0^\infty \frac{\mu}{R}\frac{\partial (u\sigma_{11} + v\sigma_{12} + w\sigma_{13})}{\partial r}\,\mathrm{d}z \\ &+ \frac{[\mu(u\sigma_{31} + v\sigma_{32} + w\sigma_{33})]_\mathrm{w}}{R} + \int_0^\infty \frac{\mu\sigma_{ij}}{R}\frac{\partial u_j}{\partial x_i}\,\mathrm{d}z + \int_0^\infty \frac{\mu'(u\sigma_{31} + v\sigma_{32} + w\sigma_{33})}{R}\,\mathrm{d}z \\ &- \int_0^\infty \frac{\mu'}{R}\frac{\partial (uw)}{\partial r}\,\mathrm{d}z - \int_0^\infty \frac{\mu' uw}{R^2}\,\mathrm{d}z + \frac{(\mu' K)_\mathrm{w}}{R} + \frac{(\mu' w^2)_\mathrm{w}}{R} + \int_0^\infty \frac{\mu'' K}{R}\,\mathrm{d}z \\ &+ \int_0^\infty \frac{\mu'' w^2}{R}\,\mathrm{d}z - \int_0^\infty \left[\frac{(\tilde{\mu}U'U')'}{2R}\frac{\partial u^2}{\partial z} - \frac{(\tilde{\mu}V'V')'}{2R}\frac{\partial v^2}{\partial z} - \frac{(\tilde{\mu}U'V')'}{R}\frac{\partial (uv)}{\partial z}\right] \mathrm{d}z \\ &- \int_0^\infty \frac{(\tilde{\mu}U'U')}{R}\left[\frac{\partial (u\sigma_{31})}{\partial z} - \sigma_{31}^2\right] - \int_0^\infty \frac{(\tilde{\mu}V'V')}{R}\left[\frac{\partial (v\sigma_{32})}{\partial z} - \sigma_{32}^2\right] \mathrm{d}z \\ &- \int_0^\infty \frac{(\tilde{\mu}U'V')}{R}\left[\frac{\partial (u\sigma_{32} + v\sigma_{31})}{\partial z} - 2\sigma_{31}\sigma_{32}\right] \mathrm{d}z \\ &- \int_0^\infty \frac{(\tilde{\mu}U'U')}{R}\frac{\partial (w\sigma_{31})}{\partial r}\,\mathrm{d}z - \int_0^\infty \frac{(\tilde{\mu}U'V')}{R}\frac{\partial (w\sigma_{32})}{\partial r}\,\mathrm{d}z + \int_0^\infty \frac{(\tilde{\mu}U'U')\sigma_{31}}{R}\frac{\partial w}{\partial r}\,\mathrm{d}z \\ &+ \int_0^\infty \frac{(\tilde{\mu}U'V')\sigma_{32}}{R}\frac{\partial w}{\partial r}\,\mathrm{d}z.\end{aligned}$$

So

$$\begin{aligned}
&\int_0^\infty \Bigg[\underbrace{U\frac{\partial \overline{K}}{\partial r}}_{a} + \underbrace{\frac{\partial\left(\overline{up}\right)}{\partial r}}_{b} - \underbrace{\frac{\partial}{\partial r}\left(\overline{u\sigma_{11}} + \overline{v\sigma_{12}} + \overline{w\sigma_{13}}\right)}_{c}\Bigg]\,\mathrm{d}z \\
&= \underbrace{\int_0^\infty \left(-\overline{uw}\frac{\partial U}{\partial z} - \overline{vw}\frac{\partial V}{\partial z} - \frac{1}{Re}\overline{w^2}\frac{\partial W}{\partial z}\right)\mathrm{d}z}_{\mathrm{I}} - \underbrace{\int_0^\infty \overline{\sigma_{ij}\frac{\partial u_j}{\partial x_i}}\,\mathrm{d}z}_{\mathrm{II}} \\
&\underbrace{- \int_0^\infty \frac{1}{Re}\overline{up}\,\mathrm{d}z + (\overline{wp})_W}_{\mathrm{III}} \underbrace{- (\overline{u\sigma_{31}} + \overline{v\sigma_{32}} + \overline{w\sigma_{33}})_W}_{\mathrm{IV}} \\
&\underbrace{+ \left[\int_0^\infty \overline{u^2}U\,\mathrm{d}z + \int_0^\infty \overline{v^2}U\,\mathrm{d}z + \int_0^\infty \frac{\partial \overline{K}}{\partial z}W\,\mathrm{d}z\right]}_{\mathrm{V}} \\
&\underbrace{+ \frac{1}{Re}\left\{\int_0^\infty \left[\mu\overline{\frac{\partial^2 u}{\partial z^2}u} + \frac{\partial\mu}{\partial z}\overline{\frac{\partial u}{\partial z}u}\right]\mathrm{d}z + \int_0^\infty \left[\mu\overline{\frac{\partial^2 v}{\partial z^2}v} + \frac{\partial\mu}{\partial z}\overline{\frac{\partial v}{\partial z}v}\right]\mathrm{d}z\right\}}_{\mathrm{VI}} \\
&\underbrace{+ + \int_0^\infty \left[\mu\overline{\frac{\partial^2 w}{\partial z^2}w} + \frac{\partial\mu}{\partial z}\overline{\frac{\partial w}{\partial z}w}\right]\mathrm{d}z\right\}}_{\mathrm{VI}}. \qquad (2.51)
\end{aligned}$$

Here, an overbar denotes a period-averaged quantity, such that $\overline{uv} = uv^* + u^*v$ (where * indicates the complex conjugate), and the subscript W denotes quantities evaluated at the wall. Terms on the left-hand side of Equation (2.51) can be identified as: (a) the average disturbance kinetic energy convected by the radial mean flow, (b) work done by the perturbation pressure, and (c) work done by the viscous stresses across the boundary layer. On the right-hand side we have: (I) the Reynolds-stress energy production term, (II) the viscous dissipation energy term, (III) pressure work terms, (IV) contributions from work done on the wall by viscous stresses, (V) terms arising from streamline curvature effects and the three-dimensionality of the mean flow, and (VI) the non-Newtonian viscosity terms. The energy equation is then normalized by the integrated mechanical energy flux to give

$$\begin{aligned}
-2\bar{\alpha}_\mathrm{i} = &\underbrace{(P_1 + P_2 + P_3)}_{I} + \underbrace{D}_{II} + \underbrace{(PW_1 + PW_2)}_{III} + \underbrace{(S_1 + S_2 + S_3)}_{IV} \\
&+ \underbrace{(G_1 + G_2 + G_3)}_{V} + \underbrace{(N_1 + N_2 + N_3)}_{VI}. \qquad (2.52)
\end{aligned}$$

The terms PW_2, S_1, S_2 and S_3 in the energy balance Equation (2.52) are identically zero due to the boundary conditions for the flow. The stability

effects of both shear-thinning and shear-thickening Carreau fluids will be investigated by calculating the total energy of the system, which is the sum of the energy production and dissipation terms. An increased total energy would show a destabilising effect on the modes, while decreased total energy reveals a stabilising effect on the mode.

Chapter 3

Effect of radially-anisotropic roughness on the Carreau model

In this chapter, the solution to the equations of the generalized non-Newtonian fluids using a Carreau model [27] is found for the radially anisotropic roughness-radial grooves. After finding solutions for the base flow velocity profiles, the local convective linear stability analysis is conducted. As discussed in [32, 35], the partial-slip boundary conditions do not affect the perturbation equations. That is, the governing stability equations are unaffected by surface roughness within the MW model. This approach is based on the logic of not double-counting the effects of roughness which has been open to the criticism (private communication, Garrett 2019). Therefore, this chapter will consider explicitly the effect of imposing the MW model within the perturbation equations to determine whether a material change occurs in the results.

The stability analysis of the Carreau fluids is conducted using the spectral Chebyshev method developed by Alveroglu *et al.* [32, 38] to compute the neutral curves for the convective instability. Thus, the system of stability equations is solved for the perturbation eigenfunctions. Besides, the neutral stability are plotted for the Type I and Type II instability modes for a range of η parameters and variation of power-index parameters. After that, the growth rates of the Carreau model for these cases are obtained. The effects of surface roughness on the growth rates of the the Type I mode are discussed. Furthermore, the energy analysis is solved here to confirm the results of the prior linear stability analysis, thereby giving some physical insight into the

responses. Also, a Chebyshev discretization method is used to solve the energy analysis equations derived in Chapter 2.5.

The steady mean flow solution for Carreau model with the radially anisotropic roughness (radial grooves) is presented in Section 3.1. The neutral stability curves is provided in Section 3.2, while the neutral stability curves for the convective instability by applying the partial-slip boundary conditions in the steady mean flow and in the disturbances for radially anisotropic roughness is given in Section 3.3. The effect of radially anisotropic roughness for a range of power-index is investigated in Section 3.4. Finally, key points will be drawn in Section 3.5.

3.1 *The steady mean flow results*

This section aims to identify the solutions of the steady mean for the Carreau model with the effect of the radially anisotropic roughness that corresponds to radial grooves on the disk surface. This is achieved by setting the roughness parameters in the partial-slip boundary conditions as $\lambda = 0, \eta > 0$ which is obtained from MW model [33]. The steady mean flow Equations (2.20, 2.21) of the Carreau model are solved using the MATLAB solver (see Subsection 2.3.1) with the partial-slip boundary conditions (2.23, 2.24). The mean flow profiles are computed for the three velocity components (U, V, W) for disks with different magnitudes of radial grooves and various values of power-law index parameters.

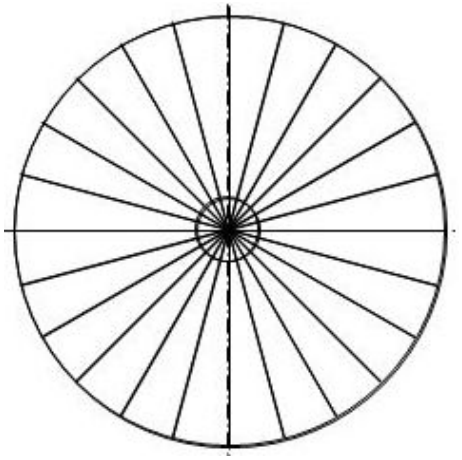

Figure 3.1: Radial grooves.

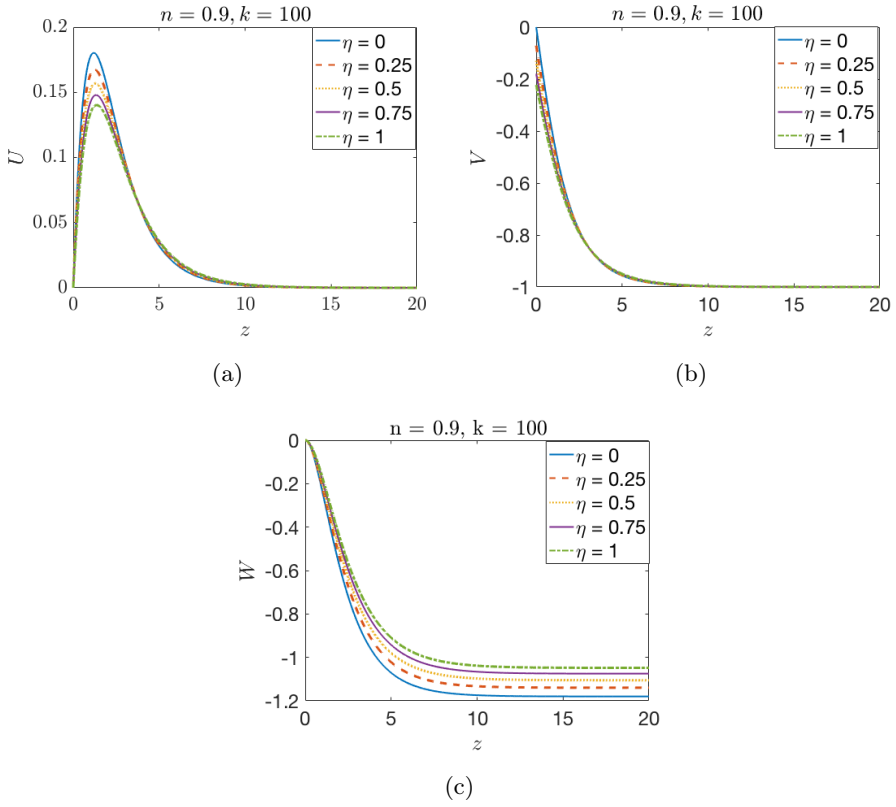

Figure 3.2: Mean flow components of the Carreau flow in the case of radially anisotropic roughness for shear-thinning fluid. (a) U-profile, (b) V-profile, (c) W-profile.

The radial mean flow profiles U are presented in Figures (3.2) and (3.3) (a) while, the azimuthal mean flow component V is presented in Figures (3.2) and (3.3) (b). The flow component W, in the axial direction, is presented in Figures (3.2) and (3.3) (c). The initial values of $U'(0)$, $V'(0)$ and $W(z_\infty)$ are important for the computation of the flow profiles and are shown in Tables (3.1) and (3.2) for various values of roughness parameters. The initial values for Newtonian flow are identical to those obtained by Cooper *et al.* [35]. Hence, the results are presented as follows: $n = 0.9$ and $n = 1.1$. Other values such as $n = 0.6$, $n = 0.7$, $n = 1.2$ and $n = 1.4$ can be found in Appendices (A.1) and (A.2) with their initial values.

Figures (3.2) and (3.3) (a) for the U profiles clearly show, there is a reduction in the magnitude of the radial wall jet, combined with an increase in radial grooves for all flows in both shear-thinning and shear-thickening. The physical sense behind this condition is that the increased roughness size would act to hold back the base of the wall jet, according to Garrett *et al.* [36]. On the other

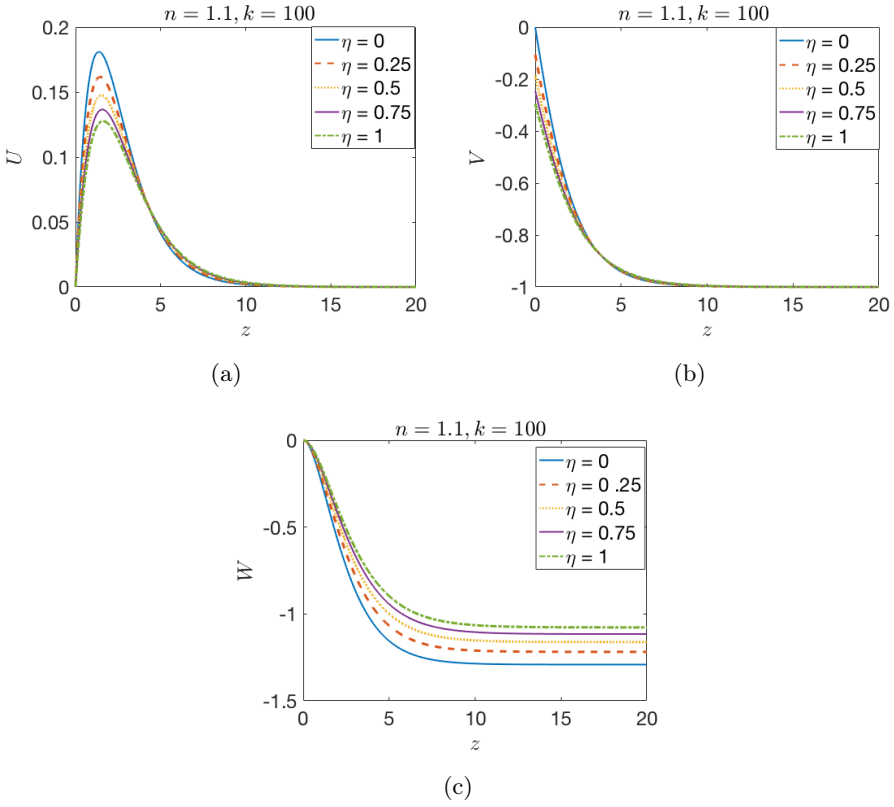

Figure 3.3: Mean flow components of the Carreau flow in the case of radially anisotropic roughness for shear-thickening fluid. (a) U-profile, (b) V-profile, (c) W-profile.

hand, the reduction rate of the radial wall jet is substantially modified with η that increases when n changes from 0.6 to 1.4. Hence, the maximum value for the radial flow profile U is reduced for increasingly shear-thinning Carreau fluid. However, it increases with the increasingly shear-thickening Carreau fluids. We also observe that the U profile infection point is moved towards the disk surface, which is interpreted as narrowing of the fluid boundary layer. Moreover, the location of the maximum value of U remains nearly unchanged for both $n < 1$ and $n > 1$, but moves slightly towards the disk surface for as roughness is increased. These changes of the U component are similar to those observed in the smooth case for increased surface roughness.

Figures (3.2) and (3.3) (b) show that the wall value of the azimuthal velocity profile V increases when the radial grooves (i.e the non-zero η) are gradually increase. Therefore, this finding is consistent with the results in the case of Newtonian flow (see Cooper *et al.* [35] and [33]). Likewise, the Figures (3.2) and (3.3) (c) highlight that the magnitude of axial flow W for all flows is

reduced when the radial grooves increase. In other words, the amount of flow entrained into the boundary layer reduced for the Non-Newtonian fluids when the roughness is increases.

Table 3.1: Numerical values of the mean velocity flow parameters $U'(0)$, $V'(0)$ and $W(z_\infty)$ for shear-thinning $n = 0.9$.

Parameters	$U'(0)$	$-V'(0)$	$-W(z_\infty)$
$\eta = 0$	0.6440	0.7968	0.7659
$\eta = 0.25$	0.4953	0.6128	0.7134
$\eta = 0.50$	0.4073	0.5038	0.6766
$\eta = 0.75$	0.3486	0.4305	0.6483
$\eta = 1$	0.3049	0.3772	0.6253

Table 3.2: Numerical values of the mean velocity flow parameters $U'(0)$, $V'(0)$ and $W(z_\infty)$ for shear-thickening $n = 1.1$.

Parameters	$U'(0)$	$-V'(0)$	$-W(z_\infty)$
$\eta = 0$	0.4137	0.4892	1.0148
$\eta = 0.25$	0.3534	0.4178	0.9531
$\eta = 0.50$	0.3099	0.3664	0.9045
$\eta = 0.75$	0.2767	0.3272	0.8648
$\eta = 1$	0.2505	0.2962	0.8313

3.2 *The convective instability for the radial-grooves*

In this section, the local convective instabilities are assessed through a linear stability in the case of the radial grooves that are distributed over the rotating disk. The convective instability is determined by the computed solutions of the perturbation Equations (2.42). The local convective instability is analysed in terms of both the neutral curves in (3.2.1) and the growth rates in (3.2.2). The perturbation quantities are subject to zero boundary conditions at both the disk surface and in the far-field. This ensures that the perturbations to the steady flow are contained within the boundary layer and the effects of surface roughness are not double-counted within the analysis [35, 50]. That is, the boundary conditions are as follows:

$$\hat{u}(z=0) = \hat{v}(z=0) = \hat{w}(z=0) = \hat{w}'(z=0) = 0, \tag{3.1a}$$

$$\hat{u}\,(z\to\infty) = \hat{v}\,(z\to\infty) = \hat{w}\,(z\to\infty) = \hat{p}\,(z\to\infty) = 0. \tag{3.1b}$$

The conditions at $z = 0$ represent the no-slip condition at the wall. The conditions at $z \to 1$ assume that all disturbances decay at a great distance from the disk. At this point, it is possible to set the frequency to zero, so that $\omega = 0$. This highlights the importance of the spatial instability of stationary vortices that rotate with the rough disk in the rotating frame of reference.

3.2.1 *Neutral curves*

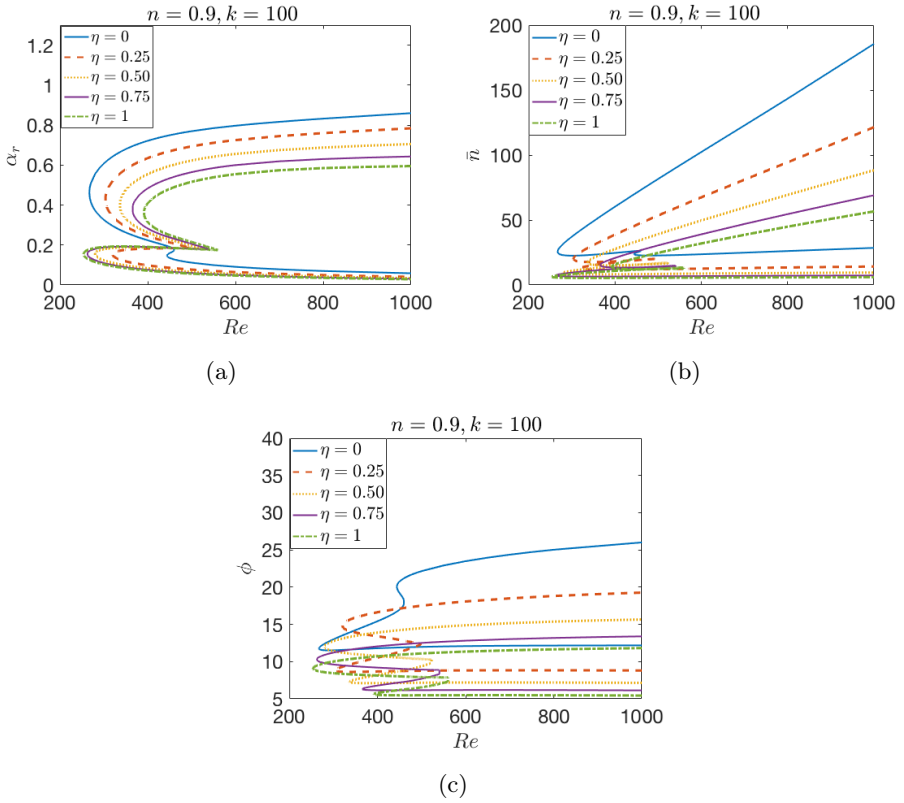

Figure 3.4: Neutral curves of the convective instability for the Carreau flow over radially anisotropic roughness with $n = 0.9$.

Two spatial branches are found to determine the convective instability characteristics of the system. Neutral curves, defined by neutral spatial growth $\alpha_i = 0$, are calculated for a variety of shear-thinning and -thickening fluids using the Carreau viscosity model over rough surfaces. The Type I mode results from the (inviscid) inflectional behaviour of mean-flow components and appears as the upper lobe in neutral curves. The Type II mode arises from the (viscous) streamline curvature and Coriolis effects and appears as a smaller

lower lobe. The neutral curves of the Carreau flow are presented for (Re, α_r), $(Re, \bar{n})$ and (R, ϕ)-planes, where $\bar{n}$ and ϕ are defined from Equations (2.44) and (2.43).

The figures depicted in this section show the neutral stability data for a range of η and two values n. Other values of n for this case and their critical values can be seen in Appendices (A.3) and (A.4). It is seen from the shear-thinning fluid in Figure (3.4) (a) that increasing the level of roughness increases the critical Reynolds number, stabilising the type I mode. Conversely, the Type II mode is initially destabilised as η is increases. After a threshold value of the parameter $\eta = 0.5$, the Type II mode onsets earlier than the Type I mode and becomes the dominant instability mechanism in the system. The result of the curve in the Newtonian fluids (i.e. $\eta = 0$) is consistent with those found by Cooper *et al.* [35] and Alveroglu *et al.* [32], the results for critical values can be seen from Table (3.3).

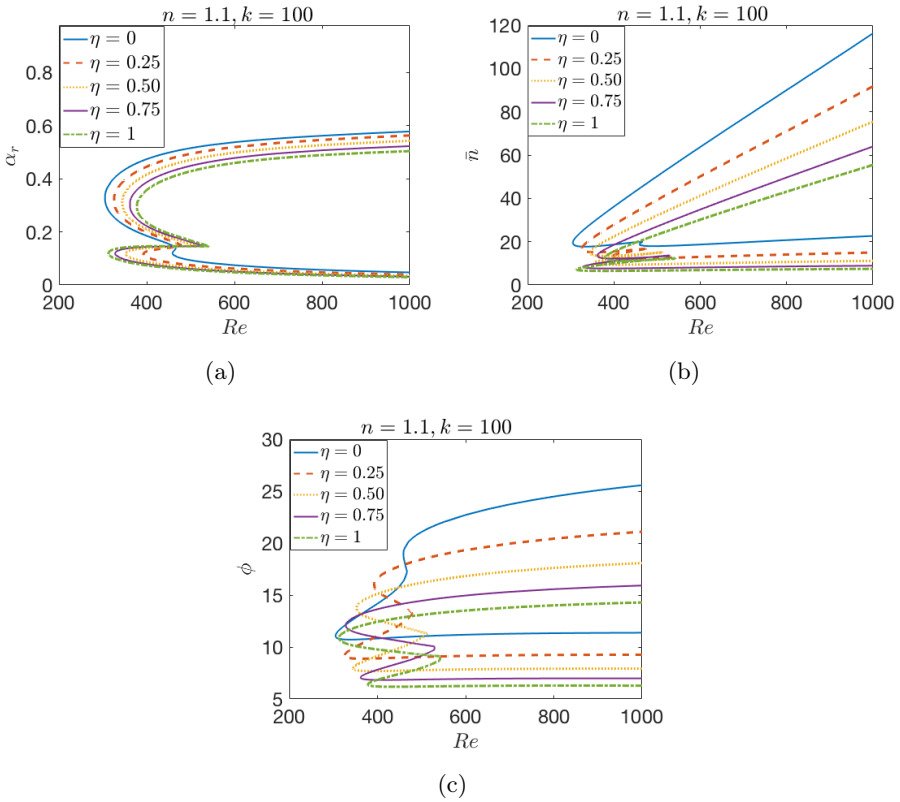

Figure 3.5: Neutral curves of the convective instability for the Carreau flow over radially anisotropic roughness with $n = 1.1$.

Table 3.3: The values of the critical Reynolds number Re, $\bar{n}$ and wave angle ϕ on the both modes Type I and (Type II) for $n = 0.9$.

Parameters	Re	$\bar{n}$	ϕ
$\eta = 0$	267.06(433.91)	46.32(23.82)	11.78(20.02)
$\eta = 0.25$	303.65(319.19)	20.21(12.81)	8.81(14.80)
$\eta = 0.50$	336.18(279.45)	17.29(9.22)	7.27(12.00)
$\eta = 0.75$	365.18(262.23)	15.36(7.40)	6.30(10.27)
$\eta = 1$	391.40(253.69)	13.94(6.27)	5.61(9.06)

Table 3.4: The values of the critical Reynolds number Re, $\bar{n}$ and wave angle ϕ on the both modes Type I and (Type II) for $n = 1.1$.

Parameters	Re	$\bar{n}$	ϕ
$\eta = 0$	304.69(458.65)	19.54(18.72)	11.06(18.96)
$\eta = 0.25$	325.12(391.33)	16.76(12.97)	9.16(15.96)
$\eta = 0.50$	343.98(351.57)	14.92(10.07)	7.93(13.71)
$\eta = 0.75$	361.28(327.76)	13.54(8.33)	7.05(12.08)
$\eta = 1$	377.23(312.51)	12.48(7.16)	6.38(10.84)

The neutral curves of the shear-thinning flow in terms of the number of spiral vortices are revealed in Figure (3.4) (b). There is a substantial decrease in the number of vortices along the upper branch of the neutral curve as well as a slight decrease along the lower branch. Furthermore, Figure (3.4) (c) shows a significant decrease in the vortex angle ϕ along both the upper and lower branches of the neutral curves with increased η. This is in addition with the strong stabilising effect on the Type I mode.

For the shear-thickening fluid in Figure (3.5) (a), it is clear that the neutral curves reveal the strong stabilising effect of increased roughness parameters on both modes in terms of critical Reynolds number. The effect of increasing the radial grooves diminishes the Type I lobe in terms of the width whereas it expands the Type II mode. Conversely, there is a decrease in the number of vortices and the vortex angle along the upper branch and a slight decrease along the lower branches for increased roughness as illustrated in Figures (3.5) (b) and (c). The critical values of both modes in the smooth case are in very close agreement with the existing results in the literature, as evidence in Table (3.4).

3.2.2 *The growth rate*

The growth rates of the Type I instability mode are presented for shear-thinning and -thickening Carreau fluids for the radially-anisotropic case at

$Re = Re_c + 25$. Here Re_c is the critical Reynolds number presented in Tables (3.3) and (3.4) for the onset of the Type I mode of instability. That is, they are presented at a fixed distance into the neutral curve. More importantly, the growth rate of the instability mode is measured as the absolute value of the negative imaginary part of the radial wavenumber, $|\alpha_i|$, at particular values of the vortex number $\bar{n}$ for each level of roughness.

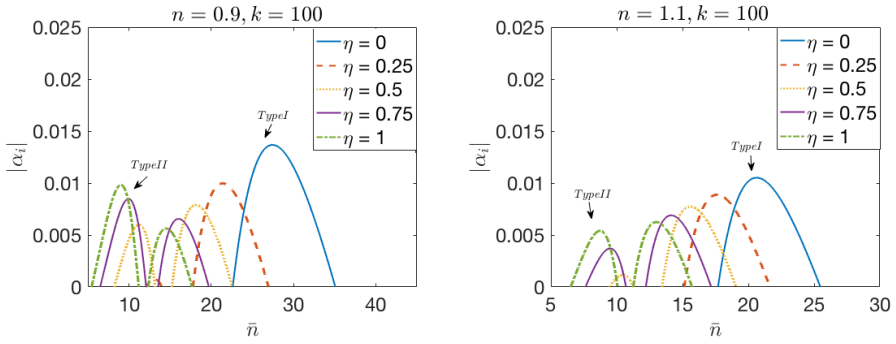

(a) (b)

Figure 3.6: Growth rates of type I and type II instability modes at $Re = Re_c + 25$ for the case of radial grooves within (a) shear-thinning and (b) shear-thickening, respectively.

Moreover, Figures (3.6) (a) and (b) show the stabilising effect of radial grooves for Carreau fluids of each flow is detected in the Type I mode in the shear-thinning and shear-thickening regimes. That is, the value of the most rapidly growing the Type I mode decreases with an increase in roughness parameter η. These results also show the destabilisation of the Type II mode of each flow with an increase in the roughness size. Therefore, the value of the most rapidly growing the Type II mode is indicated by increases proportionally to the surface roughness. Overall, the maximum growth rate shifts to lower values of $\bar{n}$ for both modes. This signals the reduction in the number of vortices as a result of the increase in the surface roughness level. Moreover, to ensure the levels of roughness are sufficiently high, the Type II growth rate exceeds the Type I growth rate. The critical parameters obtained for each flow are thus presented in Tables (3.3) and (3.4). Similarly, the discussion of the growth rates for the Newtonian flow is provided by Cooper *et al.*, where the flow results are included as a validation.

3.3 The novel approach for the perturbations

This section is a novel approach which extends the slip-velocity model for roughness from the base flow to be included in the perturbations terms. So, the no-slip conditions are replaced by the partial-slip conditions for the steady-mean flow and it is applied to the boundary conditions of the perturbation quantities. Therefore, Equations (2.42) will be computed within the roughness boundary conditions as defined below:

$$\hat{u}(z=0) = \lambda\, \hat{u}'[1 + k^2(\hat{u}'^2 + \hat{u}'^2)^{(n-1)/2}] \tag{3.2a}$$

$$\hat{v}(z=0) = \eta\, \hat{v}'[1 + k^2(\hat{u}'^2 + \hat{u}'^2)^{(n-1)/2}] \tag{3.2b}$$

$$\hat{w}(z=0) = 0,\ \hat{w}'(z=0) = -2\hat{u} \tag{3.2c}$$

and

$$\hat{u}\,(z \to \infty) = \hat{v}\,(z \to \infty) = \hat{w}\,(z \to \infty) = \hat{p}\,(z \to \infty) = 0 \tag{3.3}$$

These conditions are identical to the ones used in the previous analysis of the mean flow section under the MW model. The implementation of the boundary conditions a significant advantage of using these variables.

3.3.1 Neutral curves

As mentioned in the previous section, the two instability modes contribute to the neutral curves for the Carreau model. The upper lobe is the Type I mode of instability that is attributed to an inflectional crossflow velocity component, and the second branch Type II mode of instability that is corresponded to streamline curvature and other viscous effects. As defined by neutral spatial growth $\alpha_i = 0$, neutral curves have been calculated for a variety of shear-thinning and -thickening fluids for various values of $\eta = 0.1, 0.2, 0.3, 0.4$. The neutral curves of the Carreau flow are presented here for (Re, α_r), $(Re, \bar{n})$ and (R, ϕ)-planes.

Figures (3.7) and (3.8) show the neutral curves arise from the analysis of both models for the Carreau flow over radially anisotropic roughness. This occurs in both the shear-thinning and shear-thickening regimes. Although they result in different values from the previous ones (See Subsection 3.2.1), both collections of neutral curves reveal the same qualitative behaviour. Here, the

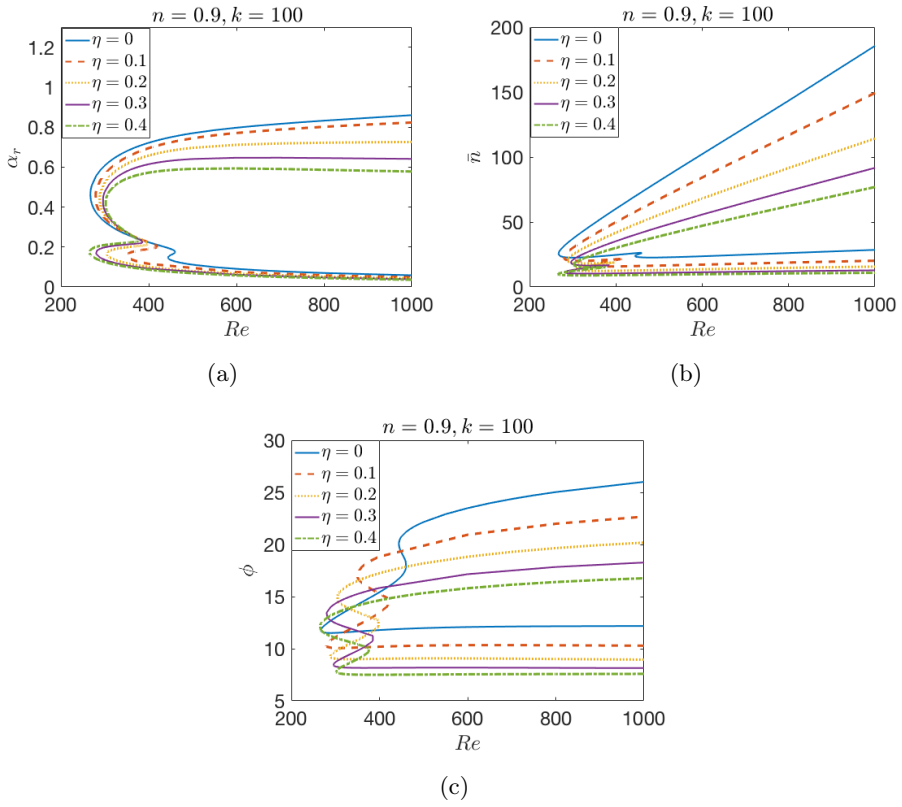

Figure 3.7: Neutral curves of the convective instability for the Carreau flow over radially anisotropic roughness with $n = 0.9$.

Type I lobe is diminished in terms of critical Re when the values of roughness increase. As for the Type II mode, it dominates in terms of critical Re with increased the values of roughness, and the type II mode dominate the stability characteristics. At this point, it is possible to consider the effect of shear-thinning and shear-thickening fluids as stabilising despite its destabilising effects on Type II mode. Of importance is that the critical Reynolds numbers Re_c are greatly altered from those in the previous Subsection 3.2.1 (see Tables (3.5) and (3.6)).

In light of the figures, the wavenumbers neutral curves clearly shift downwards due to increasing the values of roughness. As for their effects on shear-thinning and shear-thickening fluids in terms of the critical Reynolds number, radial grooves have a strong stabilising effect on the Type I mode, while they have destabilising effect Type II in terms of width of the instability region. Furthermore, the numbers of vortices and the wave angle demonstrate a remarkable decrease occurs along the upper and lower branches of the neutral curves when η is increases, as Figures (3.7) show.

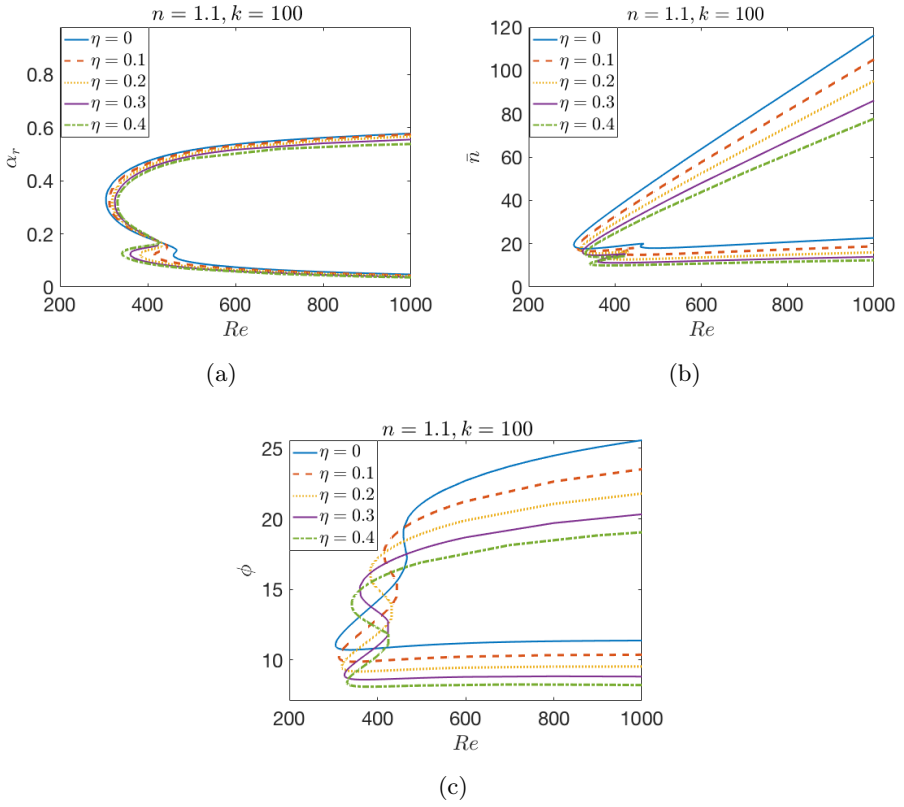

Figure 3.8: Neutral curves of the convective instability for the Carreau flow over radially anisotropic roughness with $n = 1.1$.

Table 3.5: The values of the critical Reynolds number Re, $\bar{n}$ and wave angle ϕ on the both modes Type I and (Type II) for $n = 0.9$.

Parameters	Re	$\bar{n}$	ϕ
$\eta = 0$	267.06(433.91)	46.32(23.82)	11.78(20.02)
$\eta = 0.1$	278.66(349.40)	22.93(16.89)	10.30(17.05)
$\eta = 0.2$	287.96(304.25)	20.74(13.37)	9.25(14.89)
$\eta = 0.3$	295.47(279.56)	18.77(11.28)	8.46(13.31)
$\eta = 0.4$	301.58(264.75)	17.21(9.86)	7.82(12.08)

Table 3.6: The values of the critical Reynolds number Re, $\bar{n}$ and wave angle ϕ on the both modes Type I and (Type II) for $n = 1.1$.

Parameters	Re	$\bar{n}$	ϕ
$\eta = 0$	304.69(458.65)	19.54(18.72)	11.06(18.96)
$\eta = 0.1$	312.02(414.61)	18.27(15.60)	10.20(17.47)
$\eta = 0.2$	318.73(382.32)	17.12(13.41)	9.52(16.10)
$\eta = 0.3$	324.88(359.60)	16.23(11.66)	8.92(15.15)
$\eta = 0.4$	330.49(341.27)	15.33(10.65)	8.43(13.957)

3.3.2 *The growth rate*

The same method used in Section (3.2.2) can be re-applied in this context. This is to study the effect of the radially anisotropic roughness on the growth rates of the instability modes of the Carreau model boundary layer flow with partial-slip conditions. Calculations have been carried out for type I mode at $Re = Re_c + 25$. The growth rates of the secondary Type II mode are not involved here due to their very small value compared to the dominant Type I mode. Figures (3.9) (a) and (b) show the growth rates of the Type I instability

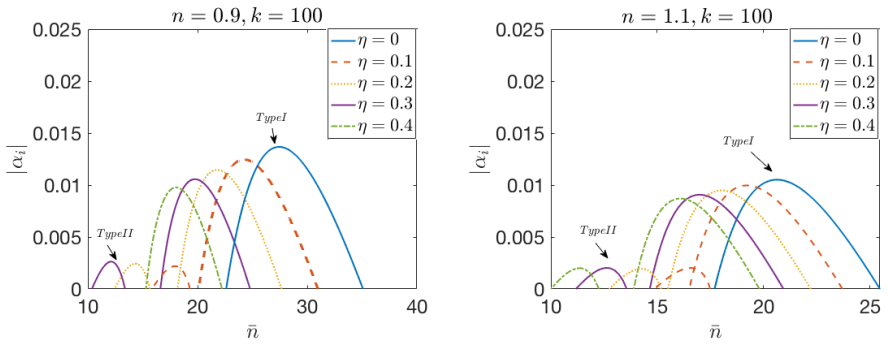

(a) (b)

Figure 3.9: Growth rates of Type I and Type II instability modes as a function of vortex number $\bar{n}$ at $Re = Re_c + 25$ for the radial grooves with (a) shear-thinning and (b) shear-thickening, respectively.

modes within the Carreau model, where $Re = Re_c + 25$ is a function of the vortex number $\bar{n}$ for each level of roughness. The values of the critical Reynolds number Re_c for both $n = 0.9$ and $n = 1.1$ are shown in Tables (3.5) and (3.6) for the onset of the convective instability of the Type I mode. The maximum growth rate thus shifts to lower values of $\bar{n}$ for this mode, thereby indicating a decrease in the number of vortices along upper and lower branches. This occurs when the level of surface roughness increases.

3.4 *Energy analysis results*

The energy balance calculation is carried out at the location of maximum amplification of the Type I mode at $Re = Re_c + 25$. Here Re_c is the critical Reynolds number for the onset of the Type I mode of instability for the particular rough surface being considered. The results for various levels of radial grooves roughness are compared to the Newtonian case in Figure (3.10).

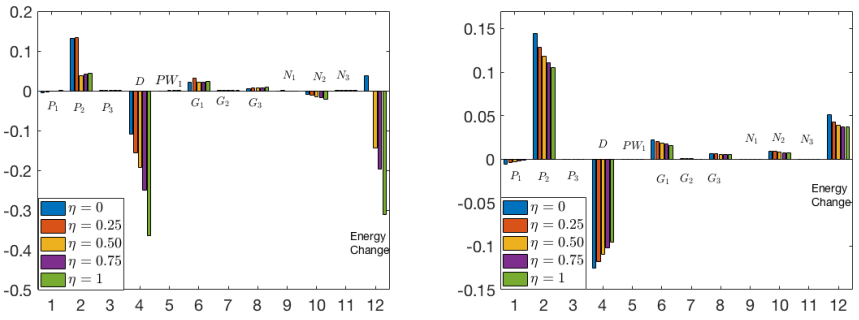

(a) $n = 0.9$. (b) $n = 1.1$.

Figure 3.10: Energy balance of Type I instability at $Re = Re_c + 25$ for $n = 0.9$ and $n = 1.1$, respectively.

The purpose of the energy analysis is to establish the underlying physical mechanisms behind the effects of roughness disks of the Carreau boundary layer flows for both shear-thinning and shear-thickening regimes. Therefore, it is important to consider the energy balance Equation (2.51) of any eigenmode of the perturbation Equations (2.42). It is worthy to note that the positive terms in that equation contribute to the energy production, unlike the negative ones that remove energy from the system. The eigenmode of a disturbance is amplified ($\alpha_i < 0$) when energy is produced by the disturbance outweighs energy dissipated in the system. It is possible to interpret the effect of increasing the size of the surface roughness on the instability modes of both regimes for the Carreau fluids in light of this formulation. This is done by calculating the total energy of the system which is the sum of the energy production and dissipation terms. Increasing the total energy for higher values of the roughness parameters shows a destabilising effect on the modes. In contrast, a reduced total energy indicates a stabilisation effect.

Figures (3.10) (a) and (b) show the energy balance calculations of the case of radial grooves for the Type I mode for both shear-thinning and -thickening

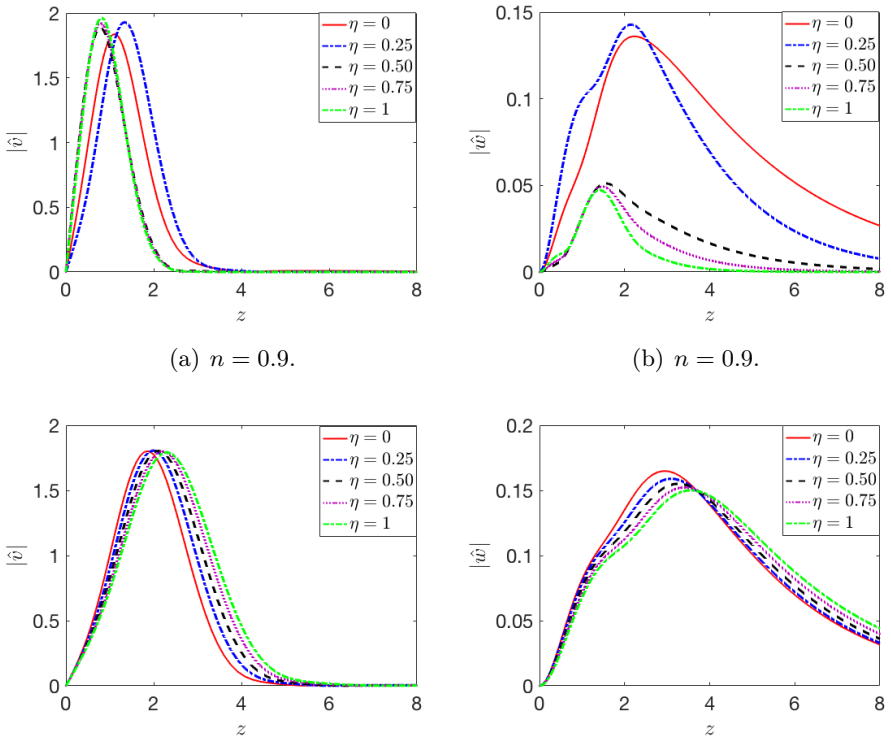

(a) $n = 0.9$. (b) $n = 0.9$.

(c) $n = 1.1$. (d) $n = 1.1$.

Figure 3.11: Type I mode for the azimuthal and the axial disturbance velocity profiles of Carreau model in the case of a radial grooves rotating disk at $Re = Re_c + 25$ for shear-thinning and -thickening fluids, respectively.

fluids, respectively. The destabilisation effect, i.e., reduction in the energy of the system that occurs when η increases, can be seen from the Figures. This effect mainly results from the reduction in the energy production term P_2 as well as in the energy dissipation term D for each flow. However, decreasing of the G_1 and G_3 terms and a substantial increasing of the viscous dissipation for increased radial grooves lead to a destabilisation effect of the Type I mode in this flow. It is also worthwhile to note that the reduction in all terms decreases when $n = 0.9$ and $n = 1.1$. Additional, non-Newtonian viscosity effects, indicated by N_i, do not play a role in the instability in general. This means that non-Newtonian viscosity acts to change the steady flow although no stability response to this inviscid is reported.

The azimuthal velocity perturbation $\hat{v}$ and the axial velocity perturbation, $\hat{w}$, are demonstrated to provide some explanations about the energy trends of the Carreau flow for the Type I mode (Figures (3.11) provides more details). Besides, the structure of $\hat{v}$ disturbance profiles remains unchanged when the

profiles move away from the wall as η increases. The significant decay of the P_2 term in $n < 1$ is attributed to a reduction in the amplitude of the axial velocity perturbation, $\hat{w}$. Therefore, for both $n < 1$ and $n > 1$ flows, the decrease in that term results from the strong reduction in the maximum amplitude of the axial profile $\hat{w}$ when the roughness increases.

3.5 *Conclusion*

In this chapter, the mean flow equations are solved for a range of roughness surfaces. This is achieved by using the approach of Miklavčič & Wang [33] parameters with modification and a variety of fixed power-index values for the Carreau model. In light of the numerical results, anisotropic roughness helps to decrease the magnitude of the radial wall jet when η increases for all n.

Then we considered both the Type I and II modes for the onset of linear convective instability within the boundary-layer flows for both shear-thinning and shear-thickening Carreau fluids. Furthermore, radially anisotropic roughness on the convective instability of stationary disturbances is believed to have a strong stabilising effect on the Type I instability mode in terms of the critical Reynolds number for the onset of the convective instability for both $n = 0.9$ and $n = 1.1$. However, the Type II mode has a slight destabilising effect as this type of roughness level is increased and it becomes more dominate for sufficiently high levels. Moreover, Tables (3.3)-(3.6) show that the numbers of vortices, $\bar{n}$, and the vortex angle, ϕ, are decreased at all values of power-low index as radially anisotropic roughness is increased. Moreover, imposing the MW model for the mean flow or for the mean flow within the perturbations equations results in a quite similar behaviour. Nevertheless, the latter seems different quantitatively in terms of critical values with the increased of the roughness. Also, the results of the novel method lead to more stabilizing effects and less destabilizing effects on type I and the type II, respectively. Physically, the radial grooves correspond to slip in the azimuthal direction which means it is not aligned in the radial direction. As a result, there is some competing effect especially for the type II mode, where it seems that some developing instabilities are convected azimuthally and they keep growing for a given radial location. Overall, our findings are consistent with those presented by Al-Malki [54] for Newtonian boundary-layer flows.

To support the results of the analysis of the convective neutral curves, the effect of the growth rates of the Type I instability for a range of roughness and power-index parameters has been examined. An energy balance equation is conducted and derived from the stability equations to establish the underly-

ing physical mechanisms behind the effects of rough surfaces on two values of power-index n. The total energy of the system influenced by the sum of energy production and dissipation. This makes it possible to identify the effects of surface roughness on the stabilisation of shear-thinning and shear-thickening fluids. Contributions to the energy change of the system have been identified as the term P_2 and the term D, production by the Reynolds stresses and conventional viscous dissipation. An increased energy change in a rough case, compared with the smooth case. (i.e., when $\lambda = \eta = 0$), indicates destabilisation of the modes, whereas a reduced energy change indicates a stabilisation. The energy balance of terms for the system of flows is calculated for the Type I mode at the location of maximum amplification at $Re = Re_c + 25$ for this surface roughness type. The behaviour of the energy balance terms is qualitatively consistent with the neutral curve behaviours as Section 3.2 argues. Overall, the energy analysis has revealed that radially anisotropic roughness (radial grooves) helps to reduce the energy production of the Type I mode for both fluids. This is a stabilisation effect on the Type I mode and destabilising Type II.

Chapter 4

Effect of azimuthally-anisotropic roughness on the Carreau model

In this chapter, the boundary-layer equations for the generalized non-Newtonian using a Carreau model [27] fluid have been solved to obtain the steady mean flow profiles and highlight the effects of azimuthally anisotropic roughness-concentric grooves). The chapter also examines the effects of this roughness on the convective instability mechanisms within fixed values of shear-thinning and shear-thickening flows. This chapter investigates the effects of including partial-slip boundary conditions into the perturbations equations. The convective instability of Carreau fluids with the effects of azimuthally anisotropic roughness will be determined by using the spectral Chebyshev method used by Alveroglu *et al.* [32, 38]. Therefore, the system of stability equations will be solved for the perturbation eigenfunctions and the curves of neutral stability are plotted of both the Type I and Type II modes for a range of λ parameters and fixed values of power-index parameters. After that, the growth rates of the Carreau model for this case are investigated. The effects of surface roughness on the growth rates of each instability mode are discussed. In addition, the energy analysis of the effects of azimuthally anisotropic roughness is solved to confirm the results of the prior linear stability analysis.

The steady mean flow solution is given in Section 4.1. The neutral stability curves that apply the partial slip in the mean flow only are presented in Section 4.2. Also, the neutral stability curves and the growth rate by applying the partial-slip within the mean flow and the disturbances are computed in

Section 4.3. The energy analysis within the effect of azimuthally anisotropic for fixed values of power-index parameters is presented in Section 4.4. Finally, a conclusions will be drawn in Section 4.5.

4.1 *The steady mean flow results*

In this section, we solve the steady mean flow and study the effects of the azimuthally anisotropic roughness on the mean flow components of the Carreau model. The azimuthally anisotropic surface roughness corresponds to concentric grooves on the disk surface and is achieved by setting the roughness parameters in the partial-slip boundary conditions to $\lambda > 0, \eta = 0$ within the MW model. The steady mean flow Equations (2.20, 2.21) of the Carreau model are solved using the MATLAB solver (see Subsection 2.3.1) with the partial-slip boundary conditions (2.23, 2.24). The mean flow profiles are computed the three velocity profiles (U, V, W) for disks with different sizes of radial grooves and various values of power-law index parameters. Figures (4.2) and (4.3) show the effect of the azimuthally anisotropic surface roughness on the mean flow components U in the radial direction, V in the azimuthal direction, and W in the axial direction on shear-thinning and shear-thickening fluids.

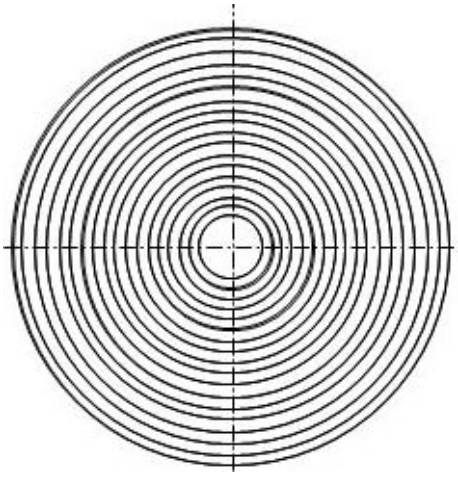

Figure 4.1: Concentric grooves.

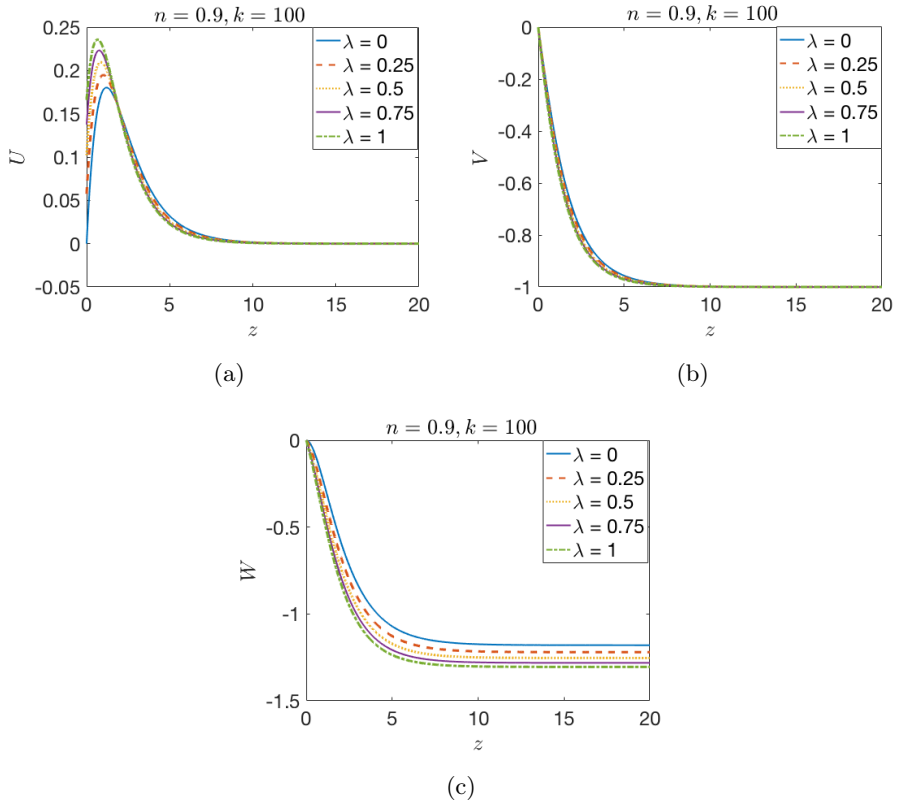

Figure 4.2: Mean flow components of the Carreau flow in the case of azimuthally anisotropic roughness for shear-thinning fluid. (a) U-profile, (b) V-profile, (c) W-profile.

Table 4.1: Numerical values of the mean velocity flow parameters $U'(0)$, $V'(0)$ and $W(z_\infty)$ for shear-thinning $n = 0.9$.

Parameters	$U'(0)$	$-V'(0)$	$-W(z_\infty)$
$\lambda = 0$	0.6440	0.7968	0.7659
$\lambda = 0.25$	0.4786	0.9629	0.8190
$\lambda = 0.50$	0.3766	1.0547	0.8529
$\lambda = 0.75$	0.3090	1.1116	0.8753
$\lambda = 1$	0.2615	1.1500	0.8910

Table 4.2: Numerical values of the mean velocity flow parameters $U'(0)$, $V'(0)$ and $W(z_\infty)$ for shear-thickening $n = 1.1$.

Parameters	$U'(0)$	$-V'(0)$	$-W(z_\infty)$
$\lambda = 0$	0.4137	0.4892	1.0148
$\lambda = 0.25$	0.3401	0.5635	1.0769
$\lambda = 0.50$	0.2867	0.6122	1.1236
$\lambda = 0.75$	0.2469	0.6460	1.1585
$\lambda = 1$	0.2165	0.6706	1.1860

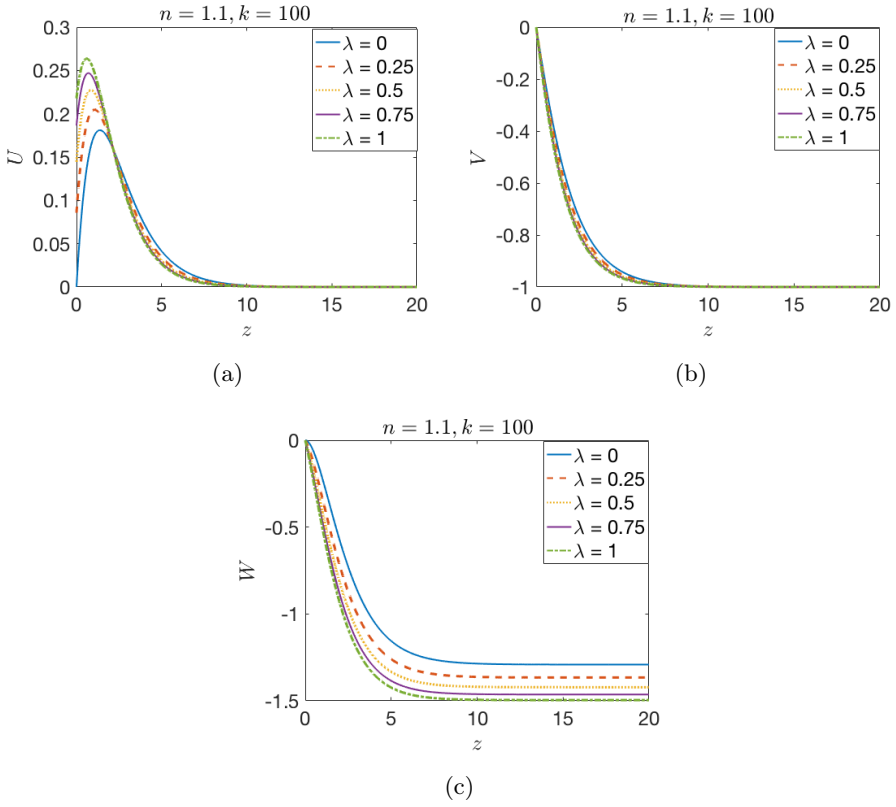

Figure 4.3: Mean flow components of the Carreau flow in the case of azimuthally anisotropic roughness for shear-thickening fluid. (a) U-profile, (b) V-profile, (c) W-profile.

The radial mean flow components U are presented in Figures (4.2) and (4.3) (a), and the azimuthal mean flow porfile V is presented in Figures (4.2) and (4.3) (b). The flow component W in the axial direction is presented in Figures (4.2) and (4.3) (c). The initial values of $U'(0)$, $V'(0)$ and $W(z_\infty)$ are given for various values of roughness parameters in Tables (4.1) and (4.2). Our findings are consistent with Cooper *et al* [35] in terms of the Newtonian flow. The results here are presented for $n = 0.9$ and $n = 1.1$. For further figures and data, the parameters $n = 0.6$, $n = 0.7$, $n = 1.2$ and $n = 1.4$ can be found in Appendices (B.1) and (B.2) with their initial values.

It can be seen from Figures (4.2) and (4.3) (a) that with increasing λ, the location of the maximum value of U moves towards the disk surface with increased roughness for all $n > 1$ and $n < 1$. Increasing this parameter also increases the radial wall jet, thereby reducing the wall shear stress and causing a less impactful viscous interaction between the disk and the fluid. Hence, the ability of the disk to accelerate the fluid is diminished, and this results

in a reduced peak in the U profile. Furthermore, there is an increase in the radial jet and a slight thinning of the boundary layer, as is evident in Figures (4.2) and (4.3) (a). As the figures show us, the concentric grooves increase the fluid into the boundary layer. This has little effect on the mean azimuthal velocity as seen in Figures (4.2) and (4.3) (b). Also, figures (4.2) and (4.3)(c) show that azimuthally anisotropic roughness on the disk surface increases the magnitude of the axial flow for increased λ for all flows, as reported in Tables (4.1 and 4.2). Therefore, the fluid amount entrained into boundary-layer is increased when roughness increases.

4.2 *The convective instability for the concentric-grooves*

This section concerns the occurrence of convective instabilities in the case of the concentric grooves distributed in a radial direction over the rotating disk. The convective instability is solved by the computed solutions of the perturbation Equations (2.42) using the spectral Chebyshev method stated in (2.4.1). The local convective instability is analysed in terms of neutral curves in (4.2.1) and the growth rates in (4.2.2). The perturbation quantities are subject to zero boundary conditions (3.3) at both the disk surface and in the far-field. This ensures that the perturbations to the steady flow are contained within the boundary layer and the effects of surface roughness are not double-counted within the analysis [35, 50].

4.2.1 *Neutral curves*

This section presents the neutral stability curves for a range of concentric grooves and fixed power-index parameters. They have been calculated for values of the surface grooves distributed in a radial direction ranging for fixed values of $n = 0.6$ to $n = 1.4$ in increments of 0.1. The results of $n = 0.9$ and 1.1 are presented here, the other values can be found in Appendices (B.3) and (B.4) with their critical values. As discussed in Chapter 3, the points on the curves are solutions to the system where $\alpha_i = 0$. The region outside of the curve indicates that the disturbed flow will decay to be in steady situation (i. e $\alpha_i > 0$), whereas the region inside or the close to the neutral curves shows unstable flow parameters when a disturbance grows exponentially (i.

e $\alpha_i < 0$). The stability of the flow will be interpreted through the critical Reynolds number Re_c that is defined as the minimum Reynolds number for which instability occurs. One lobe maps out the neutral curve as there is only one minima of the modified branch 1. This lobe is identified as the Type I instability mode. This spatial branch behaviour is typical and are different to the two lobed branches. The neutral curves of the Carreau flow with the concentric grooves are plotted for (Re, α_r), $(Re, \bar{n})$ and (R, ϕ)-planes. Neutral curves for azimuthally anisotropic roughness case are produced for

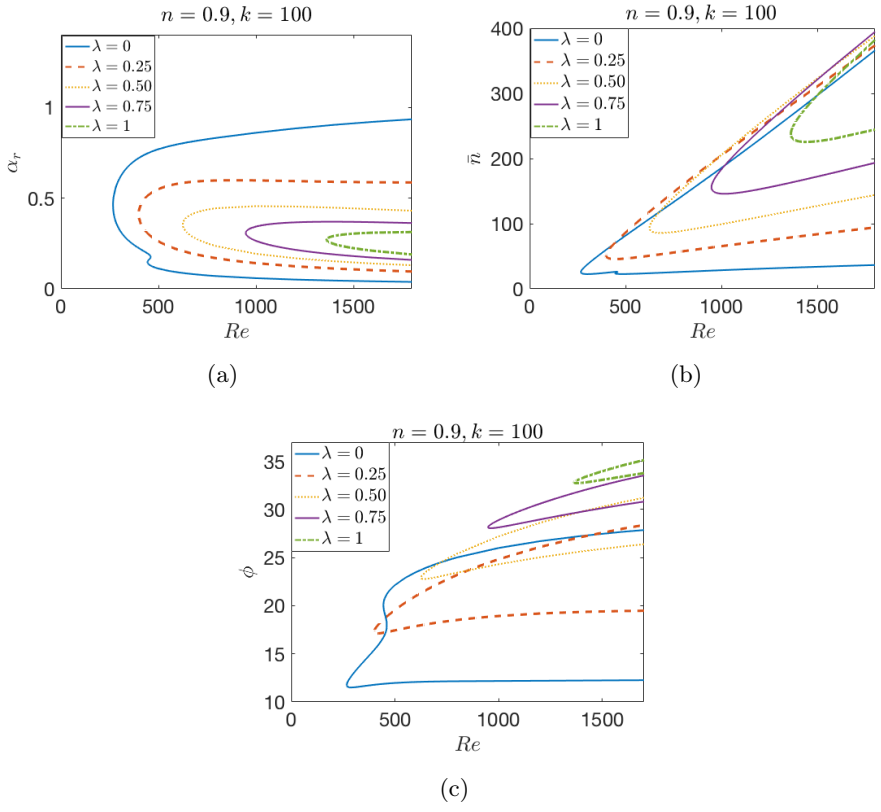

Figure 4.4: Neutral curves of the convective instability for the Carreau flow over azimuthally anisotropic roughness with $n = 0.9$.

shear-thinning and -thickening (see Figures (4.4) and (4.5)). As Figures (4.4) (a) show that increasing the number λ stabilises both the Type I and Type II modes in terms of the critical Reynolds number and the width of the unstable region. Moreover, the lower lobe of the neutral curve vanishes immediately in the presence of even modest levels of roughness. Therefore, this will lead to the Type I mode becoming the dominant form of instability mechanism for the Carreau model in $n < 1$. Similarly, Figures (4.4) (b) and (c) present that the number of the stationary vortices $\bar{n}$ and the wave angle ϕ for this

case. This indicates that increase roughness has a significant stabilising effect along on the upper and lower branches. Clearly, the results are consistent with those of Alveroglu *et al.* [32], Cooper*et al.* [35] in the case of Newtonian fluids (as reported in Tables (4.3) and (4.4)). The neutral curves in Figure (4.5)

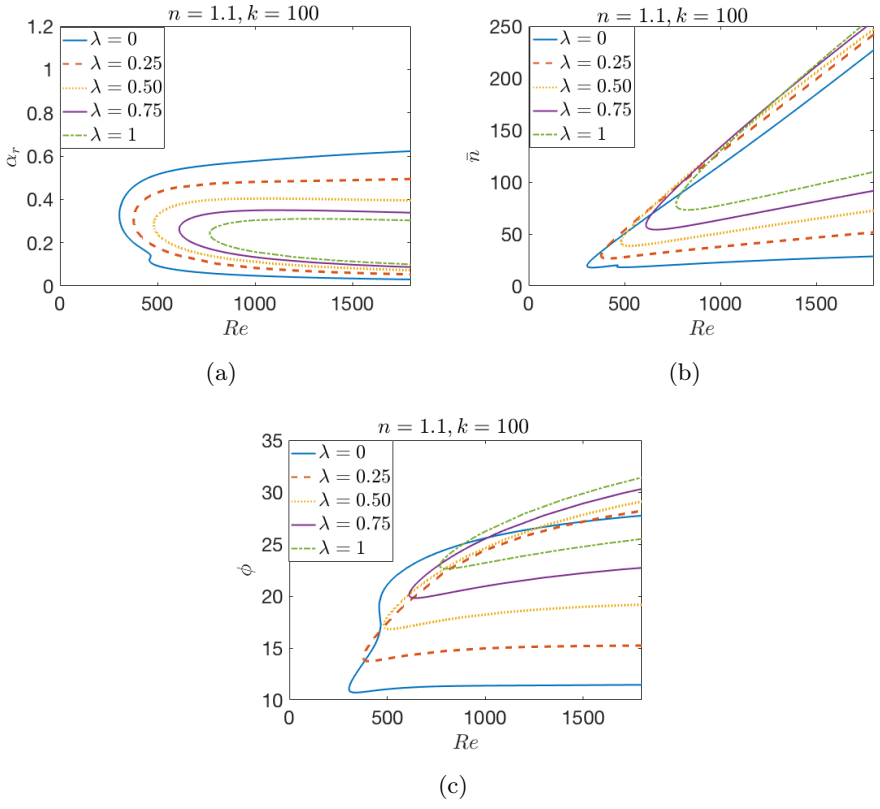

Figure 4.5: Neutral curves of the convective instability for the Carreau flow over azimuthally anisotropic roughness with $n = 1.1$.

(a) reveal that concentric grooves keep their strong stabilising effect in terms of the critical Reynolds number and the width. It is noticed here that the effect is less effective compared to the effect of this grooves on shear-thinning in terms of critical the Reynolds number. Similarly, Figures (4.5) (b) and (c) show the number of stationary vortices $\bar{n}$ and the wave angle ϕ for this case. This indicates that increasing roughness has a significant stabilizing effect on the upper and lower branches. Our results are again consistent with those of Alveroglu *et al.* [32], Cooper*et al.* [35] in the case of Newtonian fluid.

Table 4.3: The values of the critical Reynolds number Re, $\bar{n}$ and wave angle ϕ on the both modes Type I and (Type II) for $n = 0.9$.

Parameters	Re	$\bar{n}$	ϕ
$\lambda = 0$	267.06(433.91)	46.32(23.82)	11.78(20.02)
$\lambda = 0.25$	398.21(−)	51.18(−)	17.29(−)
$\lambda = 0.50$	624.80(−)	93.68(−)	22.90(−)
$\lambda = 0.75$	947.45(−)	156.25(−)	28.23(−)
$\lambda = 1$	1361.66(−)	237.80(−)	32.79(−)

Table 4.4: The values of the critical Reynolds number Re, $\bar{n}$ and wave angle ϕ on the both modes Type I and (Type II) for $n = 1.1$.

Parameters	Re	$\bar{n}$	ϕ
$\lambda = 0$	304.69(458.65)	19.54(18.72)	11.06(18.96)
$\lambda = 0.25$	377.04(−)	29.23(−)	14.05(−)
$\lambda = 0.50$	481.01(−)	42.25(−)	17.13(−)
$\lambda = 0.75$	611.90(−)	58.70(−)	20.11(−)
$\lambda = 1$	768.01(−)	78.53(−)	22.91(−)

4.2.2 *The growth rate*

The growth rates of the Type I instability mode are presented for shear-thinning and -thickening Carreau fluids for the azimuthally-anisotropic at $Re = Re_{critical} + 25$; that is, at a fixed distance into the neutral curve. Note that the growth rate of the instability mode is measured as the absolute value of the negative imaginary part of the radial wavenumber, $|\alpha_i|$, at particular values of the vortex number $\bar{n}$ for each level of roughness. Since the Type II mode vanishes at even modest levels of all surface roughness under our model and it is not considered here.

Figures (4.6) (a) and (b) obviously show the stabilising effect of the concentric grooves on the Type I mode for Carreau fluids of each flow. Of particular interest is the most rapidly growing mode because they are likely to dominate and occur in the experiments. The figures reveal that the maximum growth rate shifts to higher values of $\bar{n}$, suggesting an increase in the number of vortices with the roughness level. These results highlight the behaviour of shifting maximum growth rates with number of spiral vortices $\bar{n}$ for shear-thinning and -thickening Carreau fluids in this case. In contrast to that substantial increase, the value of the maximum growth rate decreases for increased roughness, that is a stabilising effect of the roughness. The critical parameters obtained for

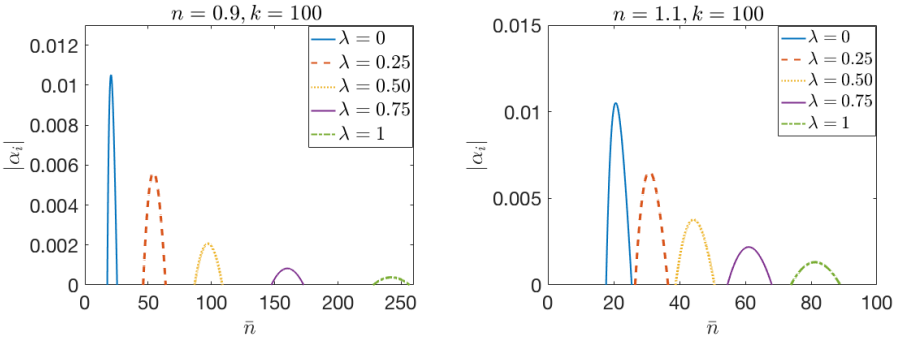

(a) (b)

Figure 4.6: Growth rates of Type I instability at $Re = Re_c + 25$ over azimuthally anisotropic roughness with the shear-thinning and shear-thickening.

each flow emphasise these results, as Tables (4.3) and (4.4) illustrate.

4.3 *The novel approach for the perturbations*

Using the same methodology and Equations that used in Section 3.3 to explore the occurrence of convective instabilities in the case of the concentric grooves distributed over the rotating disk within the partial-slip conditions defined in Equations (3.2) and (3.3).

4.3.1 *Neutral curves*

Two spatial branches are found to determine the convective instability characteristics of the system. The neutral curves, defined by $\alpha_i = 0$, have been calculated for $\lambda = 0.1, 0.2, 0.3, 0.4$ in increments of 0.1 at two fixed values of power- index. This range is considered sufficient to capture the convective instability characteristics of the concentric grooves within the Carreau model that is fixed at power-index parameters. The neutral curves of the Carreau flow are presented for (Re, α_r), $(Re, \bar{n})$ and (R, ϕ)-planes where $\bar{n}$ and ϕ are defined in the Equations (2.44) and (2.43). Critical Reynolds numbers for the onset of dominant type I modes are given in Tables (4.5) and (4.6).

Figure (4.7) (a) reveals the neutral curves of the related flow azimuthally

anisotropic for $n < 1$. It shows that decreasing the λ parameters ($\lambda > 0$) has a stabilising effect on the the Type I mode in terms of the critical Reynolds number. In addition, the lower branch of the neutral curve vanishes immediately in the presence of even modest levels of roughness. The other two parameters also show the effects of surface roughness are the number of the stationary vortices $\bar{n}$ and the vortex angle ϕ. Figures (4.7) (b) and (c) show that the number of vortices and the vortex angle substantially increase along the upper and lower branches in contrast with the strong stabilising effect for increased roughness.

Also, the neutral curves neutral curves of this flow for $n > 1$ are presented in Figure (4.8) (a), (b) and (c). These figures clearly show that concentric grooves keep their strong stabilising effect on this flow in terms of the critical Reynolds number and the width of unstable region. However, the effect of this case on the shear-thinning in terms of critical the Reynolds number is stronger when it is compared to this case.

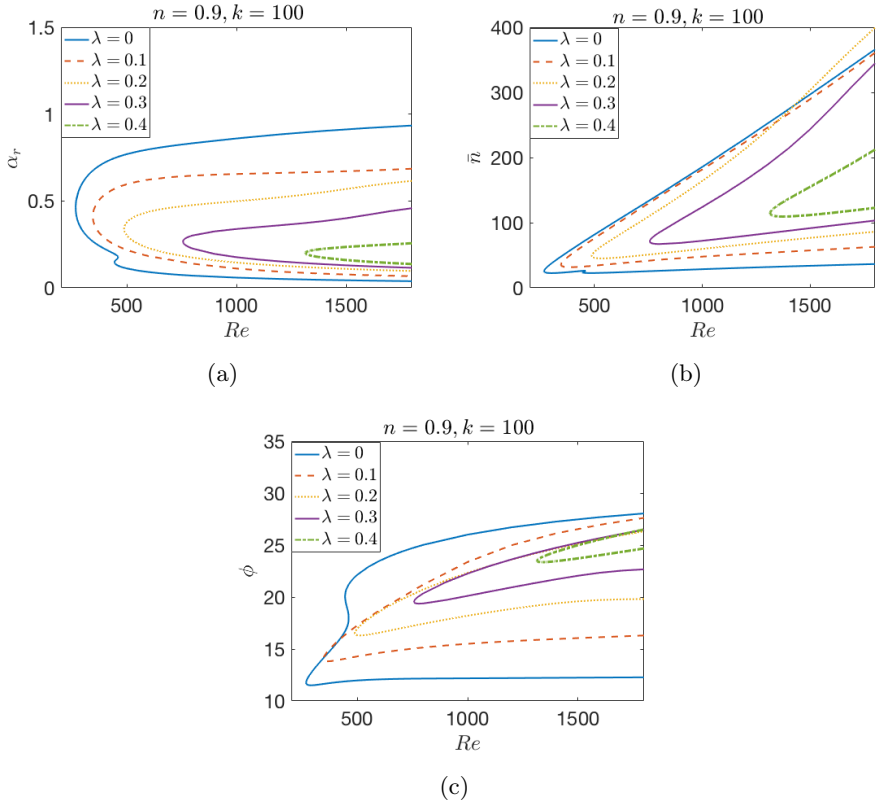

Figure 4.7: Neutral curves of the convective instability for the Carreau flow over azimuthally-anisotropic roughness with $n = 0.9$.

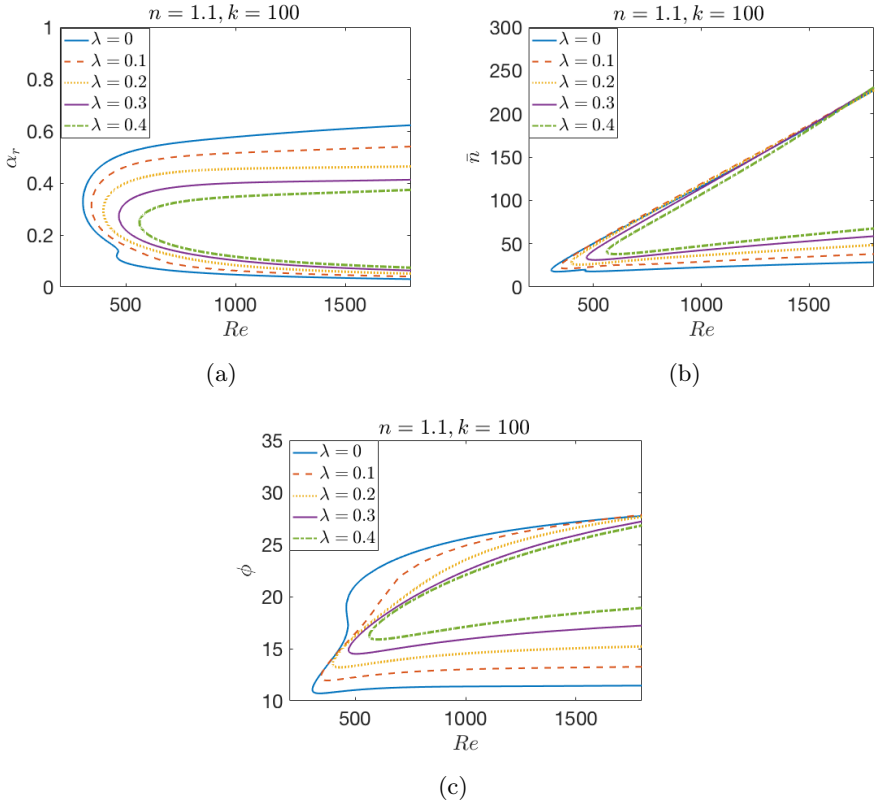

Figure 4.8: Neutral curves of the convective instability for the Carreau flow over azimuthally-anisotropic roughness with $n = 1.1$.

Table 4.5: The values of the critical Reynolds number Re, $\bar{n}$ and wave angle ϕ on the both modes type I and (type II) for $n = 0.9$.

Parameters	Re	$\bar{n}$	ϕ
$\lambda = 0$	267.06(433.91)	46.32(23.82)	11.78(20.02)
$\lambda = 0.1$	345.46(−)	35.46(−)	14.04(−)
$\lambda = 0.2$	487.90(−)	49.10(−)	16.52(−)
$\lambda = 0.3$	756.34(−)	69.92(−)	19.18(−)
$\lambda = 0.4$	1314.33(−)	114.41(−)	23.48(−)

Table 4.6: The values of the critical Reynolds number Re, $\bar{n}$ and wave angle ϕ on the both modes type I and (type II) for $n = 1.1$.

Parameters	Re	$\bar{n}$	ϕ
$\lambda = 0$	304.69(458.65)	19.54(18.72)	11.06(18.96)
$\lambda = 0.1$	343.53(−)	23.42(−)	12.29(−)
$\lambda = 0.2$	397.20(−)	28.23(−)	13.55(−)
$\lambda = 0.3$	468.25(−)	33.90(−)	14.85(−)
$\lambda = 0.4$	562.56(−)	40.73(−)	16.27(−)

Furthermore, the two lobed structure of the neutral curves in the case of a smooth surface, $\lambda = 0$, again disappears for even modest levels of roughness. The increase in the number of vortices and the vortex angle have a similar style as $n < 1$, as is indicated in Figures (4.7) (b)-(c). Overall, these values gradually increase for increased surface roughness levels. Moreover, roughness acts to stabilise the Type I mode of instability, with particular sensitivity to azimuthally anisotropic case. However, the Type II mode is suppressed in the case of azimuthally anisotropic roughness and the lower lobe is vanishes for even modest levels of roughness.

4.3.2 *The growth rate*

Following the same method used in (4.2.2) to consider the effect of concentric grooves on the growth rates of the instability modes of the Carreau model within the partial-slip conditions for the Type I. The growth rates of the secondary the Type II mode are not involved here due to their very small value compared to the dominant the Type I mode.

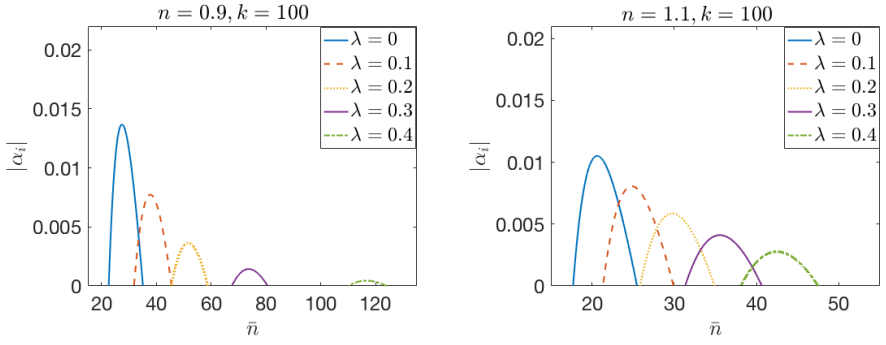

(a) (b)

Figure 4.9: Growth rates of Type I instability at $Re = Re_c + 25$ over azimuthally anisotropic roughness with the shear-thinning and shear-thickening.

Figures (4.9) (a) and (b) indicate growth rates of the Type I instability mode at a fixed distance into the neutral curve, as a function of the vortex number $\bar{n}$ for each level of roughness at $Re = Re_c + 25$. The results clearly show the stabilising effect of azimuthally anisotropic roughness on the Type I mode of each n. Furthermore, the figures reveal that the maximum growth rate shifts to lower values of $\bar{n}$, indicating an increase in the number of vortices as an effect of increased surface roughness parameters. Obviously, the maximum

growth rate for all values of this case increases when the power-index increases, too. In general, all the results of growth rates are consistent with the critical Reynolds numbers for each flow presented previously.

4.4 *Energy analysis results*

The results of solving the energy balance Equation (2.51) are provided here for the case of azimuthally anisotropic surface roughness. The goal is to establish the underlying physical mechanisms behind the effects of radially grooved disks on the Carreau model flows boundary layer flows for both shear-thinning and -thickening fluids. The maximum growth rates obtained in Section (4.2.2) are used here to obtain the energy balance for flows. The energy balance calculation is applied at the location of maximum amplification of the Type I mode at $Re = Re_c + 25$. Here Re_c is the critical Reynolds number for the onset of the Type I mode of instability for the particular rough surface being considered. Results for the value of roughness $\lambda = 0$ are compared to the Newtonian case in Figure (4.10).

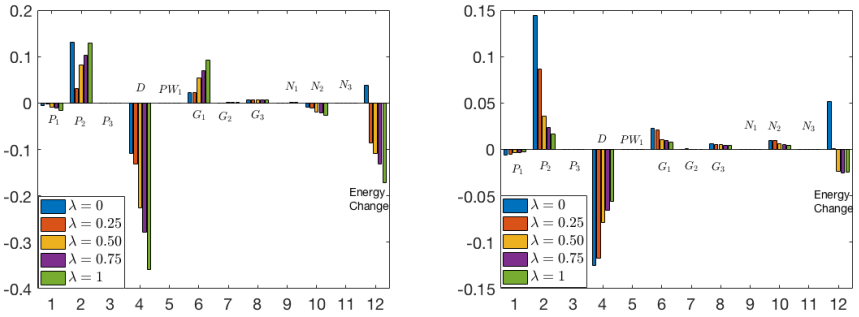

(a) $n = 0.9$. (b) $n = 1.1$..

Figure 4.10: Energy balance of Type I instability at $Re = Re_c + 25$ for $n = 0.9$ and for $n = 1.1$, respectively.

Note that the positive terms in that equation contribute to the energy production whereas the negative terms remove energy from the system. The eigenmode of a disturbance is amplified ($\alpha_i < 0$) when the energy produced by the disturbance outweighs energy dissipated in the system. The effect of surface roughness on the instability modes of both shear-thinning and shear-thickening Carreau fluids can be interpreted from this formulation by calculating the total energy of the system which is the sum of the energy production and dissipation

terms. Increasing the total energy for higher values of the roughness parameters shows a stabilising effect on the modes. the Type II mode disappears at even modest sizes of concentric grooves in each flow. Therefore, the energy balance for the Type I mode only is provided here.

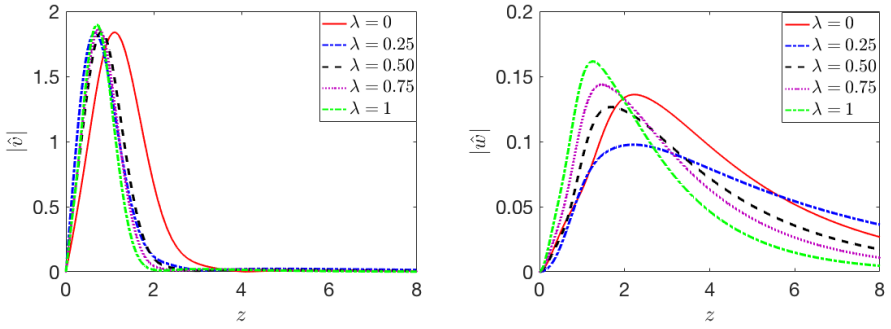

(a) $n = 0.9$. (b) $n = 0.9$.

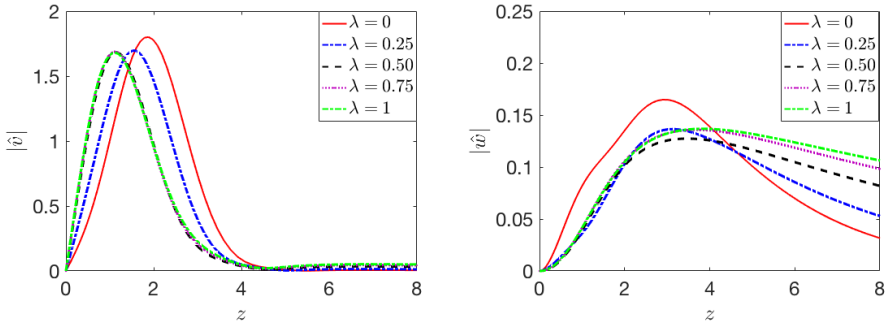

(c) $n = 1.1$. (d) $n = 1.1$.

Figure 4.11: Type I mode for the azimuthal and the axial disturbance velocity profiles of Carreau model in the case of a concentric groove rotating disk at $Re = Re_c + 25$ for $n = 0.9$ and $n = 1.1$, respectively.

Figures (4.10) (a) and (b) show the energy balance calculations for a range of concentric grooves of Type I mode for both shear-thinning and shear-thickening fluids, respectively. Here, the results are normalized by the mechanical energy flux of the most energetic mode within each figure and so comparisons can be made at different values of λ. Two different figures can not however be directly compared. Clearly, there is a stabilisation effect on the Type I mode for the flows of $n = 0.9$ and $n = 1.1$. This effect results from reducing the energy production in term P_2 as well as from dissipating it in term D. However, it is worth noting that P_2 has a primary effect on the total energy that indicates the stability behaviour of the flow while the term of dissipation energy D has a slight effect on the total energy in the case. In

addition, the energy removing effects of the terms arise from the streamline curvature effects and the three dimensionality of the mean flow turns into an energy production for positive values. So, these terms contribute to energy production in the system. Moreover, as we discussed in the previous case, there is a negligible effect on the energy balance for non-Newtonian terms N_i. The modified viscosity is therefore again seen to act to establish new steady flows which are unstable through inviscid effects. This is as expected for the inviscid Type I mode.

In Figure (4.11) there are two disturbance profiles for this case for the Type I instability mode. It is obvious from these figures that when we increase the roughness parameter, the disturbance profiles are not changed with the profiles and it is close to the wall especially for $|\hat{v}|$ in $n < 1$. For $n > 1$, there is strong decrease of the P_2, due to a decrease in the amplitude of the axial velocity perturbation, $|\hat{w}|$ and the amplitude of both disturbance profiles reduces when λ. increases.

4.5 *Conclusion*

In this chapter, the mean flow is solved for the mean flow equations for a range of concentric grooves parameters using the approach of Miklavčič & Wang parameters with modification and a variety of power-index values for the Carreau model with some modification because the viscosity independent from the shear rate. It is noticed from our numerical results that anisotropic roughness with these grooves on the mean flow results are to decrease the magnitude of the radial wall jet as λ is increased. This the opposite of the radially-anisotropic roughness as increase the magnitudes of the axial direction and also increase the magnitudes of the radial and wall jets of λ increased.

We obtain that on the Type I mode the onset of linear convective instability of boundary-layer flows for both shear-thinning and shear-thickening Carreau fluids. Here the effects of azimuthally anistropic of roughness on the Carreau model for two kinds of boundary conditions within the perturbation equations are investaigted. The first one is the smooth boundary condition and the second one is the partial-slip approach of Miklavcic & Wang [1] with modification. The effects of this type of roughness on the convective instability of stationary disturbances demonstrate that it has a strong stabilising effect on the Type I instability mode in terms of the critical Reynolds number for the onset of the convective instability for both $n = 0.9$ and $n = 1.1$. Moreover, the number of vortices, $\bar{n}$, and the vortex angle, ϕ, are decreased at all values of power low

index as λ increases, as is shown in Tables (4.3)-(4.6).

The effects of roughness are examined in the case of azimuthally anisotropic on the convective instability of stationary disturbances on the Carreau fluid for shear-thinning fluid when $n < 1$ or shear-thickening fluid $n > 1$. The neutral curves have revealed that both have a strong stabilising effect on both the Type I and Type II modes. In terms of the number of the vortices $\bar{n}$ and the vortex angle ϕ, the increased surface roughness acts to increase both of them despite being noticeable on the upper-branch modes. In general, it is found that the effects that arise when imposing the partial-slip within the disturbances equations are somewhat more pronounced than when using the MW approach for the steady mean flow only.

The results of the analysis of the convective neutral curves are confirmed by studying the effect of the growth rates of the Type I instability for a range of roughness and power-index parameters. An energy balance equation is conducted and derived from the stability equations in Chapter 2.5 for two values of power-index n. All physical processes (both energy production and dissipation) are weakened by the introduction of shear-thinning shear-thickening fluids to identify the effects of surface roughness. Moreover, non-Newtonian viscosity is believed to play a negligible role in the dominant instability mechanisms. The results instead suggest that their benefit comes from modifying the steady flow profiles which, in turn, are more stable to inviscid Type I effects. The behaviours of the energy balance terms are qualitatively consistent with the neutral curve behaviours. Overall, it is found that a disk with concentric grooves has a stronger stabilizing effect effect than the radial grooves in previous chapter. The reason as mentioned by Al-Malki [54] that there is a slip in the radial direction and the developing of the vorticity within the boundary layer that leads to the instability forming is effectively swept or slips downstream in the radial direction. Thus, concentric grooves act to increase this radial flow effect and delaying transition in the boundary layer. substantially, concentric grooves merge in somehow and prevent developing instabilities downstream so this lead to stabilize the flow.

Chapter 5

Effect of isotropic roughness on the Carreau model

In this chapter, the solution of the boundary-layer equations for the generalized non-Newtonian fluids determines the steady mean profiles for a Carreau model [27] with isotropic roughness surface. It also examines the effect of the roughness on the convective linear stability analysis. As discussed in the previous chapter the partial-slip boundary conditions does not affect the perturbation equations; that is, the governing stability equations are unaffected by surface roughness within the MW model. However, the MW model is also implemented to the perturbation equations for this case too for shear-thinning and shear-thickening Carreau fluid. Thus, the system of stability equations is solved for the perturbation eigenfunctions and the curves of neutral stability are plotted for both the Type I and Type II modes for a variation of $\lambda = \eta > 0$ parameters and fixed power-index. Furthermore, the growth rates of the Carreau model for this case are found. The effects of surface roughness on the growth rates is studied for Type I instability mode. Lastly, the energy analysis is solved to confirm the results of the prior linear stability analysis.

For consistency, the structure of this chapter follows Chapters 3 and 4. The steady mean flow solution is presented in Section 5.1.The convective instability is solved by applying the partial slip in the mean flow only in Section 5.2 whereas the convective instability by applying the partial-slip within the mean flow and the disturbances in solved Section 5.3 for isotropic roughness. The effect of isotropic roughness on the energy analysis equations is investigated in Subsection 5.4. Finally, conclusions are drawn in Section 5.5.

5.1 *The steady mean flow results*

The steady mean flow is solved to examine the effects of isotropic roughness on the mean flow components of the Carreau model. The isotropic surface roughness corresponds to radial and concentric grooves on the disk surface and is implemented by setting the roughness parameters in the partial-slip boundary conditions to $\lambda = \eta > 0$ within the MW model. The steady mean flow Equations (2.20, 2.21) of the Carreau model are computed using the MATLAB solver (see Subsection 2.3.1 for more details) with the partial-slip boundary conditions (2.23, 2.24). The mean flow profiles are computed for three velocity components (U, V, W) for disks with different values of roughness and fixed values of power-law index parameters. Figures (5.2) and (5.3) indicate the effect of the isotropic surface roughness on the mean flow components for shear-thinning and shear-thickening fluids.

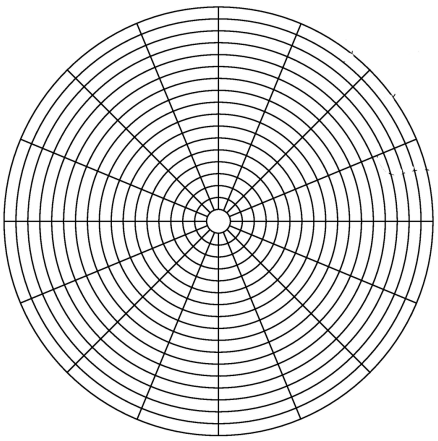

Figure 5.1: Isotropic roughness distribution.

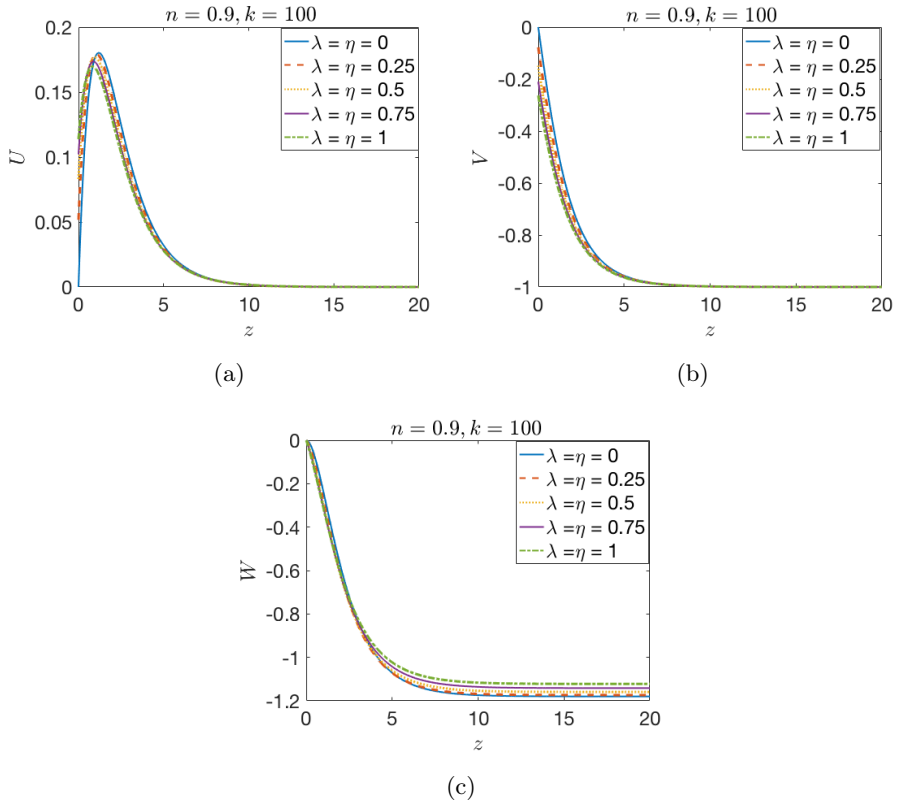

Figure 5.2: Mean flow components of the Carreau flow over isotropically rough disk for shear-thinning fluid. (a) U-profile, (b) V-profile, (c) W-profile.

Table 5.1: Numerical values of the mean velocity flow parameters $U'(0)$, $V'(0)$ and $W(z_\infty)$ for shear-thinning $n = 0.9$.

Parameters	$U'(0)$	$-V'(0)$	$-W(z_\infty)$
$\lambda = \eta = 0$	0.6440	0.7968	0.7659
$\lambda = \eta = 0.25$	0.3633	0.7008	0.7503
$\lambda = \eta = 0.50$	0.2353	0.5906	0.7254
$\lambda = \eta = 0.75$	0.1674	0.5055	0.7018
$\lambda = \eta = 1$	0.1267	0.4410	0.6808

Table 5.2: Numerical values of the mean velocity flow parameters $U'(0)$, $V'(0)$ and $W(z_\infty)$ for shear-thickening $n = 1.1$.

Parameters	$U'(0)$	$-V'(0)$	$-W(z_\infty)$
$\lambda = \eta = 0$	0.4137	0.4892	1.0148
$\lambda = \eta = 0.25$	0.2873	0.4689	1.0005
$\lambda = \eta = 0.50$	0.2097	0.4282	0.9726
$\lambda = \eta = 0.75$	0.1603	0.3877	0.9421
$\lambda = \eta = 1$	0.1271	0.3522	0.9127

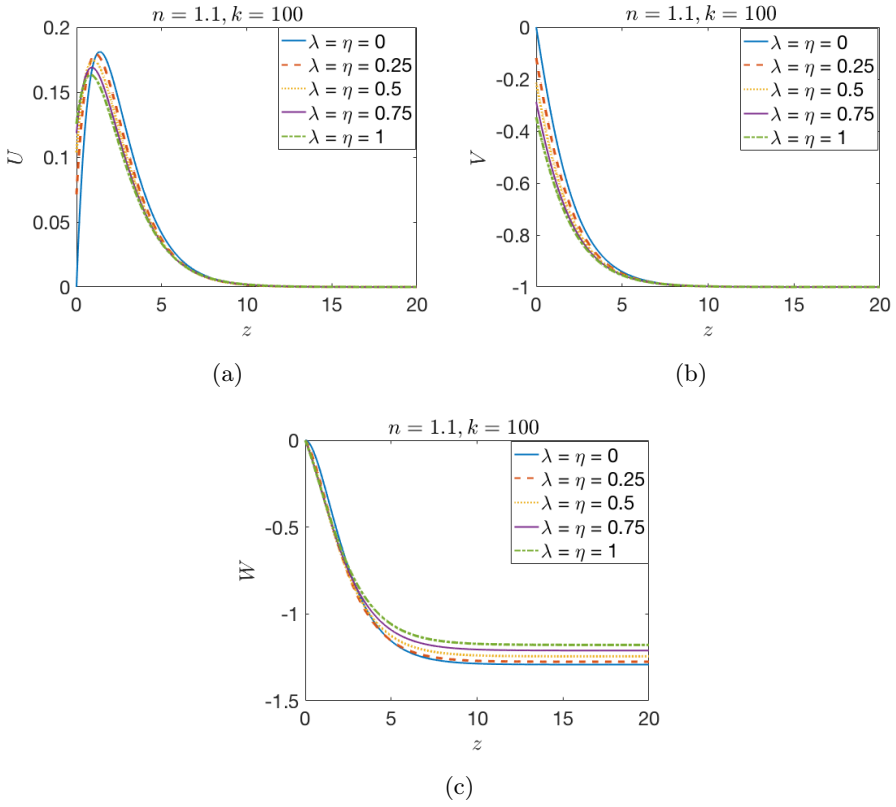

Figure 5.3: Mean flow components of the Carreau flow over isotropically rough disk for shear-thickening fluids. (a) U-profile, (b) V-profile, (c) W-profile

The radial mean flow profiles U are indicated in Figures (5.2) and (5.3) (a). The azimuthal mean flow component V is provided in Figures (5.2) and (5.3) (b), while the flow component W in the axial direction is presented in Figures (5.2) and (5.3) (c). The initial values of $U'(0)$, $V'(0)$ and $W(z_\infty)$ are important for the computation of the flow profiles and appear in Tables (5.1) and (5.2) for various values of $\lambda = \eta > 0$. The initial values for Newtonian flow ($\lambda = \eta = 0$) agree with those appearing in Cooper *et al.* [35] Tables (5.1) and 5.2 for the isotropic case. The results are presented here for $n = 0.9$ and $n = 1.1$. Other values ($n = 0.6$, $n = 0.7$, $n = 1.2$ and $n = 1.4$) can be found in Appendices (C.1) and (C.2) with their initial values.

In both Figures (5.2) and (5.3) (a), the radial velocity component U of the flow reduces and moves towards the disk surface as a result of increased isotropic roughness, thereby decreasing the radial wall jet. Regarding the azimuthal profile in Figures (5.2) and (5.3) (b), the wall value of the component increases as roughness is increased which is similar to the concentric groove case discussed in Section 3.1. Increasing the non-zero $\lambda = \eta \neq 0$ leads to a

reduced radial jet that moves toward the disk. Furthermore, it has little effect on the boundary-layer thickness for the axial profile as is seen in Figures (5.2) and (5.3) (c). Interestingly, for each particular regime of the Carreau flow, the effect of isotropic roughness on the mean flow profiles are similar to the effects of the concentric grooves case. Therefore, the effects observed for radial concentric grooves in Sections 3.1 and 4.1 are combined for the isotropic case.

5.2 *The convective instability for the isotropic case*

This section aims to address the convective instabilities in the case of isotropic roughness over the rotating disk. The convective instability is determined by computing the solutions of the perturbation Equations (2.42) and implementing the spectral Chebyshev method provided in (2.4.1). Likewise, the stability equations are solved as primitive variables over 100 collocation points distributed between the upper and lower boundaries. The local convective instability is analysed in terms of neutral curves in (5.2.1) and the growth rates in (5.2.2). Here the perturbation quantities are subject to zero boundary conditions at both the disk surface and in the far-field. This ensures that the perturbations to the steady flow are contained within the boundary layer and the effects of surface roughness are not double-counted within the analysis [35, 50]. The perturbation Equation. (2.42) is subject to Equation (3.3).

5.2.1 *Neutral curves*

The neutral curves defined by the neutral spatial growth $\alpha_i = 0$, have been calculated for fixed values of shear-thinning and -thickening fluids using the Carreau viscosity model with isotropic rough surfaces. The characteristics of the Carreau fluid are determined by n and k parameters. The relaxation parameter is fixed by selecting $k = 100$, the power-law index n is fixed, where the isotropic parameters vary. Two spatial branches are found to determine the convective instability characteristics of the system. The Type I mode results from the (inviscid) inflectional behaviour of mean-flow components and appears as the upper lobe in neutral curves. The Type II mode arises from the (viscous) streamline curvature and Coriolis effects and appears as a smaller lower lobe. The neutral curves of the Carreau flow are produced for (Re, α_r), $(Re, \bar{n})$ and (R, ϕ)-planes. Each curve encloses a region in which the boundary-

layer is connectively unstable. The results of $n = 0.9$ and 1.1 are presented here, the other values can be found in Appendices (C.3) and (C.4) with their critical values.

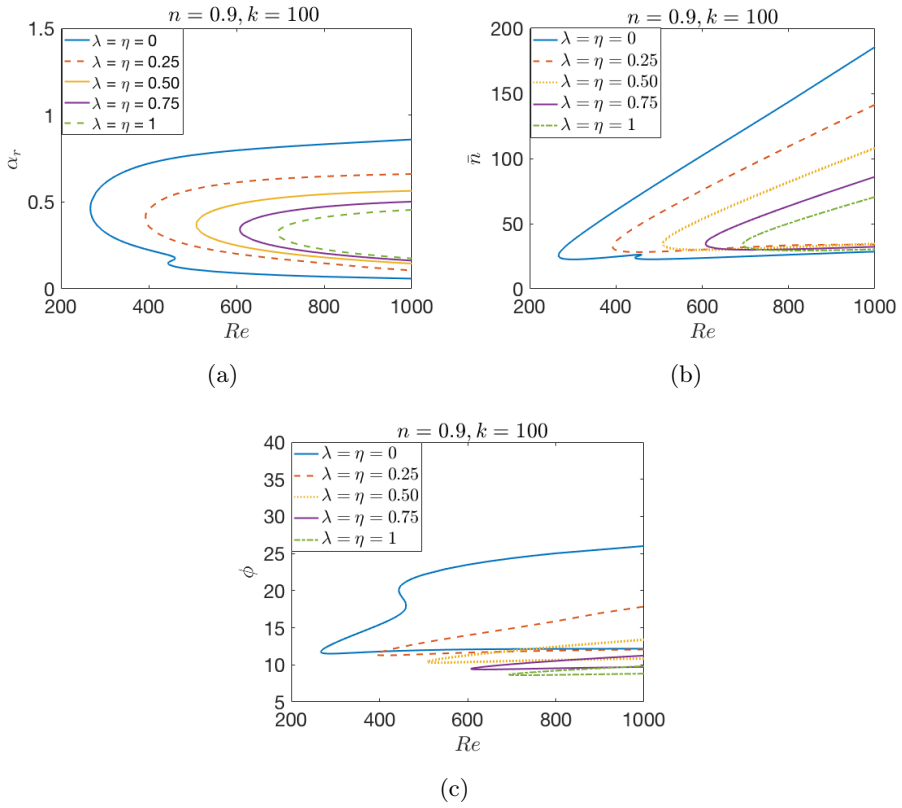

Figure 5.4: Neutral curves of the convective instability for the Carreau flow over isotropic roughness with $n = 0.9$.

The isotropic case for shear-thinning and -thickening is illustrated in Figures (5.4) and (5.5). Increasing levels of isotropic roughness has a strong stabilisation effect on both of the Type I and Type II instability modes for $n < 1$ and $n > 1$ as evidence in Figures (5.4) and (5.5) (a). Thus, the Type I mode is strengthened and becomes the dominant for this case. Here the Type II mode vanishing completely for relatively modest levels of isotropic roughness and only being visible as a distinct lower lobe for $\lambda = \eta = 0$. The effect on the Type I mode is also much stronger in terms of critical number Re, while has more reductions in terms of the width of the unstable region with an increase in the roughness values.

Figures (5.4) and (5.5) (b) demonstrate the effects of isotropic roughness on the number of vortices $\bar{n}$ for this flow. It can be seen from the figure that the number of vortices decreases along the upper branch of the neutral curves

as roughness is increases. However, there is a slight increase in the number of vortices along the lower branches of the neutral curves as the roughness parameter is increased. This seems to be a combination of the effects of the azimuthal and radial roughness cases. This is because concentric grooves leads to a decrease while radial grooves lead to an increase in the number of vortices.

The effects of isotropic roughness on the vortex angle are presented in Figures (5.4) and (5.5) (c). We observe that the effects of varying isotropic roughness decrease the vortex angle ϕ along both the upper and lower branches and this opposite to number of vortices. The numerical predictions of the critical parameters at the onset of convective instability are presented in Tables (5.3) and (5.4) for each flow discussed here. The critical values of the Type I mode are in very good agreement with the existing results in the literature for the Newtonian case as well as for the results identified in [32, 35].

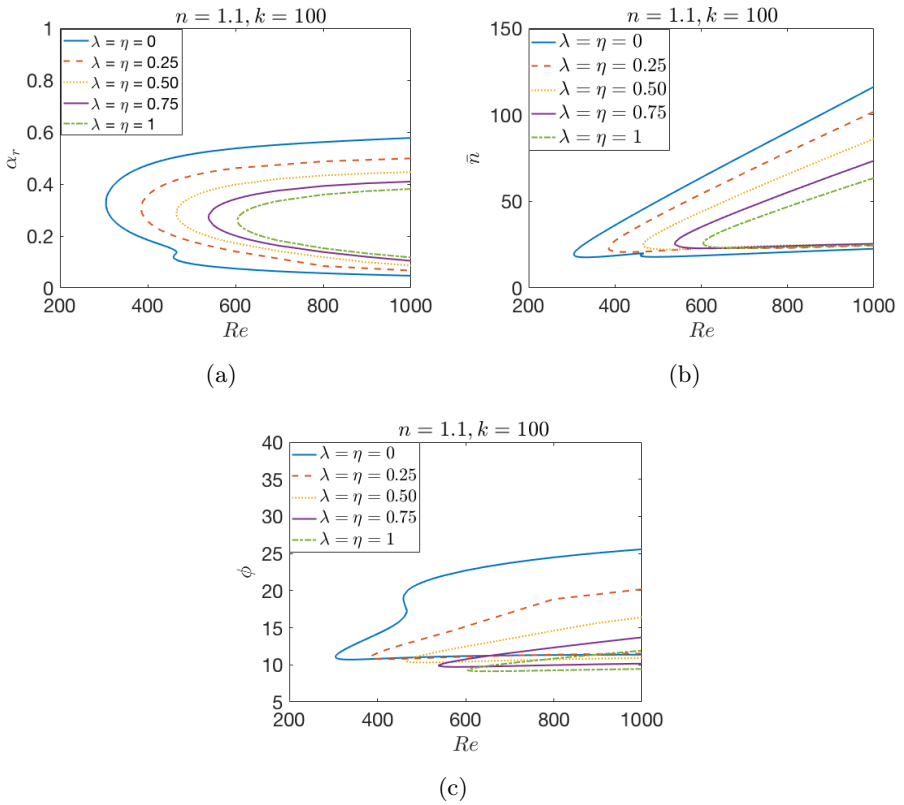

Figure 5.5: Neutral curves of the convective instability for the Carreau flow over isotropic roughness with $n = 1.1$.

Table 5.3: The values of the critical Reynolds number Re, $\bar{n}$ and wave angle ϕ on the both modes Type I and (Type II) for $n = 0.9$.

Parameters	Re	$\bar{n}$	ϕ
$\lambda = \eta = 0$	267.06(433.91)	46.32(23.82)	11.78(20.02)
$\lambda = \eta = 0.25$	392.20(−)	32.44(−)	11.41(−)
$\lambda = \eta = 0.50$	508.30(−)	34.66(−)	10.46(−)
$\lambda = \eta = 0.75$	607.66(−)	34.63(−)	9.45(−)
$\lambda = \eta = 1$	693.74(−)	33.93(−)	8.67(−)

Table 5.4: The values of the critical Reynolds number Re, $\bar{n}$ and wave angle ϕ on the both modes Type I and (Type II) for $n = 1.1$.

Parameters	Re	$\bar{n}$	ϕ
$\lambda = \eta = 0$	304.69(458.65)	19.54(18.72)	11.06(18.96)
$\lambda = \eta = 0.25$	385.11(−)	22.98(−)	11.03(−)
$\lambda = \eta = 0.50$	465.49(−)	24.87(−)	10.53(−)
$\lambda = \eta = 0.75$	538.87(−)	25.68(−)	9.90(−)
$\lambda = \eta = 1$	604.74(−)	25.88(−)	8.46(−)

5.2.2 *The growth rate*

The growth rates of the Type I instability mode within shear-thinning and -thickening are obtained for the isotropic case at $Re = Re_c + 25$; that is, at a fixed distance into the neutral curve as a function of the vortex number $\bar{n}$ at each size of roughness. Note that the growth rate of the instability mode is measured as a variation of the absolute value of the negative imaginary part of the radial wavenumber, $|\alpha_i|$, at particular values of the vortex number $\bar{n}$ for each level of roughness. The growth rates of the Type II mode are not considered here, owing to their very small value in compared to the dominant Type I mode. So, we only present here the growth rates of the Type I instability mode.

The effect of isotropic roughness on the growth rates of the instability modes of the Carreau boundary layer flows can be seen in Figures (5.6) (a) and (b). They depict the stabilising effect of isotropic roughness on the Type I mode of each flow as the value of the maximum growth rate decreases corresponding to an increase the roughness values. Moreover, location of the maximum growth rate shifts to higher values of $\bar{n}$, and this indicates an increase in the number of vortices as an effect of increased surface roughness level λ and η. It is observed in the isotropic roughness case, there is a much

stronger stabilizing effect on the Type I mode in terms of growth rate reduction. Therefore, The overall effect of this case is still to reduce the number of vortices.

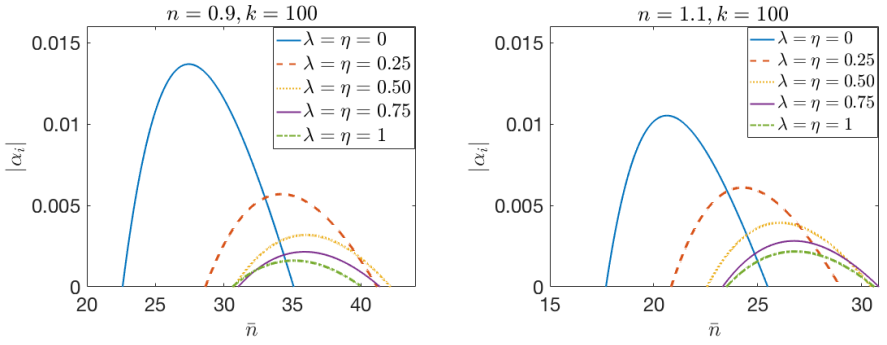

(a) (b)

Figure 5.6: Growth rates of Type I instability at $Re = Re_c$+25 for both shear-thinning (a) and shear-thickening (b) in the case of isotropic roughness.

5.3 *The novel approach for the perturbations*

This part is concerned with the occurrence of convective instabilities in the case of the isotropic roughness over the rotating disk. The convective instability is obtained by solving the perturbation Equations (2.42) system as a quadratic eigenvalue problem and imposing the partial-slip boundary condition defined in Chapter (3.2) within Equations (3.2) and (3.3).

5.3.1 *Neutral curves*

The Figures here depict the neutral stability data for a range of isotropic roughness parameters and fixed power-law index parameters of the Carreau model. The points on the curves are defined by neutral spatial growth as $\alpha_i = 0$. It is found for $0.1 \leq \lambda = \eta \leq 0.4$ in increments of 0.1 within shear-thinning and -thickening Carreau fluids. The neutral curves are plotted for (Re, α_r), $(Re, \bar{n})$ and (R, ϕ)-planes. Each curve encloses a region in which the boundary layers are convectively unstable (i.e. a disturbance grows exponentially as $\alpha_i < 0$, whereas the region outside of the curve indicates that the disturbed flow

will decay to the steady state as $\alpha_i > 0$). Two spatial branches arise from crossflow and streamline-curvature instability modes are found that determine the convective instability characteristics for each size of roughness.

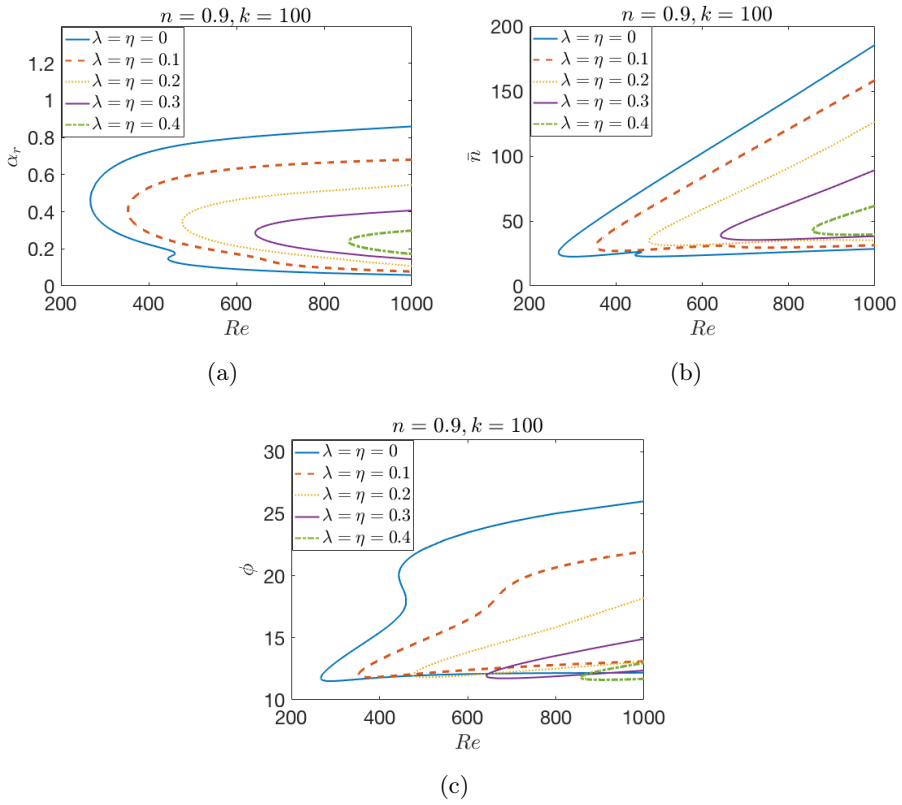

Figure 5.7: Neutral curves of the convective instability for the Carreau flow over isotropic roughness with $n = 0.9$.

It can be seen in Figures (5.7 and 5.8) (a) that as the roughness is increased, the critical Reynolds number is also significantly increased and stabilises the type I mode. Therefore, the effect on the Type I mode is even more strongly stabilising than radial grooves. Moreover, the Type II mode is stabilised in the same way as observed for the concentrically grooves and vanishes even for modest levels of isotropic roughness. Thus, the Type I mode considered the dominant instability mechanism of both flows in this case. Also, in Tables (5.5) and (5.6), the critical Reynolds number at which the Type I mode onsets increases with roughness level, especially for $n = 0.9$ compared to $n = 1.1$. Also, the width of instability region shrinks with an increase in the roughness level for shear-thinning more than for -thickening cases. Overall, both flows (i.e shear-thinning and -thickening) have significant stabilising effects

In terms of the number of vortices (see Figures (5.7)and (5.8) (b)), there is a slight variation in the number of vortices along both branches as for both flow with increased roughness. In Figure (5.8)(c), it can be observed that the critical wave angles follow the same trends with changing roughness parameters as seen in Figure (5.7) (c). The effect of increasing roughness parameters is to decrease the vortex angle of each flow for the Carreau flow along both the upper and lower branches. It is also observed that the vortex angle at the critical Reynolds number decreases continuously as the power-index n increases along the lower branch. Critical data for the range of $\lambda = \eta$ and n values considered are presented in Tables (5.5) and (5.6).

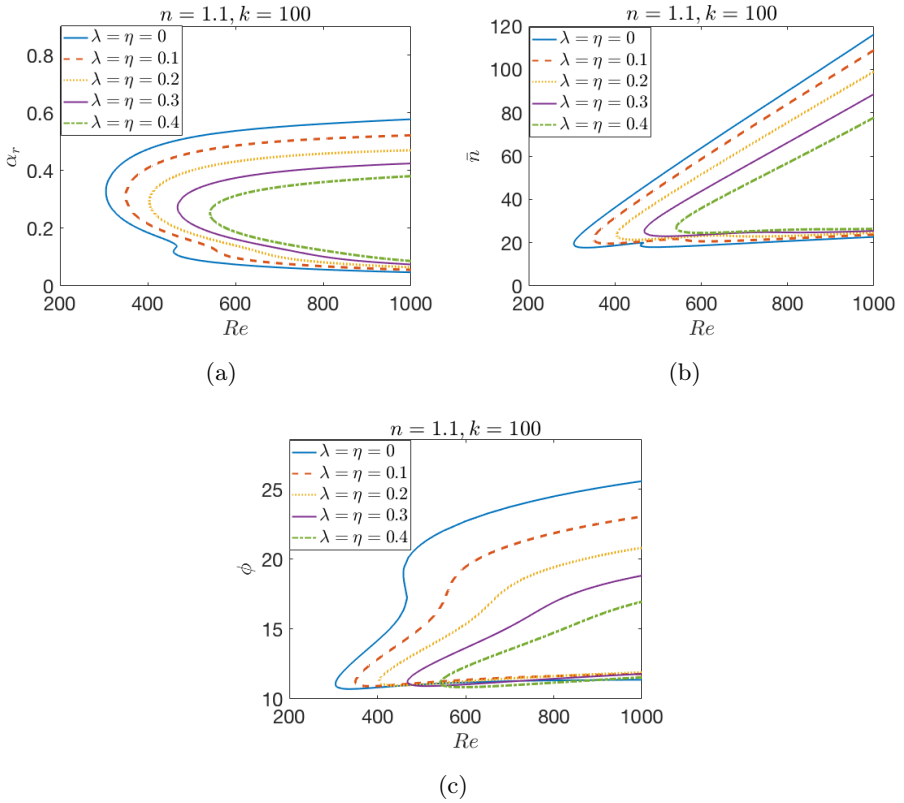

Figure 5.8: Neutral curves of the convective instability for the Carreau flow over isotropic roughness with $n = 1.1$.

Table 5.5: The values of the critical Reynolds number Re, $\bar{n}$ and wave angle ϕ on the both modes Type I and (Type II) for $n = 0.9$.

Parameters	Re	$\bar{n}$	ϕ
$\lambda = \eta = 0$	267.06(433.91)	46.32(23.82)	11.78(20.02)
$\lambda = \eta = 0.1$	352.30(−)	30.60(−)	12.01(−)
$\lambda = \eta = 0.2$	476.27(−)	34.84(−)	12.02(−)
$\lambda = \eta = 0.3$	642.66(−)	38.93(−)	11.96(−)
$\lambda = \eta = 0.4$	855.07(−)	42.53(−)	11.69(−)

Table 5.6: The values of the critical Reynolds number Re, $\bar{n}$ and wave angle ϕ on the both modes type I and (type II) for $n = 1.1$.

Parameters	Re	$\bar{n}$	ϕ
$\lambda = \eta = 0$	304.69(458.65)	19.54(18.72)	11.06(18.96)
$\lambda = \eta = 0.1$	349.32(−)	21.59(−)	11.23(−)
$\lambda = \eta = 0.2$	403.88(−)	23.59(−)	11.26(−)
$\lambda = \eta = 0.3$	467.95(−)	25.30(−)	11.20(−)
$\lambda = \eta = 0.4$	541.99(−)	26.96(−)	11.14(−)

5.3.2 *The growth rate*

This section adopts the methodology highlighted in Section (5.2.2) to examine the effects of isotropic roughness on the growth rates of the instability modes of the Carreau model boundary layer flows. Calculations have been carried out for the Type I mode at $Re = Re_c + 25$. The growth rates of the secondary Type II mode are not included here due to their very small value compared to the dominant Type I mode.

Figure (5.9) (a) and (b) clearly reveal the stabilising effect of isotropic roughness on the Type I mode and the maximum growth rate decreases for increased the values of roughness parameters. Moreover, the maximum growth rate is shifted to lower number of vortices. The number of spiral vortices at the maximum growth rate location is predicted to decease compared with the Newtonian case. Furthermore, the maximum growth rate for all values of roughness parameters are reduced with the chosen values of the power-index values. The overall effect of isotropic roughness reduces the number of vortices. Thus, the stabilising results seen here agree with the critical values for each flow reported in Tables (5.5) and (5.6).

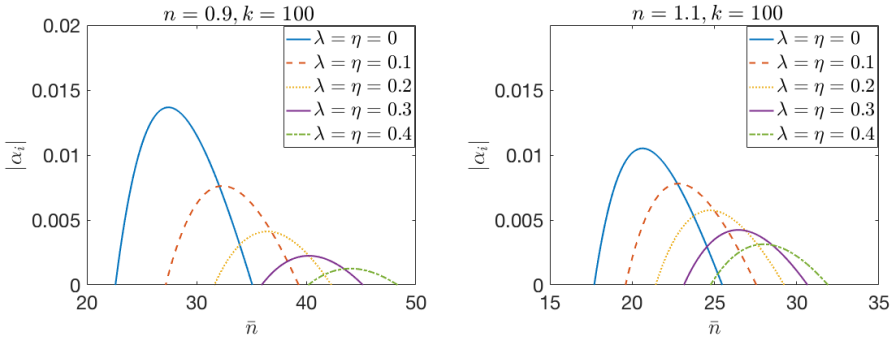

(a) (b)

Figure 5.9: Growth rates of Type I instability at $Re = Re_c + 25$ for both shear-thinning (a) and shear-thickening (b) in the case of isotropic roughness.

5.4 *Energy analysis results*

The energy balance calculation is analysed at the location of maximum amplification of the Type I mode at $Re = Re_c + 25$. Here Re_c is the critical Reynolds number for the onset of the Type I mode of instability for the particular rough surface considered. Results for various levels of roughness are compared to the Newtonian case in Figure (5.10). The energy balance calculations of the dominant Type I mode aims to establish the underlying physical mechanisms behind the effects of roughness disks for fixed values of shear-thinning and shear-thickening Carreau fluids.

As discussed in Chapter 4, the energy balance Equation (2.51) can be done for any eigenmode of the perturbation Equations (2.42). Again here the positive terms in that equation contribute to the energy production, whereas the negative terms remove energy from the system. The eigenmode of a disturbance is amplified ($\alpha_i < 0$) when the energy produced by the disturbance outweighs energy dissipated in the system. So, it is possible to use this formulation to interpret the effect of surface roughness on the instability modes of both regimes of Carreau fluids. This is solves by calculating the total energy of the system which is the sum of the energy production and dissipation terms. Increasing the total energy for higher values of the roughness parameters shows a destabilising effect on the modes. In contrast, a reduced total energy would indicate a stabilisation effect.

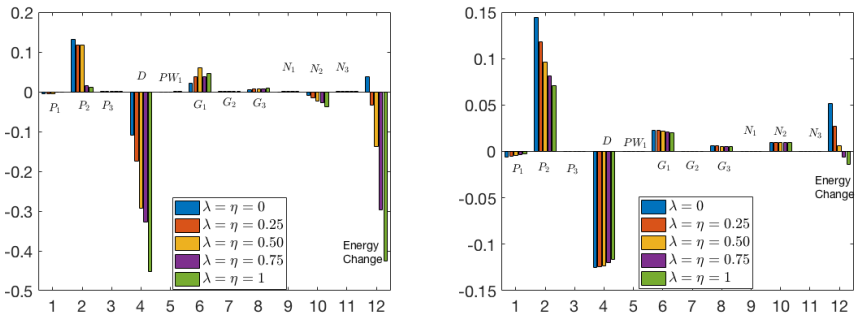

(a) $n = 0.9$. (b) $n = 1.1$.

Figure 5.10: Energy balance of Type I instability at $Re = Re_c + 25$ for shear-thinning and shear-thickening Carreau fluids in the case of isotropic roughness.

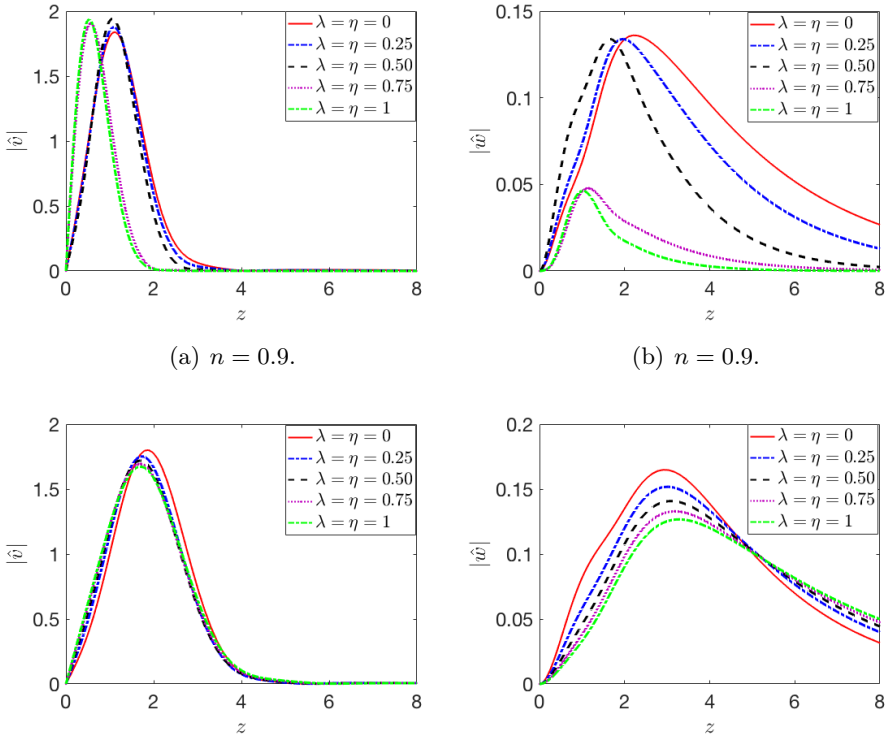

(a) $n = 0.9$. (b) $n = 0.9$.

(c) $n = 1.1$. (d) $n = 1.1$.

Figure 5.11: Type I mode for the azimuthal and the axial disturbance velocity profiles of Carreau model in the case of isotropic rotating disk at $Re = Re_c + 25$ for shear-thinning and shear-thickening Carreau fluids.

Figures (5.10) (a) and (b) present the energy balance calculation of the Type I mode for isotropic roughness for both shear-thinning and -thickening fluids, respectively. Clearly, the stabilisation effect obtained for each flow in the system is due to a strong decrease in energy changes of the flows when roughness increases. This effect arises mainly from the changes in the energy production term P_2 and in the energy dissipation term D. Both energy production and dissipation in each flow decrease for higher values of λ and η. Furthermore, the energy removing effects of the G_1, G_2 and G_3 terms arise from the streamline curvature and the three dimensionality of the mean flow result in an energy production effect for both cases. In other words, these terms contribute to energy production in the system. In addition, there is a negligible effect on the energy balance for non-Newtonian terms N_i. The modified viscosity is therefore again seen to establish new steady flows which are unstable through inviscid effects. This is as expected for the inviscid Type I mode.

It is interesting to provide some explanation about the energy trends of the Carreau model of flows by analysing the form of azimuthal velocity perturbation, $\hat{v}$, and the axial velocity perturbation, $\hat{w}$. These profiles contribute to the dominant energy production term P_2 and energy dissipation term D. The magnitudes of the two disturbance profiles are given in Figure (5.11) for $n = 0.9$, $n = 1.1$ for isotropic rough disk case for the Type I instability mode. It can be seen from the figures that there is no change in the general form of $\hat{v}$ disturbance profiles and it is translated close to the wall as the roughness parameters increase. The reduction of the P_2 term for each flow is due to the reduction in the amplitude of the axial velocity perturbation, $\hat{w}$ (as evidence in Figure (5.11) (b)). The decrease in the dissipation D for $n = 1.1$ is owing to the increase of the maximum value of the azimuthal velocity profile $\hat{v}$.

5.5 *Conclusion*

In this chapter, the mean flow equations are solved for a range of values of isotropic surface roughness. Here, the approach of Miklavčič & Wang parameters with some modifications and a variety of fixed values of the power index for the Carreau model. The numerical results show that isotropic roughness decreases the magnitude of the radial wall jet as $\lambda = \eta$ is increased.

Isotropic roughness is found to have a strong stabilising effect on both of the Type I and Type II modes of instability in terms of postponing the onset of the convective instability. Furthermore, it is observed that increased surface

roughness acts to increase the number of vortices along the upper branch for both of n. However, increasing the values of roughness, $\lambda = \eta$, acts to reduce the value of the vortex angle ϕ along both branches. The critical Reynolds numbers, the number of vortices and the vortex angle of shear-thinning and shear-thickening for the onset of both modes are reported in Tables (5.3)-(5.6), respectively.

The chapter also examined the effect of the growth rates of the Type I instability for a range of roughness and power-index parameters for the isotropic case. An energy balance analysis is also carried out and derived from the stability equations to study the effects of the isotopic rough surfaces on two values of power-index n. The total energy of the system is affected by the the sum of energy production and dissipation. This, as a result, determines the effects of the isotropic surface roughness on the stabilisation of both shear-thinning and shear-thickening fluids. Factors that contribute to change in the energy system have been identified as the terms P_2 and the term D, production by the Reynolds stresses and conventional viscous dissipation. The behaviour of the energy balance terms are qualitatively consistent with the neutral curve behaviours in Section 5.2. Overall, the energy analysis has revealed that isotropic roughness acts to reduce energy production of the Type I mode for both fluids. This results in a stabilisation effect on the Type I mode.

Chapter 6

Effect of shear-thinning and shear-thickening Carreau fluids on the roughness surface

Several research studies have presented numerical results for the generalized non-Newtonian fluids with the no-slip conditions. Mitschka & Ulbrecht [41] were the first to obtain the solution of the mean flow. The Power-law flow they used was equivalent to the solution for the Newtonian fluid flow given by von Kármán [55], where the power-law index n was equal to unity. Concerning the alternative Carreau models, Dabrowski [56] addressed the problem of the flow due to a rotating disk for shear-thinning and -thickening fluids. More recently, Griffiths [2] has presented the mean flows and an analysis of their stability using asymptotic and numerical approaches for Carreau fluids. All of these previous studies consider the von Kármán flow with the no-slip conditions. In the context of the rotating disk problem, no previous studies have utilised the form of the Carreau rheological model with partial-slip conditions, as this chapter aims to do.

In this chapter, the boundary-layer equations for generalized non-Newtonian fluids are solved to obtain the steady mean profiles for various power-indices of the Carreau model with fixed roughness parameters. Then, the linear perturbation equations are solved to study the occurrence of linear convective instabilities. The Chebyshev collocation method described in Subection (2.4.1) has been applied to solve the perturbation equations. Abdulameer *et al.* [51] used this numerical method to compute the neutral curves for the convective instability of non-Newtonian (Power-law) flow for the BEK system. Thus, the

system of stability equations is solved for the perturbation eigenfunctions and the neutral curves are plotted for fixed roughness parameters and variation of power-index. After that, the growth rates of the Carreau model for shear-thinning and -thickening fluids are obtained and compared for different cases of fixed roughness parameters. The energy analysis is solved here to confirm the results of the prior linear stability analysis. Chebyshev discretization method is used to solve the equations and investigate the effect of surface roughness and for a range of power index parameters. This method is used too in the work for BEK system for both Newtonian fluid by Alveroglu *et al.* [38] and non-Newtonian flow by Abdulameer *et al.* [51]. Some of results presented here of course also appear in the previous chapters, but we are particularly concerned here with the effect of the fluid properties for fixed values of roughness. Most of the content of this chapter appears in the literature as Alqarni *et al.* [57].

The steady mean flow solution is presented in Section 6.1. The neutral stability curves in obtained within the MW model for the mean flow only in Section 6.2 while this model imposed too within both the steady mean flow and the disturbances in Section 6.3 for three kinds of roughness surface. The effect of shear-thinning and -thickening on the energy analysis equations is investigated and this is presented in Section 6.4. Finally, conclusion are drawn in Section 6.5.

6.1 *The steady mean flow results*

The steady mean flow of the Carreau model are computed Equations (2.20, 2.21) using the MATLAB solver (see Subsection 2.3.1 for more details) with the partial-slip boundary conditions (2.23, 2.24). The mean flow profiles are computed for three velocity components (U, V, W) for radially anisotropic, azimuthally anisotropic and isotropic roughness surface cases (see Subsections 3.1, 4.1 and 5.1 for more details).

The resulting profiles of this section are depicted in Figures (6.1)-(6.3) at three examples of surface roughness for various values of n. The value of k parameter is fixed at 100 in order to maintain consistency throughout the remainder of this study; this is consistent with [2, 51]. The numerical code for the steady flow has been validated against various prior studies in the literature. In particular, our numerical values reported in Table (6.2) agree entirely with [35, 50] when $n = 1$, and with [58] when $n \neq 1$ in Tables (6.1) and (6.2). In all calculations we use the integration domain $0 < z < 20$ up

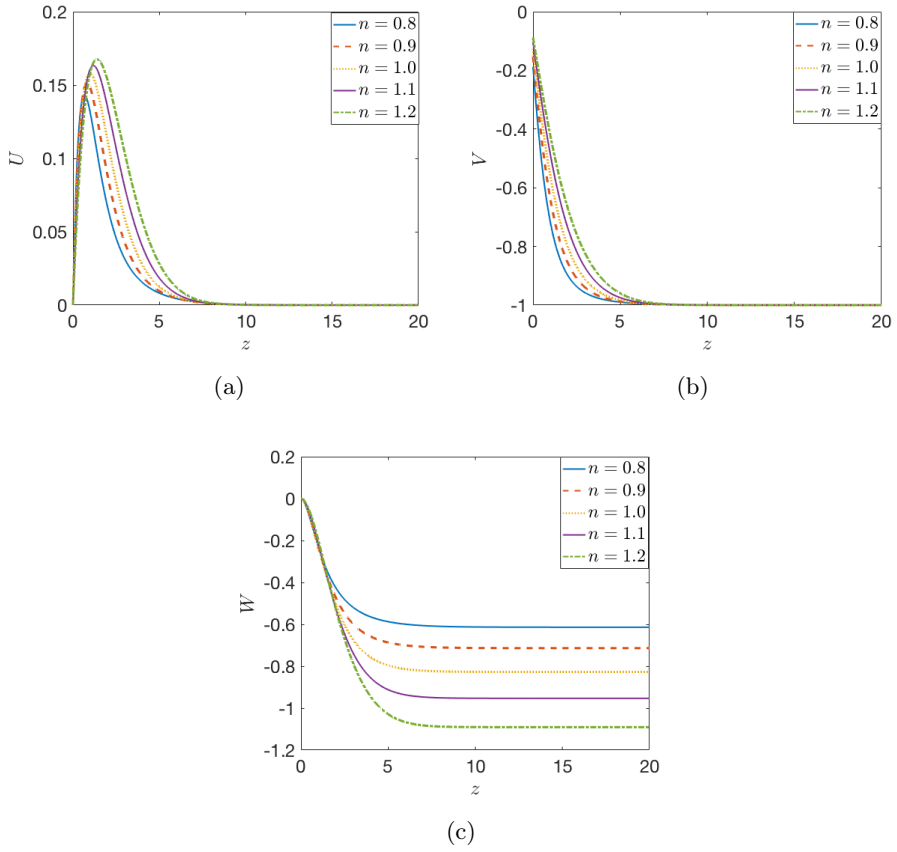

Figure 6.1: Mean flow components of the Carreau flow over radially anisotropically rough disk for shear-thinning and shear-thickening fluids, $\eta = 0.25$, $\lambda = 0$. (a) U-profile, (b) V-profile, (c) W-profile.

through the boundary layer. We find that this leads to converged far-field values at all n and λ, η. Further increases beyond $z_\infty = 20$ have no material effect on the results. This domain is consistent with related studies in the literature [42, 51, 59].

Figure (6.1) indicates the effects of various values of power-index over a rough rotating disk for radial grooves ($\eta = 0.25$, $\lambda = 0$). The radial-flow profiles reveal that increasing n results in the wall jet moving outwards along the z-axis. That is, the boundary-layer thickness increases with $n > 1$ (shear-thickening) and narrows for $n < 1$ (shear-thinning). Furthermore, the growth in the peak value shows an increased jet effect for shear-thickening fluids. In the azimuthal velocity profile, the wall value of V increases with n; further evidence of an increasing/narrowing boundary-layer thickness. With regards the normal velocity component, we observe that increasing n leads to greater

Table 6.1: Numerical values of the mean velocity flow parameters $U'(0)$, $V'(0)$ and $W(z_\infty)$ for shear-thickening $n = 1.1, 1.2$.

Parameters	n	$-U'(0)$	$V'(0)$	$W(z_\infty)$
Radially anisotropic roughness (radial grooves)				
$\eta = 0.25$	1.1	0.3534	0.4178	0.9531
	1.2	0.3020	0.3507	1.0906
Azimuthally anisotropic roughness (concentric grooves)				
$\lambda = 0.25$	1.1	0.3401	0.5635	1.0769
	1.2	0.2906	0.4498	1.2211
Isotropic roughness				
$\eta = \lambda = 0.25$	1.1	0.2873	0.4689	1.0005
	1.2	0.2542	0.3897	1.1424

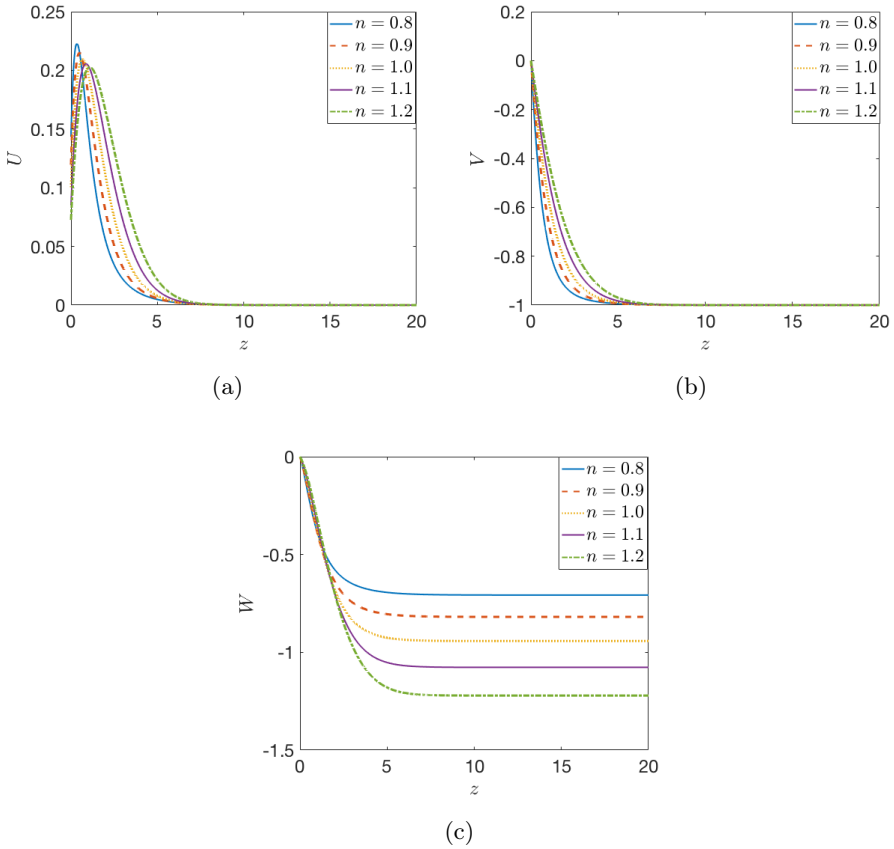

(a) (b)

(c)

Figure 6.2: Mean flow components of the Carreau flow over azimuthally anisotropically rough disk for shear-thinning and -thickening fluids, $\eta = 0$, $\lambda = 0.25$. (a) U-profile, (b) V-profile, (c) W-profile.

fluid entrainment into the boundary layer. That is, shear-thickening fluids act to entrain a greater volume of fluid into the boundary layer and shear-thinning a lesser volume. This is consistent with the boundary-layer thickening/ thinning effects observed in radial and azimuthal flow components. Other values ($\eta = 0.50$, $\eta = 0.75$ and $\eta = 1$) with their initial values can be seen in Appendices (D.1.1) and (D.2.1).

Figure (6.2) shows the case of concentric grooves ($\lambda = 0.25$, $\eta = 0$) and we see mostly similar responses to n in the azimuthal and normal flow components. However, there is some subtly different behaviour observed in the radial profile: while a shear-thickening fluid again acts to thicken the boundary layer, the radial jet is in fact accelerated for shear-thinning fluids. Other values ($\lambda = 0.50$, $\lambda = 0.75$ and $\lambda = 1$) with their initial values can be seen in Appendices (D.1.2) and (D.2.2).

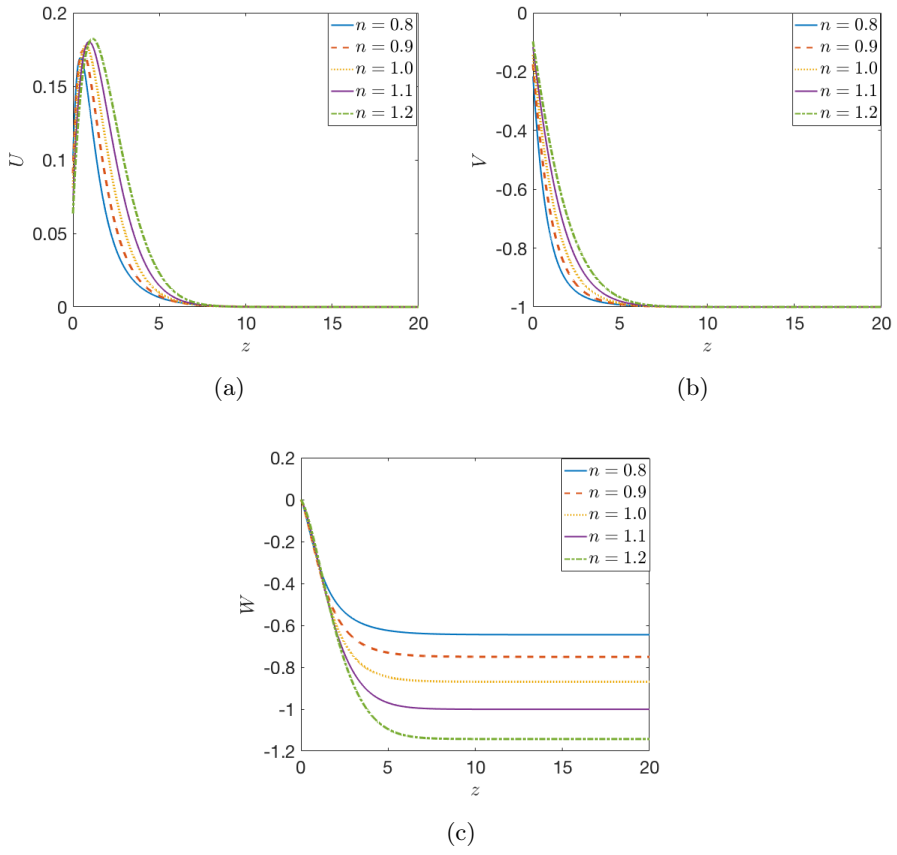

Figure 6.3: Mean flow components of the Carreau flow in the case of isotropic roughness, $\lambda = \eta = 0.25$. (a) U-profile, (b) V-profile, (c) W-profile.

Figure (6.3) shows the mean-flow profiles for isotropic roughness ($\lambda = \eta =$

0.25) are similar to those in the radial case. Other values ($\lambda = \eta = 0.50$, $\lambda = \eta = 0.75$ and $\lambda = \eta = 1$) with their initial values can be seen in Appendices (D.1.3) and (D.2.3).

Table 6.2: Numerical values of the mean velocity flow parameters $U'(0)$, $V'(0)$ and $W(z_\infty)$ for Newtonian fluid and shear-thinning $n = 1, 0.9, 0.8$.

Parameters	n	$U'(0)$	$-V'(0)$	$-W(z_\infty)$
Radially anisotropic roughness (radial grooves)				
$\eta = 0.25$	1.0	0.4170	0.5034	0.8269
	0.9	0.4953	0.6128	0.7134
	0.8	0.5904	0.7522	0.6137
Azimuthally anisotropic roughness (concentric grooves)				
$\lambda = 0.25$	1.0	0.4018	0.7251	0.9425
	0.9	0.4786	0.9629	0.8190
	0.8	0.5736	1.3277	0.7074
Isotropic roughness				
$\eta = \lambda = 0.25$	1.0	0.3242	0.5706	0.8693
	0.9	0.3633	0.7008	0.7503
	0.8	0.4016	0.8658	0.6447

6.2 *The convective instability*

Here Equations are solved (2.42) with the aim of studying the occurrence of convective instabilities of shear-thinning and -thickening Carreau flow. For each n in the particular range of interest, two spatial branches determine the convective instability characteristics of the system. The local convective instability is analysed in terms of neutral curves in (6.2.1) and the growth rates in (6.2.2). The perturbation Equations (2.42) are subject to zero boundary conditions (3.3).

6.2.1 *Neutral curves*

This section calculates the spatial branches for each n and Re for a given wave number β and the frequency ω and the value of α satisfies the dispersion relation is calculated for a variety of shear-thinning and -thickening fluids using the Carreau viscosity model with fixed values rough surfaces. As discussed previously, structurally the neutral curve is divided into two lobes or branches: the upper branch that represents the type I crossflow instability and the lower

branch representing the type II centrifugal instability. The spatial branches for the cases when $n < 1$, $n = 1$ and $n > 1$ are plotted for (Re, α_r), $(Re, \bar{n})$ and (R, ϕ)-planes. Example neutral curves resulting from our analyses for all n are shown in Figures (6.4)-(6.6) and critical Reynolds numbers for the onset of instabilities are shown in Tables (6.3)- (6.5).

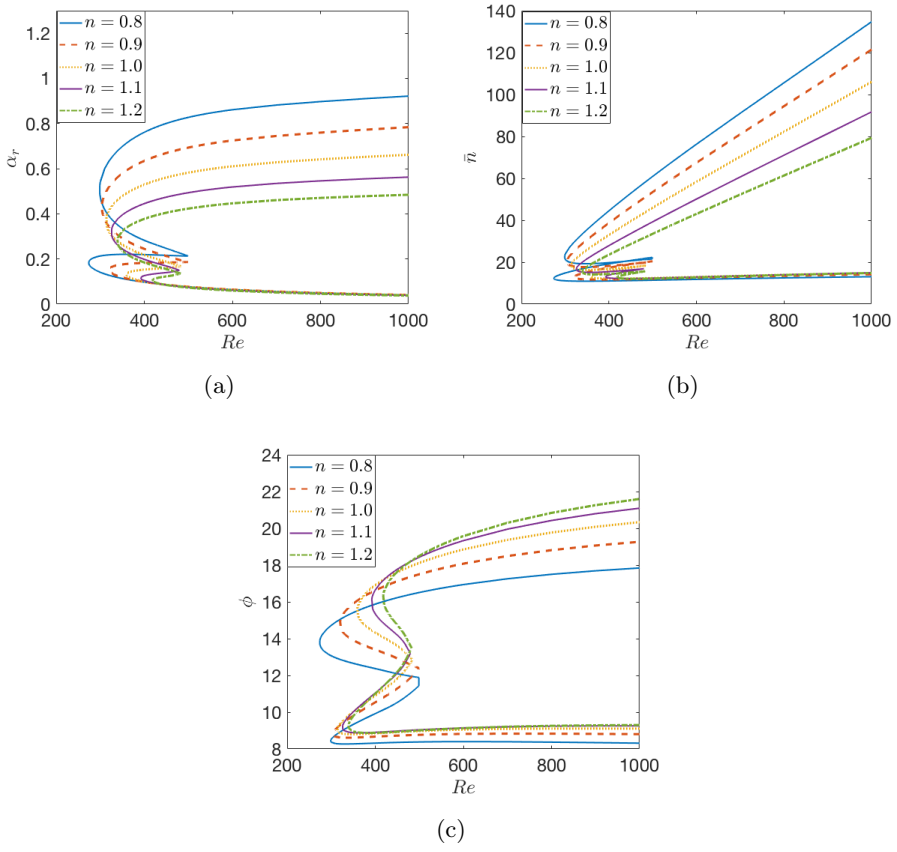

Figure 6.4: Neutral curves of the convective instability for the Carreau flow over radially-anisotropically rough disk with $n = 0.8, 0.9, 1.0, 1.1, 1.2$ with $\eta = 0.25$, $\lambda = 0$.

Figures (6.5)-(6.6) (a) and (b) show that stability of the boundary layers over isotropic and azimuthally-anisotropic rough surfaces is dominated by the Type I mode; this is evident from their single-lobed structure. The data presented in Tables (6.3) , (6.4) and (6.5) further suggests that, for these surfaces, there is a maximum value of Re_c achieved at around $n = 1.2$. Further movement in n either side of this acts to stabilise the boundary layer in terms of increasing the critical Reynolds number. However, it is clear that shear-thinning fluids have the greatest stabilising effect. Additional figures with

their critical values are provided in Appendices (D.3) and (D.4) for three cases of roughness surface.

Parameters	n	Re	$\bar{n}$	ϕ
Radially anisotropic				
$\eta = 0.25$	0.8	298.51(273.67)	22.54(12.32)	8.11(13.77)
	0.9	303.65(319.19)	20.21(12.81)	8.71(14.79)
	1.0	313.09(358.72)	18.35(13.03)	9.07(15.60)
	1.1	323.12(391.33)	16.76(12.97)	9.26(15.94)
	1.2	338.80(417.76)	15.45(12.74)	9.33(16.21)

Table 6.3: The values of the critical Reynolds number Re, $\bar{n}$ and wave angle ϕ on the both modes Type I and (Type II).

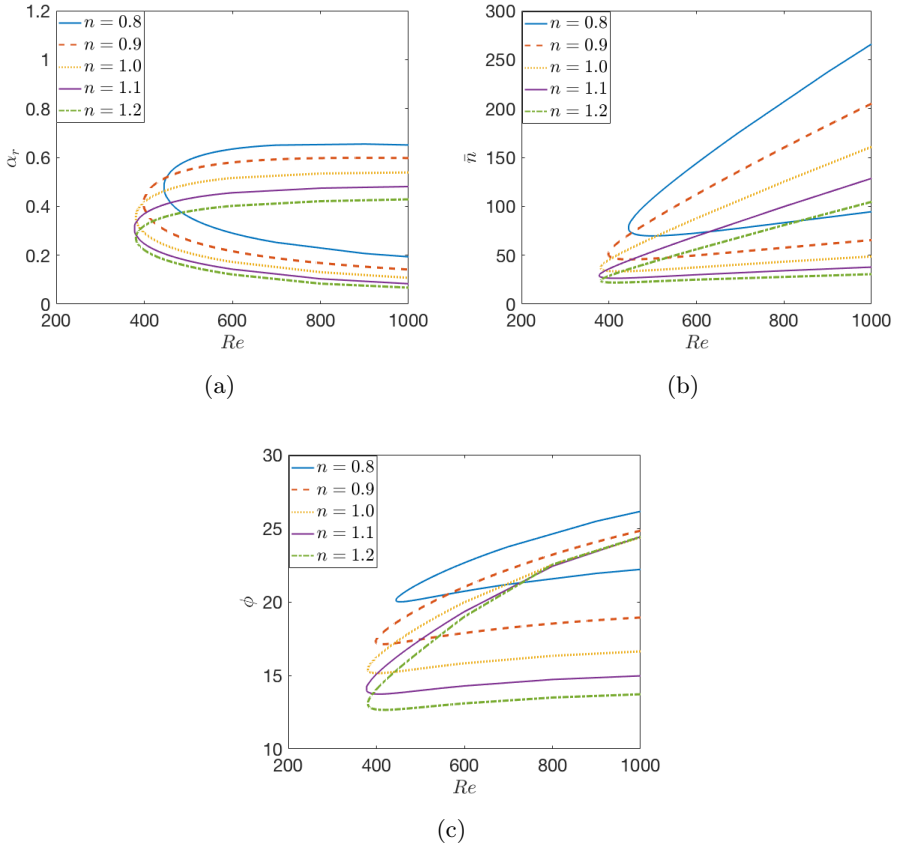

Figure 6.5: Neutral curves of the convective instability for the Carreau flow over azimuthally-anisotropically rough disk with $n = 0.8$, 0.9, 1.0, 1.1, 1.2 with $\lambda = 0.25$, $\eta = 0$.

In contrast, both the Type I and II modes are important over radially anisotropic rough surfaces, as shown in the distinct lobes in Figures (6.4) (a)

and (b). Furthermore, it is seen that shear-thinning fluids are destabilising over such surfaces and the critical Reynolds numbers of both modes modes increase when n increases, too. Although our results are only presented for $\lambda, \eta = 0.25$, similar qualitative behaviour is obtained at all other roughness levels.

Parameters	n	Re	$\bar{n}$	ϕ
Azimuthally anisotropic				
$\lambda = 0.25$	0.8	444.46(−)	78.18(−)	24.15(−)
	0.9	398.21(−)	51.18(−)	19.84(−)
	1.0	380.68(−)	37.31(−)	17.31(−)
	1.1	377.04(−)	29.23(−)	15.58(−)
	1.2	380.86(−)	24.03(−)	14.31(−)

Table 6.4: The values of the critical Reynolds number Re, $\bar{n}$ and wave angle ϕ on the both modes Type I and (Type II).

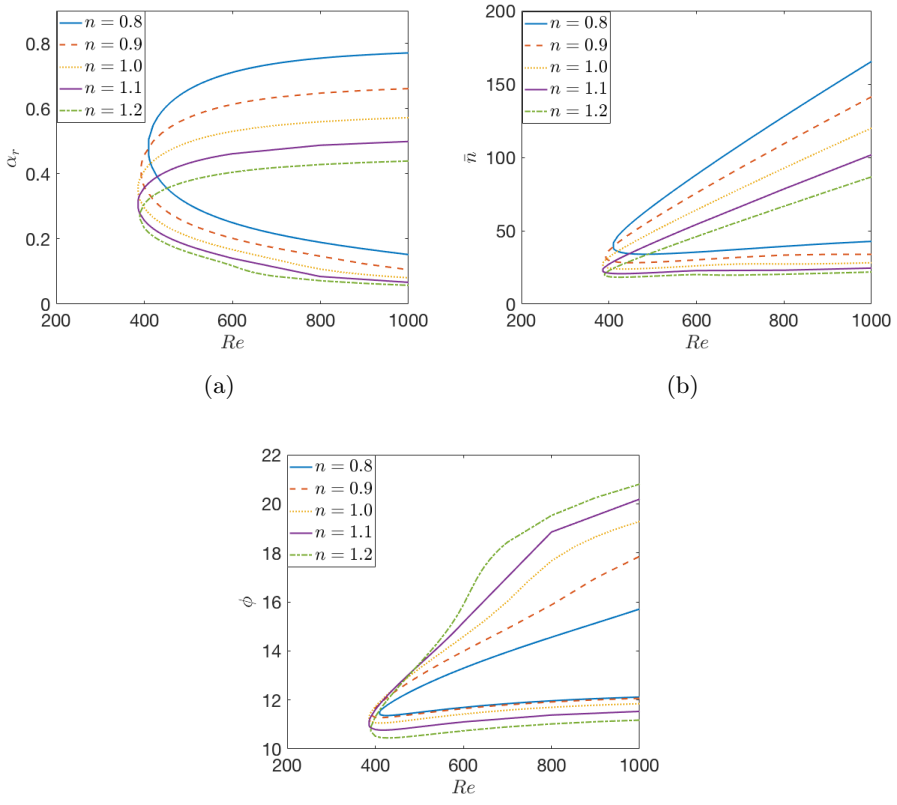

Figure 6.6: Neutral curves for the convective instability of an isotropically-rough rotating disk with $n = 0.8$, 0.9, 1.0, 1.1, 1.2 with $\lambda = \eta = 0.25$.

Also, Figure (6.4) (c) shows the qualitatively different results for Carreau fluids in terms of the wave angle. When $n < 1$ and $n > 1$ increases then the type I and type II critical Reynolds numbers increases, however, the lower-branch structure appears to be largely unaffected and the effect of decreasing n is much more noticeable on the upper-branch modes. Figures (6.5)-(6.6) (c) clearly indicate that as the shear-thickening parameter increases so the critical Reynolds numbers decrease. More generally in these figures, we would consider the effect of both shear-thinning and -thickening to be stabilising as the area enclosed by the wavenumber neutral curves is decreases in this case.

Parameters	n	Re	$\bar{n}$	ϕ
Isotropic roughness				
$\lambda = \eta = 0.25$	0.8	408.49(−)	39.81(−)	12.11(−)
	0.9	392.20(−)	32.44(−)	12.24(−)
	1.0	385.36(−)	27.04(−)	12.11(−)
	1.1	385.11(−)	22.98(−)	11.71(−)
	1.2	389.45(−)	20.12(−)	11.36(−)

Table 6.5: The values of the critical Reynolds number Re, $\bar{n}$ and wave angle ϕ on the both modes Type I and (Type II).

6.2.2 *The growth rate*

The growth rates of the Type I instability mode are presented for shear-thinning and -thickening Carreau fluids for the three cases of the roughness: radially-anisotropic and azimuthally anisotropic and isotropic roughness at $Re = Re_c + 25$; that is, at a fixed distance into the neutral curve. Note that the growth rate of the instability mode is measured as the absolute value of the negative imaginary part of the radial wavenumber, $|\alpha_i|$, at particular values of the vortex number $\bar{n}$ for each level of roughness. The Type II mode vanishes at even modest levels of some surface roughness under the model and so is not considered here due to the dominant Type I mode and also Carreau fluids have only a slight effect in the cases of both concentric grooves and isotropic roughness. So, the growth rate of the Type II instability mode is presented here for the radial grooves only.

Figure (6.7) (a) shows shear-thickening fluids to be the most stable in terms of the delayed onset of instability and the weakest subsequent development for radially-anisotropic surface roughness. It is also interesting to note the effect that shear-thinning and -thickening fluids have on the mode number (number of spiral vortices) $\bar{n}$ under all roughness types: the number of spiral vortices

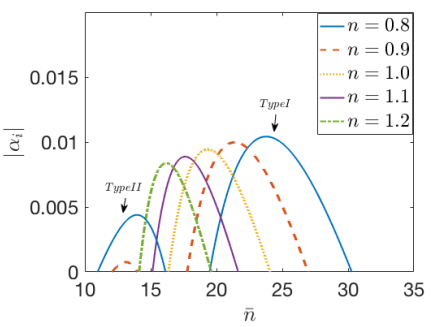

(a) $\eta = 0.25, \lambda = 0.$

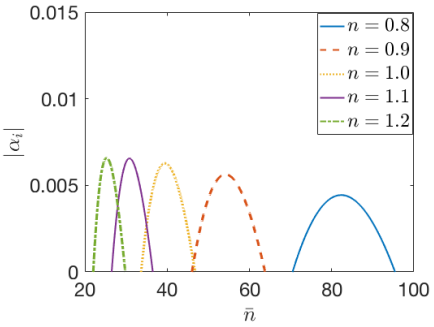

(b) $\lambda = 0.25, \eta = 0.$

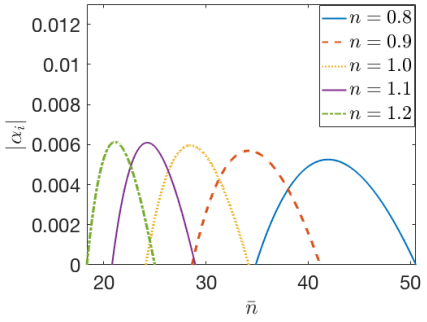

(c) $\eta = \lambda = 0.25.$

Figure 6.7: Growth rates of Type I and Type II instability at $Re = Re_c + 25$ in the cases of both anisotropic roughness (a) and (b) and isotropic roughness (c).

is reduced with increased n. In contrast, Figures (6.7) (b) and (c) reveal the stabilising effect on the growth rates of the Type I mode for both isotropic and azimuthally-anisotropic roughness. That is, even though there appears to be some stabilising effect in terms of the onset of instability (Re_c) when moving n either side of $n = 1.1$, the subsequent development of that instability is quelled by shear-thinning fluids.

6.3 *The novel approach for the perturbations*

This part discusses with the occurrence of convective instabilities in the case shear-thinning and -thickening over the rotating disk. The convective instability is obtained by solving the perturbation Equations (2.42) system as a quadratic eigenvalue problem according to the partial-slip boundary condition

defined in Chapter (3.2) in Equations (3.2).

6.3.1 *Neutral curves*

Neutral curves are produced for a range of different power-index with three cases of roughness and the comparisons between them are presented here. The standard neutral curve plots, the Reynolds number of the flow is plotted against different variables in order to identify the range of stability that the flow should have. These variables are α_r and number of vortices $\bar{n}$ and the wave angle ϕ. Figures (6.8)-(6.10) show the relationship of neutral curve with increasing power-index for various cases of roughness.

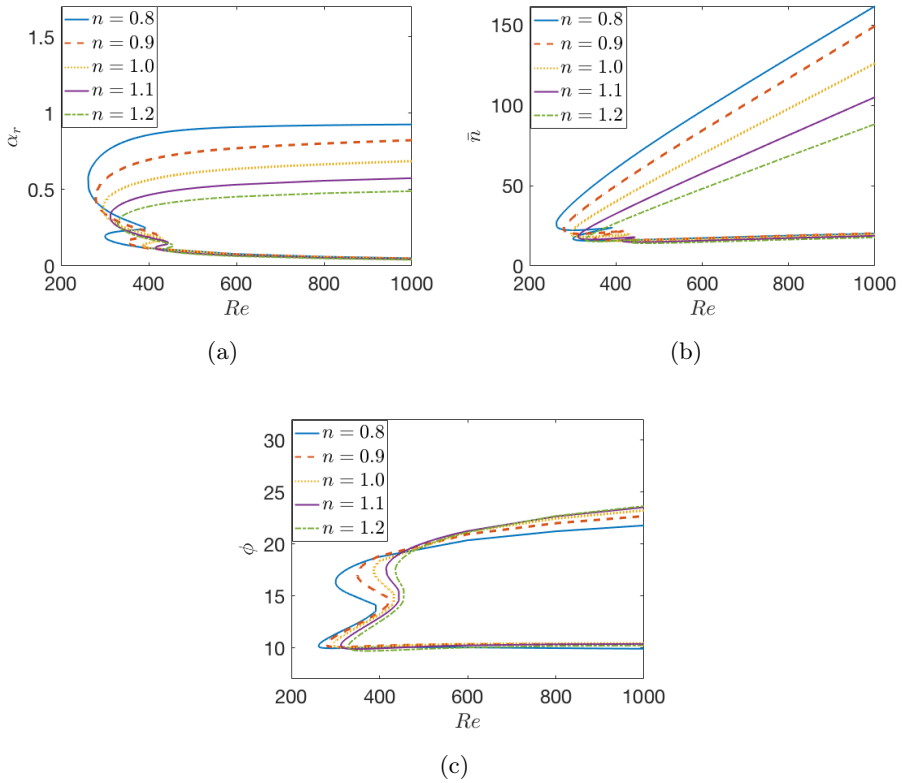

Figure 6.8: Neutral curves of the convective instability for the Carreau flow over radially anisotropically rough disk with $n = 0.8$, 0.9, 1.0, 1.1, 1.2.

The effect of increasing power-index n in a concentrically grooved disk case in terms of width shrinks the Type I lobe. However, a stark destabilising effect

has been noticed on the Type II as seen in Figure (6.8) (a). In contrast, Figures (6.9) and (6.10) (a) indicate that both $n > 1$ and $n < 1$ have a stabilising effect on both the Type I and Type II modes in terms of the critical Reynolds number on the radial grooves. Furthermore, the effect on the Type I mode is stronger compared to the concentric grooves case. It also is found that the Type II mode is vanished when n increases.

It is found that a similar effect of the shear-thinning and -thickening on the isotropic roughness where the Type I mode has strong stabilising effect. It also observed that the Type II mode is stabilised in the same way as seen for the radially grooved disk. Overall, shear-thinning and -thickening Carreau fluids have a destabilising effect on radially-anisotropic that is promoted when n is increases; this is in contrast to have a slight stabilising effect on the Type I mode that is promoted when n increases on the azimuthally anisotropic and isotropic roughness.

Parameters	n	Re	$\bar{n}$	ϕ
Radially anisotropic				
$\eta = 0.1$	0.8	261.28(300.17)	25.98(16.94)	10.17(16.31)
	0.9	278.66(349.40)	22.93(16.89)	10.30(17.05)
	1.0	295.34(386.80)	20.34(16.30)	9.07(15.60)
	1.1	312.02(414.61)	18.27(15.60)	10.20(17.47)
	1.2	328.84(435.86)	16.56(14.77)	10.09(17.40)

Table 6.6: The values of the critical Reynolds number Re, $\bar{n}$ and wave angle ϕ on the both modes Type I and (Type II).

Parameters	n	Re	$\bar{n}$	ϕ
Azimuthally anisotropic				
$\lambda = 0.1$	0.8	377.93(−)	47.61(−)	15.46(−)
	0.9	345.46(−)	35.46(−)	14.04(−)
	1.0	339.11(−)	28.14(−)	17.31(−)
	1.1	343.53(−)	23.42(−)	12.29(−)
	1.2	353.14(−)	20.12(−)	11.72(−)

Table 6.7: The values of the critical Reynolds number Re, $\bar{n}$ and wave angle ϕ on the both modes Type I and (Type II).

The effect of shear-thinning and -thickening Carreau fluids in terms of the number of vortices, it can be seen in Figure (6.8) (b) a concentrically grooved disk tends to lower the number of vortices as n increased. The same behaviour in the other two cases, by increasing power-index n leads to a decrease in the number of vortices on the a radially grooved disk and isotropic roughness in Figures (6.9) and (6.10) (b). Critical parameters for the onset of the Type I and Type II modes are given in Tables (6.6), (6.7) and (6.8). Figures (6.8), (6.9) and (6.10)(c) represent neutral curves in terms of the wave angles. It can be

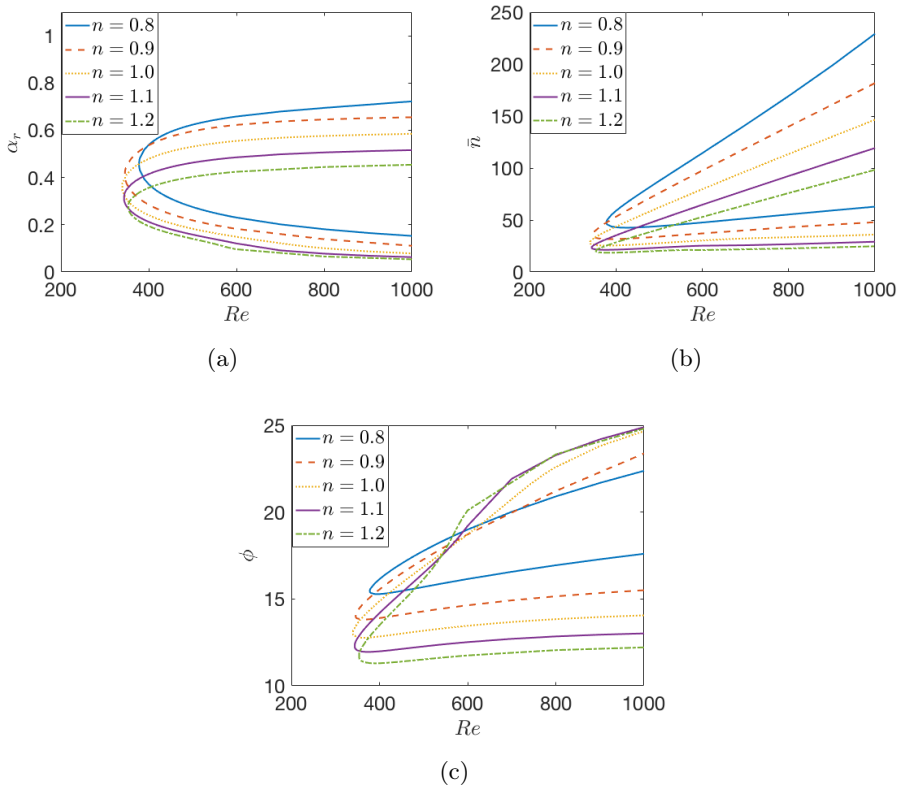

Figure 6.9: Neutral curves of the convective instability for the Carreau flow over azimuthally-anisotropically rough disk with $n = 0.8$, 0.9, 1.0, 1.1, 1.2.

seen that all of them tend to lower number of the wave angles on Type I whilst on Type II leads to an increase in the wave angles on a concentrically grooved disk as n increased. We notice that the increased in azimuthally anisotropic the wave angles for the Newtonian (i.e $n = 1$) fluid is more obvious than other. Moreover, as n increases the change on the upper lobe is noticeable but slight change of the lower lobe on radially-anisotropic. The lower lobe of the neutral curve vanishes immediately for each value of n in the radial grooves and isotopic roughness.

6.3.2 *The growth rate*

Using the same method adopted in Section (6.2.2) to study the effect of both shear-thinning and -thickening fluids on the growth rates. Calculations have been carried out for type I mode at $Re = Re_c + 25$. Results for various cases

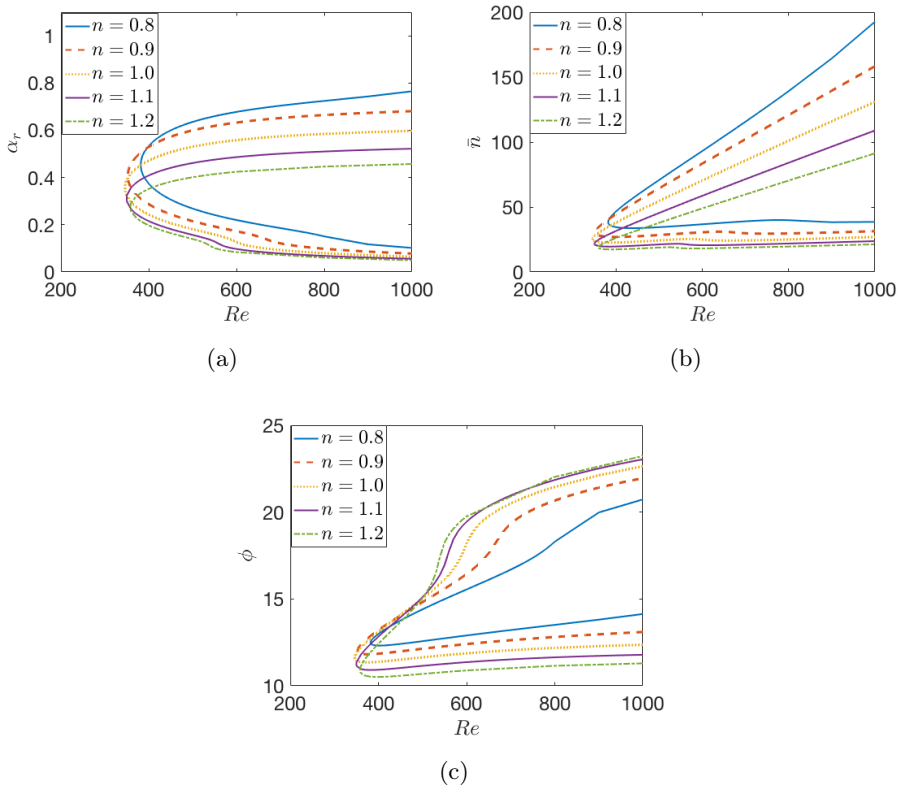

Figure 6.10: Neutral curves for the convective instability of an isotropically-rough rotating disk with $n = 0.8$, 0.9, 1.0, 1.1, 1.2.

Parameters	n	Re	$\bar{n}$	ϕ
Isotropic roughness				
$\lambda = \eta = 0.1$	0.8	381.93(−)	38.40(−)	12.48(−)
	0.9	352.30(−)	30.60(−)	12.01(−)
	1.0	345.75(−)	25.24(−)	12.11(−)
	1.1	349.32(−)	21.59(−)	11.23(−)
	1.2	358.00(−)	18.95(−)	10.90(−)

Table 6.8: The values of the critical Reynolds number Re, $\bar{n}$ and wave angle ϕ on the both modes Type I and (Type II).

of roughness are compared to the Newtonian case in Figure (6.11).

In the case of disk with radial grooves (6.11) (a), it can be seen that the maximum amplification shifts to lower values of $\bar{n}$, suggesting a deceasing in the number of vortices over the disk for $n > 1$ and $n < 1$. For both concentric grooves and isotropic roughness (6.11) (b) and (c), there is a decrease in the value of $\bar{n}$. In general, it is noted that the behaviour of the shifting maximum growth rates with number of spiral vortices $\bar{n}$ for Carreau fluids is the same

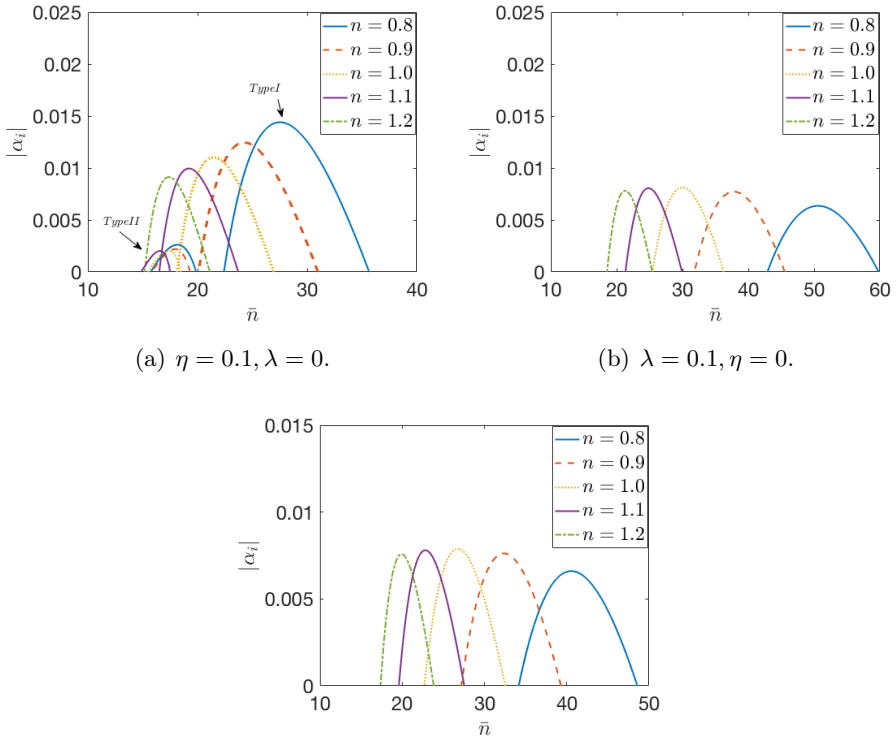

(a) $\eta = 0.1, \lambda = 0.$

(b) $\lambda = 0.1, \eta = 0.$

(c) $\eta = \lambda = 0.1.$

Figure 6.11: Growth rates of Type I instability at $Re = Re_c + 25$ in the cases of both anisotropic roughness (a) and (b) and isotropic roughness (c).

for the smooth case. So,the number of spiral vortices is increased for shear-thinning and -thickening Carreau fluids for all roughness cases.

6.4 *Energy analysis results*

The maximum growth rates obtained in section (6.2.2) for each flow are used here to find the energy balance for Carreau flows. The energy balance calculation is applied at the location of maximum amplification of the Type I mode at $Re = Re_c + 25$. Here Re_c is the critical Reynolds number for the onset of the Type I mode of instability for the particular three rough surface cases being considered. Results for various levels of roughness are compared to the Newtonian case in Figure (6.12). The aim of the energy analysis is to establish the underlying physical mechanisms behind the effects of roughness

disks of the Carreau boundary layer flows for shear-thinning and -thickening fluids. By considering the energy balance Equation (2.51) of any eigenmode of the perturbation Equations (2.42).

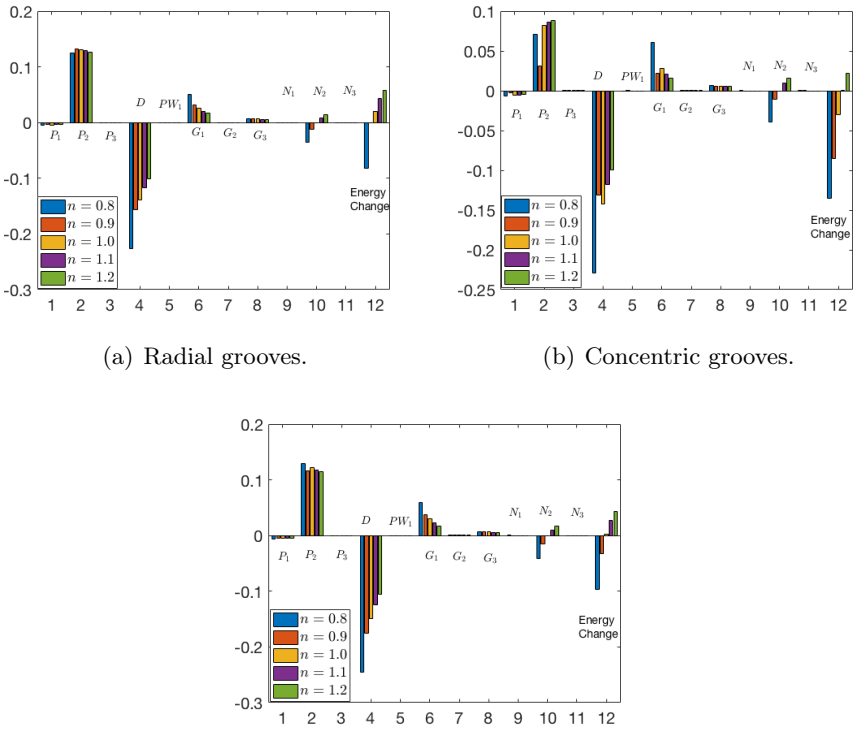

(a) Radial grooves.

(b) Concentric grooves.

(c) Isotropic case.

Figure 6.12: Energy balance of Type I instability at $Re = Re_c + 25$ for shear-thinning and -thickening fluids.

Note that, the positive terms in that equation contribute to the energy production whereas the negative terms remove energy from the system. The eigenmode of a disturbance is amplified ($\alpha_i < 0$) when the energy produced by the disturbance outweighs energy dissipated in the system. The effect of surface roughness on the instability modes of both shear-thinning and -thickening Carreau fluids can be interpreted from this formulation by calculating the total energy of the system which is the sum of the energy production and dissipation terms. Increased the total energy for higher values of the roughness parameters shows a destabilising effect on the modes. In contrast a reduced total energy indicates a stabilisation effect.

Figures (6.12)(a) indicates a destabilisation effect on the Type I mode in case of radially anisotropic roughness. In particular, increased power index n leads to growth in the energy production term P_2. It is also worth noting that

the energy producing in the terms G_1 and G_3 notably decreases. In contrast to the radially-anisotropic case is the azimuthally-anisotropic and isotropic cases.

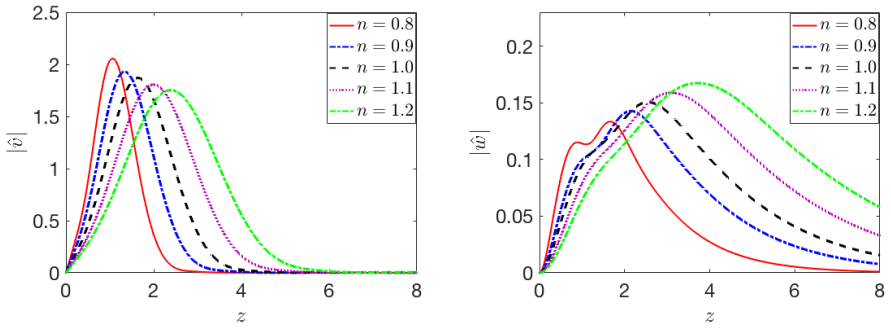

(a) $\eta = 0.25, \lambda = 0.$ (b) $\eta = 0.25, \lambda = 0.$

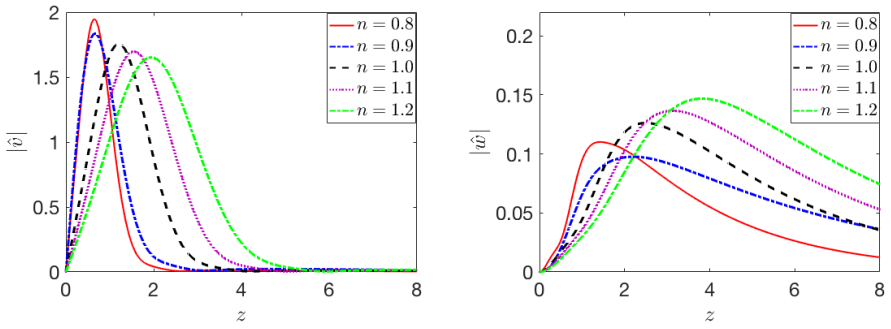

(c) $\lambda = 0.25, \eta = 0.$ (d) $\lambda = 0.25, \eta = 0.$

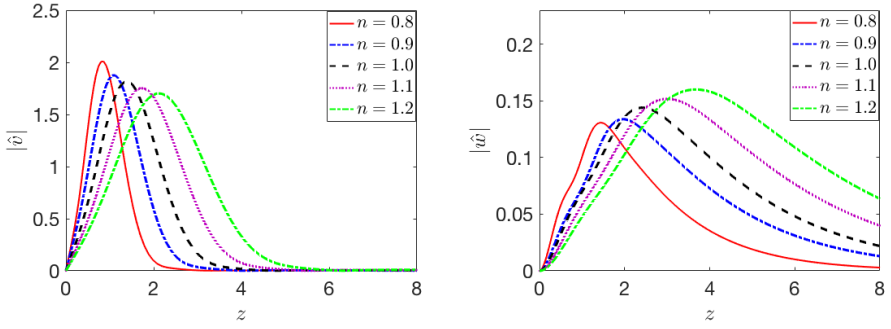

(e) $\lambda = \eta = 0.25.$ (f) $\lambda = \eta = 0.25.$

Figure 6.13: Type I mode profiles for the azimuthal and the axial disturbance velocity profiles of Carreau model at $Re = Re_c + 25$ for shear-thinning and -thickening fluids.

It can be seen from Figure (6.12) (b) the energy balance calculation for azimuthally-anisotropic. Clearly, there is a stabilisation effect obtained in the

Type I mode due to a strong decrease in total energy of the flow as n parameter is increased. The main reason of this effect is the large reductions in the energy production term $P2$, the energy dissipation term D and the non-Newtonian viscosity N_2. The changes in the other terms seem to be negligible. However, a small stabilising effect can be observed for shear-thickening fluids due to a reduction in the total energy. Figure (6.12) (c) shows a similar stabilising effect of isotropic roughness on the Type I mode.

The disturbance profiles are the azimuthal velocity perturbation, $\hat{v}$, and the axial velocity perturbation, $\hat{w}$, which consider to be the dominant energy production term P_2. The magnitudes of these two disturbance profiles are presented in Figures (6.13) (a)-(f) for three cases of roughness within shear-thinning and -thickening Carreau fluids. Figure (6.13) (a) and (b) can be seen that the general form of both the disturbance profiles are changed with the profiles being simply translated towards the wall as n increased for the case of a concentric grooved disk. In the case of a radially grooved disk and isotropic case. Figures (6.13) (c)-(f) that strong increase of the P_2 term for each flow is due to the growth of the amplitude of the axial velocity perturbation, $\hat{w}$. The reduction in the dissipation rate of the system is due to the decrease of the maximum value of the azimuthal velocity profile $\hat{v}$.

6.5 *Conclusion*

In this chapter, the mean flow profiles have been obtained for the mean flow equations for a range values of shear-thinning and -thickening fluids under the Carreau flow model. The numerical results indicate that anisotropic roughness with radial grooves on the mean flow results are to decrease the magnitude of the radial wall jet as η increased. This opposes the of the azimuthally anisotropic roughness as increase the magnitudes of the axial direction and also increase the magnitudes of the radial and wall jets of λ increased for all n. Furthermore, the effect of isotropic roughness on the properties of mean flow components U, V, W are similar to the effects observed in the radial grooves case, but it is less effective. Also, the effects of the isotropic case can be seen as a combination of the effects for radial and concentric grooves.

Of importance also is the Type I mode for the onset of linear convective instability of boundary-layer flows for both shear-thinning and -thickening Carreau fluids with the three cases roughness surface. The first part is for the smooth boundary condition and the second one is the partial-slip approach of Miklavcic & Wang [1] with modification. The effects of radially anisotropic

roughness on the convective instability of stationary disturbances on this flow demonstrated that has a strong stabilising effect on the Type I instability mode in terms of the critical Reynolds number for the onset of the convective instability for both $n = 0.9$ and $n = 1.1$. However, the Type II mode has a slight destabilising effect as this type of roughness level is increased and it becomes more dominate for sufficiently high levels. Moreover, we can observe from Tables (6.3) and (6.6) that the numbers of vortices, $\bar{n}$, and the vortex angle, ϕ, are decreased at all values of power-law index as radially anisotropic roughness is increased.

We then continue the effects of roughness in the azimuthally anisotropic on the convective instability of stationary disturbances on the Carreau fluid for shear-thinning when $n < 1$ or shear-thickening $n > 1$. The neutral curves reveal that both have a strong stabilising effect on the Type I and Type II instabilities. Moreover, the Type I and Type II critical Reynolds numbers decrease, indicating an advanced onset of convective instability. The area encompassed by the neutral curves is increased. For the number of the vortices $\bar{n}$ and the vortex angle ϕ we have seen that increased surface roughness acts to increase both of them, despite being more noticeable in the upper-branch modes.

In the case of the isotropic roughness has a strong stabilising effect on both of the Type I and Type II modes instability in terms of postponing the onset of the convective instability. Also, it is observed that increased surface roughness acts to increase the number of vortices along the upper branch for both of n. However, increasing the roughness, $\lambda = \eta$ acts to reduce the value of the vortex angle ϕ along both branches. The critical Reynolds numbers, the number of vortices and the vortex angle of shear-thinning and shear-thickening for the onset of both modes are reported in Tables (6.5) and (6.8) .

The chapter also examined the effect of the growth rates of the Type I instability for three cases of roughness and variety power-index parameters. An energy balance equation is considered and calculated to establish the underlying physical mechanisms behind the effects of power-index n parameters on different cases of roughness. The total energy of the system is affected by the physical processes via energy production and dissipation terms. The results of the energy analysis are consistent with the results of the neutral curves for both shear-thinning and shear- thickening fluids. Overall, the effect of both shear-thinning and shear- thickening fluids have revealed that radially-anisotropic roughness (radial grooves) and isotropic roughness acts to reduce energy production of the Type I mode for both fluids. This is a stabilisation effect on the Type I mode which is the opposite effect of azimuthally-anisotropic roughness on Type II mode.

Chapter 7

Conclusion and Future work

This thesis is concerned with the convective instability of the boundary-layer flow over rough rotating disks for a category of non-Newtonian fluids, abiding by the generalised viscosity law due to the Carreau model. A detailed summary and conclusions drawn from the results of each investigation can be found at the end of each chapter. However, in Section (7.1) reviews key findings results and makes some general conclusions, while Section (7.2) provides suggestions for further areas for research in the light of this thesis.

7.1 *Completed work*

This thesis investigates the effects of surface roughness on the convective instability characteristics of a generalised Newtonian fluid, modelled as a Carreau fluid. The non-Newtonian flows rotating boundary-layer flows study by Griffiths for the Carreau model [42] is combined with the effects of surface roughness. The viscosity function of Carreau fluids is controlled by two parameters, n and the relaxation parameter k. The partial-slip boundary conditions have been used under the MW approach with modifications to model a rotating disk with radially anisotropic, azimuthally anisotropic and isotropic surface roughness. The problem has been formulated in a rotating reference frame attached to the disk surface, where all disturbances are assumed to be stationary in this frame; that is, disturbances are fixed in place by the roughness and rotate with the disk. Besides, the boundary-layer approximation is applied to

the Navier-Stokes equations in order to construct the governing leading order equations. The non-dimensionalised governing continuity and boundary-layer equations are solved to obtain the solutions of steady mean of flows.

Furthermore, the mean flow profiles are obtained for the Carreau model with the different types of roughness imposed. Moreover, mean flow profiles have been computed for a range of shear-thinning and -thickening flows over the three surface conditions. The numerical results show that radially anisotropic roughness has an opposite effect on the mean flows to azimuthally anisotropic roughness in the sense that it increases the magnitudes of the axial flow and also increases the magnitudes of the radial and wall jets as λ is increased. Furthermore, the effects of isotropic roughness on the properties of mean flow components U, V, W are similar to the effects observed in the radially anisotropic roughness despite being less pronounced. Also, the effects of the isotropic roughness can be seen as a combination of the effects of radial and concentric grooves.

A subsequent linear stability analysis is then performed on each roughness model to solve the eigenvalue problem with a collocation approach based on Chebychev polynomials. Neutral curves have been calculated that prescribe the parameter regions for instability. Also, critical values of the Reynolds number, spiral vortex number and spiral vortex orientation angles have been computed. Two approaches to modelling the effects of surface roughness have been considered for each roughness type, in contrast to the current literature. The first approach aims to impose a partial-slip boundary conditions on the steady flow only (consistent with Cooper *et al.* [35] and Garrett *et al.* [36]). The second imposes the partial-slip approach to both the steady flow and perturbations. The literature argues that the first approach avoids double counting the effects of roughness, but this approach has recently received some criticism (Garrett, private communication).

Consistent with the von Kármán Newtonian boundary-layer flow over smooth surfaces, the non-Newtonian flow over rough surfaces (under both approaches) exhibits two types of instability: the Type I mode originating inviscid effects, and the Type II mode of viscous effects. It is found that the introduction of surface roughness has an obvious stabilising effect on both shear-thinning and -thickening flows in general. Each of the three types of surface roughness considered here postpone the onset of the Type I instability by increasing the critical Reynolds number, and both isotropic and azimuthally-anisotropic surface roughness (concentric grooves) entirely eliminates the Type II mode instability. The effects of radially anisotropic roughness (radial grooves) on the convective instability of stationary disturbances demonstrate a strong stabilising effect on the Type I instability mode in terms of the critical Reynolds number for the

onset of the convective instability for both $n = 0.9$ and $n = 1.1$. However, the Type II mode has a slight destabilising effect as this type of roughness level increases and becomes dominate for sufficiently high levels of radially anisotropic roughness.

Furthermore, the effects of roughness have been considered for shear-thinning when $n < 1$ and shear-thickening $n > 1$ flows. Moreover, the neutral curves have a strong stabilising effect on both the Type I and Type II instabilities. Moreover, the Type I and Type II critical Reynolds numbers decrease, indicating an advanced onset of convective instability. The area encompassed by the neutral curves is increased. For the number of the vortices $\bar{n}$ and the vortex angle ϕ we have seen that increased surface roughness acts to increase both of them and this is more noticeable on the upper-branch modes.

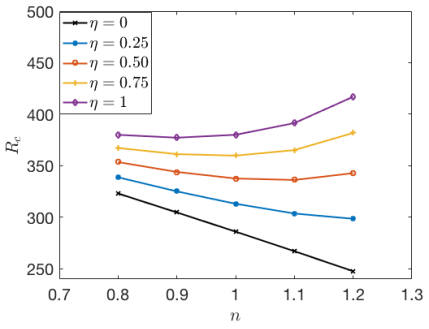

(a) Radial grooves.

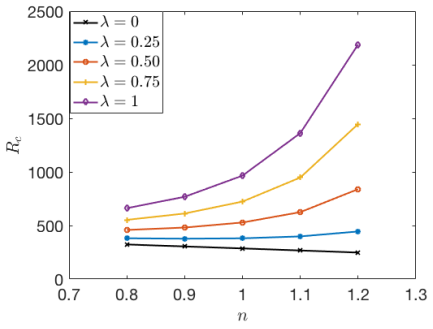

(b) Concentric grooves.

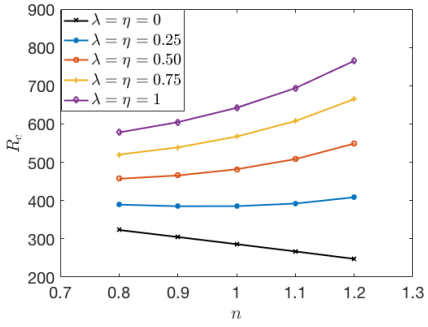

(c) Isotropic case.

Figure 7.1: Plot of the type I critical Reynolds number versus various values of n, (a) radial grooves, (b) concentric grooves, and (c) isotropic roughness.

Figure (7.1) shows a range of roughness values with their associated type I critical Reynolds numbers at various roughness values and different values of power-index. The figures from (a)-(c) reveal high values of the critical Reynolds

number as all roughness levels and power-indices are increased for all shear-thinning and shear-thickening. Furthermore, we notice that increasing both η and n in (7.1) (a) indicate a lower value of the critical Reynolds number than those seen in (7.1) (b) and (c). Thus, the concentric grooves case has a strong stabilising effect than the radial grooves and the isotropic roughness cases for this mode as evidence in this figure.

Also, isotropic roughness has a strong stabilising effect on the Type I and Type II modes in terms of postponing their onset. Furthermore, it is observed that increased surface roughness acts to increase the number of vortices along the upper branch for both of n. However, increasing the values of roughness, $\lambda = \eta$, acts to reduce the value of the vortex angle ϕ along both branches. The critical Reynolds numbers, the number of vortices and the vortex angle of shear-thinning and shear-thickening are presented for the onset of both modes.

The growth rates of the dominant instability mode have been considered at a fixed distance into the neutral curve and a complementary energy analysis is completed. The energy balance of terms for the system of flows are calculated for the Type I mode at the location of maximum amplification at $Re = Re_c+25$ for each surface roughness type. The behaviour of the energy balance terms are qualitatively consistent with the neutral curve behaviours for the entire chapters. So, the energy analysis has revealed that radially-anisotropic roughness and isotropic roughness act to reduce energy production of the Type I mode for both fluids. This is a stabilisation effect on the Type I mode that is reversed by azimuthally-anisotropic roughness. This has a destabilisation effect on the Type I mode.

The response of the instability modes to the change in the shear-thinning and -thickening properties of the fluid is more subtle. For both isotropic and azimuthally anisotropic surface roughness, there appears to be a particular value of $n > 1$ (that is, shear-thickening fluid) that gives the minimum critical Reynolds number. Any changes to n either side of this lead to delayed instability, with particular sensitivity observed for shear-thinning fluids. The maximum growth rates within the unstable regime are found to reduce linearly with increasingly shear-thinning fluids. In contrast, shear-thickening fluids are more stable for radially anisotropic roughness in terms of both the delayed onset of instability and its subsequent linear growth.

These qualitative effects are seen under both approaches to modelling roughness but quantitative differences are found after incorporating partial slip in the perturbation equations. The effects of roughness within partial-slip conditions added to the purturbation equations for the isotropic and the azimuthally anisotropic roughness are able to increase the critical Re and reduce the amplitudes of both the Type I and II modes and this is in a similar way to

that observed by [35] and [36] but it is more obvious for this method. Overall, isotropic surface roughness is seen to have the most significant effect on delaying the onset of convective instability at all values n and this is supported by the growth rate of the most dangerous Type I modes. Therefore, Moreover, adding the MW model to the perturbation equations help to delay the transition from laminar to turbulence for the Carreau mdoel. This means these fluids led to reduce skin-friction drag in enclosed rotor-stator devices observed in rotor-stator type engineering applications. Therefore, it is the most effective type of distributed surface roughness discussed in this thesis and is used as a passive-drag reduction mechanism. These results allow us to be confident in our conclusions about the stabilising effects of roughness on the convective instabilities within the boundary layer for Type I for the isotropic case.

7.2 *Future work*

There are numerous additional research areas that could be explored following the work published here. In view of the results of the current theoretical study, it will be instructive to conduct relevant experiments to verify the analyses presented here and shed light on the appropriate approach to incorporating partial-slip in the perturbing quantities. For the non-Newtonian rotating disk flows, linear stability analysis for power-law model [22] could be investigated, as we have done in chapters (3), (4), (5) and (6). The convective instability characteristics of the BEK system of flows using a linear approach with the parallel flow approximation for both power-law and Carreau fluids is another potential research area. Each chapter could also be extended by considering the travelling convective instability modes following the study of [35]. Studying non-stationary modes would then permit a study the absolute instability, following the approach introduced by Lingwood [60]. Of additional interest would be an investigation of different model of effects roughness on the Carreau flows using the approaches developed by, for example, the YHP model [34] (a MATLAB code is done for this model see Appendix (E.1)).

Another possible area of future work would be to consider the effects of the surface roughness for other two-dimensional or three-dimensional boundary-layer flows such as those over a rotating sphere. Recently, Segalini & Garrett [61] presented a new solution for the steady boundary layer flow over a rotating sphere that includes the boundary layer eruption at the equator. Thus, the effects of surface roughness using the MW model [33] and the YHP model [34] could be incorporated as an extension to this work. Moreover, the effects on

non-parallel mean-flows could be investigated following the work by Davies and Carpenter [62] for von Kármán. Additionally, the solution for the steady three-dimensional boundary layer Newtonian flow over a rotating sphere is presented taking into account the surface roughness using the MW model (see Appendix (E.2)). This helps to study the disturbance eigenfunctions and plot curves showing neutral stability. Furthermore, the asymptotic linear stability analysis could also be conducted to confirm the results in the limit of high Reynolds number behaviour.

Appendices

Appendix A

Radially-anisotropic roughness

A.1 Additional mean flow figures

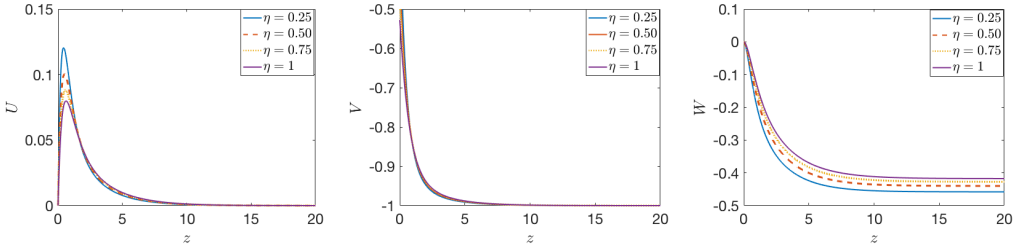

(a) (b) (c)

Figure A.1: Mean flow components of the Carreau flow in the case of radially anisotropic roughness $n = 0.6$.

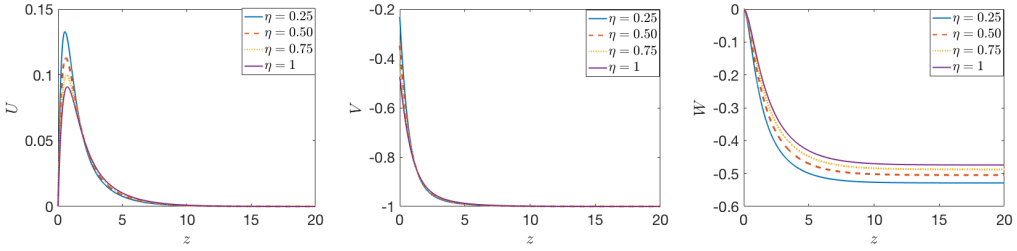

(a) (b) (c)

Figure A.2: Mean flow components of the Carreau flow in the case of radially anisotropic roughness $n = 0.7$.

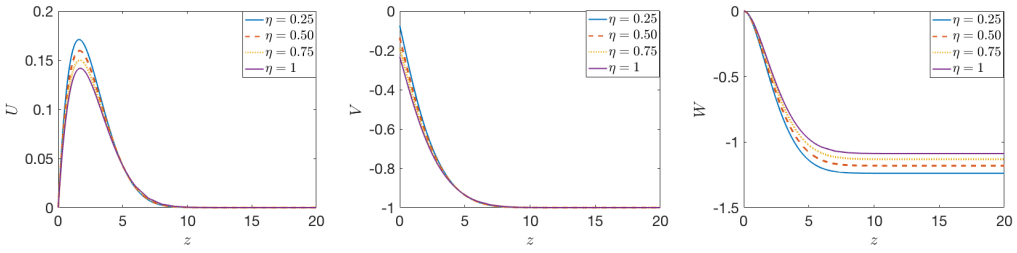

(a) (b) (c)

Figure A.3: Mean flow components of the Carreau flow in the case of radially anisotropic roughness $n = 1.3$.

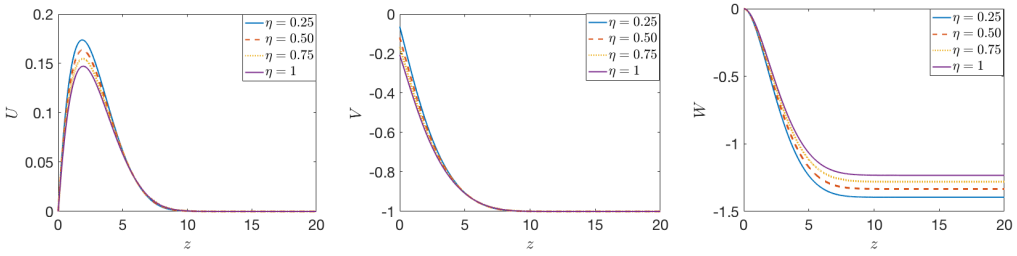

(a) (b) (c)

Figure A.4: Mean flow components of the Carreau flow in the case of radially anisotropic roughness $n = 1.4$.

A.2 Additional mean flow data

Table A.1: Numerical values of the mean velocity flow parameters $U'(0)$, $V'(0)$ and $W(z_\infty)$ for shear-thinning fluid $n = 0.6$.

Parameters	$U'(0)$	$-V'(0)$	$-W(z_\infty)$
$\eta = 0.25$	0.8295	0.2862	0.4581
$\eta = 0.50$	0.5882	0.4059	0.4400
$\eta = 0.75$	0.4618	0.4779	0.4274
$\eta = 1$	0.3826	0.5278	0.4175

Table A.2: Numerical values of the mean velocity flow parameters $U'(0)$, $V'(0)$ and $W(z_\infty)$ for shear-thinning fluid $n = 0.7$.

Parameters	$U'(0)$	$-V'(0)$	$-W(z_\infty)$
$\eta = 0.25$	0.7028	0.2320	0.5285
$\eta = 0.50$	0.5268	0.3478	0.5047
$\eta = 0.75$	0.4260	0.4218	0.4875
$\eta = 1$	0.3597	0.4747	0.4740

Table A.3: Numerical values of the mean velocity flow parameters $U'(0)$, $V'(0)$ and $W(z_\infty)$ for shear-thickening fluid $n = 1.3$.

Parameters	$U'(0)$	$-V'(0)$	$-W(z_\infty)$
$\eta = 0.25$	0.2603	0.0744	1.2382
$\eta = 0.50$	0.2380	0.1361	1.1807
$\eta = 0.75$	0.2194	0.1882	1.1311
$\eta = 1$	0.2037	0.2330	1.0877

Table A.4: Numerical values of the mean velocity flow parameters $U'(0)$, $V'(0)$ and $W(z_\infty)$ for shear-thickening fluid $n = 1.4$.

Parameters	$U'(0)$	$-V'(0)$	$-W(z_\infty)$
$\eta = 0.25$	0.2265	0.0639	1.3948
$\eta = 0.50$	0.2101	0.1185	1.3337
$\eta = 0.75$	0.1961	0.1659	1.2801
$\eta = 1$	0.1839	0.2075	1.2325

A.3 Additional neutral stability figures

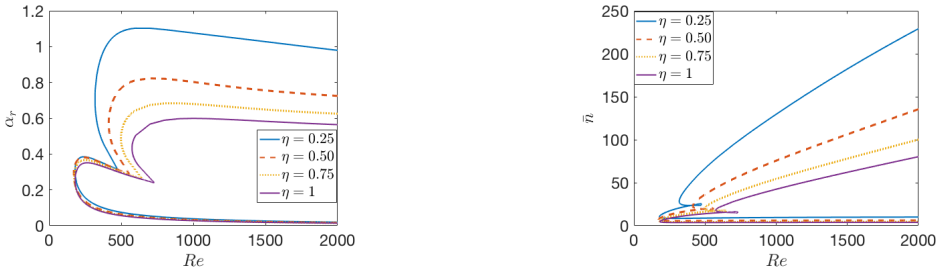

(a) (b)

Figure A.5: Neutral curves for the Carreau flow over radially anisotropic roughness with $n = 0.6$.

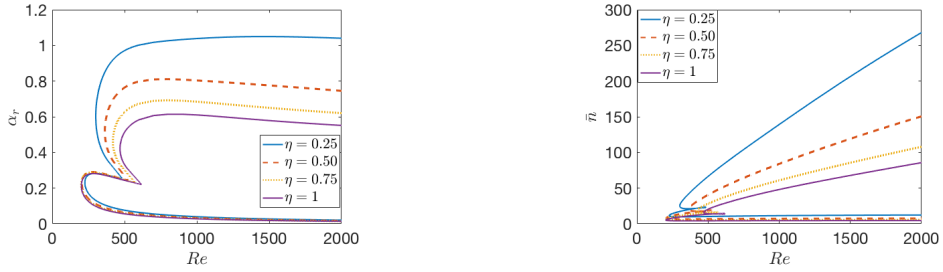

(a) (b)

Figure A.6: Neutral curves for the Carreau flow over radially anisotropic roughness with $n = 0.7$.

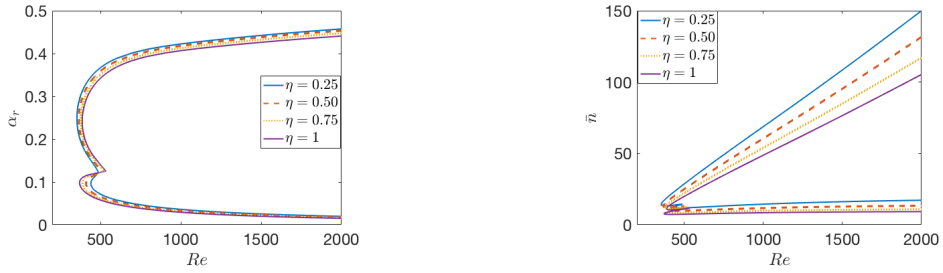

(a) (b)

Figure A.7: Neutral curves for the Carreau flow over radially anisotropic roughness with $n = 1.3$.

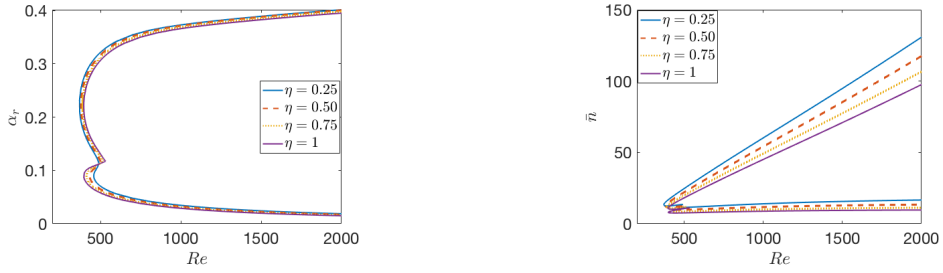

(a) (b)

Figure A.8: Neutral curves for the Carreau flow over radially anisotropic roughness with $n = 1.4$.

A.4 Additional critical values data

Table A.5: The values of the critical Reynolds number Re and $\bar{n}$ on the both modes type I and (type II) for $n = 0.6$.

Parameters	Re	$\bar{n}$
$\eta = 0.25$	318.02(179.07)	28.43(10.47)
$\eta = 0.50$	413.43(171.30)	22.89(7.16)
$\eta = 0.75$	497.97(174.52)	19.99(5.69)
$\eta = 1$	574.63(180.22)	13.94(4.85)

Table A.6: The values of the critical Reynolds number Re and $\bar{n}$ on the both modes type I and (type II) for $n = 0.7$.

Parameters	Re	$\bar{n}$
$\eta = 0.25$	300.92(225.32)	25.22(11.47)
$\eta = 0.50$	363.69(204.07)	20.64(7.90)
$\eta = 0.75$	418.84(200.14)	17.97(6.27)
$\eta = 1$	468.54(201.09)	16.18(5.30)

Table A.7: The values of the critical Reynolds number Re and $\bar{n}$ on the both modes type I and (type II) for $n = 1.3$.

Parameters	Re	$\bar{n}$
$\eta = 0.25$	353.57(439.48)	14.32(12.40)
$\eta = 0.50$	365.24(409.57)	13.14(10.34)
$\eta = 0.75$	376.22(386.81)	12.19(8.88)
$\eta = 1$	386.56(369.58)	11.41(7.81)

Table A.8: The values of the critical Reynolds number Re and $\bar{n}$ on the both modes type I and (type II) for $n = 1.4$.

Parameters	Re	$\bar{n}$
$\eta = 0.25$	369.13(458.03.03)	13.41(12.02)
$\eta = 0.50$	378.49(433.35)	12.43(10.30)
$\eta = 0.75$	387.40(412.73)	11.65(9.02)
$\eta = 1$	395.90(396.01)	10.98(8.04)

Appendix B

Azimuthally-anisotropic roughness

B.1 Additional mean flow figures

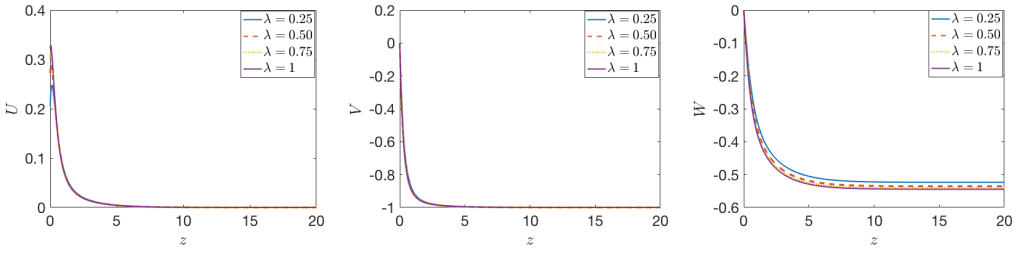

(a) (b) (c)

Figure B.1: Mean flow components of the Carreau flow in the case of azimuthally anisotropic roughness $n = 0.6$.

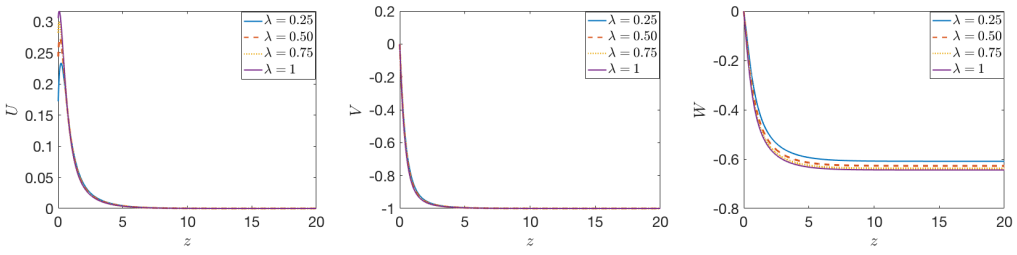

(a) (b) (c)

Figure B.2: Mean flow components of the Carreau flow in the case of azimuthally anisotropic roughness $n = 0.7$.

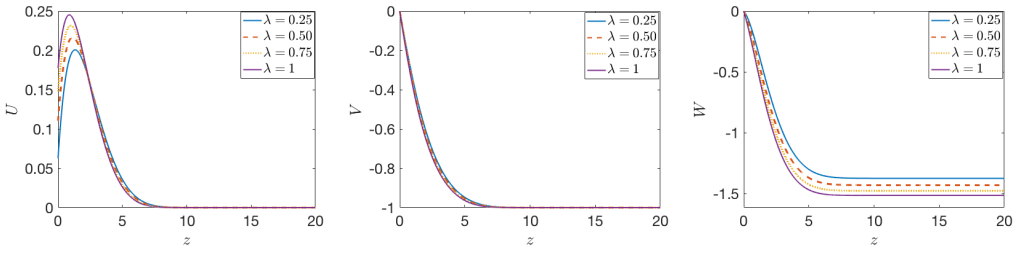

(a) (b) (c)

Figure B.3: Mean flow components of the Carreau flow in the case of azimuthally anisotropic roughness $n = 1.3$.

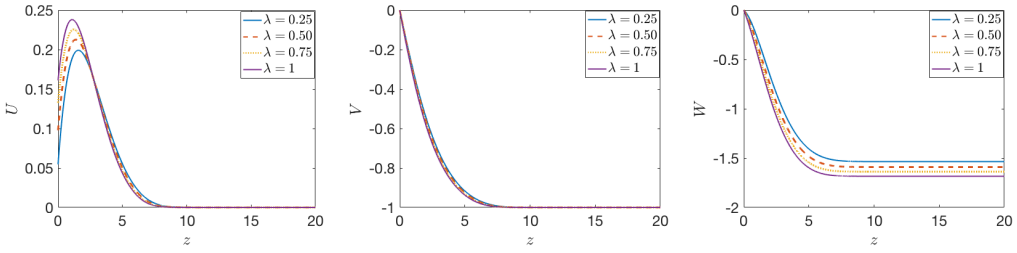

(a) (b) (c)

Figure B.4: Mean flow components of the Carreau flow in the case of azimuthally anisotropic roughness $n = 1.4$.

B.2 Additional mean flow data

Table B.1: Numerical values of the mean velocity flow parameters $U'(0)$, $V'(0)$ and $W(z_\infty)$ for shear-thinning fluid $n = 0.6$.

Parameters	$U'(0)$	$-V'(0)$	$-W(z_\infty)$
$\lambda = 0.25$	0.8197	2.9150	0.5237
$\lambda = 0.50$	0.5440	3.1684	0.5356
$\lambda = 0.75$	0.4053	3.2903	0.5414
$\lambda = 1$	0.3226	3.3615	0.5448

Table B.2: Numerical values of the mean velocity flow parameters $U'(0)$, $V'(0)$ and $W(z_\infty)$ for shear-thinning fluid $n = 0.7$.

Parameters	$U'(0)$	$-V'(0)$	$-W(z_\infty)$
$\lambda = 0.25$	0.6882	1.9151	0.6087
$\lambda = 0.50$	0.4880	2.0962	0.6275
$\lambda = 0.75$	0.3762	2.1922	0.6377
$\lambda = 1$	0.3056	2.2510	0.6441

Table B.3: Numerical values of the mean velocity flow parameters $U'(0)$, $V'(0)$ and $W(z_\infty)$ for shear-thickening fluid $n = 1.3$.

Parameters	$U'(0)$	$-V'(0)$	$-W(z_\infty)$
$\lambda = 0.25$	0.2508	0.3672	1.3743
$\lambda = 0.50$	0.2211	0.3948	1.4306
$\lambda = 0.75$	0.1971	0.4156	1.4767
$\lambda = 1$	0.1776	0.4317	1.5148

Table B.4: Numerical values of the mean velocity flow parameters $U'(0)$, $V'(0)$ and $W(z_\infty)$ for shear-thickening fluid $n = 1.4$.

Parameters	$U'(0)$	$-V'(0)$	$-W(z_\infty)$
$\lambda = 0.25$	0.2185	0.3057	1.5354
$\lambda = 0.50$	0.1957	0.3269	1.5906
$\lambda = 0.75$	0.1767	0.3434	1.6377
$\lambda = 1$	0.1611	0.3566	1.6836

B.3 Additional neutral stability figures

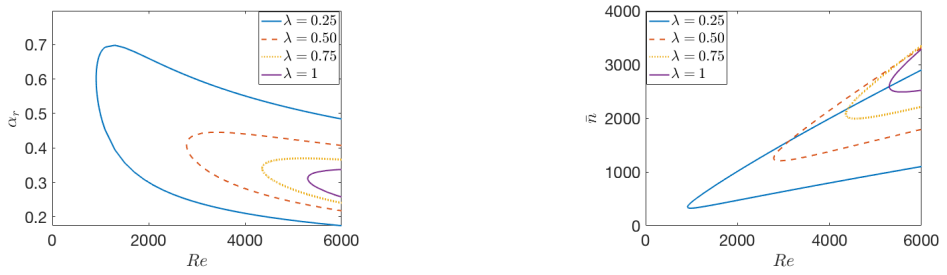

(a) (b)

Figure B.5: Neutral curves for the Carreau flow over azimuthally anisotropic roughness with $n = 0.6$.

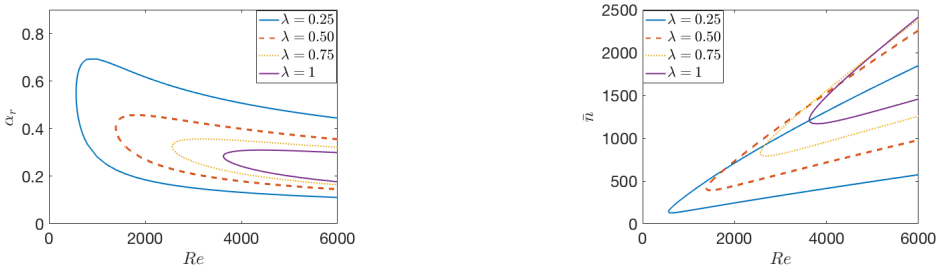

(a) (b)

Figure B.6: Neutral curves for the Carreau flow over azimuthally anisotropic roughness with $n = 0.7$.

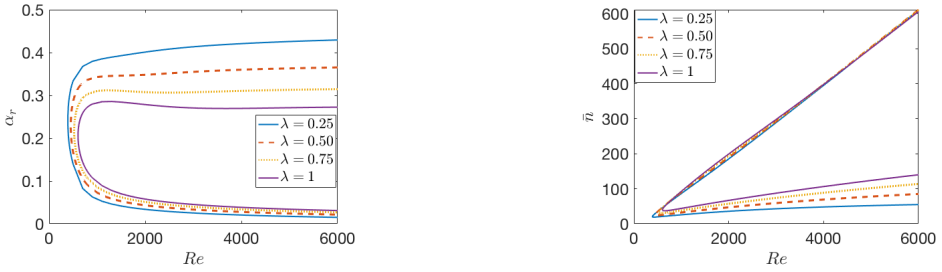

(a) (b)

Figure B.7: Neutral curves for the Carreau flow over azimuthally anisotropic roughness with $n = 1.3$.

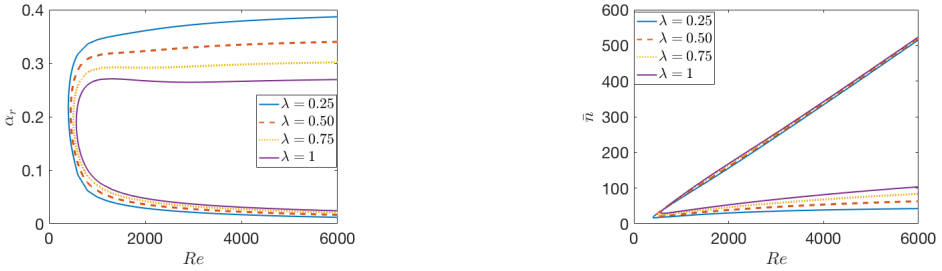

(a) (b)

Figure B.8: Neutral curves for the Carreau flow over azimuthally anisotropic roughness with $n = 1.4$.

B.4 Additional critical values data

Table B.5: The values of the critical Reynolds number Re and $\bar{n}$ on the both modes type I and (type II) for $n = 0.6$.

Parameters	Re	$\bar{n}$
$\lambda = 0.25$	911.48(−)	363.46(−)
$\lambda = 0.50$	2786.69(−)	1256.07(−)
$\lambda = 0.75$	4353.07(−)	2076.82(−)
$\lambda = 1$	5298.69(−)	2596.93(−)

Table B.6: The values of the critical Reynolds number Re and $\bar{n}$ on the both modes type I and (type II) for $n = 0.7$.

Parameters	Re	$\bar{n}$
$\lambda = 0.25$	561.46(−)	141.11(−)
$\lambda = 0.50$	1387.15(−)	412.35(−)
$\lambda = 0.75$	2561.46(−)	825.41(−)
$\lambda = 1$	3624.93(−)	1216.30(−)

Table B.7: The values of the critical Reynolds number Re and $\bar{n}$ on the both modes type I and (type II) for $n = 1.3$.

Parameters	Re	$\bar{n}$
$\lambda = 0.25$	389.02(−)	20.48(−)
$\lambda = 0.50$	449.69(−)	26.10(−)
$\lambda = 0.75$	520.93(−)	32.60(−)
$\lambda = 1$	601.46(−)	39.93(−)

Table B.8: The values of the critical Reynolds number Re and $\bar{n}$ on the both modes type I and (type II)for $n = 1.4$.

Parameters	Re	$\bar{n}$
$\lambda = 0.25$	399.88(−)	18.03(−)
$\lambda = 0.50$	448.35(−)	21.90(−)
$\lambda = 0.75$	503.82(−)	26.33(−)
$\lambda = 1$	565.98(−)	31.26(−)

Appendix C

Isotropic roughness

C.1 Additional mean flow figures

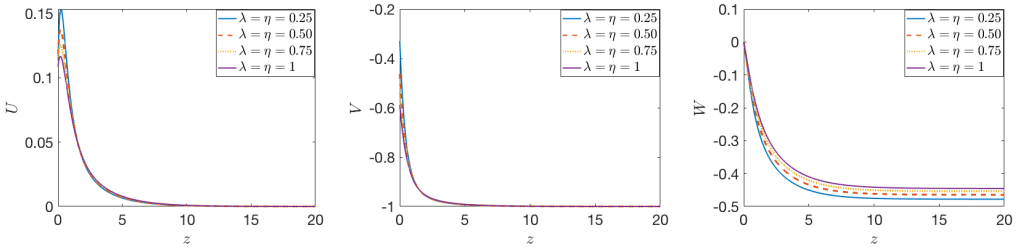

(a) (b) (c)

Figure C.1: Mean flow components of the Carreau flow in the case of isotropic roughness $n = 0.6$.

roughness

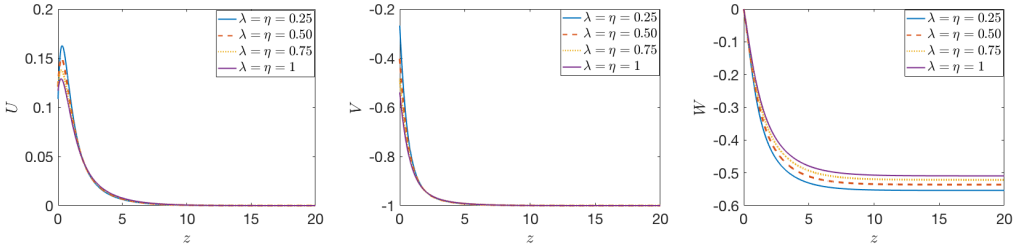

(a) (b) (c)

Figure C.2: Mean flow components of the Carreau flow in the case of isotropic roughness $n = 0.7$.

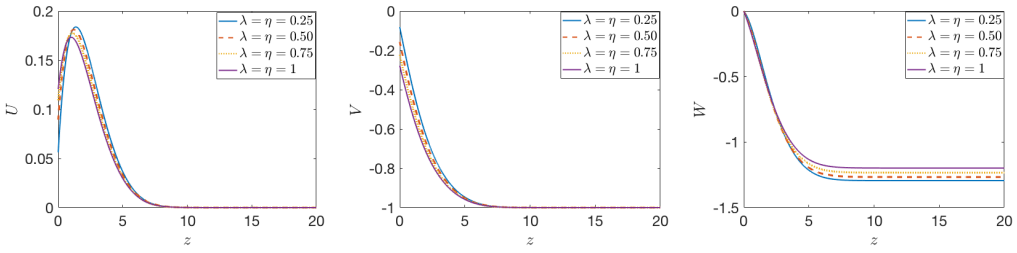

(a) (b) (c)

Figure C.3: Mean flow components of the Carreau flow in the case of isotropic roughness $n = 1.3$.

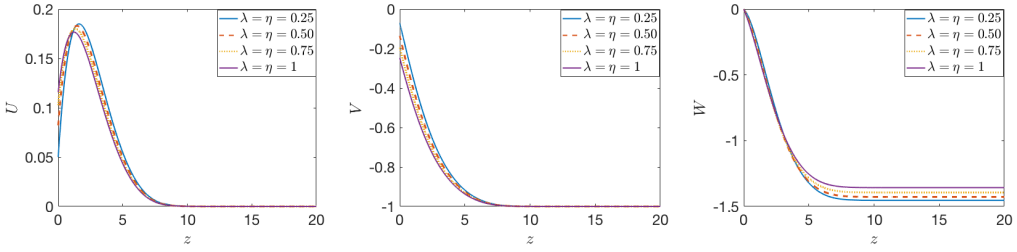

(a) (b) (c)

Figure C.4: Mean flow components of the Carreau flow in the case of isotropic roughness $n = 1.4$.

C.2 Additional mean flow data

Table C.1: Numerical values of the mean velocity flow parameters $U'(0)$, $V'(0)$ and $W(z_\infty)$ for shear-thinning fluid $n = 0.6$.

Parameters	$U'(0)$	$-V'(0)$	$-W(z_\infty)$
$\lambda = \eta = 0.25$	0.4541	1.3161	0.4779
$\lambda = \eta = 0.50$	0.2366	0.9262	0.4645
$\lambda = \eta = 0.75$	0.1519	0.7190	0.4540
$\lambda = \eta = 1$	0.1085	0.5900	0.4454

Table C.2: Numerical values of the mean velocity flow parameters $U'(0)$, $V'(0)$ and $W(z_\infty)$ for shear-thinning fluid $n = 0.7$.

Parameters	$U'(0)$	$-V'(0)$	$-W(z_\infty)$
$\lambda = \eta = 0.25$	0.4341	1.0705	0.5537
$\lambda = \eta = 0.50$	0.2432	0.8043	0.5361
$\lambda = \eta = 0.75$	0.1610	0.6449	0.5214
$\lambda = \eta = 1$	0.1169	0.5396	0.5093

Table C.3: Numerical values of the mean velocity flow parameters $U'(0)$, $V'(0)$ and $W(z_\infty)$ for shear-thickening fluid $n = 1.3$.

Parameters	$U'(0)$	$-V'(0)$	$-W(z_\infty)$
$\lambda = \eta = 0.25$	0.2251	0.3277	1.2939
$\lambda = \eta = 0.50$	0.1791	0.3140	1.2665
$\lambda = \eta = 0.75$	0.1455	0.2964	1.2331
$\lambda = \eta = 1$	0.1206	0.2784	1.1981

Table C.4: Numerical values of the mean velocity flow parameters $U'(0)$, $V'(0)$ and $W(z_\infty)$ for shear-thickening fluid $n = 1.4$.

Parameters	$U'(0)$	$-V'(0)$	$-W(z_\infty)$
$\lambda = \eta = 0.25$	0.2000	0.2789	1.4539
$\lambda = \eta = 0.50$	0.1644	0.2714	1.4276
$\lambda = \eta = 0.75$	0.1370	0.2601	1.3938
$\lambda = \eta = 1$	0.1158	0.2476	1.3573

C.3 Additional neutral stability figures

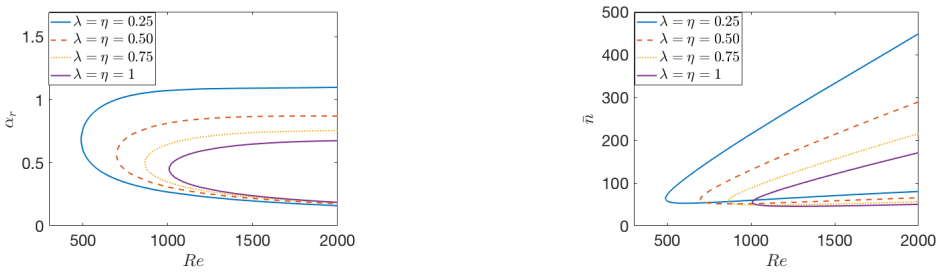

(a) (b)

Figure C.5: Neutral curves for the Carreau flow isotropic roughness with $n = 0.6$.

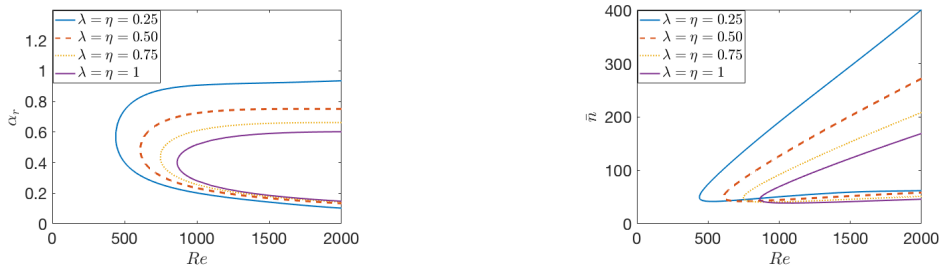

(a) (b)

Figure C.6: Neutral curves for the Carreau flow over isotropic roughness with $n = 0.7$.

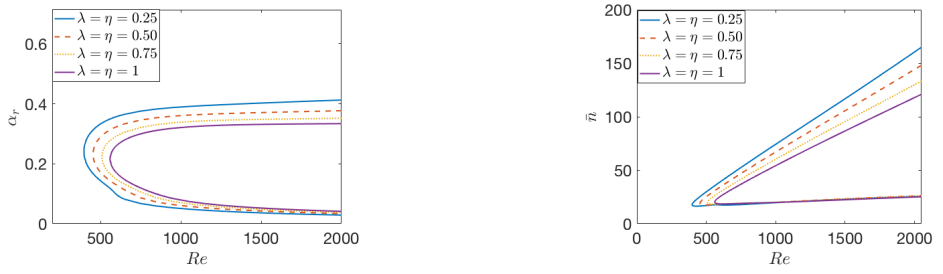

(a) (b)

Figure C.7: Neutral curves for the Carreau flow over isotropic roughness with $n = 1.3$.

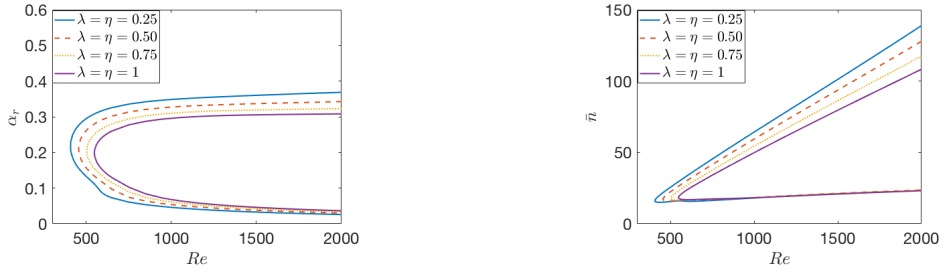

(a) (b)

Figure C.8: Neutral curves for the Carreau flow isotropic roughness with $n = 1.4$.

C.4 Additional critical values data

Table C.5: The values of the critical Reynolds number Re and $\bar{n}$ on the both modes type I and (type II) for $n = 0.6$.

Parameters	Re	$\bar{n}$
$\lambda = \eta = 0.25$	488.90(−)	64.14(−)
$\lambda = \eta = 0.50$	697.52(−)	61.87(−)
$\lambda = \eta = 0.75$	864.61(−)	58.53(−)
$\lambda = \eta = 1$	1007.61(−)	55.07(−)

Table C.6: The values of the critical Reynolds number Re and $\bar{n}$ on the both modes type I and (type II) for $n = 0.7$.

Parameters	Re	$\bar{n}$
$\lambda = \eta = 0.25$	438.48(−)	49.88(−)
$\lambda = \eta = 0.50$	608.58(−)	50.41(−)
$\lambda = \eta = 0.75$	746.33(−)	48.50(−)
$\lambda = \eta = 1$	863.59(−)	46.25(−)

Table C.7: The values of the critical Reynolds number Re and $\bar{n}$ on the both modes type I and (type II) for $n = 1.3$.

Parameters	Re	$\bar{n}$
$\lambda = \eta = 0.25$	397.05(−)	17.88(−)
$\lambda = \eta = 0.50$	454.17(−)	19.21(−)
$\lambda = \eta = 0.75$	508.78(−)	20.02(−)
$\lambda = \eta = 1$	559.59(−)	20.39(−)

Table C.8: The values of the critical Reynolds number Re and $\bar{n}$ on the both modes type I and (type II) for $n = 1.4$.

Parameters	Re	$\bar{n}$
$\lambda = \eta = 0.25$	407.01(−)	16.16(−)
$\lambda = \eta = 0.50$	455.79(−)	17.25(−)
$\lambda = \eta = 0.75$	503.25(−)	17.99(−)
$\lambda = \eta = 1$	547.98(−)	18.41(−)

Appendix D

Shear-thinning and -thickening

D.1 Additional mean flow figures

D.1.1 Radially-anisotropic roughness

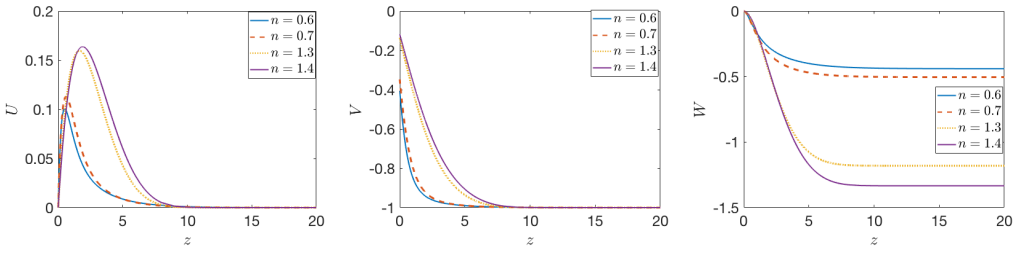

(a) (b) (c)

Figure D.1: Mean flow components of the Carreau flow for shear-thinning and -thickening fluids with $\eta = 0.50$, $\lambda = 0$.

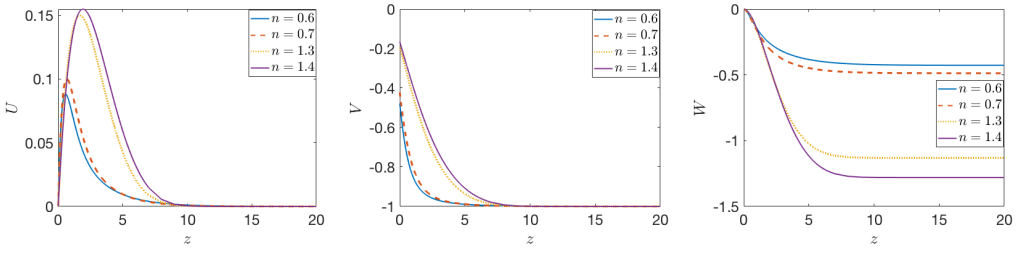

(a) (b) (c)

Figure D.2: Mean flow components of the Carreau flow for shear-thinning and -thickening fluids with $\eta = 0.75$, $\lambda = 0$.

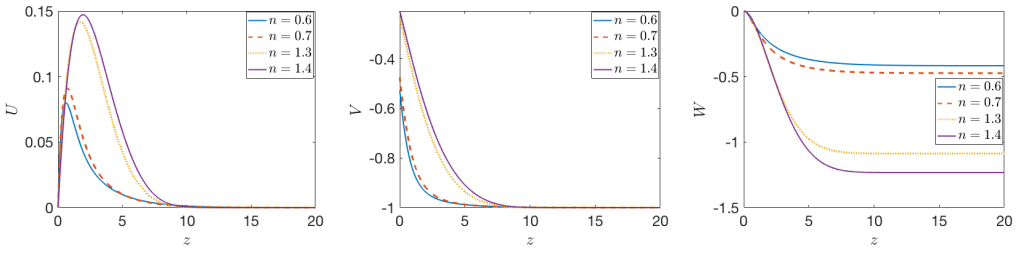

(a) (b) (c)

Figure D.3: Mean flow components of the Carreau flow for shear-thinning and -thickening fluids with $\eta = 1$, $\lambda = 0$.

D.1.2 Azimuthally-anisotropic roughness

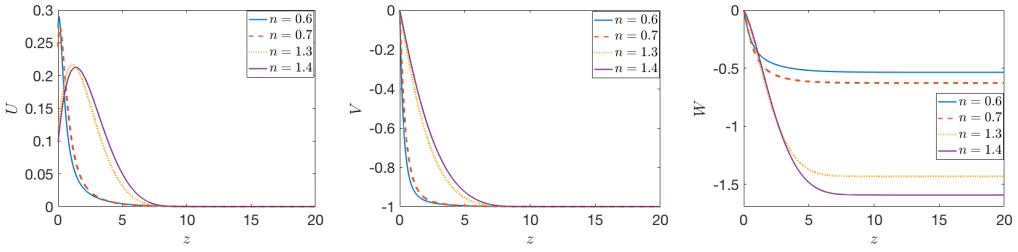

(a) (b) (c)

Figure D.4: Mean flow components of the Carreau flow for shear-thinning and -thickening fluids with $\lambda = 0.50$, $\eta = 0$.

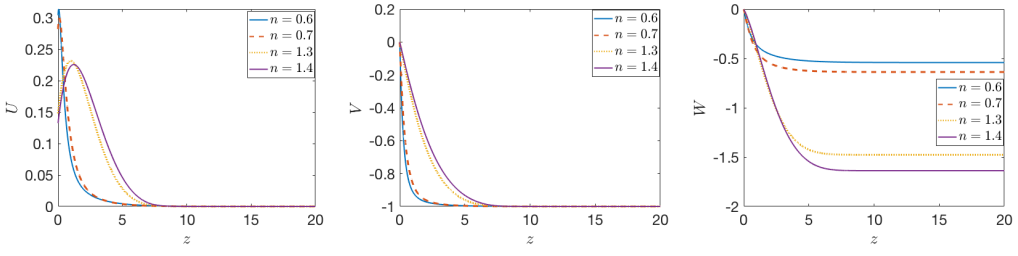

(a) (b) (c)

Figure D.5: Mean-flow components of the Carreau flow for shear-thinning and -thickening fluids with $\lambda = 0.75$, $\eta = 0$.

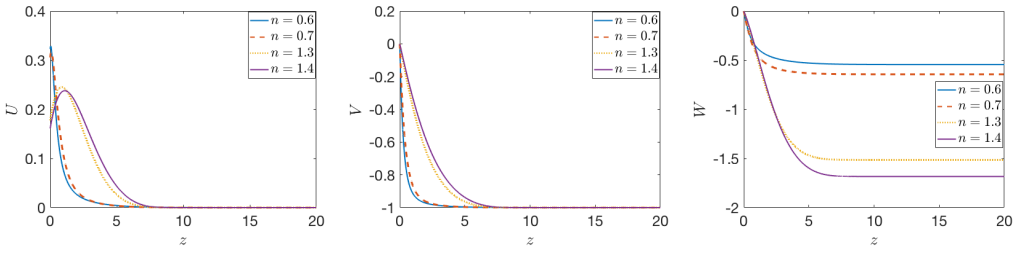

(a) (b) (c)

Figure D.6: Mean flow components of the Carreau flow for shear-thinning and -thickening fluids with $\lambda = 1$, $\eta = 0$.

D.1.3 Isotropic roughness

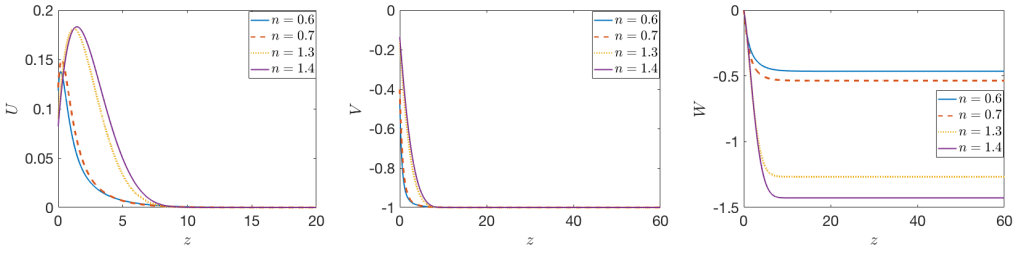

(a) (b) (c)

Figure D.7: Mean flow components of the Carreau flow for shear-thinning and -thickening fluids with $\lambda = \eta = 0.50$.

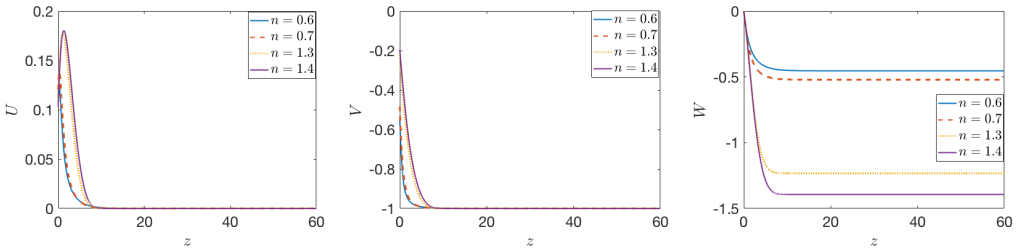

(a) (b) (c)

Figure D.8: Mean flow components of the Carreau flow for shear-thinning and -thickening fluids with $\lambda = \eta = 0.75$.

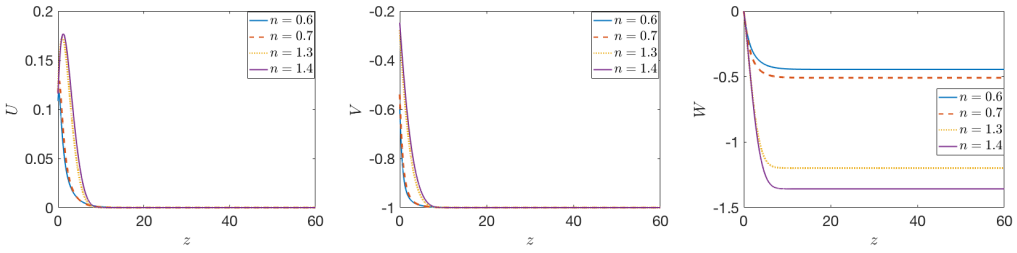

(a) (b) (c)

Figure D.9: Mean-flow components of the Carreau flow for *shear-thinning* and -*thickening* fluids with $\lambda = \eta = 1$.

D.2 Additional mean flow data

D.2.1 Radially-anisotropic roughness

Table D.1: Numerical values of the mean velocity flow parameters $U'(0)$, $V'(0)$ and $W(z_\infty)$ for $\eta = 0.50$.

Parameters	$U'(0)$	$-V'(0)$	$-W(z_\infty)$
$n = 0.6$	0.5882	0.8117	0.4400
$n = 0.7$	0.5268	0.6955	0.5047
$n = 1.3$	0.2380	0.2721	1.1807
$n = 1.4$	0.2101	0.2370	1.3337

Table D.2: Numerical values of the mean velocity flow parameters $U'(0)$, $V'(0)$ and $W(z_\infty)$ for $\eta = 0.75$.

Parameters	$U'(0)$	$-V'(0)$	$-W(z_\infty)$
$n = 0.6$	0.4618	0.6371	0.4274
$n = 0.7$	0.4260	0.5623	0.4875
$n = 1.3$	0.2194	0.2509	1.1311
$n = 1.4$	0.1961	0.2212	1.2801

Table D.3: Numerical values of the mean velocity flow parameters $U'(0)$, $V'(0)$ and $W(z_\infty)$ for $\eta = 1$.

Parameters	$U'(0)$	$-V'(0)$	$-W(z_\infty)$
$n = 0.6$	0.3826	0.5278	0.4175
$n = 0.7$	0.3597	0.4747	0.4740
$n = 1.3$	0.2037	0.2330	1.0877
$n = 1.4$	0.1839	0.2075	1.2325

D.2.2 Azimuthally-anisotropic roughness

Table D.4: Numerical values of the mean velocity flow parameters $U'(0)$, $V'(0)$ and $W(z_\infty)$ for $\lambda = 0.50$.

Parameters	$U'(0)$	$-V'(0)$	$-W(z_\infty)$
$n = 0.6$	0.5440	3.1684	0.5356
$n = 0.7$	0.4880	2.0962	0.6275
$n = 1.3$	0.2211	0.3948	1.4306
$n = 1.4$	0.1957	0.3269	1.5906

Table D.5: Numerical values of the mean velocity flow parameters $U'(0)$, $V'(0)$ and $W(z_\infty)$ for $\lambda = 0.75$.

Parameters	$U'(0)$	$-V'(0)$	$-W(z_\infty)$
$n = 0.6$	0.4053	3.2903	0.5414
$n = 0.7$	0.3762	2.1922	0.6377
$n = 1.3$	0.1971	0.4156	1.4767
$n = 1.4$	0.1767	0.3434	1.6377

Table D.6: Numerical values of the mean velocity flow parameters $U'(0)$, $V'(0)$ and $W(z_\infty)$ for $\lambda = 1$.

Parameters	$U'(0)$	$-V'(0)$	$-W(z_\infty)$
$n = 0.6$	0.3226	3.3615	0.5448
$n = 0.7$	0.3056	2.2510	0.6441
$n = 1.3$	0.1776	0.4317	1.5148
$n = 1.4$	0.1611	0.3566	1.6836

D.2.3 Isotropic roughness

Table D.7: Numerical values of the mean velocity flow parameters $U'(0)$, $V'(0)$ and $W(z_\infty)$ for $\lambda = \eta = 0.50$.

Parameters	$U'(0)$	$-V'(0)$	$-W(z_\infty)$
$n = 0.6$	0.2366	0.9262	0.4645
$n = 0.7$	0.2432	0.8043	0.5361
$n = 1.3$	0.1791	0.3140	1.2665
$n = 1.4$	0.1644	0.2714	1.4276

Table D.8: Numerical values of the mean velocity flow parameters $U'(0)$, $V'(0)$ and $W(z_\infty)$ for $\lambda = \eta = 0.75$.

Parameters	$U'(0)$	$-V'(0)$	$-W(z_\infty)$
$n = 0.6$	0.1519	0.7190	0.4540
$n = 0.7$	0.1610	0.6449	0.5214
$n = 1.3$	0.1455	0.2964	1.2331
$n = 1.4$	0.1370	0.2601	1.3938

Table D.9: Numerical values of the mean velocity flow parameters $U'(0)$, $V'(0)$ and $W(z_\infty)$ for $\lambda = \eta = 1$.

Parameters	$U'(0)$	$-V'(0)$	$-W(z_\infty)$
$n = 0.6$	0.1085	0.5900	0.4454
$n = 0.7$	0.1169	0.5396	0.5093
$n = 1.3$	0.1206	0.2784	1.1981
$n = 1.4$	0.1158	0.2476	1.3573

D.3 Additional neutral stability figures

D.3.1 Radially-anisotropic roughness

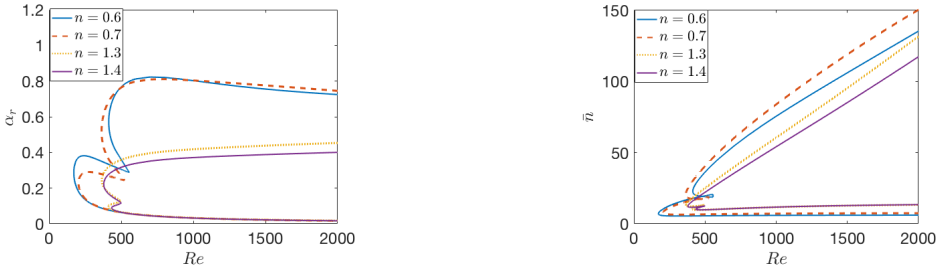

(a) (b)

Figure D.10: Neutral curves for the Carreau flow for $\eta = 0.50$.

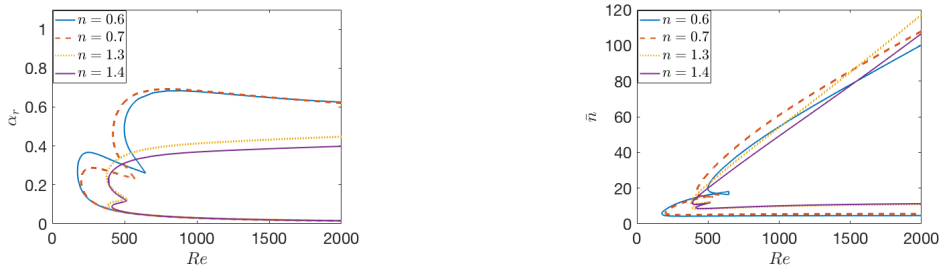

(a) (b)

Figure D.11: Neutral curves for the Carreau flow for $\eta = 0.75$.

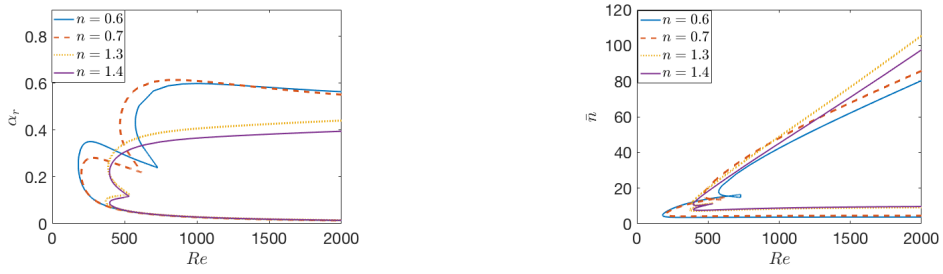

(a) (b)

Figure D.12: Neutral curves for the Carreau flow for $\eta = 1$.

D.3.2 Azimuthally-anisotropic roughness

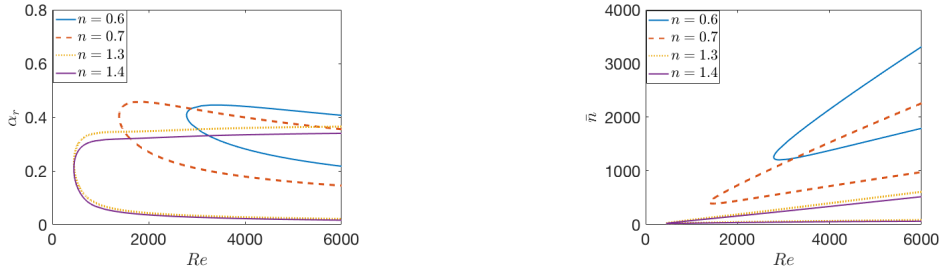

(a) (b)

Figure D.13: Neutral curves for the Carreau flow for $\lambda = 0.50$.

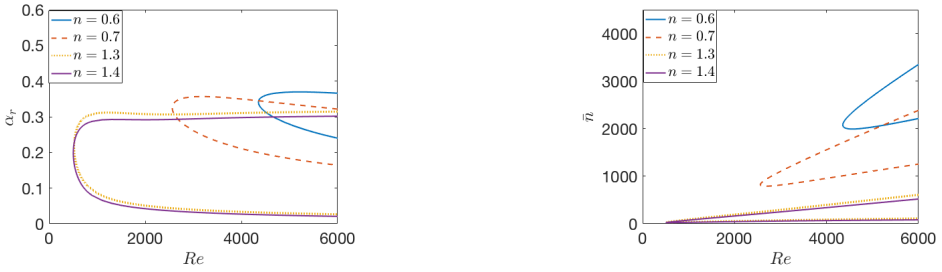

(a) (b)

Figure D.14: Neutral curves for the Carreau flow for $\lambda = 0.75$.

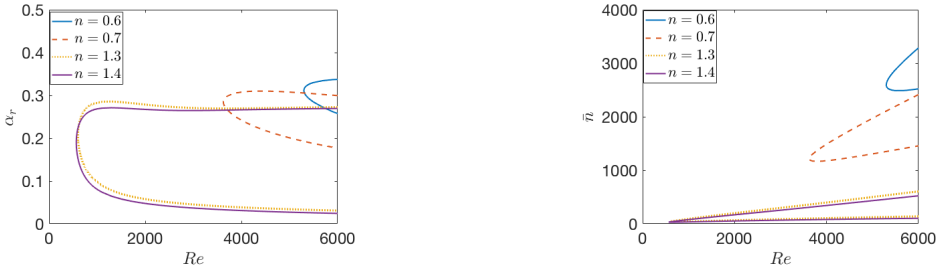

(a) (b)

Figure D.15: Neutral curves for the Carreau flow for $\lambda = 1$.

D.3.3 Isotropic roughness

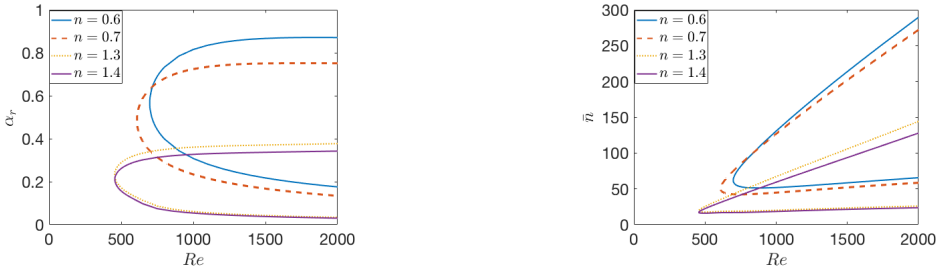

(a) (b)

Figure D.16: Neutral curves for the Carreau flow for $\lambda = \eta = 0.50$.

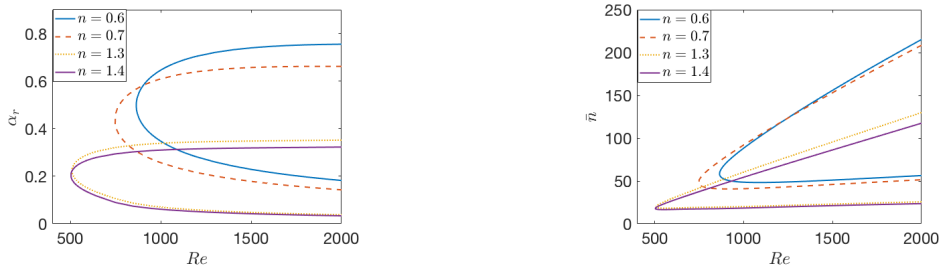

(a) (b)

Figure D.17: Neutral curves for the Carreau flow for $\lambda = \eta = 0.75$.

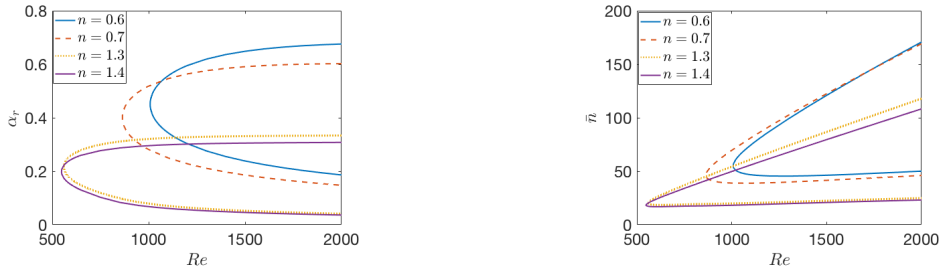

(a) (b)

Figure D.18: Neutral curves for the Carreau flow for $\lambda = \eta = 1$.

D.4 Additional critical values data

D.4.1 Radially-anisotropic roughness

Table D.10: The values of the critical Reynolds number Re and $\bar{n}$ on the both modes type I and (type II) for $\eta = 0.50$.

Parameters	Re	$\bar{n}$
$n = 0.6$	431.43(171.30)	22.89(7.16)
$n = 0.7$	363.69(204.07)	20.64(7.90)
$n = 1.3$	365.24(409.57)	13.14(10.34)
$n = 1.4$	378.40(433.35)	12.43(10.30)

Table D.11: The values of the critical Reynolds number Re and $\bar{n}$ on the both modes type I and (type II) for $\eta = 0.75$.

Parameters	Re	$\bar{n}$
$n = 0.6$	497.97(174.52)	19.99(5.69)
$n = 0.7$	418.84(200.14)	17.97(6.27)
$n = 1.3$	376.22(386.81)	12.19(8.88)
$n = 1.4$	387.40(412.73)	11.65(9.02)

Table D.12: The values of the critical Reynolds number Re and $\bar{n}$ on the both modes type I and (type II) for $\eta = 1$.

Parameters	Re	$\bar{n}$
$n = 0.6$	574.63(180.22)	18.00(4.85)
$n = 0.7$	468.54(201.09)	16.18(5.30)
$n = 1.3$	386.56(369.58)	11.41(7.81)
$n = 1.4$	395.90(396.01)	10.98(8.04)

D.4.2 Azimuthally-anisotropic roughness

Table D.13: The values of the critical Reynolds number Re and $\bar{n}$ on the both modes type I and (type II) for $\lambda = 0.50$.

Parameters	Re	$\bar{n}$
$n = 0.6$	2786.69(−)	1256.07(−)
$n = 0.7$	1387.15(−)	412.35(−)
$n = 1.3$	449.69(−)	26.10(−)
$n = 1.4$	448.35(−)	21.90(−)

Table D.14: The values of the critical Reynolds number Re and $\bar{n}$ on the both modes type I and (type II) for $\lambda = 0.75$.

Parameters	Re	$\bar{n}$
$n = 0.6$	4353.07(−)	2076.82(−)
$n = 0.7$	2561.46(−)	825.41(−)
$n = 1.3$	520.93(−)	32.60(−)
$n = 1.4$	503.82(−)	26.33(−)

Table D.15: The values of the critical Reynolds number Re and $\bar{n}$ on the both modes type I and (type II) for $\lambda = 1$.

Parameters	Re	$\bar{n}$
$n = 0.6$	5298.69(−)	2596.93(−)
$n = 0.7$	3624.93(−)	1216.30(−)
$n = 1.3$	601.46(−)	39.93(−)
$n = 1.4$	565.98(−)	31.26(−)

D.4.3 Isotropic roughness

Table D.16: The values of the critical Reynolds number Re and $\bar{n}$ on the both modes type I and (type II) for $\lambda = \eta = 0.50$.

Parameters	Re	$\bar{n}$
$n = 0.6$	697.52(−)	61.87(−)
$n = 0.7$	608.58(−)	50.41(−)
$n = 1.3$	454.17(−)	19.21(−)
$n = 1.4$	455.79(−)	17.25(−)

Table D.17: The values of the critical Reynolds number Re and $\bar{n}$ on the both modes type I and (type II) for $\lambda = \eta = 0.75$.

Parameters	Re	$\bar{n}$
$n = 0.6$	864.61(−)	58.53(−)
$n = 0.7$	746.33(−)	48.50(−)
$n = 1.3$	508.78(−)	20.02(−)
$n = 1.4$	503.25(−)	17.99(−)

Table D.18: The values of the critical Reynolds number Re and $\bar{n}$ on the both modes type I and (type II) for $\lambda = \eta = 1$.

Parameters	Re	$\bar{n}$
$n = 0.6$	10007.61(−)	55.07(−)
$n = 0.7$	863.59(−)	46.25(−)
$n = 1.3$	559.59(−)	20.39(−)
$n = 1.4$	547.98(−)	18.41(−)

Appendix E

Future work

E.1 YHP model MATLAB code

Main file:

```
clear;
clc;

a=0
gamma=0.1;
delta=gamma*a;

dr=0.001;

load('vonKarman.mat');
fr=yvK(1,:);
gr=yvK(2,:);
hr=yvK(3,:);
dfr=yvK(4,:);
dgr=yvK(5,:);
xr=xvK;

fall=[];
gall=[];
hall=[];
dfall=[];
dgall=[];
rall=[];

```

```
%xr=linspace(0,20,5000);
%fr=interp1(xvK,yvK(1,:),xr);
%gr=interp1(xvK,yvK(2,:),xr);
%hr=interp1(xvK,yvK(3,:),xr);
%dfr=interp1(xvK,yvK(4,:),xr);
%dgr=interp1(xvK,yvK(5,:),xr);

options=odeset('RelTol',1e-8,'AbsTol',1e-9);
%options=odeset('RelTol',eps,'AbsTol',1e-9);

for n=1:1:100

    r=n*dr
    solinit = bvpinit(xr,[0.1 -1 -1 0 0]);
    solinit.y=[fr; gr; hr; dfr; dgr]; % initialise the
        solution of ODE with the results from the
        previous timestep

    %sol = bvp5c(@(x,y) karmanpde(x,y,fr,gr,xr,delta,
        gamma,r,dr),@karmanbc,solinit);
    sol = bvp5c(@(x,y) karmanpde2(x,y,fr,gr,hr,dfr,dgr,
        xr,delta,gamma,r,dr),@karmanbc,solinit);

    x=linspace(0,20,2000);
    y=deval(sol,x);
    %plot(x,y(1,:));
    %hold on;

    fr=y(1,:);
    gr=y(2,:);
    hr=y(3,:);
    dfr=y(4,:);
    dgr=y(5,:);

    fall=[fall; fr];
    gall=[gall; gr];
    hall=[hall; hr];
    dfall=[dfall; dfr];
    dgall=[dgall; dgr];
    rall=[rall; r];

end
```

```
63
64 % average over r
65 fbar=[];
66 gbar=[];
67 hbar=[];
68 for m=1:1:2000
69     fbar=[fbar mean(fall(:,m))];
70     gbar=[gbar mean(gall(:,m))];
71     hbar= [hbar mean(hall(:,m))];
72 end
73 plot(xr,fbar);
74 xlabel('z');
75 ylabel('$\bar{f}$','interpreter','latex');
76 hold on;
```

YHP model PDE:

```
1  function dydx = karmanpde2(x,y,fr,gr,hr,dfr,dgr,xr,delta
       ,gamma,r,dr)
2
3  % interpolate the results from the previous step
4  f1=interp1(xr,fr,x);
5  g1=interp1(xr,gr,x);
6  h1=interp1(xr,hr,x);
7  df1=interp1(xr,dfr,x);
8  dg1=interp1(xr,dgr,x);
9
10 % roughness expression
11 s=delta*cos(2*pi*r/gamma);
12 sp=-delta*sin(2*pi*r/gamma)*(2*pi/gamma);
13 spp=-delta*cos(2*pi*r/gamma)*((2*pi/gamma)^2);
14
15 % setup of equations
16
17 eq1=-2*f1-r*(y(1)-f1)/dr;
18
19 term1=r*f1.*(y(1)-f1)/dr;
20 term2=h1.*y(4);
21 term3=(1+(r-dr)*sp*spp/(1+sp^2)).*(f1.^2);
22 term4=(1+g1).^2./(1+sp^2);
23 term5=1+sp^2;
24 eq2=(term1+term2+term3-term4)/term5;
```

```
25
26 term1=r*f1.*(y(2)-g1)/dr;
27 term2=h1.*y(5);
28 term3=2*f1.*(1+g1);
29
30 eq3=(term1+term2+term3)/term5;
31
32 dydx = [y(4); y(5); eq1; eq2; eq3];
```

Boundary conditions:

```
1 function res = karmanbc(ya,yb)
2 res = [ ya(1); ya(2); ya(3); yb(1); yb(2)+1 ];
```

E.2 Rotating-Sphere

E.2.1 Mean flow

Consider a steadily rotating sphere with angular velocity Ω in an otherwise quiescent fluid. Also, let the problem be written in a fixed reference frame in a spherical coordinate system where (r, θ, ϕ) denotes the radial, azimuthal and tangential coordinates respectively. Adopted to our reference frame let (u, v, w) denote the velocities in the θ, ϕ and r directions respectively. The flow field is assumed to spherically symmetric and (u, v, w) are independent of ϕ. This reduces the steady polar Navier-Stokes equations and incompressible continuity equation to the following form. Here all the physical quantities are scaled by the density,ρ, the angular velocity, Ω, and the sphere radius, R. The boundary layer thickness is estimated by $\epsilon \approx \nu/\omega^2 R$ where ν is the kinematic viscosity. This will introduce the small perturbation parameter of the problem, namely $\epsilon = \delta/R$. The mean-flow equations formulated as

$$\frac{\partial u}{\partial \theta} + r\frac{\partial w}{\partial r} + u\cot\theta + 2w = 0, \tag{E.1a}$$

$$\frac{u}{r}\frac{\partial u}{\partial \theta} + w\frac{\partial u}{\partial r} + \frac{1}{r}(uw - v^2\cot\theta) = -\frac{1}{r}\frac{\partial P}{\partial \theta} + \frac{1}{r^2 R_s}\left[\frac{\partial^2 u}{\partial^2 \theta} + \cot\theta\frac{\partial u}{\partial \theta} + r^2\frac{\partial^2 u}{\partial r^2} + 2r\frac{\partial u}{\partial r} + \left(2\frac{\partial w}{\partial \theta} - +2r\frac{u}{\sin^2\theta}\right)\right], \tag{E.1b}$$

$$\frac{u}{r}\frac{\partial v}{\partial \theta} + w\frac{\partial v}{\partial r} + \frac{1}{r}(vw + uv\cot\theta) = \frac{1}{r^2 R_s}\left[\frac{\partial^2 v}{\partial^2 \theta} + \cot\theta\frac{\partial v}{\partial \theta} + r^2\frac{\partial^2 v}{\partial r^2} + 2r\frac{\partial v}{\partial r} + \left(\frac{-v}{\sin^2\theta}\right)\right], \tag{E.1c}$$

$$\frac{u}{r}\frac{\partial w}{\partial \theta} + w\frac{\partial w}{\partial r} + \frac{1}{r}(-u^2 - v^2) = -\frac{\partial P}{\partial r} + \frac{1}{r^2 R_s}\left[\frac{\partial^2 w}{\partial^2 \theta} + \cot\theta\frac{\partial w}{\partial \theta} + r^2\frac{\partial^2 w}{\partial r^2} + 2r\frac{\partial w}{\partial r} + \left(2(w + u\cot\theta) - 2\frac{u}{\partial\theta}\right)\right], \tag{E.1d}$$

Here Re_s is the Reynolds number based on the sphere radius and can be defined as $Re_s = \Omega R^2/\nu = \epsilon^{-2}$. Following the study of ([63],[64]) and the study by ([61]) recently, we introduce the scaling as $\zeta = (r-1)/\epsilon)$ for the coordinate and non-dimensionalisation using these asymptotic formula

$$\begin{aligned} u &= U_0 + \epsilon\, U_1 + \mathcal{O}(\epsilon^2), \\ v &= V_0 + \epsilon\, V_1 + \mathcal{O}(\epsilon^2), \\ w &= \epsilon\, W_0 + \epsilon^2\, W_1 + \mathcal{O}(\epsilon^3), \\ p &= \epsilon\, P_0 + \mathcal{O}(\epsilon^2), \end{aligned} \tag{E.2}$$

Substituting Equations (E.2.1) into Equations (E.1) we obtain the the boundary layer equations and they are consistent with the ones derived in the literature

$$\frac{\partial U}{\partial \theta} + \frac{\partial W}{\partial \zeta} + U\cot\theta = 0, \tag{E.3a}$$

$$U\frac{\partial U}{\partial \theta} + W\frac{\partial U}{\partial \zeta} - V^2\cot\theta) = \frac{\partial U}{\partial \zeta^2}, \tag{E.3b}$$

$$U\frac{\partial V}{\partial \theta} + W\frac{\partial V}{\partial \zeta} + UV\cot\theta) = \frac{\partial V}{\partial \zeta^2}, \tag{E.3c}$$

Where (U, V, W) here is U_0, V_0 and W_0 respectively. The non-dimensional boundary conditions are expressed as

$$\begin{aligned} U &= \lambda\frac{\partial U}{\partial \zeta}, \\ V &= \eta\frac{\partial V}{\partial \zeta} + \sin\theta, \end{aligned} \tag{E.4}$$

$$W(0) = 0, \tag{E.5}$$

and

$$U = 0,\ V = 0 \quad \text{as}\ \zeta \to \infty. \tag{E.6}$$

These boundary conditions are derived from MW approach which assumes that roughness can be modelled by a modification of the no-slip conditions at

the disk surface. In particular, the model assumes partial slip at the sphere surface but is otherwise identical to the smooth surface formulation. where primes denote differentiation with respect to ζ, and the two parameters η and λ give empirical measures of the roughness in the radial and azimuthal directions.

E.2.2 *Steady mean flow solutions*

In order to solve Equations (E.3) at particular latitudes. a series expansion solution in powers of θ, constructing a solution of the form

$$\begin{aligned} U(\zeta,\theta) &= F_1\theta + F_3\theta 3 + F_5\theta^5 + F_7\theta^7, \\ V(\zeta,\theta) &= G_1\theta + G_3\theta 3 + G_5\theta^5 + G_7\theta^7, \\ W(\zeta,\theta) &= H_1\theta + H_3\theta 3 + H_5\theta^5 + H_7\theta^7, \end{aligned} \tag{E.7}$$

Where F_i, G_i and H_i are functions of the non-dimensional variable ζ and parameter θ, and $i = 1, 3, 5, ...$ are dimensionless and are funtions of an appropriate coordinate ζ where This is consistent with the series solution originally proposed by Howarth [63] and Banks [64] where $\theta = 0$. Also, the boundary conditions can take this form.

$$\begin{aligned} F_m(0) &= \lambda F'_m(0), \\ G_m(0) &= \eta G'_m(0) + \frac{(-1)^{\frac{m-1}{2}}}{m!}, \\ H_m(0) &= 0, \end{aligned} \tag{E.8}$$

and

$$F_m = G_m = 0 \quad \text{as}\, \zeta \to \infty. \tag{E.9}$$

It is interesting to note that after substituting the above series expansions into equations (E.3) we will have the first order equations are written below (E.2.2) in Equations and they are the same form as the von Kármán equations for the rotating disk. We therefore see there is a the similarity of the polar region with the rotating disk. So the von Kármán equations can be solved with a similarity solution of a similar form, and by asymptotically expanding in θ the series expansions will be the best option for a good approximation especially the area around the pole.

$$\begin{aligned} F_1^2 + H_1F'_1 - G_1^2 &= F'_1, \\ 2F_1G_1 + H_1G'_1 &= G'_1, \\ 2F_1 + H'_1 &= 0, \end{aligned} \tag{E.10}$$

The boundary layer Equations (E.3) and the boundary conditions Equations (E.6) are solved in order to get the mean flow. This will give us the mean boundary layer flow near the sphere surface which is expected to be similar to the flow on the rotating disk. The methodology to solve these equations is similar to that used by [18]. The solution by [64] is used up to $\theta = 6$. Beyond this polar angle the finite difference method is applied using space-marching for the θ direction and Newton method for the ζ direction. More specifically, three-point backwards differences are used for θ derivatives and central differencing for the ζ derivatives. The detailed implementation of the algorithm is given in [61]. The domain was discretised into 200 grid points uniformly distributed in the wall-normal direction between the sphere surface and $\eta_max = 20$, and 1000 uniformly distributed points between the pole and the equator. The tolerance for convergence of the Newton-Raphson method is such that the corrections should be less than $\theta < 10^{-5}$ of the equatorial tangential velocity. The resulting flow of the velocity components are presented in Subsection E.2.3, Subsection E.2.4 and Subsection E.2.5 that contain a variety of roughness parameters with a single value of a latitude. also, in Subsection 2.3.1 presents a single value of rough parameters at each latitude θ.

E.2.3 *Radially anisotropic roughness*

Table E.1: Numerical values of the mean velocity flow parameters $U'(0)$, $V'(0)$ and $W(\zeta_\infty)$ for $\theta = 20$

Parameters	$U'(0)$	$-V'(0)$	$-W(\zeta_\infty)$
$\eta = 0$	0.1516	0.1863	0.8683
$\eta = 0.25$	0.1244	0.1527	0.8125
$\eta = 0.50$	0.1062	0.1303	0.7707
$\eta = 0.75$	0.0931	0.1142	0.7374
$\eta = 1$	0.0831	0.1019	0.7099

Table E.2: Numerical values of the mean velocity flow parameters $U'(0)$, $V'(0)$ and $W(\zeta_\infty)$ for $\theta = 80$

Parameters	$U'(0)$	$-V'(0)$	$-W(\zeta_\infty)$
$\eta = 0$	0.2550	0.3533	0.6235
$\eta = 0.25$	0.2213	0.3151	0.5919
$\eta = 0.50$	0.1961	0.2842	0.5665
$\eta = 0.75$	0.1764	0.2590	0.5454
$\eta = 1$	0.1606	0.2381	0.5274

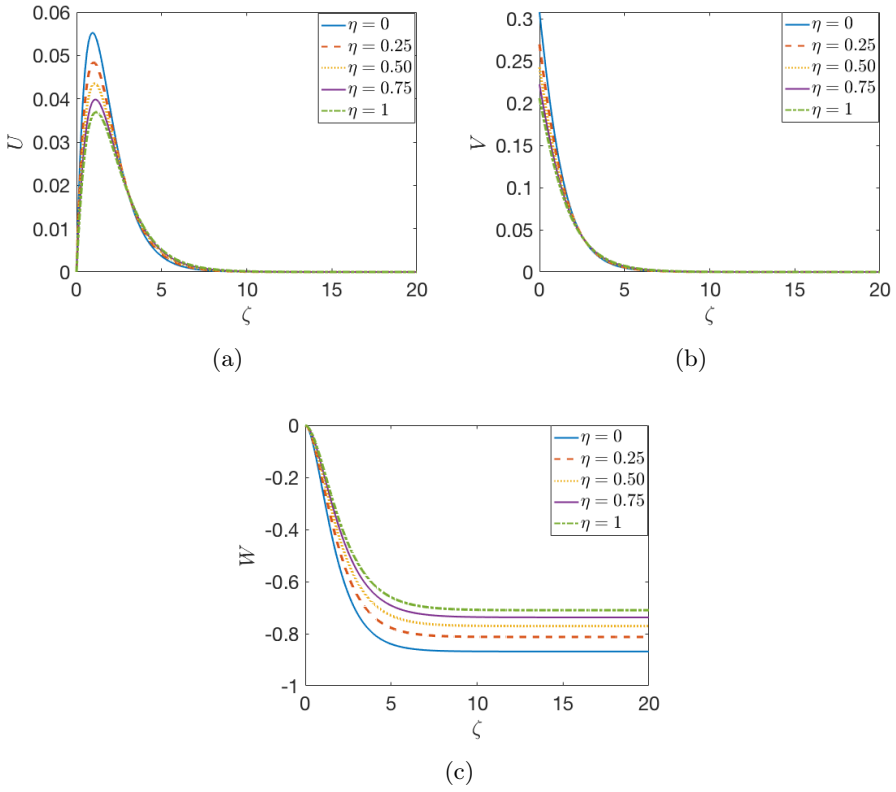

Figure E.1: Sphere boundary-layer velocity profiles for $\theta = 20$. (a) U-profile, (b) V-profile, (c) W-profile

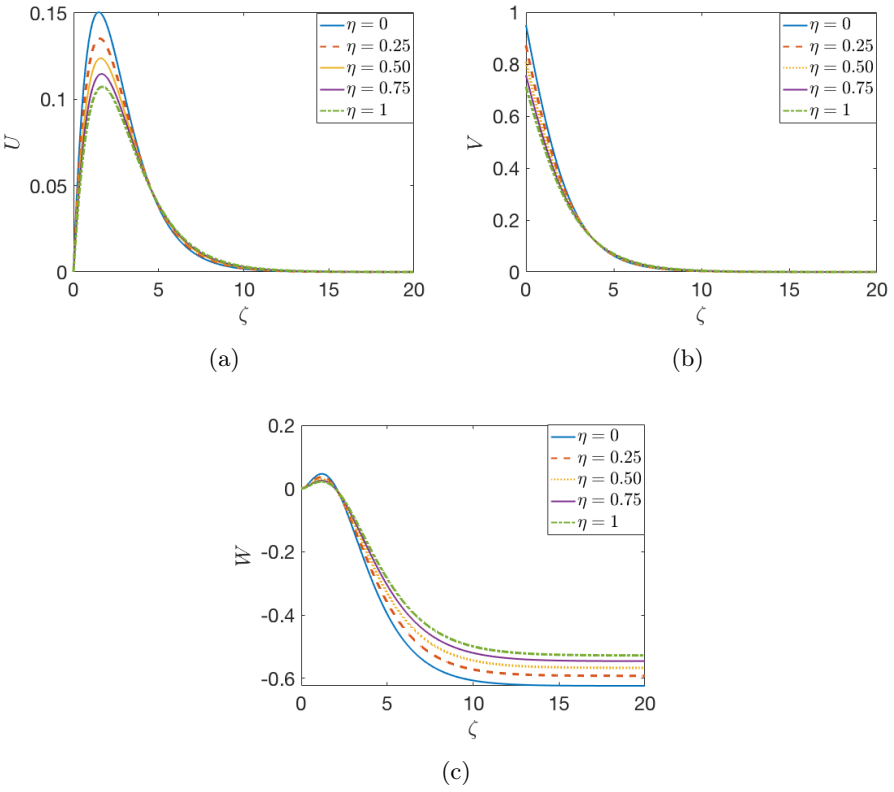

Figure E.2: Sphere boundary-layer velocity profiles for $\theta = 80$. (a) U-profile, (b) V-profile, (c) W-profile

E.2.4 *Azimuthally anisotropic roughness*

Table E.3: Numerical values of the mean velocity flow parameters $U'(0)$, $V'(0)$ and $W(\zeta_\infty)$ for $\theta = 20$

Parameters	$U'(0)$	$-V'(0)$	$-W(\zeta_\infty)$
$\lambda = 0$	0.1516	0.1863	0.8683
$\lambda = 0.25$	0.1199	0.2179	0.9237
$\lambda = 0.50$	0.0983	0.2374	0.9628
$\lambda = 0.75$	0.0830	0.2503	0.9907
$\lambda = 1$	0.0717	0.2594	1.0114

Table E.4: Numerical values of the mean velocity flow parameters $U'(0)$, $V'(0)$ and $W(\zeta_\infty)$ for $\theta = 80$

Parameters	$U'(0)$	$-V'(0)$	$-W(\zeta_\infty)$
$\lambda = 0$	0.2550	0.3533	0.6235
$\lambda = 0.25$	0.2250	0.3923	0.6552
$\lambda = 0.50$	0.2002	0.4241	0.6804
$\lambda = 0.75$	0.1793	0.4491	0.7003
$\lambda = 1$	0.1606	0.4687	0.7161

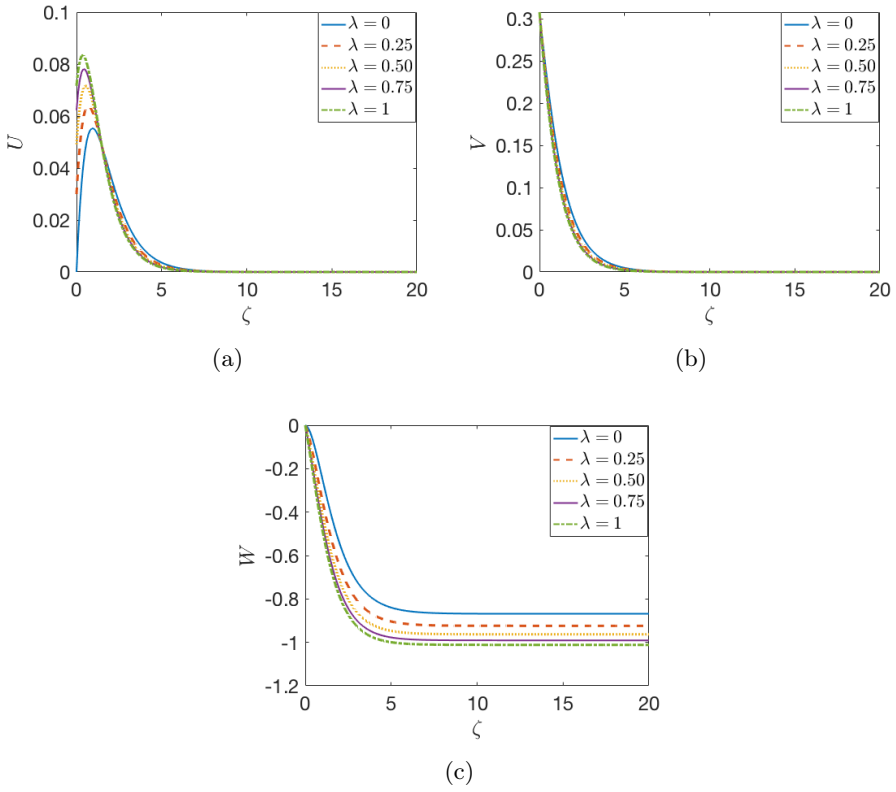

Figure E.3: Sphere boundary-layer velocity profiles for $\theta = 20$. (a) U-profile, (b) V-profile, (c) W-profile

E.2.5 *Isotropic roughness*

Table E.5: Numerical values of the mean velocity flow parameters $U'(0)$, $V'(0)$ and $W(\zeta_\infty)$ for $\theta = 20$

Parameters	$U'(0)$	$-V'(0)$	$-W(\zeta_\infty)$
$\lambda = \eta = 0$	0.1516	0.1863	0.8683
$\lambda = \eta = 0.25$	0.0972	0.1724	0.8533
$\lambda = \eta = 0.50$	0.0675	0.1523	0.8273
$\lambda = \eta = 0.75$	0.0500	0.1346	0.8007
$\lambda = \eta = 1$	0.0389	0.1201	0.7761

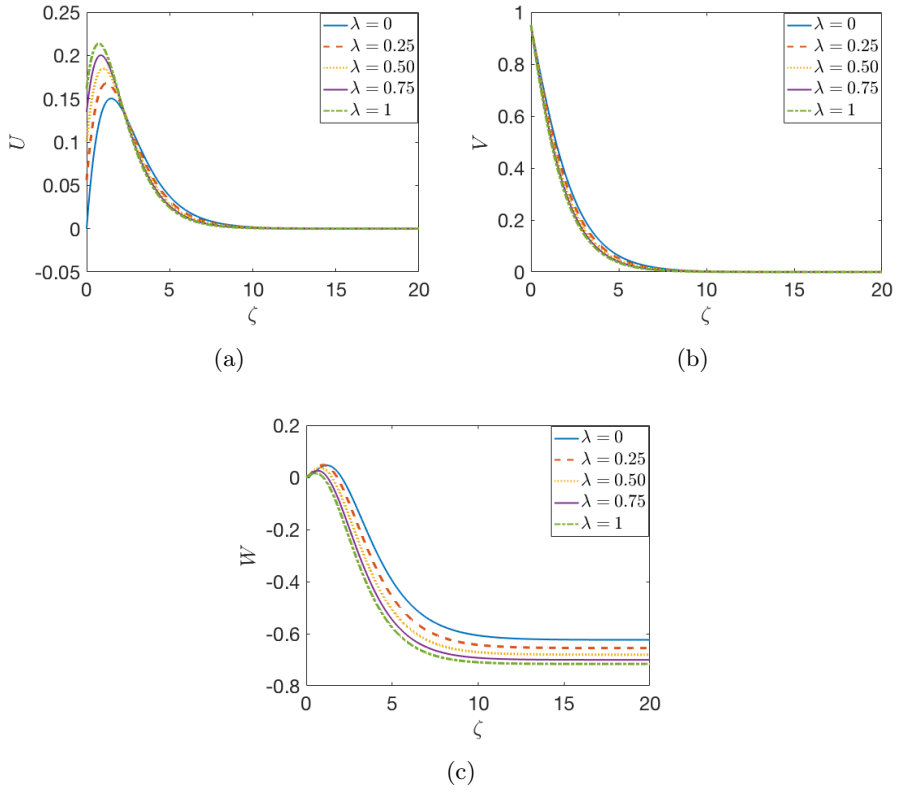

Figure E.4: Sphere boundary-layer velocity profiles for $\theta = 80$. (a) U-profile, (b) V-profile, (c) W-profile

Table E.6: Numerical values of the mean velocity flow parameters $U'(0)$, $V'(0)$ and $W(\zeta_\infty)$ for $\theta = 80$

Parameters	$U'(0)$	$-V'(0)$	$-W(\zeta_\infty)$
$\lambda = \eta = 0$	0.2550	0.3533	0.6235
$\lambda = \eta = 0.25$	0.1927	0.3457	0.6170
$\lambda = \eta = 0.50$	0.1488	0.3273	0.6041
$\lambda = \eta = 0.75$	0.1180	0.3052	0.5896
$\lambda = \eta = 1$	0.0960	0.2834	0.5753

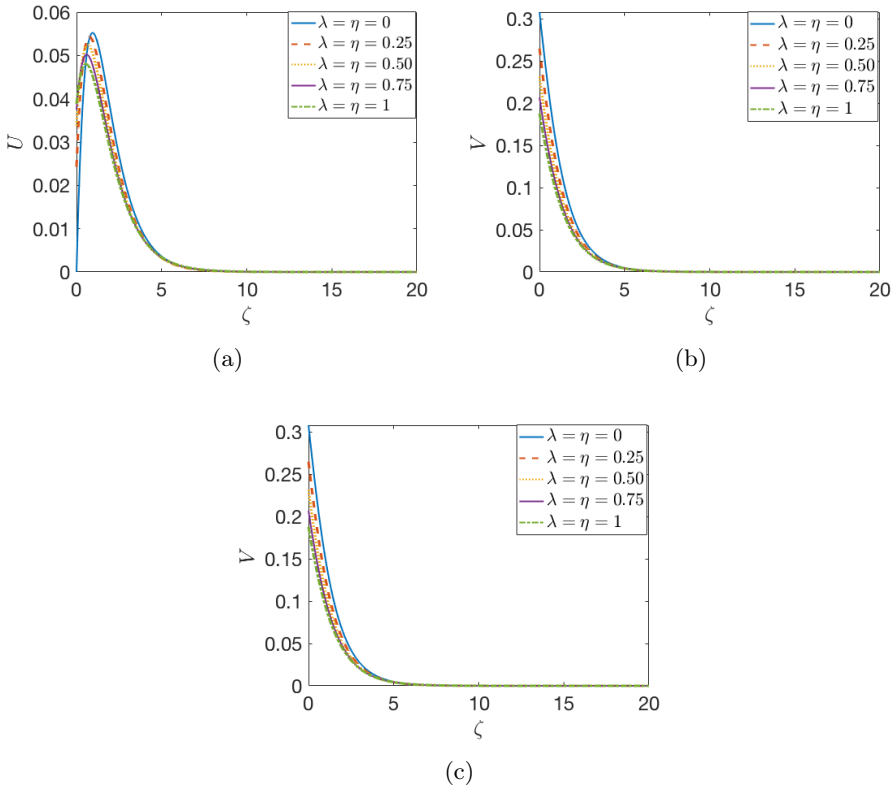

Figure E.5: Sphere boundary-layer velocity profiles for $\theta = 20$. (a) U-profile, (b) V-profile, (c) W-profile

E.2.6 *The effect of the latitude*

Table E.7: Numerical values of the mean velocity flow parameters $U'(0)$, $V'(0)$ and $W(\zeta_\infty)$ at various latitudes for $\lambda = \eta = 0.25$

Parameters	$U'(0)$	$-V'(0)$	$-W(\zeta_\infty)$
$\theta = 20^\circ$	0.0972	0.1724	0.8533
$\theta = 30^\circ$	0.1398	0.2471	0.8344
$\theta = 40^\circ$	0.1750	0.3080	0.8078
$\theta = 50^\circ$	0.2005	0.3511	0.7732
$\theta = 60^\circ$	0.2137	0.3735	0.7304
$\theta = 70^\circ$	0.2122	0.3724	0.6787
$\theta = 80^\circ$	0.1927	0.3457	0.6170

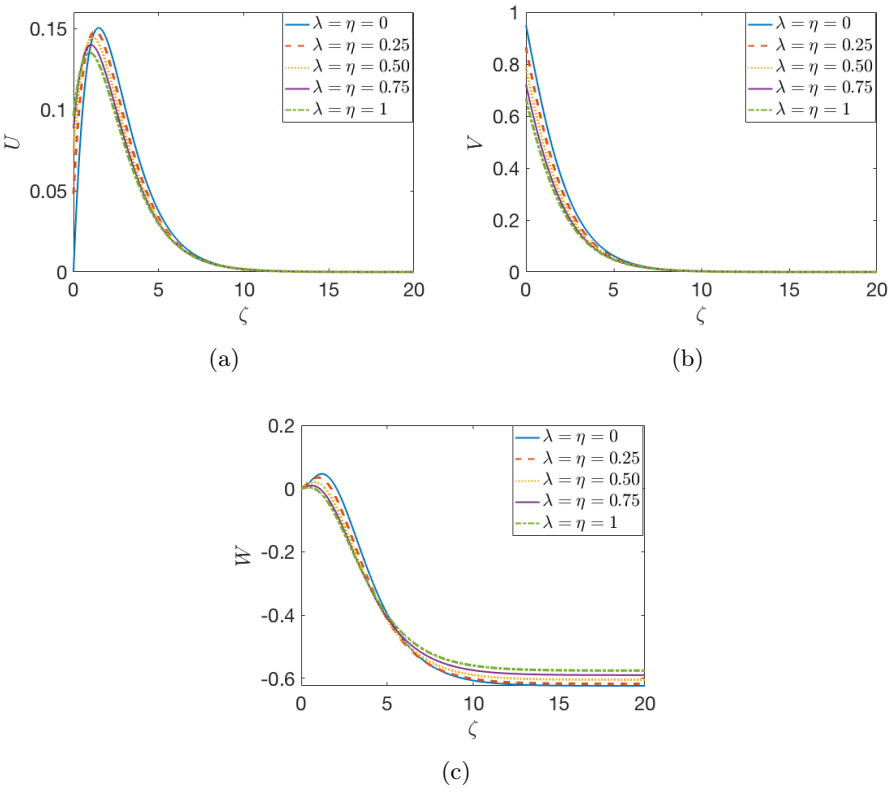

Figure E.6: Sphere boundary-layer velocity profiles for $\theta = 80$. (a) U-profile, (b) V-profile, (c) W-profile

E.2.7 Stability analysis

This equations are non-dimensionalised with respect to the local radial position r_a. Therefore, The local similarity variable are defined by

$$U(\zeta) = U^* + u^*, \qquad V(\zeta) = V^* + v^*, \qquad W(\zeta) = W^* + w^*, \qquad P(\zeta) = P^* + p^*. \tag{E.11}$$

After subtracting them into the mean flow equations.The equations governing the perturbations can be yield as

$$\boldsymbol{\nabla} \cdot \hat{\boldsymbol{u}} = 0, \tag{E.12}$$

$$\frac{\partial \hat{\boldsymbol{u}}}{\partial t} + (\hat{\boldsymbol{u}} \cdot \boldsymbol{\nabla})\boldsymbol{u} + (\boldsymbol{u} \cdot \boldsymbol{\nabla})\hat{\boldsymbol{u}} = -\frac{1}{\rho}\nabla\hat{p} + \nu\boldsymbol{\nabla}^{\mathbf{2}} \cdot \hat{\boldsymbol{u}}.$$

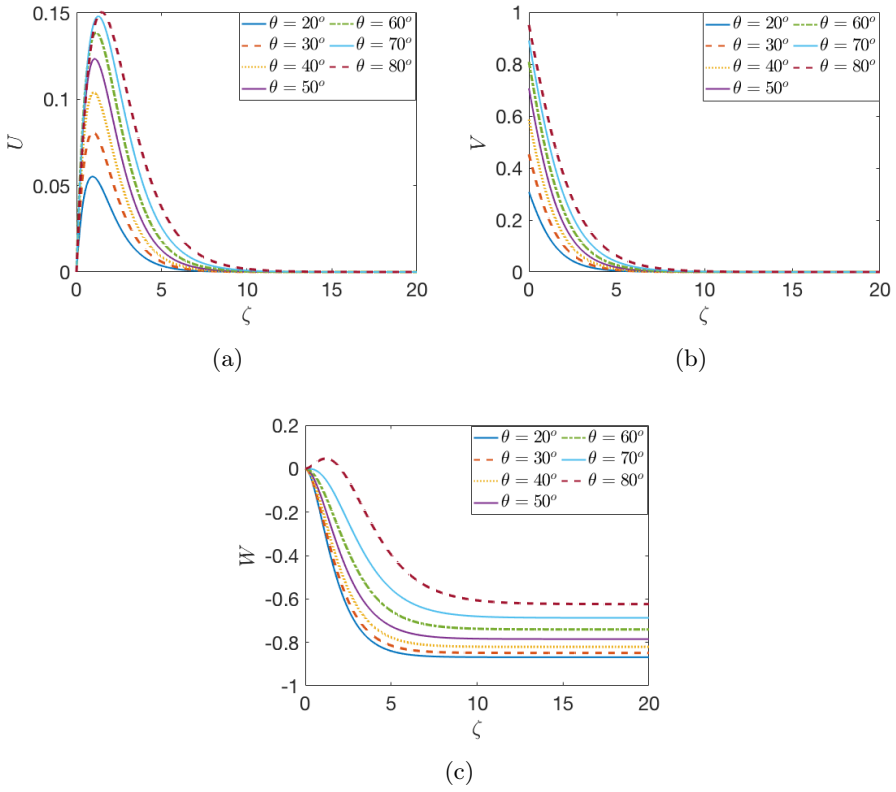

Figure E.7: Sphere boundary-layer velocity profiles at various latitudes for $\lambda = \eta = 0$. (a) U-profile, (b) V-profile, (c) W-profile

Some terms in the momentum equation can be expressed here as

$$\begin{aligned}(\hat{\boldsymbol{u}} \cdot \boldsymbol{\nabla})\boldsymbol{u} =& \frac{u}{r}\frac{\partial u}{\partial \theta} + w\frac{\partial u}{\partial r} + \frac{v}{rsin\theta}\frac{u}{\partial \phi} + \frac{1}{r}(uw - v^2\cot\theta) \\ & \frac{u}{r}\frac{\partial v}{\partial \theta} + w\frac{\partial v}{\partial r} + \frac{v}{rsin\theta}\frac{v}{\partial \phi}\frac{1}{r}(vw + uv\cot\theta) \\ & \frac{u}{r}\frac{\partial w}{\partial \theta} + w\frac{\partial w}{\partial r} + + \frac{v}{rsin\theta}\frac{w}{\partial \phi}\frac{1}{r}(-u^2 - v^2),\end{aligned} \tag{E.13}$$

$$\begin{aligned}(\boldsymbol{u} \cdot \boldsymbol{\nabla})\hat{\boldsymbol{u}} =& \frac{u}{r}\frac{\partial u}{\partial \theta} + w\frac{\partial u}{\partial r} + \frac{1}{r}(uw - v^2\cot\theta) \\ & \frac{u}{r}\frac{\partial v}{\partial \theta} + w\frac{\partial v}{\partial r} + \frac{1}{r}(vw + uv\cot\theta) \\ & \frac{u}{r}\frac{\partial w}{\partial \theta} + w\frac{\partial w}{\partial r} + \frac{1}{r}(-u^2 - v^2),\end{aligned} \tag{E.14}$$

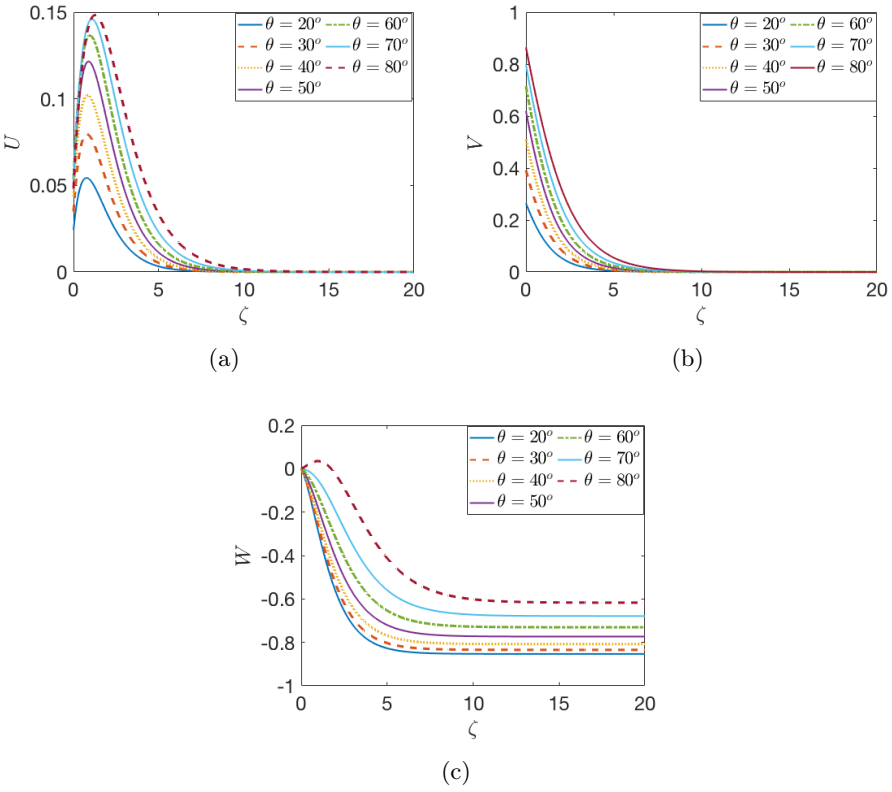

Figure E.8: Sphere boundary-layer velocity profiles at various latitudes for $\lambda = \eta = 0.25$. (a) U-profile, (b) V-profile, (c) W-profile

The perturbation velocity $\hat{u}$ and pressure $\hat{p}$ can be expanded in the normal-mode form

$$(u, v, w, p) = (\hat{u}, \hat{v}, \hat{w}, e^{\mathrm{i}(\alpha\theta + \beta sine(\theta)\phi - \omega t)}) \tag{E.15}$$

Here $\alpha = \alpha_\mathrm{r} + \mathrm{i}\alpha_\mathrm{i}$ is the radial wave number, β is the azimuthal wave number (which is real) and ω is the frequency of the disturbances expressed in the rotating frame. Also the number of completed cycles of the perturbations around the azimuthal angle defined as $\bar{n} = \bar{\beta} Re$. Furthermore, non-dimensionalising the perturbation parameters by substituting the following formula:

$$u(\zeta) = a\Omega\hat{u}, \qquad v(\zeta) = a\Omega\hat{v}, \qquad w(\zeta) = a\Omega\hat{w}, \qquad p(\zeta) = a\Omega\hat{p}. \tag{E.16}$$

$$\alpha = \alpha^* \delta^*, \qquad \beta = \beta^* \delta^*, \qquad l = \frac{1}{1 + \delta\xi}, \tag{E.17}$$

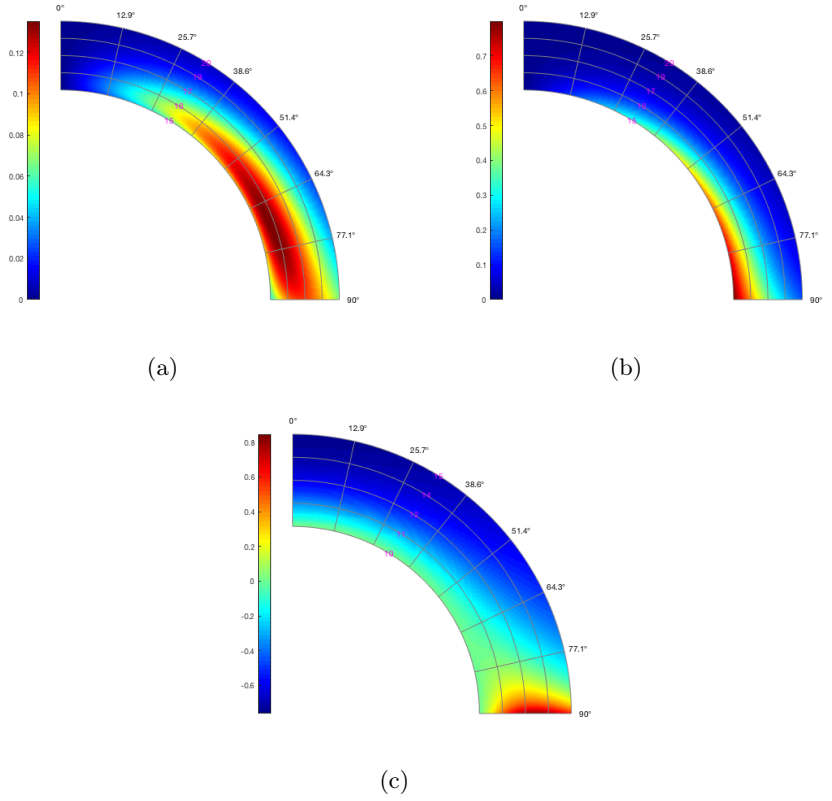

(a) (b)

(c)

Figure E.9: Contours of the mean flow velocity components with $\lambda = \eta = 0.25$. (a) U-profile, (b) V-profile, (c) W-profile

and imposing (E.15) into (E.2.7) and (E.2.7), ignoring all the terms R^2, the eigenvalue problem can be written as

$$\frac{\hat{w}}{\xi} + 2l\frac{\hat{w}}{Re} + l\Big[\Big(i\alpha + \frac{\cot\theta}{Re}\Big)\hat{u} + i\bar{\beta}\hat{v}\Big] = 0, \tag{E.18a}$$

$$\frac{l}{Re}W\frac{\hat{u}}{\xi}\Big[\Big(i\alpha U + i\bar{\beta}V - i\omega\Big) + \frac{l}{Re}\frac{\partial U}{\partial\theta}\Big]\hat{u} - 2l\frac{V\hat{v}\cot\theta}{Re}\Big(\frac{\partial U}{\partial\xi} + \frac{lU}{Re}\Big)\hat{w} = -i\alpha l\hat{p} + \frac{1}{Re}\Big[\frac{\partial^2\hat{u}}{\partial\xi} - l^2\Big(\alpha^2 + \beta^2\Big)\hat{u}\Big], \tag{E.18b}$$

$$\frac{l}{Re}W\frac{\hat{v}}{\xi}\Big[\Big(i\alpha U + i\bar{\beta}V - i\omega\Big) + \frac{l}{Re}U\cot\theta\Big]\hat{v} - 2l\frac{l\hat{u}}{Re}\Big(\frac{\partial V}{\partial\theta} + V\cot\theta\Big) + \Big(\frac{\partial V}{\partial\xi} + \frac{Vl}{Re}\Big)\hat{w} = -i\beta l\hat{p} + \frac{1}{Re}\Big[\frac{\partial^2\hat{v}}{\partial\xi} - l^2\Big(\alpha^2 + \beta^2\Big)\hat{v}\Big], \tag{E.18c}$$

$$\frac{l}{Re}W\frac{\hat{w}}{\xi}\Big[\Big(i\alpha U+i\bar{\beta}V-i\omega\Big)+\frac{1}{Re}\frac{\partial W}{\partial\theta}\Big]\hat{w}-2l\frac{U\hat{u}}{Re}-2l\frac{V\hat{v}}{Re}=-\frac{\hat{p}}{\xi}$$
$$+\frac{1}{Re}\Big[\frac{\partial^2\hat{w}}{\partial\xi}-l^2\Big(\alpha^2+\beta^2\Big)\hat{w}\Big], \quad \text{(E.18d)}$$

l factor can be expected to be 1. The orientation angle of the stationary vortices with respect to a circle centred on the axis of rotation is given as

$$\phi=\tan^{-1}\left(\frac{\bar{\beta}}{\bar{\alpha}}\right)\Leftrightarrow\tan\left(\frac{\pi}{2}-\phi\right)=\frac{\alpha r}{\beta}, \quad \text{(E.19)}$$

References

[1] M. Miklavčič and C. Wang, "The flow due to a rough rotating disk," *Zeitschrift für Angewandte Mathematik und Physik (ZAMP)*, vol. 55, no. 2, pp. 235–246, 2004.

[2] P. T. Griffiths, *Hydrodynamic stability of non-Newtonian rotating boundary-layer flows*. PhD thesis, University of Birmingham, 2016.

[3] N. Gregory, J. Stuart, and W. Walker, "On the stability of three-dimensional boundary layers with application to the flow due to a rotating disk," *Philosophical Transactions of the Royal Society of London A: Mathematical, Physical and Engineering Sciences*, vol. 248, no. 943, pp. 155–199, 1955.

[4] H. A. Nasr-El-Din, A. M. Al-Mohammed, A. Al-Aamri, O. A. Al-Fuwaires, *et al.*, "Reaction of gelled acids with calcite," *SPE Production & Operations*, vol. 23, no. 03, pp. 353–361, 2008.

[5] P. J. Schmid and D. S. Henningson, *Stability and transition in shear flows*, vol. 142. Springer Science & Business Media, 2012.

[6] P. G. Drazin and W. H. Reid, *Hydrodynamic stability*. Cambridge university press, 2004.

[7] P. Huerre, G. Batchelor, H. Moffatt, and M. Worster, "Open shear flow instabilities," *Perspectives in fluid dynamics*, pp. 159–229, 2000.

[8] P. Huerre and P. A. Monkewitz, "Local and global instabilities in spatially developing flows," *Annual review of fluid mechanics*, vol. 22, no. 1, pp. 473–537, 1990.

[9] T. von Kármán, "Über laminare und turbulente Reibung," *Z. Angew. Math. Mech.*, vol. 1, pp. 233–252, 1921.

[10] W. Cochran, "The flow due to a rotating disc," in *Mathematical Proceedings of the Cambridge Philosophical Society*, vol. 30, pp. 365–375, Cambridge University Press, 1934.

[11] G. K. Batchelor, "Note on the class of solutions of the Navier-Stokes equations representing steady non-rotationally symmetric flow," *Q. J. Mech. Appl. Math.*, vol. 4, pp. 29–41, 1951.

[12] V. U. Bödewadt, "Die drehströmung über festem grunde," *ZAMM-Journal of Applied Mathematics and Mechanics/Zeitschrift für Angewandte Mathematik und Mechanik*, vol. 20, no. 5, pp. 241–253, 1940.

[13] R. J. Lingwood, "An experimental study of absolute instability of the rotating-disk boundary-layer flow," *J. Fluid Mech.*, vol. 314, pp. 373–405, 1996.

[14] M. R. Malik, "The neutral curve for stationary disturbances in rotating-disk flow," *J. Fluid Mech.*, vol. 164, pp. 275–287, 1986.

[15] P. Hall, "An asymptotic investigation of the stationary modes of instability of the boundary layer on a rotating disc," in *Proceedings of the Royal Society of London A: Mathematical, Physical and Engineering Sciences*, vol. 406, pp. 93–106, The Royal Society, 1986.

[16] J. Gajjar, "Nonlinear critical layers in the boundary layer on a rotating disk," *Journal of Engineering Mathematics*, vol. 57, no. 3, pp. 205–217, 2007.

[17] R. Lingwood and S. Garrett, "The effects of surface mass flux on the instability of the bek system of rotating boundary-layer flows," *European Journal of Mechanics-B/Fluids*, vol. 30, no. 3, pp. 299–310, 2011.

[18] S. J. Garrett and N. Peake, "The stability and transition of the boundary layer on a rotating sphere," *Journal of Fluid Mechanics*, vol. 456, pp. 199–218, 2002.

[19] S. J. Garrett, Z. Hussain, and S. Stephen, "The cross-flow instability of the boundary layer on a rotating cone.," 2009.

[20] Z. Hussain, S. J. Garrett, and S. Stephen, "The centrifugal instability of the boundary-layer flow over slender rotating cones," *Journal of fluid mechanics*, vol. 755, 2014.

[21] P. Mitschka and J. Ulbrecht, "Nicht-newtonsche flüssigkeiten iv. strömung nicht-newtonscher flüssigkeiten ostwald-de-waeleschen typs in der umgebung rotierender drehkegel und scheiben," *Collection of Czechoslovak Chemical Communications*, vol. 30, no. 8, pp. 2511–2526, 1965.

[22] J. P. Denier and R. E. Hewitt, "Asymptotic matching constraints for a boundary-layer flow of a power-law fluid," *J. Fluid Mech.*, vol. 518, pp. 261–279, 2004.

[23] H. Andersson, E. De Korte, and R. Meland, "Flow of a power-law fluid over a rotating disk revisited," *Fluid Dynamics Research*, vol. 28, no. 2, pp. 75–88, 2001.

[24] J. P. Denier and R. E. Hewitt, "Asymptotic matching constraints for a boundary-layer flow of a power-law fluid," *Journal of Fluid Mechanics*, vol. 518, pp. 261–279, 2004.

[25] P. T. Griffiths, "Flow of a generalised newtonian fluid due to a rotating disk," *Journal of Non-Newtonian Fluid Mechanics*, vol. 221, pp. 9–17, 2015.

[26] E. Bingham, "An investigation of the laws of plastic flow. bul bur standards 13: 309-353," 1916.

[27] P. J. Carreau, "Rheological equations from molecular network theories," *Transactions of the Society of Rheology*, vol. 16, no. 1, pp. 99–127, 1972.

[28] P. Griffiths, S. J. Garrett, and S. Stephen, "The neutral curve for stationary disturbances in rotating disk flow for power-law fluids," *Journal of Non-Newtonian Fluid Mechanics*, vol. 213, pp. 73–81, 2014.

[29] P. Carpenter, "The right sort of roughness," *Nature*, vol. 388, no. 6644, pp. 713–714, 1997.

[30] R. B. Carrillo Jr, M. S. Reibert, and W. S. Saric, "Distributed-roughness effects on stability and transition in swept-wing boundary layers," 1997.

[31] J. H. Fransson, A. Talamelli, L. Brandt, and C. Cossu, "Delaying transition to turbulence by a passive mechanism," *Physical review letters*, vol. 96, no. 6, p. 064501, 2006.

[32] B. Alveroglu, A. Segalini, and S. J. Garrett, "The effect of surface roughness on the convective instability of the BEK family of boundary-layer flows," *Euro. J. Mech. (B/Fluids)*, vol. 56, pp. 178–187, 2016.

[33] M. Miklavčič and C. Wang, "The flow due to a rough rotating disk," *Zeitschrift für angewandte Mathematik und Physik ZAMP*, vol. 55, no. 2, pp. 235–246, 2004.

[34] M. S. Yoon, J. M. Hyun, and J. S. Park, "Flow and heat transfer over a rotating disk with surface roughness," *International journal of heat and fluid flow*, vol. 28, no. 2, pp. 262–267, 2007.

[35] A. J. Cooper, J. H. Harris, S. J. Garrett, M. Özkan, and P. J. Thomas, "The effect of anisotropic and isotropic roughness on the convective stability of the rotating disk boundary layer," *Phys. Fluids*, vol. 27, p. 014107, 2015.

[36] S. J. Garrett, A. J. Cooper, J. H. Harris, M. Özkan, A. Segalini, and P. J. Thomas, "On the stability of von Kármán rotating-disk boundary layers with radial anisotropic surface roughness," *Phys. Fluids*, vol. 28, p. 014104, 2016.

[37] S. O. Stephen, "Effects of partial slip on rotating-disc boundary-layer flows," 2016.

[38] B. Alveroglu, A. Segalini, and S. J. Garrett, "An energy analysis of convective instabilities of the bödewadt and ekman boundary layers over rough surfaces," *European Journal of Mechanics-B/Fluids*, vol. 61, pp. 310–315, 2017.

[39] B. Sahoo and H. Sharma, "Effects of partial slip on the steady von karman flow and heat transfer of a non-newtonian fluid," *Bulletin of the Brazilian Mathematical Society*, vol. 38, no. 4, pp. 595–609, 2007.

[40] R. B. Bird, R. C. Armstrong, and O. Hassager, "Dynamics of polymeric liquids. vol. 1: Fluid mechanics," 1987.

[41] P. Mitschka and J. Ulbrecht, "Nicht-Newtonsche Flüssigkeiten IV. Strömung Nicht-newtonsche Flüssigkeiten Ostwald-de Waelescher Typs in der Umgebung Rotierender Drehkegel und S chieben," *Coll. Czech. Chem. Comm.*, vol. 30, pp. 2511–2526, 1965.

[42] P. T. Griffiths, "Flow of a generalised Newtonian fluid due to a rotating disk," *J. Non-Newtonian Fluid Mech.*, vol. 221, pp. 9–17, 2015.

[43] P. T. Griffiths, S. O. Stephen, A. P. Bassom, and S. J. Garrett, "Stability of the boundary layer on a rotating disk for power law fluids," *J. Non-Newtonian Fluid Mech.*, vol. 207, pp. 1–6, 2014.

[44] P. T. Griffiths, S. J. Garrett, and S. O. Stephen, "The neutral curve for stationary disturbances in rotating disk flow for power-law fluids," *J. Non-Newtonian Fluid Mech.*, vol. 213, pp. 73–81, 2014.

[45] E. C. Bingham, "An investigation of the laws of plastic flow," *Bull. U. S. Bur. of Standards*, vol. 13, pp. 309–352, 1916.

[46] P. J. Carreau, "Rheological Equations from Molecular Network Theories," *Trans. Soc. Rheolo.*, vol. 16:1, pp. 99–127, 1972.

[47] C. Nouar and I. Frigaard, "Stability of plane couette–poiseuille flow of shear-thinning fluid," *Physics of Fluids*, vol. 21, no. 6, p. 064104, 2009.

[48] C. Nouar, A. Bottaro, and J. Brancher, "Delaying transition to turbulence in channel flow: revisiting the stability of shear-thinning fluids," *Journal of Fluid Mechanics*, vol. 592, p. 177, 2007.

[49] C. Navier, "Mémoire sur les lois du mouvement des fluides," *Mémoires de lâ€™Académie Royale des Sciences de lâ€™Institut de France*, vol. 6, no. 1823, pp. 389–440, 1823.

[50] B. Alveroğlu, *The convective instability of the BEK system of rotating boundary-layer flows over rough disks.* PhD thesis, Department of Mathematics, 2016.

[51] M. Abdulameer, P. Griffiths, B. Alveroğlu, and S. J. Garrett, "On the stability of the bek family of rotating boundary-layer flows for power-law fluids," *Journal of Non-Newtonian Fluid Mechanics*, vol. 236, pp. 63–72, 2016.

[52] E. Appelquist, *Direct numerical simulations of the rotating-disk boundary-layer flow.* PhD thesis, KTH Royal Institute of Technology, 2014.

[53] A. J. Cooper and P. W. Carpenter, "The stability of rotating-disc boundary-layer flow over a compliant wall. Part 1. Type i and ii instabilities," *J. Fluid Mech.*, vol. 350, pp. 231–259, 1997.

[54] M. Al-Malki, S. Garrett, S. Camarri, and Z. Hussain, "The effects of roughness levels on the instability of the boundary-layer flow over a rotating disk with an enforced axial flow," *Physics of Fluids*, vol. 33, no. 10, p. 104109, 2021.

[55] T. V. Kármán, "Über laminare und turbulente reibung," *ZAMM-Journal of Applied Mathematics and Mechanics/Zeitschrift für Angewandte Mathematik und Mechanik*, vol. 1, no. 4, pp. 233–252, 1921.

[56] P. P. Dabrowski, *Boundary-layer flows in non-Newtonian fluids.* PhD thesis, 2009.

[57] A. Alqarni, B. Alveroğlu, P. Griffiths, and S. Garrett, "The instability of non-newtonian boundary-layer flows over rough rotating disks," *Journal of Non-Newtonian Fluid Mechanics*, vol. 273, p. 104174, 2019.

[58] M. A. Abdulameer, *The Convective Instability of BEK Family of Non-Newtonian Rotating Boundary-Layer Flows.* PhD thesis, Department of Mathematics, 2018.

[59] S. Garrett and N. Peake, "The stability of the boundary layer on a sphere rotating in a uniform axial flow," *European Journal of Mechanics-B/Fluids*, vol. 23, no. 2, pp. 241–253, 2004.

[60] R. J. Lingwood, "Absolute instability of the boundary layer on a rotating disk," *Journal of Fluid Mechanics*, vol. 299, pp. 17–33, 1995.

[61] A. Segalini and S. J. Garrett, "On the non-parallel instability of the rotating-sphere boundary layer," *Journal of Fluid Mechanics*, vol. 818, pp. 288–318, 2017.

[62] C. Davies and P. W. Carpenter, "Global behaviour corresponding to the absolute instability of the rotating-disk boundary layer," *J. Fluid Mech.*, vol. 486, pp. 287–329, 2003.

[63] L. Howarth, "Cxxix. note on the boundary layer on a rotating sphere," *The London, Edinburgh, and Dublin Philosophical Magazine and Journal of Science*, vol. 42, no. 334, pp. 1308–1315, 1951.

[64] W. Banks, "The boundary layer on a rotating sphere," *The Quarterly Journal of Mechanics and Applied Mathematics*, vol. 18, no. 4, pp. 443–454, 1965.